Ph.D. School in Chemical Science and Technology

Cycle XXXIV

Computational and Synthetic Approaches to Drug Discovery in Anticancer and Antibacterial Chemotherapy

Scientific disciplinary sector: CHIM/08

Ph.D. Student	Federico Riu
Coordinator of the Ph.D. Programme	Prof. Stefano Enzo
Supervisor	Prof. Antonio Carta

Final exam. Academic Year 2020 – 2021

Thesis defense: January–February 2022 Session

CONTENTS:

1. List of Publications

1) F. Riu, L. Sanna, R. Ibba, S. Piras, V. Bordoni, M. A. Scorciapino, M. Lai, S. Sestito, L. Bagella, A. Carta, A comprehensive assessment of a new series of 5',6'–difluorobenzotriazole–acrylonitrile derivatives as microtubule targeting agents (MTAs), Eur. J. Med. Chem., 2021, 222, 113590. https://doi.org/10.1016/j.ejmech.2021.113590.

2) S. Piras, R. Ibba, P. Corona, F. Riu, R. Loddo, I. Delogu, G. Collu, A. Carta, Synthesis, antitumor and antiviral in vitro activities of new benzotriazole–dicarboxamide derivatives, Front. Chem., 2021, 9, 660424. https://doi.org/10.3389/fchem.2021.660424.

3) P. Corona, S. Piras, R. Ibba, F. Riu, G. Murineddu, G. Sanna, S. Madeddu, I. Delogu, R. Loddo, A. Carta, Antiviral Activity of Benzotriazole Based Derivatives, The Open Medicinal Chemistry Journal, 2020, 14, 83–98. DOI: 10.2174/1874104502014010083.

4) S. Piras, P. Corona, R. Ibba, F. Riu, G. Murineddu, G. Sanna, S. Madeddu, I. Delogu, R. Loddo, A. Carta, Preliminary Anti–Coxsackie Activity of Novel 1–[4–(5,6–dimethyl(*H*)–1*H*(2*H*)–benzotriazol–1(2)–yl)phenyl]–3–alkyl(aryl)ureas, Medicinal Chemistry, 2020, 16, 5. DOI: 10.2174/1573406416666191226142744.

5) F. Riu, A. Ruda, O. Engström, C. Muheim, H. Mobarak, J. Ståhle, P. Kosma, A. Carta, D. O. Daley, G. Widmalm, A Lead-Based Fragment Library Screening of the Glycosyltransferase WaaG from *Escherichia coli*. Manuscript in preparation.

2. Representative Abbreviations

FBDD	Fragment–based Drug Discovery
ESI–MS	Electrospray ionization mass spectrometry
CADD	Computer–aided Drug Discovery
SAR	Structure–activity relationship
MD	Molecular Dynamics
MTA/ MDA	Microtubule–targeting/ microtubule–destabilizing agents
CBSI	Colchicine–binding site inhibitors
IC_{50}	Half–maximal Inhibitory Concentration
LIE	Linear Interaction Energy
BFE	Binding Free Energy
K_D	Dissociation constant
Rha	Rhamnose
Glc	Glucose
Man	Mannose
Pico	Picoloyl ester
TBDPS	tert–Butyldiphenylsilyl
NAP	2–Naphthylmethyl
UDP	Uridine–5'–diphosphate
RMSD	Root–mean–square deviation
DIMCARB	Dimethylammonium dimethylcarbamate
TEA	Triethylamine
NOESY	^{1}H two–dimensional NOE SpectroscopY
EPI	Efflux pump inhibitor
P–gp	P–glycoprotein
ADME	Absorption – Distribution – Metabolism – Elimination
NSCLC	Non–small cell lung cancer
DMSO	Dimethyl sulfoxide
MDR/ XDR	Multi–/ extensively–drug resistance
WaaG	UDP–glucose:(heptosyl)LPS alpha–1,3–glucosyltransferase [EC:2.4.1.–]
LPS	Lipopolysaccharide
D–GlcN	D–Glucosamine
L,D–Hep	L–*glycero*–D–*manno*–heptose
Kdo	3–deoxy–D–*manno*–oct–2–ulosonic acid
SFNG	Symbol Nomenclature for Glycans

3. Abstract of the Thesis

The present Thesis consists of different Medicinal Chemistry projects which include a combination of computational and experimental approaches to Drug Discovery. The final aim is to obtain small molecules of biological interest in anticancer and antibacterial chemotherapy. Projects #1 and #2 (Chapters 5 and 6) are focused on the rational design and synthesis of two new series of small molecules with a benzotriazole scaffold functionalized with an acrylonitrile moiety as new anticancer agents acting on tubulin assembly as CBSIs (colchicine–binding site inhibitors). The functionalization of the main scaffold with fluorine atoms in different positions (5',6' or 4', respectively) led to the synthesis of two new series of benzotriazole–based small molecules. The first approach focused on the application of Molecular Docking techniques to analyze the binding pose of the molecules at the interface between α– and β–tubulin, studying electrostatic and vdW interactions. The molecules showed a good binding profile, hence they were synthesized, characterized and biologically analyzed. They displayed a good antiproliferative activity and, through a specific biological assessment, they showed to interfere with tubulin assembly and to specifically compete with colchicine for its binding pocket on tubulin. Project #3 (Chapter 7) makes use of a fragment–based drug discovery (FBDD) approach aimed to find new fragments to build new inhibiting agents for a protein called WaaG. This target is a glycosyltransferase involved in the biosynthesis of the lipopolysaccharide (LPS), present in gram–negative bacteria, such as *Escherichia coli*. Two libraries of small molecules were screened through Molecular Docking simulations. The selected ones were more in–depth assessed through a Molecular Dynamics (MD) study, to calculate their Binding Free Energy (BFE) and related K_D values, the root–mean–square deviation (RMSD) of the protein backbone (when bound to the ligands), but also protein–ligand electrostatic (mainly hydrogen bonds) and hydrophobic interactions. A study on the protein movement during the MD trajectory of WaaG *apo–protein* showed a dynamic behavior of both N– and C– domains one against each other, allowing to predict a twisting–like fashion of the protein.

Project #4 (Chapter 8) is a synthetic study on 1,2–*cis*–glycosylation reactions, aimed to optimize yield and stereoselectivity of the reactions. The goal of the synthesis is a trisaccharide; NMR investigations are ongoing for the determination of the exact conformational state of the trisaccharide. *Aeromonas salmonicida* is a gram–negative bacterium whose outer membrane is made of lipopolysaccharide (LPS). In the O–antigen of its LPS there is a trisaccharide structurally similar to the synthesized trisaccharide building

block. The full NMR characterization of the synthesized trisaccharide will be helpful in future Structure Elucidation investigations on *A. salmonicida* lipopolysaccharide.

4. General Introduction

4.1. Medicinal Chemistry: the challenge of new successful drugs

Medicinal Chemistry is an important step in the Drug Discovery process, focusing on the design, synthesis, chemical characterization, and *in vitro/in vivo* activities of novel molecules against biological targets and their physicochemical and pharmacokinetic properties. Medicinal Chemistry is a multidisciplinary field that helps Drug Discovery and Development in the early phases by synthesizing molecules with biological interest. It explores the different activities of a broad spectrum of molecules with great diversity and flexibility. Natural resources represented the starting point for Medicinal Chemistry, with a great number of natural compounds characterized by different degrees of structural complexity and a large spectrum of biological activities. Hence, the first challenge was to recognize those molecules in nature, study different methods for their extraction and explore their global profile such as structural, functional, physical and chemical features. The step forward is represented by the synthesis of analogs, with improved or, at least similar, properties and the subsequent biological assessment to determine if the newly synthetized molecules could be more active than the naturally occurring ones. If a molecule is considered sufficiently effective and safe for the human body, it can be synthesized on large scale to be developed as a drug in a proper formulation. [1]

Medicinal Chemistry is a complex chemistry field; a recent paper, published by *Murcko M. A.*, [2] listed the behavioral characteristics of a proper medicinal chemist. As general characteristics, he is obsessed with data and details, but also open to face assumptions and solve dogmas. Medicinal chemists are often highly networked and collaborative, because "great science happens everywhere". Drug discovery is defined as a "team sport" and requires scientists from different fields, so the important thing is to "remain humble" discussing with each other. A certain number of "discipline–specific characteristics" of the medicinal chemist were also identified. He always thinks about the so–called "target product profile" (TPP), *i.e.,* the characteristics the desired compounds must have to gain clinical interest. He must know how to handle the different properties of a desired compound, not

necessarily following strict chemical rules (as the excessive lipophilicity), but also thinking of the three–dimensional properties of the chemical entity, in different possible environments: *water or lipid, inside or outside the cell, in complex with the target or free*. Last but not least, medicinal chemists tend to be "resilient": if something goes wrong (*e.g.* the synthetic process), they have always a new chemical scaffold to concentrate on, not giving up on validated targets or difficulties along the synthetic pathway. [2] This Introduction will explain the importance of the Drug Discovery process, highlighting experimental and computational approaches of it and focusing on Molecular Docking and Dynamics techniques. A discussion on anticancer and antibacterial chemotherapy is also included, as a foreword to the present Thesis.

4.2. The workflow of Drug Discovery

The process of Drug Discovery (DD) is the way of identifying compounds with various pharmacological activities, which can become drug substances when incorporated into the Drug Development machinery. Drug Development involves a lot of fields such as biotechnology, biopharmaceutics, toxicology, pharmaceutical engineering and, last but not least, medicinal chemistry. [1] In recent times, taking into account the Medicinal Chemistry approach to DD, its association with Artificial Intelligence (AI) techniques is gaining interest to improve and speed up the Drug Discovery process. [1] Artificial Intelligence, and particularly its subfield Machine Learning (ML) is a branch of computer science that investigates the way of "training" and enabling computer machines to comprehend and perform tasks simulating human intelligence, hence without being explicitly programmed for those tasks. The Drug Discovery process employs AI techniques, *e.g.* for designing molecules, using labeled training datasets to train models, the so–called *supervised learning*. [3] The common goal for Medicinal Chemistry and Artificial Intelligence is the discovery of drug targets (*e.g.* a protein target), the identification of new lead compounds, refining the design considering different chemical properties of the molecules, but also designing the more suitable synthetic route to yield the compounds. [4]

The Drug Discovery process is always in progress, there are no strict rules or laws. The modern approach of designing new drugs is based on a Rational–based Drug Design, which could be divided into Structure–based and Ligand–based Drug Design. The Structure–based (or Target–focused) Drug Design is based on a growing knowledge of various biological targets, which can be represented by proteins (receptors, enzymes or amino acids), or nucleic

acids. Pursuing the Structure–based approach, some of the most important strategies for Drug Discovery are *in silico* methods or the *de novo* synthesis. In the field of *in silico* methods, Molecular Modeling strategies, such as Molecular Docking or Molecular Dynamics, as well as Molecular Mechanics, are gaining relevance in Drug Discovery and Development. They always increase the accuracy and reproducibility of the structure of several biomolecular targets and their interactions with a large scale of small molecules. [1] The modern Drug Discovery process mainly starts from the Target Identification, often represented by a protein structure. The target must be validated (Target Validation), when possible, with the support of X–ray crystallographic techniques. With the help of different approaches, as the fragment–based drug discovery (Paragraph 4.3), different small molecules, called "hit compounds", are computationally and experimentally identified and screened for a particular activity on a target. Hit compounds are strategically modified to increase selectivity and potency at lower concentrations, generating a "lead compound". The lead can be studied in terms of protein–ligand interaction and affinity, with both *in silico* (molecular docking, molecular dynamics, molecular mechanics) and experimental (biochemical assessment, X–ray crystallography) approaches. The lead compound can be further modified to increase at most its potency and bioavailability, in the Lead Optimization process, progressing from *in vitro* biological assays to preclinical studies. Some problems can occur in the progression of a lead in this path. The lead compound could not have drug–like characteristics, which means it does not possess adequate pharmaceutical properties such as solubility or reactivity. Only when a lead becomes a Drug candidate, it can progress to preclinical investigation and, luckily, to phases I/II/III clinical trials. The problem of a modest drug–like profile of a Drug candidate could include scarce ADME properties (absorption, distribution, metabolism and excretion). Therefore, ADME properties could be predicted from the early stages with *in silico* predictions. Drug candidate behavior could also be modulated by some Drug Delivery strategies, which can target the drug in the specific site of action. When the Drug Candidate can be commercialized takes the name of "drug", and it can be monitored during its entire "life" through the pharmacovigilance process. [5]
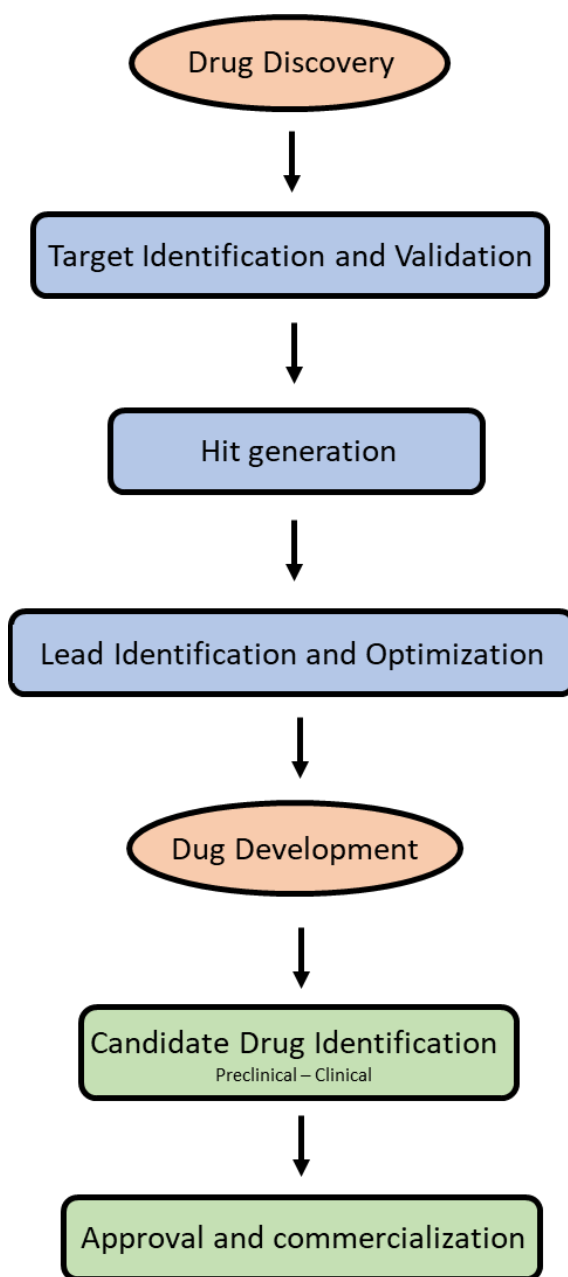
Scheme 1. Schematic workflow of Drug Discovery and Development process.

4.3. Fragment–based drug discovery (FBDD)

In the last years, Fragment–based drug discovery (FBDD) became an important approach in the early stages of Drug Discovery. FBDD invests an ensemble of biophysical and biochemical approaches and is particularly important in the Lead Identification and Optimization steps of Drug Discovery. [6–8] The process consists in identifying ligands, called fragments, with a low molecular weight (~ 250 Da) and characterized by weak binding (K_D ~ 100 – 1000 μM) and converting them into nanomolar inhibitors with strategic drug

design techniques. [9–13] They must be moderately lipophilic (cLog$P$ < ~3) and highly soluble in water. [14] In the Lead Optimization process, a lead compound must be thought of as a complex of chemical "pieces", which can be manipulated to increase the potency of the lead itself. The fragmentation of a lead in several fragments or even in functional groups tries to map out several pharmacophoric elements. [15,16] Then, the optimized fragment can be combined – linked, merged or fused – in a unique new molecule. Unfortunately, it is not already clear which are the precise rules and characteristics for the perfect fragment lead. Therefore, this field is in never–ending evolution. [17] One of the most accepted guidelines for fragments is the rule–of–three (RO3) [5,17]: a fragment could possess a $M_w \leq 300$ Da, a number of H–bond donors ≤ 3, a number of H–bond acceptors ≤ 3 and a Log$P$ value ≤ 3. Furthermore, several rotatable bonds (NROT ≤ 3) and a certain polar surface area (PSA $\leq$ 60) can be beneficial. [18]

Regarding FBDD, techniques for the evaluation of protein/fragment affinity are nuclear magnetic resonance (NMR) techniques, X–ray crystallographic screening, surface plasmon resonance (SPR) and computational approaches (Molecular Docking, Molecular Dynamics). Different NMR techniques aim to identify hit compounds for protein structures with a various range of dimensions. [19–21] NMR techniques are employed in FBDD processes monitoring changes in protein or ligands in spectra. For example, the most common ligand–focused techniques are Saturation Transfer Difference (STD) [22] and Water–LOGSY. [23,24] The advantage of these NMR techniques applied to FBDD is that their output is better as the protein dimension increases, and they can detect weak protein–ligand binding interactions. Moreover, a quantitative result of these interactions can be acquired easily, determining K_D (constant dissociation) values directly by the changes in chemical shift, and without a reference molecule.

As for the application of X–ray crystallography in FBDD, it is a successful technique that offers several advantages. Hit identification usually makes use of structural biology. [25] FBDD process based on X–ray techniques is more difficult for less accessible proteins, such as transmembrane proteins (*e.g.* GPCRs or ion channels). [26]

As concerns SPR, it is a technique used to investigate biomolecular interactions giving kinetic and binding affinity results. The target protein is immobilized on a chip and fragments are passed through it. The different mode of binding is discriminated by the change in the absorbance spectrum, and the change in reflected light reveals the mass of the fragment. Computational FBDD is particularly important in the lack of recombinant protein in a suitable form for fragment screening. [27]

Other fragment–based approaches to drug discovery are Biolayer Interferometry (BLI), [28] with similar discrimination by light as SPR, and Isothermal Titration Calorimetry (ITC), [29] which depends on the released/absorbed heat produced by a binding event. FBDD also serves itself of mass spectrometry techniques, as ESI–MS (Electrospray ionization) or NC–ESI–MS (non–covalent ESI–MS) for the detection of potential covalent bonds or other interactions between target and ligand. Chromatographic techniques such as Weak Affinity Chromatography (WAC), [30] are useful for FBDD, employing chromatography columns with an immobilized target protein. In addition, Capillary Electrophoresis (CE) is nowadays employed for the screening of fragments monitoring the changes in the electrophoretic profile for each of them, resulting in an affinity range from mM to pM. Like CE, Ultrafiltration discriminates between protein–bound or unbound fragments, with a separation system retaining only protein–ligand complexes. Lastly, several biochemical assays are used for FBDD. Common assays are often useless since they are unable to detect weak–affinity fragments. To bypass this issue, high–concentration screening assays are conducted on a variable number of fragments, to initially identify hit compounds to be further investigated. [31]

The main processes of Lead Optimization carried out by FBDD are *fragment growing*, *fragment merging/hopping* and *fragment linking*. [32]

The fragment growing process is focused on adding small atomic groups or bigger building blocks selected to improve the binding to the target; this technique aims to strategically occupy an empty pocket identified from the binding of the first–site fragment to the target protein, increasing the mutual affinity. An alternative way is offered by fragment merging (or scaffold hopping) of fragments. Knowing the binding modes of different first–site ligands, some of them can be rationally merged and synthesized, to have a synergic effect on the protein–ligand affinity. [33]

One of the most successful approaches in the hit to lead process is fragment linking. It is considered that, covalently linking two ligands, the resulting K_D is the K_D of one fragment times the K_D of the other one. [34]

Apart from FBDD, other recognized approaches to Drug Discovery are combinatorial chemistry, high–throughput screening (HTS), [35,36] but also virtual ligand screening and structure–based drug design, improving Synthesis Optimization and further biochemical assessment. [37–39]

4.4. Computer–aided drug discovery (CADD)

In modern Drug Discovery, computer–aided techniques became very important in the investigation of the interactions between a target and a ligand. The binding mode of a ligand bound to the target represents a crucial tool in Medicinal Chemistry to help the experimental shreds of evidence that lead to the structure–activity relationship (SAR). [40] In the following Paragraphs, computer–aided drug discovery (CADD) techniques, such as Molecular Docking and Molecular Dynamics, will be further discussed.

4.5. Molecular Docking in Drug Discovery

Molecular Docking is one of the main structure–based tools for the Drug Discovery process. Molecular Docking helps experimental outcomes by analyzing more in–depth the interaction between a ligand and its target. [41,42] Molecular Docking is a virtual screening approach characterized by cost–effectiveness advantage. A docking program generates several ligand poses as the most favorable ligand/protein spatial conformations. The process which determines the entity of the interaction is called *scoring*, and it is calculated by a simplistic scoring function. [43,44] The limitation of the docking methodology could be the great simplification of the protein–ligand interaction to make benefit from the immediacy of the technique. The inaccuracies could be found in the pose ranking and the calculation of the affinity energy, hence computational researchers are always pushing to generate more correct scoring functions. [45]

To remedy this deficiency, Molecular Docking is more often accompanied by other ligand–protein interactions techniques, like molecular dynamics (MD). Also the interpretation of the results is very relevant in different steps of Drug Discovery, such as Hit Identification and Lead Optimization. [46,47] The visual inspection is an important part of the post–docking evaluation of the results. [48]

In the visual inspection, the first evaluation is initially focused on the hydrogen bonds (important for binding selectivity and affinity) relative to their strength and geometry. [49,50] In particular, some specific H–bonds between the ligand and some amino acids are compared to those generated with some known co–crystallized ligands with a similar chemotype. [51,52] Hydrogen bonds to the protein backbone are generally stronger in comparison to those with the more flexible side chains, in terms of stability over time. [40,53] The strength of an H–bond can vary a lot, but those detected in interactions between ligand and protein binding site vary from 16 to 60 kJ·mol^{-1} (~ 10 times less than a covalent bond). The normal H–bond distance between donor and acceptor atoms is 1.5 – 2.2 Å

(compared to 1.0 – 1.5 Å for a covalent bond). [54] A review from *Fischer et al.* [55] in 2021 reported a deep analysis on several visual inspections of docking results, conducted by computational chemists and reported in different papers. Apart from the most observed hydrogen bonds in the evaluation of ligand–protein affinity, other considered interactions are the hydrophobic interactions, pi–stacking, cation–pi interactions, water interactions and solvent–exposed areas. [55]

4.6. Molecular Dynamics in Drug Discovery

As above discussed, in the Medicinal Chemistry evaluation, Molecular Docking could be implemented with other techniques, such as Molecular Dynamics (MD). MD is a powerful method to routinely assess theoretical simulations of several types of systems (biochemical, chemical and physical). The success of this theoretical way of studying the interactions between target and ligand was accompanied by the quick development of supercomputers, powerful in terms of computing power and storage, allowing computational chemists to run simulations with bigger systems and for a longer time. [56] MD interest embraces different scientific areas as biophysics, structural biochemistry, molecular biology and the pharmaceutical industry. MD simulations allow the investigation of the dynamics and function of a certain biomolecular entity, for instance studying the change in binding free energy (BFE) of a ligand or the change in the spatial conformation of a protein in the physiological environment over time. Talking about MD studies applied to biomolecular systems, the fine parameterization is supported by different molecular mechanics force fields (FFs), such as the CHARMM36 force field. [57–59] A force field is a mathematical expression that correlates the energy of a system and the particle coordinates. It takes into account the interatomic potential energy and several other parameters, to simplify the molecule structure into a set of atoms linked by simple elastic (harmonic) forces. The simplicity is translated into quickness of the analysis, maintaining the details and the reproducibility of the system investigated. [60] Lastly, MD studies are of help in Rational Drug Design giving hints and answers related to the deep interaction of a target–ligand complex. The ligand could be endogenous or exogenous, so the investigation could interest the understanding of a signal transduction, a metabolic regulation, but also the reaction of a target protein and its surrounding environment in response to the administration of a drug. [61]

4.7. Medicinal Chemistry in Cancer Chemotherapy

Cancer is one of the most challenging diseases because of the difficulty in treatment and the increasing incidence due to different factors, as the aging of the population worldwide. The process of transformation of a normal cell into a malignant cell is mainly caused by small– or large–scale changes in DNA sequence. Human tumors mainly possess six biological characteristics: improved proliferative signaling, bypass of growth suppressor factors, cell death and immune system resistance, replicative immortality, angiogenetic ability and invasion/metastasis activity. Other important prerogatives of a tumor are genomic instability and mutation, and induced inflammation. The combination of all these abilities, which makes cancer one of the deadliest diseases worldwide, aims to create a favorable tumor microenvironment (TME). [62]

The principal therapeutic approaches in cancer are represented by surgery, radiotherapy, and systemic chemotherapy. In the past years, anticancer therapy has been a very active field of research, producing a big amount of knowledge on biological targets and new drugs. This process led to define cancer as a multifactorial disease. Therefore, modern anticancer research is mainly focused on signal transduction therapy, monoclonal therapy, immunotherapy and nanotechnology. [5]

In 1971, the National Cancer Institute (NCI) created the U.S. National Cancer Program, with the aim of better understanding the pathophysiology of cancer. Even if cancer is always more studied to explore its generation and progression, the fight against this illness is hindered by a huge amount of obstacles due to the high mutation of the cancer cells and the big variety in genetic alterations which finally lead to the insurgence of drug resistance. [5] Moreover, cancer cells are supported by a population of cancer stem cells (CSCs) which improve aberrant cell differentiation. [63–65] CSCs are a tumorigenic reservoir of self–sustaining cells and can grow in two different manners: from a normal stem cell, which faces a dysregulation of the growth process, or from a mature cell acquiring self–renewal properties. [66–68] CSCs contribute to one of the main issues in cancer treatment: their resistance to cytotoxic drugs and radiation therapies. [68]

Historically, the initial approach to cancer chemotherapy was to generate new drugs from natural products by semisynthesis or full synthesis. Some of the most famous old anticancer drugs are methotrexate, the first folate analog drug to be used for the induced remission in children with acute lymphoblastic leukemia (ALL), and cisplatin, one of the most known antitumor drugs, discovered by serendipity. These molecules are included in the so–called

"conventional chemotherapy", focused on drugs targeting the rapid cellular proliferation of cancer cells. [69]

With the advent of the new millennium, a new way of understanding chemotherapy was born with the name of "targeted chemotherapy". With a deeper study of Target Identification and Validation in Drug Discovery process, chemotherapy is now mainly based on monoclonal antibodies (*e.g.*, pertuzumab Perjeta®), which can bind antigens, preferentially or exclusively present in cancer cells, kinase inhibitors (*e.g.*, Axitinib, Inlyta®) and immunomodulatory drugs. Fundamental for the development of the modern Rational Drug Design was the X–ray crystallography, enabling the possibility to have a 3D structure of a target. In conclusion, the next–generation challenges in cancer chemotherapy are represented by facing drug resistance, which can be acquired by cancer cells even after the initial treatment. [5]

4.8. Medicinal Chemistry in Antibacterial Treatment

Antibacterial drug discovery is an evergreen fashionable branch of research, focusing on the design and synthesis of bioactive molecules able to destroy bacteria. Salvarsan [70] was the first antibacterial agent identified as active for syphilis, [71] just before the discovery of the well–known Prontosil, [72] which led to the rising of the "sulfa drug era", consisting of synthetic antibacterial agents. In 1929, Fleming made the absolute noteworthy discovery of penicillin, later recognized as fundamental for streptococcal [73] and staphylococcal infections. [74] Penicillin is a simple β–lactam compound which acylates irreversibly the cell wall proteins of bacteria, called penicillin–binding proteins (PBPs). The β–lactam ring gives rise to several new classes of antibiotics through the years, such as cephalosporins. [75,76] As concerns other classes of antibiotics, the glycopeptides were isolated from Actinoplanes and Streptomyces. [77] Well–known compounds of the family are vancomycin and teicoplanin; they are used in the treatment of resistant Gram–positive species (MRSA) such as coagulase–negative staphylococci and multi–resistant enterococci. They inhibit cell wall synthesis by interfering with a late stage in the assembly of the peptidoglycan and consequent block of cell growth, subsequently leading to cell death.

In the 1980s, the family of fluoroquinolones, with norfloxacin and ciprofloxacin as representative drugs, gave an impressive boost to the treatment of various infections. [78] The advantages of these drugs are that they are safe and can be orally administered. They inhibit an enzyme called gyrase, a topoisomerase II which introduces negative supercoils in the DNA of bacteria during its replication. [79] Fluoroquinolones also inhibit topoisomerase IV in different species like *S. pneumoniae*, *S. aureus* and *E. coli*. [80] The improvement of

potency against Gram–positive and anaerobe bacteria is the main goal of the research in fluoroquinolones. [81] Further on, erythromycin A, isolated from *Streptomyces erythraeus*, belongs to the family of macrolides. The molecules of this class of antibiotics interfere with the biosynthesis of proteins acting on an enzyme, peptidyl transferase, located in the 50S ribosomal subunit of bacteria. [82] Another class of antibiotics is represented by tetracyclines. They are known for their low toxicity and cost and a broad spectrum of activity. They are bacteriostatic, blocking the aminoacyl–tRNA on the 30S ribosome. [83] Going forward, in the last decades, only one novel class of antibiotics from basic research had a relevant clinical interest, the oxazolidinones. In the beginning, compound DUP 721 64 was discovered in the mid–1980s, but it exhibited lethal toxicity in *in vivo* assays. Compounds U–100592 65 and U–100766 66.62 are now under clinical trial, due to their activity against resistant Gram–positive bacteria. As for their mechanism of action, they seem to inhibit an early step in the protein synthesis of those bacteria. [84]

Nowadays, antibiotic resistance is a crucial problem worldwide. Antibiotic resistance consists of a decreased sensitivity for a specific antibiotic, which allows the survival of the bacterium. Antibiotic resistance has its root in: a) the possibility that patients do not comply with the right therapy; b) the over–prescription of antibiotics. Antibiotic over–prescription represents a worldwide issue for the large number of antibiotics used in intensive farming and used at a lower dose than those expected to eradicate bacteria; c) the prophylaxis against infections of immunocompromised patients. Although in past years the antibacterial development lost interest, nowadays some pharmaceutical companies are re–investing in the field, trying to improve the potency of known antibiotic treatments, but also applying new approaches to antibacterial drug discovery. [85]

5a. Introduction to microtubule−targeting agents (MTAs) for cancer chemotherapy

One of the most challenging diseases worldwide is cancer, with its multiple ways of occurring and different involved pathways. Cancer is counted among the non−communicable diseases (NCDs) and causes 22% of the entire category of NCDs. [86] Cancer treatment is an important clinical issue; the academic and industrial research in this field is focused on improving both potency and safety of the therapies. [87] Cancer is characterized by different features; one of them is the uncontrolled cell division. The cell cycle is characterized by different alternating phases: G1 (Gap 1), S (mainly DNA synthesis), G2 (Gap 2) and M (mitosis). Many cytotoxic compounds with anticancer potential activity are implicated in the blockade of the cell cycle, at different steps. [88] The main tool during the cell cycle is the mitotic spindle, mainly composed of intertwined microtubules (MT). Microtubules, consisting of heterodimers of α− and β−tubulin, are characterized by a fine−tuned equilibrium between polymerization and depolymerization; hence, anticancer drugs directed against MTs as main targets tend to interfere with this well−organized equilibrium. [89–91] Even if the targeting of microtubules is a widely used approach for anticancer field and loads of molecules were designed and synthesized, [92] in most cases, unfortunately, little is known about how these drugs affect the cell cycle leading to apoptosis. Microtubule−targeting agents (MTAs) are one of the most representative categories of compounds interfering with the cancer cell cycle; therefore, they are targeted to treat both solid and hematological tumors. [93] MTAs are conceptually sorted out taking into account their interference with the polymerization or depolymerization phases of the microtubule equilibrium: microtubule−stabilizing agents (MSAs) and microtubule−destabilizing agents (MDAs). [94] Since compounds binding to tubulin can interact with taxane−, vinca−, colchicine−, laulimalide/peluroside−, pironetin− or maytansine−binding site on tubulin, MTAs could also be classified based on their main targeting portion on the tubulin active site. [95] As for the taxanes, paclitaxel was the first MT stabilizing agent to be discovered from *Taxus brevifolia*. It is chemically a hydrophobic compound and, from the late 1960s, it became important for its antitumor effect on multiple preclinical cancer models. [96] Taxanes have a well−known activity against a large number of solid tumors, like gastric, sarcoma, melanoma, bladder, endometrial, small cell lung, hormone−refractory prostate, esophageal, and germ−cell carcinoma. [97] As for the binding of taxanes to tubulin, they bind to a unique

binding site inside the lumen of the microtubule, not competing with colchicine or vinca alkaloids. [98,99] Regarding vinca alkaloids, they were the first MTAs to become well–known in mainstream chemotherapy. [100] They have a complex binding to MTs. From the binding mode of vinblastine, it was shown its interaction between tubulin heterodimers at the inter–dimer interface, different from taxanes and colchicine binding sites. [101] Laulimalide [102] and peloruside A [103] also act as a promoter of tubulin polymerization, binding to a different binding site on tubulin. Their exact binding location on tubulin is still not clear. These compounds seem to bind to a specific site on the α–tubulin and exhibit microtubule–stabilizing effects similar to that of paclitaxel. [104] Laulimalides and pelorusides are potent MSAs, but they are in the early stages of development. As concerns pironetin, it was isolated from the culture broths of *Streptomyces sp. NK10958.* [105] Pirotenin and its derivatives block cell cycle in M–phase, showing a potent antitumor activity. [106] It is the only known molecule that binds to α–tubulin with a covalent interaction. Thus, pironetin–like compounds could be considered for the treatment of tumors resistant to β–tubulin–targeting drugs. Maytansine is a drug approved by the FDA for the treatment of breast cancer. In 2014, *Prota et al.* reported the crystal structure of the tubulin–maytansine complex. Maytansine inhibits tubulin polymerization binding to β–tubulin. [107] Colchicine is approved for the treatment of recurrent pericarditis [108] and is effective for the treatment of gout and another inflammatory disease, the familial Mediterranean fever (FMF). [109] The anti–inflammatory effect of colchicine is still unclear; it is known to block inflammation through inhibition of pro–inflammatory cytokines (*e.g.* IL–1β) caused by neutrophils and monocytes. The therapeutic activity seems to derive from the inhibition of microtubule polymerization in these cells, but it is unknown why antimitotic side effects are not manifested. [110] The colchicine–binding pocket is located on β−tubulin at its interface with α−tubulin. Agents targeting the same portion of the pocket as colchicine, then called colchicine−binding site inhibitors (CBSIs), have as representative compounds colchicine, combretastatin A−1 (CA−1) and A−4 (CA−4). [111,112] Currently, no CBSI has entered the market, even if some CBSIs have been evaluated for phase I−II clinical trials (combretastatin A−1 phosphate and A−4 phosphate, 2−methoxyestradiol and verubulin). [113] However, colchicine−binding pocket on tubulin is a neverending drug discovery challenge, [114–116] therefore we decided to proceed in finding new hints for the development of new inhibitors. Different series of benzotriazolacrylonitrile derivatives recognized as microtubule−destabilizing agents (MDAs) were synthesized from our group through the years. [117–122] From the first series of compounds, [118] it was quite evident the higher

antiproliferative effect elicited by the 1*H*−benzotriazole derivatives, while 2*H*−benzotriazole ones presented a weaker activity. Among all compounds, the lead compound (*E*)-2-(1*H*-benzo[*d*][1-3]triazol-1-yl)-3-(4-methoxyphenyl)acrylonitrile, labeled as **34**, showed an IC$_{50}$ of 0.2 µM on CCRF−CCM leukemia cell line and triggered a blockade of the cell cycle in G2/M phase in K−562 leukemia cells. In particular, our lead showed to inhibit tubulin assembly, and some computational and experimental studies confirmed compound **34** as an MDA interacting colchicine−binding site on tubulin. [121]

Chapters 5 and 6 of the present Thesis focus on the design, synthesis and biological assessment of new series of benzotriazole−based compounds acting as MTAs. Starting from compound **34**, the benzotriazole scaffold was opportunely manipulated to improve the strength of the interaction between tubulin and the ligand. A frequently pursued approach in Medicinal Chemistry optimization is the replacement of hydrogen atoms with fluorines to improve drug−likeness features such as: metabolic stability (protection of metabolically weak sites on the ligand sensitive to oxidation by cytochrome P450 [123]), lipophilicity, bioavailability and target−ligand interactions through the pK_a modification. [124,125] With this knowledge in our hands, we introduced fluorine atoms in a benzotriazole backbone of our lead **34**.

Figure 1 depicts the new series of (*E*)(*Z*)-2-(5,6-difluoro-(1*H*)2*H*-benzo[*d*][1-3]triazol-1(2)-yl)-3-(*R*)acrylonitrile (**9a**−**j**, **10e**, **11a,b**) and (*E*)-2-(1*H*-benzo[*d*][1-3]triazol-1-yl)-3-(*R*)acrylonitrile derivatives (**13d,j**), which was designed, synthesized and assessed through several biological assays. Compound **9a** was selected as the lead compound of the series through a preliminary *in vitro* screening of the National Cancer Institute (NCI) of Bethesda, USA. Both computational and experimental studies were conducted on compound **9a**, and detailed results are reported in Chapter 5, while the Experimental section is reported in Chapter 8. [126]

From the insights obtained by the evaluation of compound **9a**, the substitution with fluorine atoms on the benzotriazole scaffold seemed to be beneficial for the biological activity of the compounds, so we decided to maintain the substituent but explore other positions. A new 4'−fluoro−substituted series of compounds (**5**−**13**) was designed, synthesized and biologically evaluated. The results for this new series will be discussed in Chapter 6 of the Thesis and the Experimental section for these molecules is reported in Chapter 8.
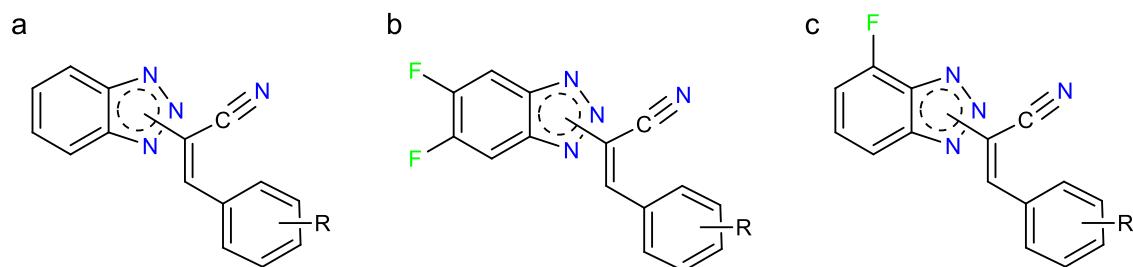
Figure 1. General structure of a) previously published derivatives b) di−fluoro (see Chapter 5) and mono–fluoro (see Chapter 6) derivatives.

5. Project #1: A comprehensive assessment of a new series of 5',6'–difluorobenzotriazole−acrylonitrile derivatives as microtubule targeting agents (MTAs)

The present project was recently published:

F. Riu, *et al.*, A comprehensive assessment of a new series of 5',6'–difluorobenzotriazole–acrylonitrile derivatives as microtubule targeting agents (MTAs), Eur. J. Med. Chem., 2021, 222, 113590. https://doi.org/10.1016/j.ejmech.2021.113590.

5.1. Results and Discussion

5.1.1. Rationale and Docking prediction

Starting from the already published benzotriazolacrylonitrile derivatives, [117–122] particularly from compound **34**, the initial idea was to introduce fluorine atoms in the main benzotriazole scaffold. The computational affinity prediction of the **34**–analog **9b** was evaluated through Molecular Docking calculations. Compound **34** and its parental compound **9b** were docked in the colchicine−binding site on tubulin. As different co−crystallized structures of the tubulin−colchicine complex are available in the Protein Data Bank, [127] crystal structure 4O2B was selected as one of the most recent and with better resolution (2.30 Å). [128] The crystal structure was manipulated through PyMOL: [129] water and other entities were removed from the workspace, apart from tubulin and colchicine. Colchicine was removed from the active site, leaving the *apo*−form of tubulin (protein without ligand, endogenous or exogenous), only α− and β−subunits of tubulin were considered for the docking studies, to have a less time−consuming system and for a better visual investigation.

Colchicine, compounds **34** and **9b** were docked in the colchicine−binding site at the interface between α− and β−tubulin. The best−predicted pose of colchicine ranked affinity energy of −9.8 kcal·mol^{-1}, compound **34** −6.7 kcal·mol^{-1} and compound **9b** −8.6 kcal·mol^{-1}. Therefore, compound **9b** demonstrated a higher affinity for tubulin binding site in comparison to compound **34,** being then worth to be synthesized. To justify these values, a deeper analysis of the different protein−ligand interactions was necessary. The two− and

three−dimensional inspection was made through different programs: PyMOL, [28] LigPlot⁺, [29] and Maestro. [130]

Analyzing the re−docked pose of colchicine, the tropolone ring showed a hydrophobic interaction with Alaα180, while the trimethoxyphenyl portion pointed towards the hydrophobic region formed by different amino acids such as Metβ259, Asnβ258, Leuβ255, Lysβ254, Aspβ251, Alaβ250, Leuβ248, Leuβ242 and Cysβ241.

As shown in Figure 2, compound **34** displayed a predominant effect of the hydrophobic interactions with the exposed amino acids of the tubulin binding site. An electrostatic contribution to the binding is given by a hydrogen bond (H−bond) between the amidic nitrogen atom of Asnα101 and its acceptor oxygen of the methoxyl group.

The fluorine atoms in compound **9b** have a beneficial effect on the benzotriazole backbone. The most−favored pose of compound **9b** showed two F⋯N electrostatic interactions, called fluorine bonds, a type of dipole−dipole interaction. [131] The electron−acceptor fluorine atom in C−5' on the benzotriazole backbone electrostatically interacts with intrinsic nitrogen atoms of Cysβ241 and Leuβ242. The benzotriazole carbon backbone has hydrophobic interactions with the carbons of the isobutyl side chain of Leuβ242. More in–depth, the benzene ring provides hydrophobic interactions with Alaβ250, Aspβ251 and Leuβ255, while the side−chain benzene moiety creates van der Waals interactions with aas located in the opposite portion of the binding pocket, such as Leuβ248, Gluα183, Lysβ254 and Asnβ258. The methoxyl group of compounds **34** and **9b** in their best−predicted pose have a different orientation, hence compound **34** can engage an H−bond with Asn101, while the same portion in compound **9b** prefers hydrophobic interactions with the surrounding aas in the binding pocket; in particular, the carbon atom of the methoxyl group have a hydrophobic interaction with Lysβ254.

Figure 3 shows a different 2D representation of the polar and nonpolar interactions between compound **9b** and the aas of tubulin active site. The methoxyl group was predicted to be the most solvent−exposed portion of the derivative, pointing toward the outer portion of the binding pocket.

Using AutoDockTools, [132] a different docking investigation was carried out on compound **9b**−tubulin complex, but some aas (Serα178, Thrα179, Alaα180 and Alaα181), recognized as crucial for the binding, were set as flexible. Even in this case, the affinity energy was higher for compound **9b** (−7.4 kcal·mol⁻¹) compared to compound **34** (−6.7 kcal·mol⁻¹). [126]
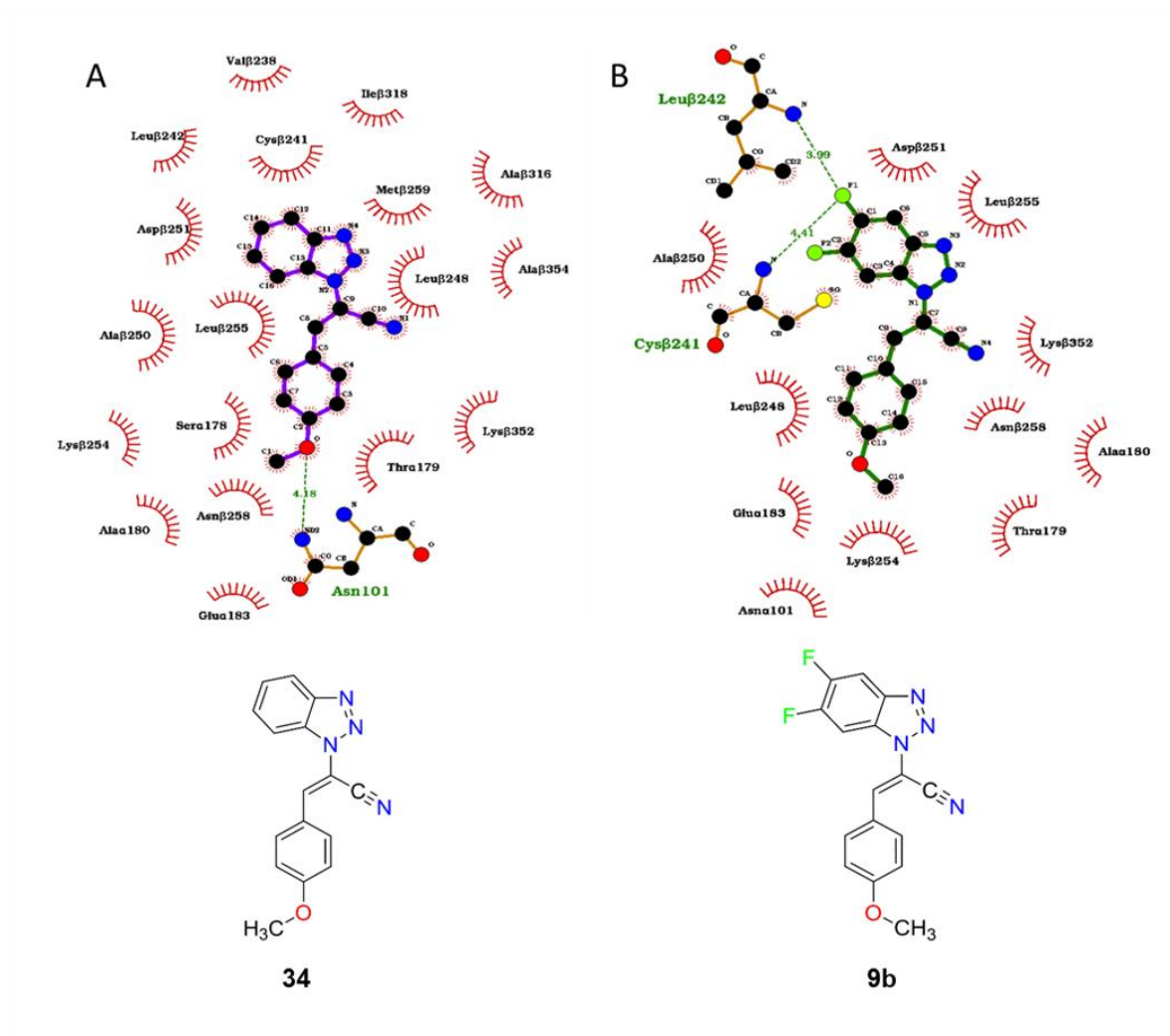
Figure 2. 2D comparison of the polar–nonpolar interactions between compounds **34** (A) and **9b** (B) and the amino acids at the interface between α− and β−tubulin. Green dashed lines represent hydrogen bonds, red hash marks hydrophobic interactions. Atom colors: carbon, black; nitrogen, blue; fluorine, green; oxygen, red. Amino acids are labeled with the residue name, the subunit and the related number. Distances are given in Å. Figure made by using LigPlot⁺. [126]

Figure 3. Ligand Interaction Diagram and LID legend of the different interactions between compound **9b** and different amino acids in the tubulin−binding pocket. [126] Residue markers are colored according to residue type (green = hydrophobic, cyan = polar, red = negative, purple = positive). Green and cyan lines represent the interactions between **9b** and the different portions of the binding pocket. The gap in the line shows the opening of the pocket. Grey atom markers on the background of ligand structure represent the solvent−accessible surface area (SASA) of that atom, and the marker size represents the amount of exposure. Each protein residue is depicted as a "guitar pick": it points away from the ligand when the aa backbone faces towards the ligand, or it points to the ligand when the aa side chain faces towards the ligand. Cut−off default of 4 Å was used. Figure made by using Maestro. [130]

5.1.2. Chemistry

A

B

Letter code	R
a	4-CH3-Ph
b	4-OCH3-Ph
c	2,3,4-OCH3-Ph
d	4-OH-Ph
e	4-NO2-Ph
f	4-F-Ph
g	4-Cl-Ph
h	4-Br-Ph
i	benzo[d][1,3]dioxol-5-yl
j	isoquinolin-5-yl

Scheme 2. (**A**) Synthetic route of (*E*)(*Z*)-2-(5,6-difluoro-(1*H*)2*H*-benzo[*d*][1,2,3]triazol-1(2)-yl)-3-(*R*)acrylonitrile (**9a−j**, **10e**, **11a,b**) and (**B**) (*E*)-2-(1*H*-benzo[*d*][1,2,3]triazol-1-yl)-3-(*R*)acrylonitrile derivatives (**13d,j**). Reaction conditions: (a) (CH$_3$COO)$_2$O, 10 min, 0 °C; (b) KNO$_3$, H$_2$SO$_4$, 2h, r.t.; (c) H$_2$SO$_4$ conc, 2h, reflux; (d) H$_2$, Pd/C, 2 h, r.t.; (e) NaNO$_2$, HCl, 20 h, r.t.; (f) ClCH$_2$CN, KOH, DMF, o/n, reflux; (g): (1) TEA, toluene, 110 °C, or (2) DIMCARB, CH$_3$CN, 60 °C or (3) piperidine, CH$_3$CN, 60 °C; reaction conditions were chosen to obtain full conversion. [126]

Scheme 2 describes the synthetic approach followed to obtain final compounds **9a−j**, **10e**, **11a,b** and **13d−j**. Scheme 2A depicts the synthesis of acetonitrile isomers **7a,b**, as starting materials for the last Knoevenagel reaction to afford the desired acrylonitrile products, shown in Scheme 2B. Starting from 3,4−difluorodianiline, the ring closure was obtained through acetylation, nitration, hydrolysis, reduction and cyclization in acidic conditions,

yielding 5',6'−difluorobenzotriazole **6**. Geometric acetonitrile isomers **7a,b** were obtained by reaction with chloroacetonitrile (ClCH₂CN) in basic conditions (KOH). Isomers in N−1' and N−2' positions on the triazole ring were used as starting materials for the final reaction. Knoevenagel condensation generally yielded *E*−isomers of the final compounds. *Z*−isomers were in some cases found in traces, not enough to be characterized. Only compound **10e** is the *Z*−isomer of the *p*−nitro derivative with the acrylonitrile chain in position N−1'. Three different reaction conditions were used: (1) triethylamine (TEA) in toluene (classic conditions previously described [117–122]), (2) DIMCARB (dimethylammonium dimethylcarbammate), both base and catalyst in the reaction, [133] in acetonitrile, and (3) piperidine in acetonitrile. The *E*− and *Z*−isomers **9e** and **10e** were obtained in the presence of DIMCARB or TEA as catalysts, respectively. Compounds **13d,j** were obtained by Knoevenagel condensation, as previously reported by us, [117–122] between the acetonitrile isomer **12a** and aldehydes **8d,j**. The acrylonitrile chain was substituted leading to compounds provided with different activity compared to similar compounds previously published by us [117–122] or by colleagues. [134] Adding the 4−hydroxyphenyl and isoquinolin−5–yl moiety as new substituents, the previous series of **34** analogs was expanded with derivatives **13d,j**. [126]

5.1.3. *E/Z isomers characterization by NMR spectroscopy*

NMR characterization of E/Z isomers was mainly investigated by Dr. M. A. Scorciapino (Department of Chemical and Geological Sciences, University of Cagliari, Italy).

To fully characterize *E*− and *Z*−isomers of this series of compounds, derivative **9i** was taken as a prototype. This compound was first obtained as an isomeric mixture with a small amount of the parental *Z*−compound. The ¹H−NMR spectrum of the mixture clearly showed distinct signals of the two compounds, without any overlap among the different resonances. The assignments for both isomers are reported in Figure 4. The two sets of peaks were easily identified also due to their different concentrations (ratio 6:1, relative intensity). Resonance labeled with A corresponds to *E*−isomer compound **9i**, those with B to the *Z*−isomer. The highest shift between the two isomers was obtained for H−4", H−6", H−7" and H−7', the closest to the unsaturation of the acrylonitrile region. [126]
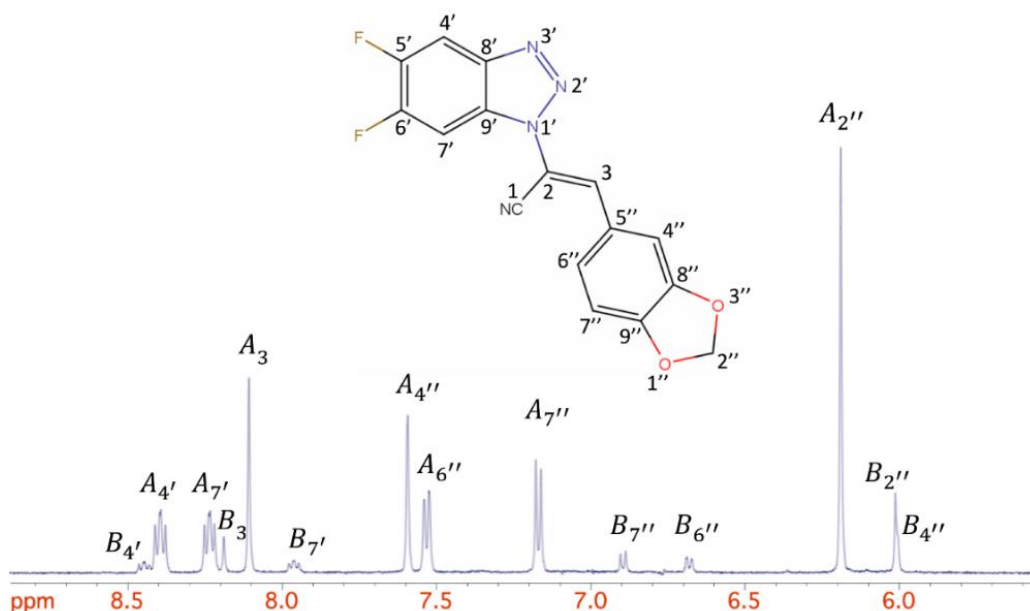
Figure 4. Representation of ¹H−NMR spectrum and full assignment of compound **9i** (*E*−isomer, A) and the correspondent *Z*−isomer (B). [126]

Further investigation interested 1D−NOESY experiments. In Figure 5, the "red thunder" sign indicates the protons selectively excited, while green triangles point toward the protons which acquire intensity through the NOE effect. The result of this technique is the selective inversion of one resonance, transferring positive magnetization during relaxation to all protons through space closer than ~ 5 Å. In Figure 5a, the resonance of H−2" of the major compound (**9i**) was selectively inverted; in Figure 5b, vinylic H−3, and positive NOE effect was received by H−4" and H−6" of the benzodioxolyl, and H−7' of the benzotriazole scaffold, while the selective inversion of the vinylic H−3 in the minor product transferred positive NOE effect only on H−4" and H−6". This proves that the major product is an *E*−isomer since H−7' can easily approach H−3 by simple rotation around C2−N1' bond. Analyzing the chemical shifts and focusing on the benzotriazole, the distance between the resonances of H−4' and H−7' is ~ 0.20 ppm for the major compound (**9i**), while the minor product (*Z*−isomer) has a distance of 0.50 ppm. In general, the same behavior of compound **9i** was noticed in the other obtained products, with a distance in the H−4' and H−7' resonances ≤ 0.15 ppm. Accordingly, due to steric reasons, all compounds are assumed to be *E*−isomer compounds except **10e**. [126]
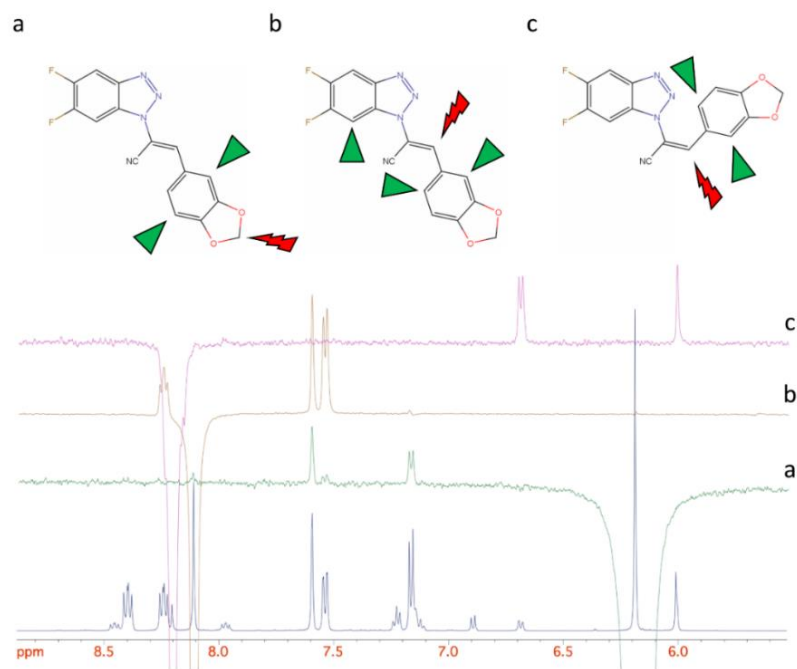
Figure 5. Superimposition of a series of selective 1D−NOESY on compound **9i**. (a) Resonance H−2″ of the *E*−isomer is selectively inverted. Resonances H−4″ and H−7″ receive positive NOE. (b) Resonance H−3 of the *E*−isomer is selectively inverted. Resonances H−4″, H−6″ and H−7′ receive positive NOE. (c) Resonance H−3 of the *Z*−isomer is selectively inverted. Resonances H−4″ and H−6″ receive positive NOE. [126]

Furthermore, the proton signals of vinylic H in **9e** and **10e** showed only a slight difference in chemical shift. An interesting effect was also highlighted by the comparison of the two ^{13}C−NMR spectra of compounds **9e** and **10e**, *E*− and *Z*−isomers respectively. As shown in Figure 6, the vinylic CH signal showed a great difference in chemical shift. [126]

Figure 6. Comparison of chemical shifts in ^{13}C−NMR spectra of compounds **9e** (blue) and **10e** (red): $\Delta\delta \sim 38$ ppm. [126]

5.2.4. Biology

5.2.4.1. Antiproliferative activity: NCI60 *in vitro* screening

The first biological evaluation was assessed through the NIC60 *in vitro* screening, offered by the National Cancer Institute (NCI) in Bethesda (Maryland, USA). The cellular panel is composed of 60 tumor cell lines, 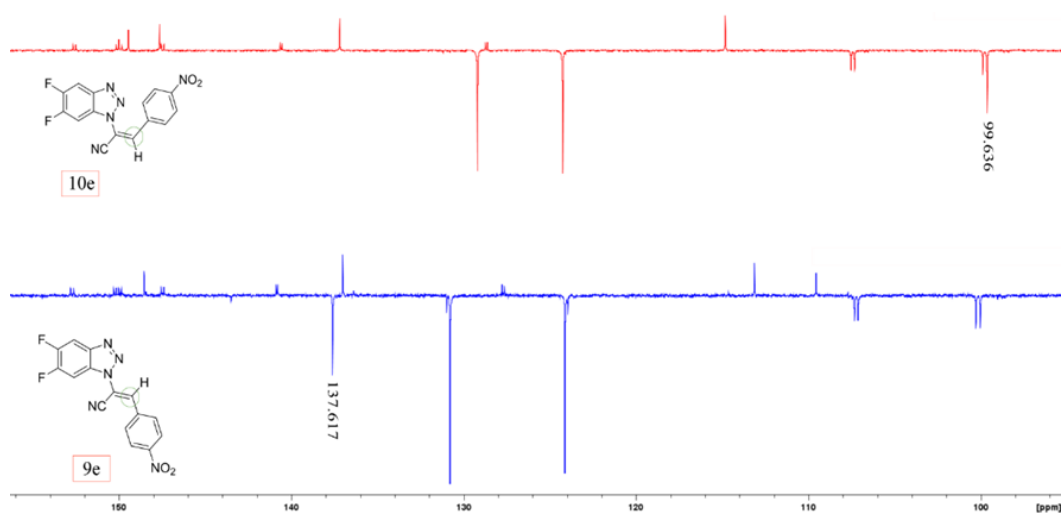grouped in 9 solid (non−small cell lung, colon, central nervous system – CNS, ovarian, renal, prostate, breast cancer, and melanoma) and hematological (leukemia) tumors. The preliminary "single dose" assay consists of an administration of each compound at 10 μM concentration, to evaluate the potential cytostatic or cytotoxic effect. Then, if a compound satisfies the threshold inhibition criteria in the minimum number of cancer cell lines, it is selected for the 5−dose assay, and the compound is tested in different concentrations ranging from 100 μM and 10 nM. The detailed NCI report for each tested compound is reported in the Supplementary Material section of the published paper. [126] In general, results confirm the trend of the previous series, [117,118] showing the higher potency of the 1*H*−benzotriazole derivatives (**9a−j**, **10e**) in comparison to the 2*H*−benzotriazole ones (**11a,b**).

Between the 1*H*−benzotriazole derivatives, compounds **9a** (*p*−CH$_3$), **9e** (*p*−NO$_2$), **9g** (*p*−Cl) and **9h** (*p*−Br) were selected for the 5−dose screening. Evaluating the inhibition potency and the number of cancer cell lines affected by this antiproliferative activity, compound **9a** resulted as the most potent antiproliferative agent of the series and was considered as lead compound. Figure 7 reports the antiproliferative activity of compound **9a**, both at 10 and 1 μM, against the entire panel of tumor cell lines. GI$_{50}$ (concentration of a cytostatic derivative for 50% of maximal inhibition of cell proliferation), TGI (tumor growth inhibition) and LC$_{50}$ (concentration of a cytotoxic derivative for 50% of maximal cellular inhibition) values, averaged for each cancer panel, were also evaluated. At 10 μM, growth inhibition (GI) in the range of 60−100% were registered in the complete panel of cancer cell lines, after treatment with compound **9a**. A cytotoxic effect was revealed in seventeen lines, with lethal percentages up to 90%. At 1 μM, it inhibited cell growth with percentages from 40 to 60% against eight tumor cell lines, and from 70 to 100% against seven cancer cell lines. General GI$_{50}$ values are up to 0.1 μM, LC$_{50}$ and TGI come up to 1 μM. [126]
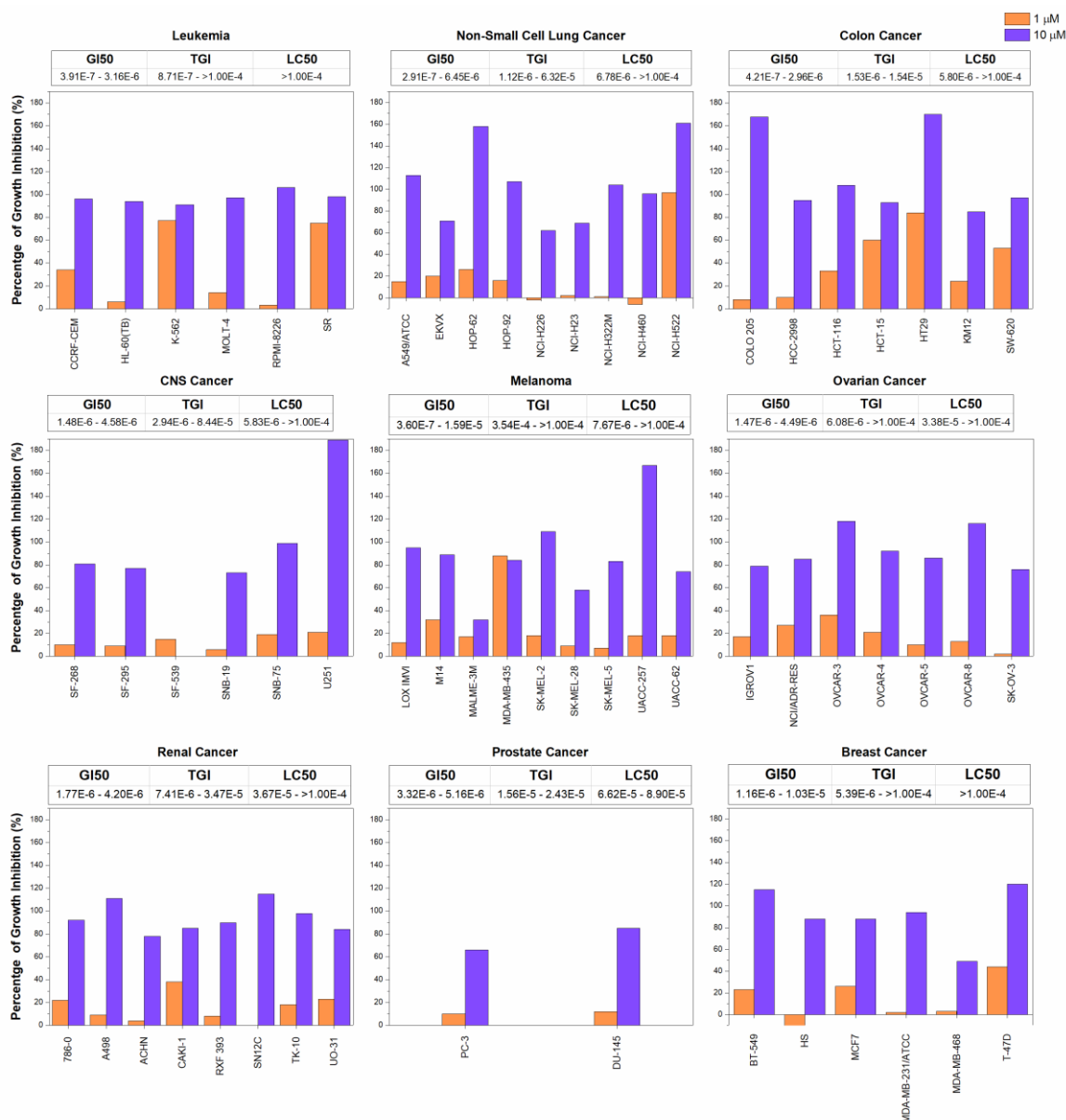
Figure 7. NCI60 *in vitro* screening for compound **9a** against the 60 NCI tumor cell lines. Percentage of Growth Inhibition (%) is reported for the treatment of each tumor cell line; each frame represents a type of cancer. For each group, a range of GI$_{50}$, TGI and LC$_{50}$ values is reported; values are expressed as a molar concentration (M). [126]

As for 1*H*−benzotriazole derivatives **13d,j**, compound **13d** did not overcome the preliminary single−dose assay, while **13j** (isoquinolin–5–yl derivative), showed good GI values both at 10 and 1 μM. At 1 μM, its best activity was measured on CCRF−CEM leukemia line, with complete inhibition of cell growth. Figure 8 shows the antiproliferative activity of **13j** on the most affected tumor cell lines. [126]
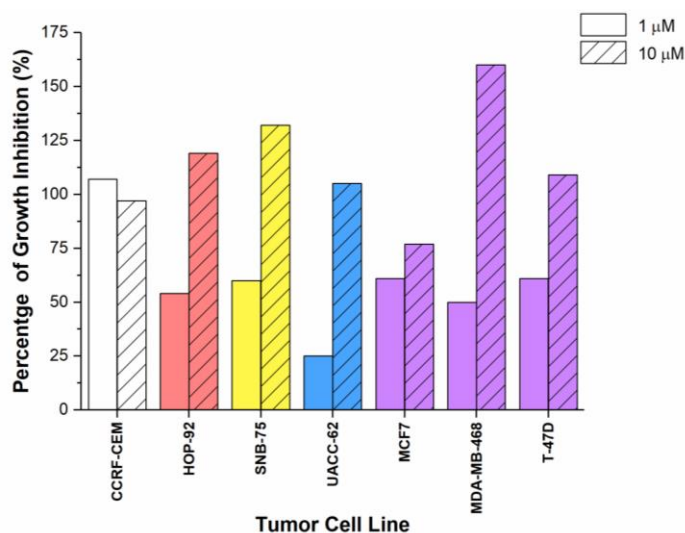
	GI50	TGI	LC50
Leukemia	2.53E-7 - 3.21E-6	2.43E-5 - >1.00E-4	>1.00E-4
NSC Lung Cancer	5.32E-7 - 2.32E-5	5.13E-6 - >1.00E-4	>1.00E-4
CNS Cancer	1.84E-7 - 3.24E-5	3.61E-6 - >1.00E-4	>1.00E-4
Melanoma	2.04E-6 - 7.71E-6	>1.00E-4	>1.00E-4
Breast Cancer	5.57E-7 - 2.97E-6	2.84E-6 - >1.00E-4	>1.00E-4

Figure 8. Bar chart of the growth inhibition percentages for the seven most representative tumor cell lines treated with compound **13j**, at 1 or 10 μM concentration. The table shows a range of GI_{50}, TGI and LC_{50} values (M) for each reported type of cancer. [126]

The following cell cycle analyses through XTT assay and flow cytometry were performed by Prof. Bagella group (Department of Biomedical Sciences, University of Sassari, Italy; Sbarro Institute for Cancer Research and Molecular Medicine, Center for Biotechnology, College of Science and Technology, Temple University, Philadelphia, USA).

5.1.4.2. IC_{50} and mechanism of action of compound 9a against HeLa cells

On this basis, compound **9a** was employed for further biological assessment. To understand if this compound could be considered as microtubule−destabilizing agent (MDA), [117–122] two types of tests were performed: XTT and flow cytometry assays.

The XTT is a colorimetric assay based on changes in the light absorbance of tetrazolium salts. These salts are absorbed into cells when added to the culture medium, then reduced by the metabolic activity of dehydrogenase enzymes, obtaining a chromogenic formazan product. This process occurs only when cells are metabolically active; therefore, XTT assay detects only viable cells. Compound **9a** was administered in the culture medium of HeLa cells at different concentrations, between 5 and 0.1 μM. After 24 and 48 h, the absorbance data were collected and the percentage of cell viability was calculated. [135] Significant

evidence was shown after 48 h of administration, with 50% of alive cells and an $IC_{50} = 3.2$ μM.

Flow cytometry shows the change in DNA content after the administration of a compound, to prove the effect of compound **9a** on the cell cycle of HeLa cells. After 24 h, the control medium has a 30% of cells in G2/M−phase; administering compound **9a** at 10 and 5 μM, an increase of cells in G2/M−phase was displayed after 24 h, 54% and 66% respectively. This increase led to a decrease of cells in G1−phase: if the control has 65% HeLa cells in G1−phase, the percentage decreases to 20% at 10 μM and 39% at 5 μM. After 48 h of treatment, an increase of cells in G2/M−phase (87%), with 10% of cells in G1−phase was detected, while at 5 μM, there is a 41% of cells in G1−phase and 50% of cells in G2/M−phase. Flow cytometry results are reported in Figure 9. [126]

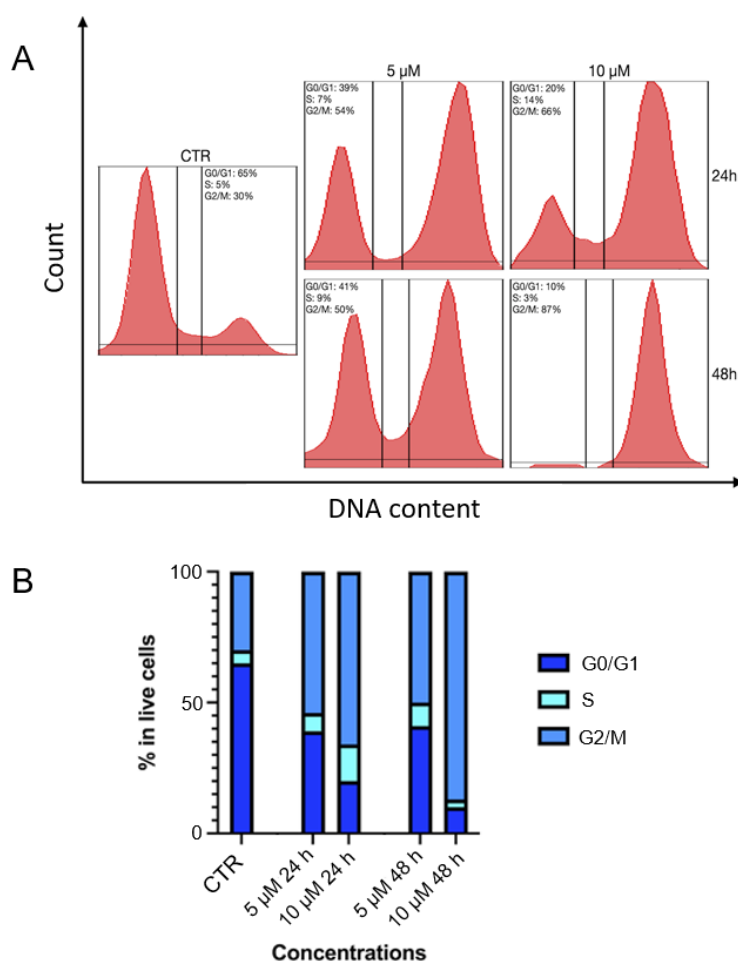**Figure 9.** Cell cycle phase distribution analysis after treatment with compound **9a** in HeLa cells. A) Cell cycle profiles of HeLa cells treated with 5 μM and 10 μM of compound **9a** after 24 or 48 h. Treatment with 5 μM of compound **9a** causes an increase of cells in G2/M−phase after 24 h with a complete block at 10 μM after 48 h from the administration. B) Histogram showing percentages of cells in the different phases. [126]

The following fluorescence microscopy screening, high−content confocal microscopy screening and the colchicine−competition assay were assessed by Dr. Michele Lai (Retrovirus Centre, Department of Translational Medicine and New Technologies in Medicine and Surgery, University of Pisa, Italy; CISUP – Centre for Instrumentation Sharing – University of Pisa, Italy).

5.1.4.3. The effect of compound 9a on cytokinesis in HeLa cells

Later, compound **9a** was further investigated through fluorescence microscopy after administration, for 4 h. An increase of cells in the G2/M−phase was previously shown, hence the number of incomplete cytokinesis events per field was counted. Figure 10 reports the results of the cytokinesis screening, where an increase of incomplete cell divisions could be appreciated starting from 0.3 µM concentration. From a conformational point of view, an overall increase in cell dimension was observed in treated HeLa cells compared to controls. This effect further confirms the cell−cycle blockade; moreover, the increase of the cytoplasmic area suggests the onset of a senescent−like phenotype. [126]
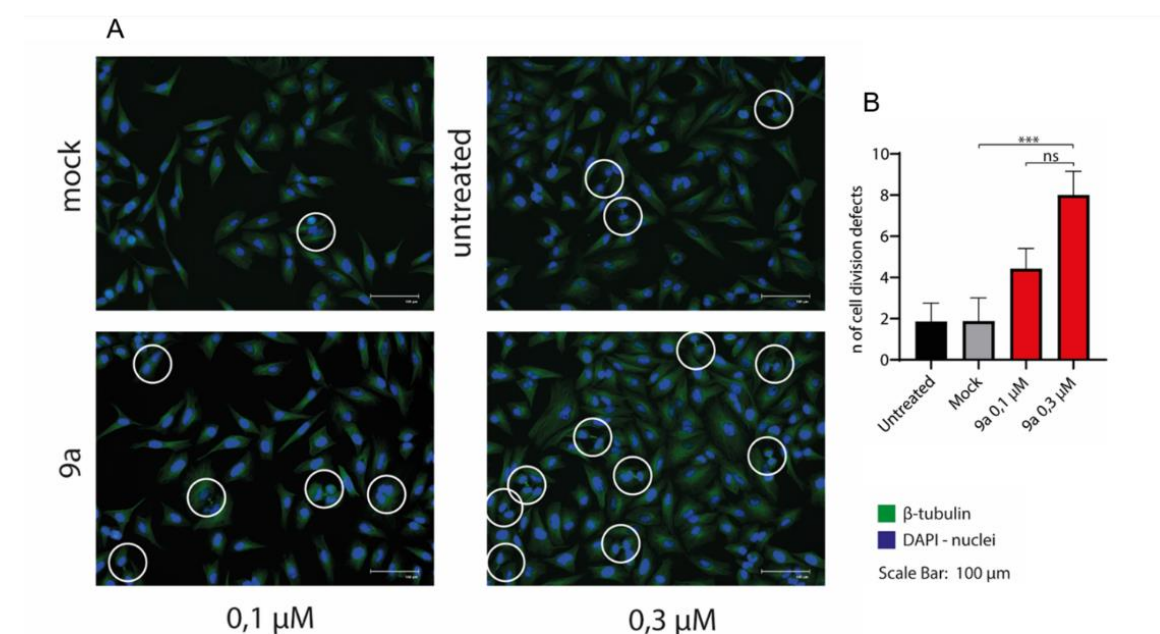

Figure 10. Fluorescence microscopy assay showing cytokinesis events in HeLa cells. A) Images, taken 48 h treatment with **9a** and controls stained with β−tubulin, show an increase of incomplete cell divisions starting from 0.3 µM. B) Kruskal−Wallis test with multiple comparisons performed on the number of incomplete cell divisions per field. *** P(< 0.0001); ns = not significant. [126]

5.1.4.4. High−content imaging on HeLa cells

To confirm the activity on the target, tubulin behavior after treatment was evaluated treating HeLa cells with compound **9a** for 24 h at different concentrations (10, 25, 50, 100 and 500 nM). Cells were stained for β−tubulin and processed through high−content confocal microscopy screening. As shown in Figure 11, β−tubulin disassembly is visible from a concentration of 50 nM. Regarding the cell shape, HeLa cells increased their dimension by three times, compared to controls. [126]
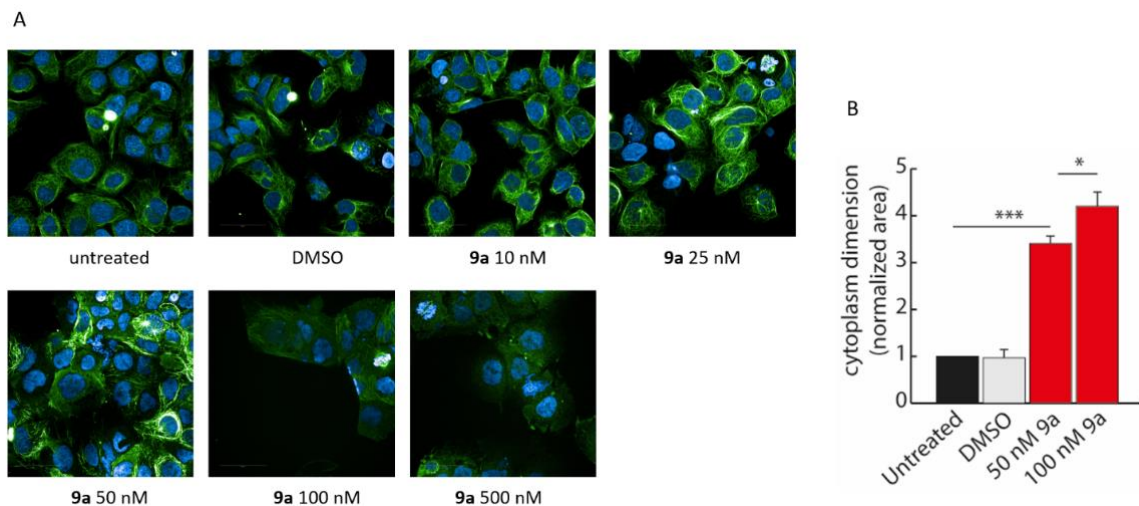
Figure 11. High content confocal screening on HeLa cells after administration of compound **9a**. A) Increasing doses of **9a** were used to treat HeLa cells for 24 h. Then, cells were stained for β−tubulin (green) and nuclei (DAPI−blue). We observed the disruption of microtubules starting from a concentration of 50 nM. B) One−way ANOVA analysis performed on cytoplasm area using high−content screening. Data are expressed as mean ± SD. Experiments were performed with three biological and three technical replicates. [126]

5.1.4.5. Compound 9a competes for the colchicine−biding site on tubulin

Together with the implication of compound **9a** in the β−tubulin disassembly, we wanted to prove the specificity of binding of this derivative to the colchicine−binding site on tubulin. A colchicine−competition assay was undertaken. Figure 12 contains a schematic representation of the effect of colchicine and compound **9a** on tubulin polymerization and their competition effect following their co−administration. Blue triangles line shows a reduction in tubulin polymerization in the presence of compound **9a**. Red triangles, instead, confirm the competition of compound **9a** with colchicine for the same binding site on tubulin, decreasing the effectiveness of colchicine. [126]

Figure 12. Schematic representation of the colchicine−competition assay on HeLa cells. Tubulin was pre−incubated with an equimolar concentration of colchicine, **9a** and **9a**+colchicine. Then, tubulin polymerization was assessed by measuring absorbance every two seconds for a total of 30 min. Statistical analy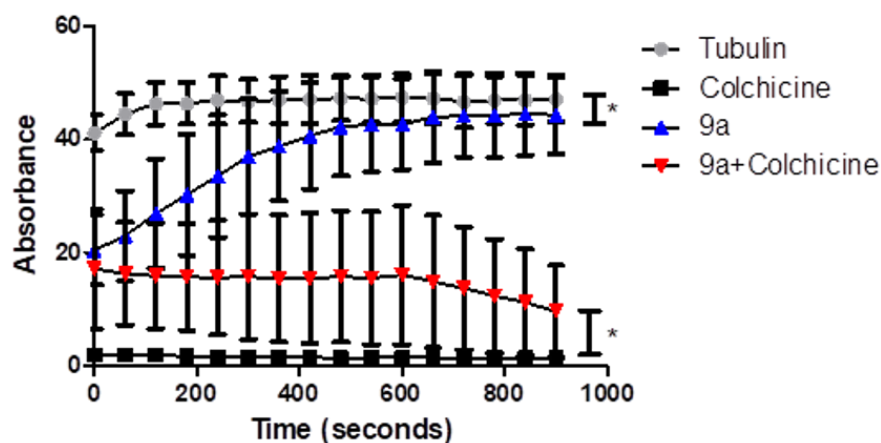ses were performed using a one−sample T test and expressed as mean ± SD, * $p \leq 0{,}01$. Side scale bars compare tubulin/**9a** (upper bar) and **9a**+colchicine/colchicine (lower bar) curves. [126]

The following Kinetics of Cytotoxicity and Proliferation assay was assessed by Kitos Biotech (Sassari, Italy).

5.1.4.6. Cytotoxicity effect of compound 9a in presence or absence of an extrusion pump inhibitor (EPI)

Overexpression of extrusion pumps (EPs) is one of the main factors responsible for drug resistance in cancer cells. The augmented activity of drug extrusion dramatically decreases the drug concentration in the cytoplasmic environment, consequently decreasing the effectiveness of the drug at its intracellular target. Therefore, we decided to test our lead compound in combination with previously synthetized EP inhibitors.

A498 and A549 cell lines were also included in the NCI60 panel used for the preliminary antiproliferative screening, hence the preliminary results showed before were used to extrapolate the concentration range to test compound **9a** in this co−administration assay. Compound **SS26** was selected from our EPI library (structure not shown for Intellectual Property rights). As reported in Figure 13, the activity of **SS26** as EPI was tested by co−administration assay with doxorubicin (known EP client) in HCT−15 colon cancer cell line. [126]
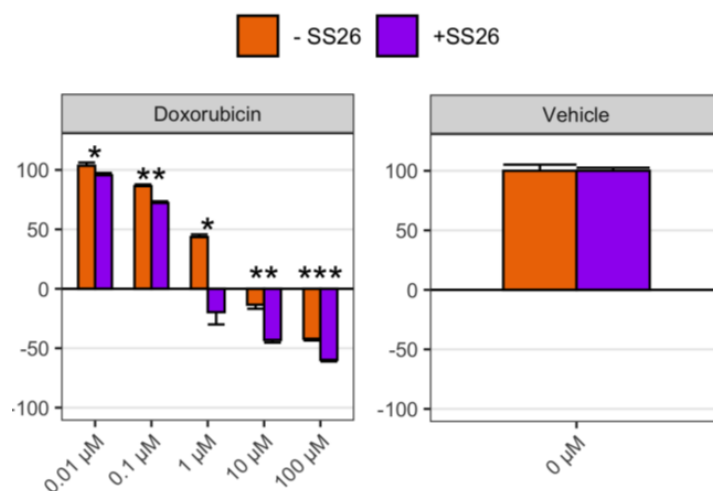
Figure 13. Biological activity of EPI **SS26**, showing the effect of doxorubicin alone or in co−administration with **SS26** in HCT−15 tumor cell line. [126]

To evaluate the effect of the combination **9a** + **SS26**, four drug−resistant cancer cell lines characterized by EP overexpression were selected, A498 and A−704 (kidney cancer), A549 (non−small cell lung cancer) and HT1197 (bladder cancer). [136]

Figure 14 shows the growth percentage of each drug−resistant cell line treated for 24, 48 and 72 h, with different concentrations of compound **9a** (16, 8, 4, 2 and 1 μM), in the presence or absence of compound **SS26**. Derivative **SS26** was always used at 1 μM as standard concentration. Data at 24 h were reported for the sake of completeness since the cell growth was not stable after one day after seeding, hence the results are not reliable. Analyzing the percentages of growth at 48 and 72 h, we can appreciate the beneficial effect of this co−administration since cell growth inhibition is greatly improved for the A−704 cell line at 48 and 72 h. [126]
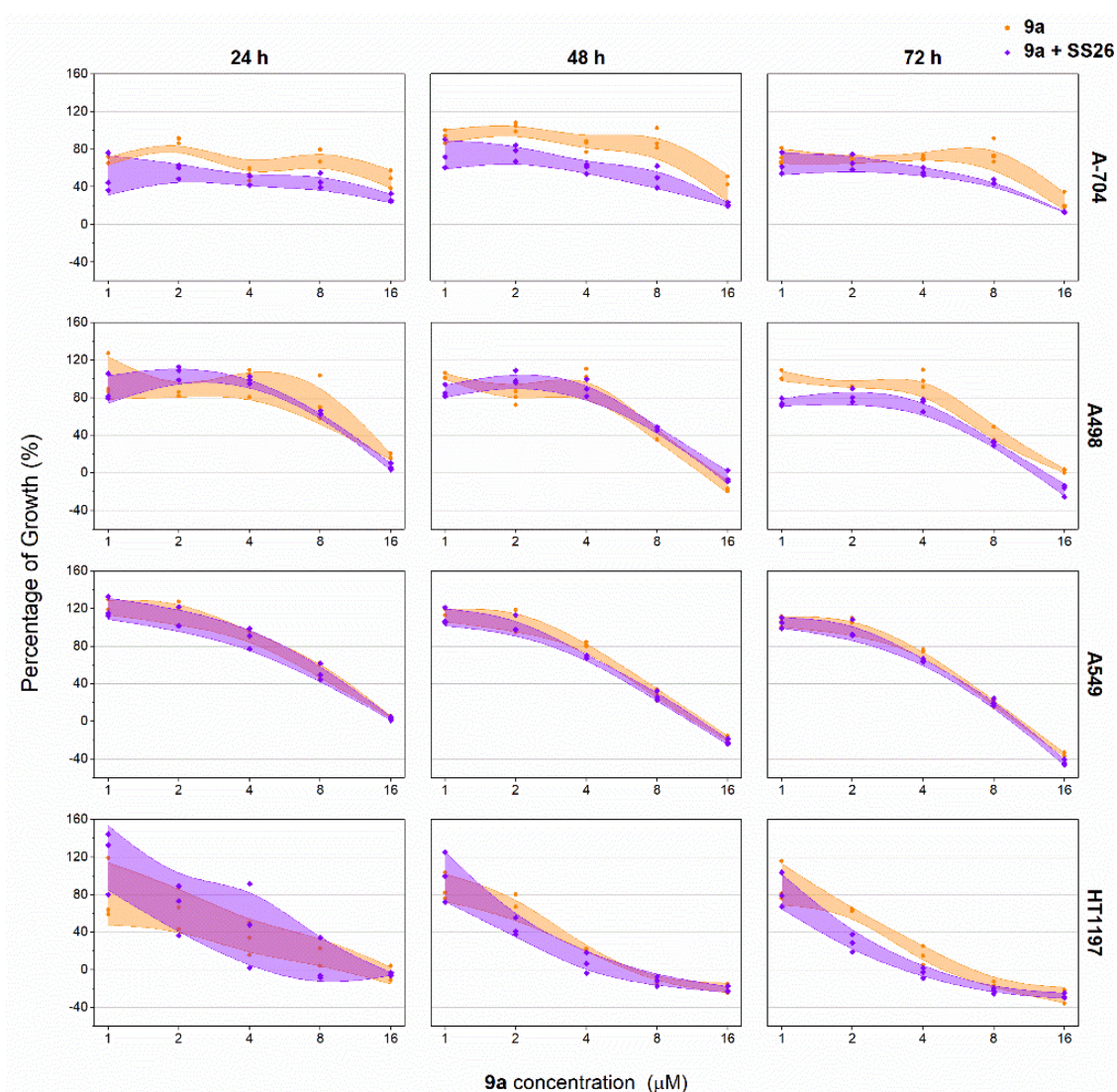
Figure 14. Co−administration assay of compound **9a** and EPI **SS26**. In the y−axis is reported the growth percentage of the tumor cells treated with compound **9a** alone and in association with EPI **SS26**. Data are reported as Loess model with 95% confidence interval. This co−administration assay highlighted different information: compound **9a** is client of extrusion pumps, being negatively influenced in its antiproliferative potency, and the increased concentration of **9a** in the cytoplasmic environment notably improves its activity. [126]
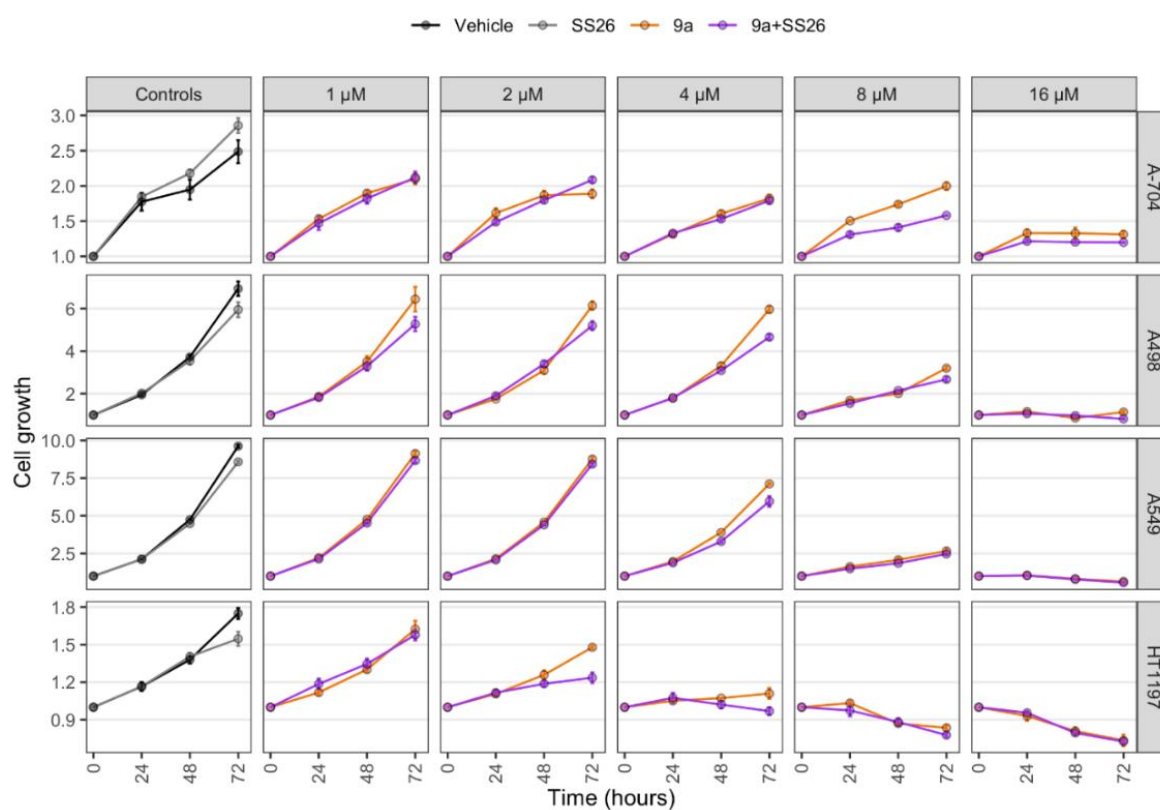
Figure 15. Cell growth analysis after treatment with compound **9a**, alone and in co−administration with EPI **SS26**. Mean ± se. [126]

Figure 15 reports in a different type of graph the results discussed above, concentrating on the raw cell growth values. Figure 16, instead, shows the concentration−dependent efficacy of the co−administration of **9a** + **SS26**, compared to the control. Table 1 contains IC_{50}, GI_{50}, TGI and LC_{50} data of the treatment of the four drug−resistant cancer cell lines treated with the above−mentioned co−administration, at 48 and 72 h. [126]
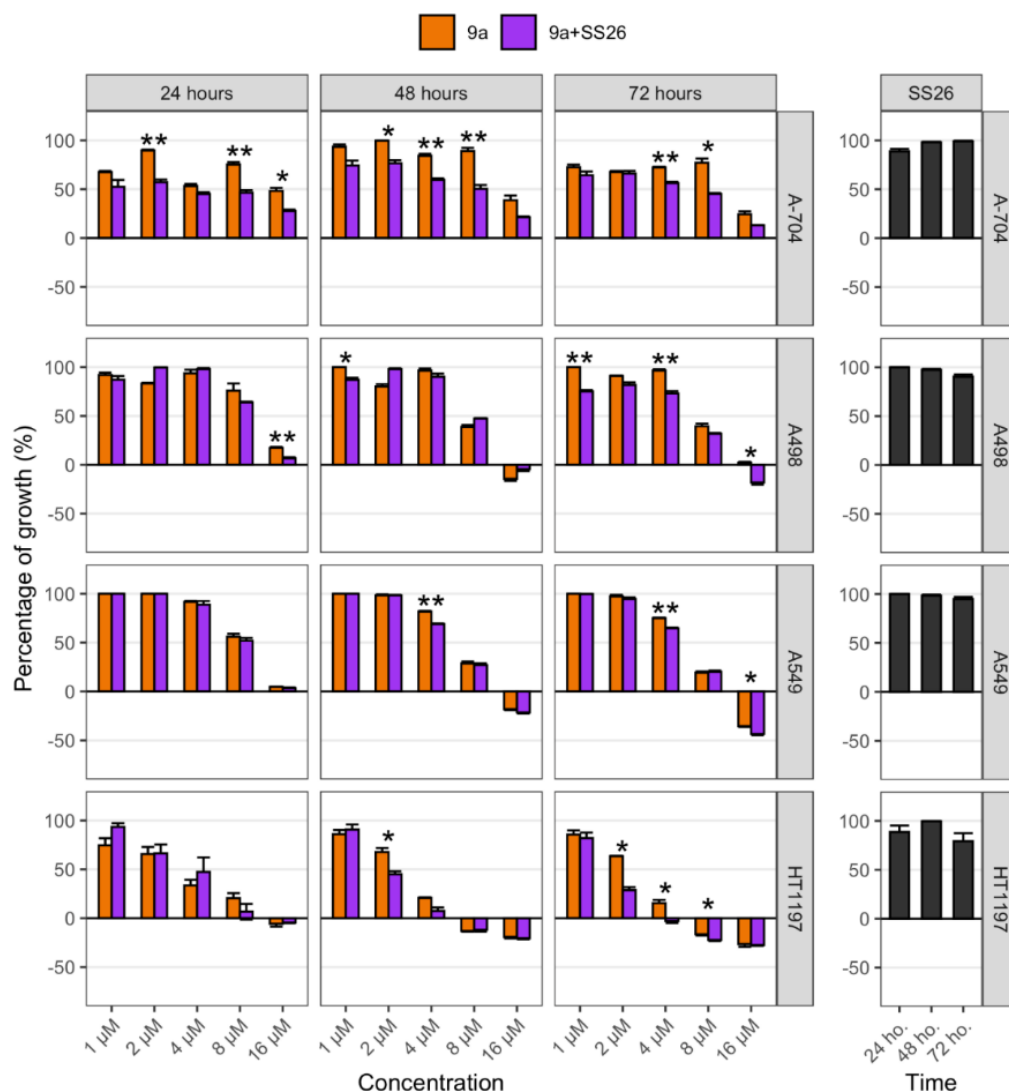
Figure 16. Analysis of the concentration−dependent efficacy for compound **9a** alone and in co−administration with EPI **SS26**. Mean ± se. One−side unpaired test for increased efficacy in co−treatment with **SS26**. p−value < 0.05 (*), < 0.01 (**), < 0.001 (***). [126]

Table 1. Determination of IC_{50}, GI_{50}, TGI, and LC_{50} values at 48 and 72 h of treatment with compound **9a** alone or in co−administration with EPI **SS26**. Mean (mean−SD − mean+SD). [126]

Cell Line	IC_{50} 9a	IC_{50} 9a + SS26	GI_{50} 9a	GI_{50} 9a + SS26	TGI 9a	TGI 9a + SS26	LC_{50} 9a	LC_{50} 9a + SS26
48 hours								
A–704	> max conc.	> max conc.	14.4 (13.8–15.1)	8.1 (6.3–9.7)	> max conc.	> max conc.	> max conc.	> max conc.
A498	8.7 (8–9.4)	9.6 (8.9–10.2)	7.1 (6.8–7.4)	7.7 (7.3–8.1)	13.1 (12.5–13.7)	15.2 (14.5–15.9)	> max conc.	> max conc.
A549	7.1 (6.9–7.3)	6.2 (6.1–6.3)	6.1 (5.9–6.4)	5.6 (5.3–5.8)	12.1 (11.5–12.7)	11.9 (11.4–12.4)	> max conc.	> max conc.
HT1197	> max conc.	> max conc.	2.7 (2.5–2.8)	1.9 (1.7–2.1)	5.8 (5.4–6.4)	4.9 (3.9–6.4)	> max conc.	> max conc.
72 hours								
A–704	> max conc.	15.3 (14.4–NA)	12.5 (11.9–13)	6.5 (5.1–7.8)	> max conc.	> max conc.	> max conc.	> max conc.
A498	7.5 (7–8.1)	6.2 (5.9–6.6)	7 (6.8–7.3)	6.1 (5.9–6.4)	> max conc.	12.6 (12.1–13.1)	> max conc.	> max conc.
A549	5.7 (5.7–5.8)	5 (4.9–5.2)	5.6 (5.4–5.8)	5.2 (4.9–5.4)	10.2 (9.8–10.6)	10.2 (9.9–10.5)	> max conc.	> max conc.
HT1197	7 (6.3–8.1)	5.4 (4.9–5.9)	2.5 (2.2–2.7)	1.5 (1.4–1.6)	5.3 (4.7–6)	3.7 (3.2–4.3)	> max conc.	> max conc.

5.1.5. Compound 9a docks in the colchicine−binding site at the interface between α− and β−tubulin

As previously carried out for compounds **34** and **9b**, a docking investigation was conducted on lead **9a** using AutoDock Vina and the same docking parameters used before. Figure 17 represents a 2D and 3D docking representation of compound **9a** best−predicted pose. As for compound **9b**, here too, the role of fluorine bonds is important. The fluorine atom on C−6' has two fluorine bonds with the amino groups of Alaβ250 and Leuβ255 of β−tubulin, with bond lengths of 4.75 and 4.96 Å, respectively.

N−3' of the triazole ring has an H−bond with the oxygen of Valβ238 of β−tubulin (4.28 Å), while the cyan group of the acrylonitrile linker interacts with the carbonyl oxygen of Alaβ317 of β−tubulin (4.29 Å). Compound **9a** also establishes different hydrophobic interactions in the colchicine−binding site, particularly with the β−subunit. More in−depth, the benzotriazole scaffold mainly interacts with some exposed amino acids such as Aspβ251, Ileβ318 and Alaβ354, while the tolyl moiety has nonpolar interactions with Leuβ248, Asnβ258, Metβ259 and Lysβ352. [126]
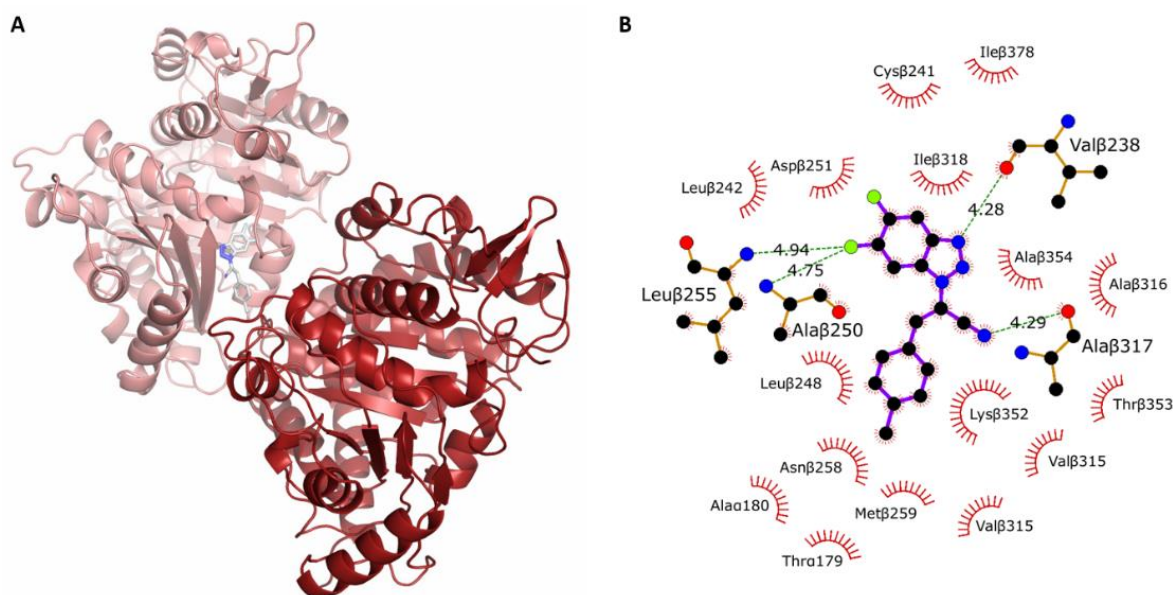
Figure 17. A) 3D structure of **9a** docking pose in the colchicine−binding site in tubulin. B) 2D representation of lead compound **9a** showing its polar/nonpolar interactions with the colchicine−binding pocket on tubulin. [126]

Focusing on the spatial conformation of the crystal structure of colchicine, its structure was superimposed with the best−predicted pose of compound **9a**. Figure 18 depicts the superimposition of these two structures in the colchicine−binding site at the interface between α− and β−tubulin. The benzotriazole scaffold of **9a** overlaps with the

trimethoxyphenyl portion of colchicine, while the acrylonitrile linker almost overlaps with one methoxyl group of the same aromatic portion on colchicine. The tolyl ring of compound **9a** overlaps with the phenoxy ring of colchicine. To sum up, the best−docked pose of compound **9a** and the deposited crystal structure of colchicine (in 4O2B) occupy the same portion of the active site and the two structures overlap in different structural portions, allowing a similar spatial conformation in the binding pocket. [126]
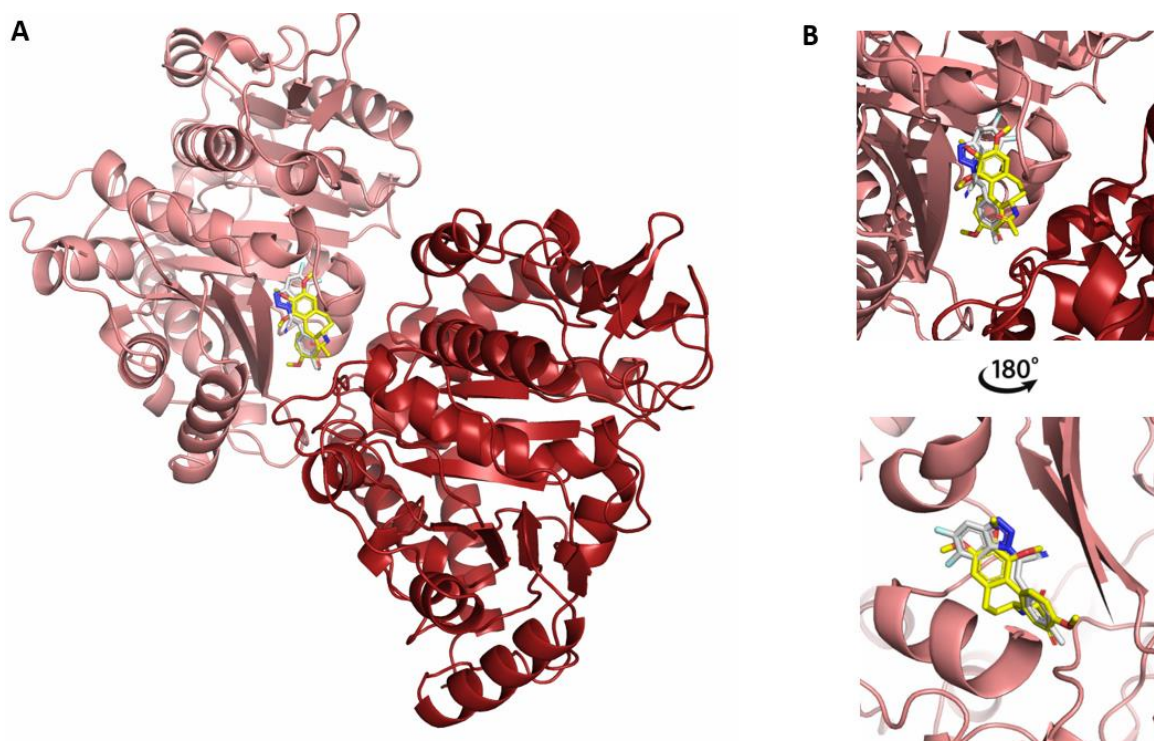
Figure 18. Superimposition of the best−predicted pose of compound **9a** (in light grey) and the crystal structure of colchicine (in yellow, PDB code: 4O2B) in the colchicine−binding pocket at the interface of α− and β−tubulin. α,β−chains of tubulin are distinguished by different colors: the β−monomer is salmon−colored, the α− one is in brick red color. [126]

Given the fact that compound **9a** docks in the colchicine−binding pocket on tubulin with a spatial conformation almost overlapping with the crystal structure of colchicine, its docked structure was compared to different crystal structures of other known CBSIs in phase I−II−III clinical trials. The interactions between tubulin and compound **9a** or the other CBSIs are reported in Figure 19. The selected CBSIs are tivantinib (TIV, PDB ID: 5CB4), [137] plinabulin (PLI, PDB ID: 5C8Y) [137] and crolibulin (CRO, PDB ID: 6JCJ). [138] Tivantinib is in phase I−II−III for the treatment of several cancers. [139–141] The discovery of the direct binding of tivantinib to the colchicine−binding site on tubulin is quite recent; its binding mode was found to overlap with that of colchicine. [142] The main electrostatic

interactions of tivantinib with tubulin active site are represented by the direct H−bonds with Asnβ256 and Alaβ315 of β−tubulin. [137] Plinabulin is in phase I−II in the treatment of several types of tumors. [143,144] It is a vascular−disrupting agent (VDA) which has tubulin depolymerization as the main mechanism of action. Also, plinabulin crystal structure could be overlapped to that of colchicine, binding a deeper portion of β−tubulin and engaging in hydrogen bonds with Gluβ198 and Valβ236. [137] The third chosen CBSI, crolibulin, has completed a phase II trial for anaplastic thyroid in combined therapy with cisplatin, [145–147] but it is also employed in the treatment of prostate adenocarcinoma [148] and gliomas. [149] Clinical application is affected by the side effects, represented by cardiovascular issues and neurotoxicity. [150,151] Its binding at the interface between α− and β−tubulin is supported mainly by three hydrogen bonds between its 2−amino, 7−amino and 3−cyano groups of the chromene portion with amino acids Thrα179 and Alaβ248 on tubulin, respectively. As shown and discussed before, the binding of the best−predicted pose of lead **9a** is mostly focused on β−tubulin, with four H−bonds with alanine, leucine and valine exposed residues of the active site. So, comparing the best−predicted pose of compound **9a** with the crystal structures of these three CBSIs and the colchicine one, we can confirm that the most favorable conformational state of compound **9a** binds in the same binding pocket, but with a different pattern of polar and nonpolar interactions with the exposed amino acids. These results indicate compound **9a** as an interesting molecule to be further investigated.

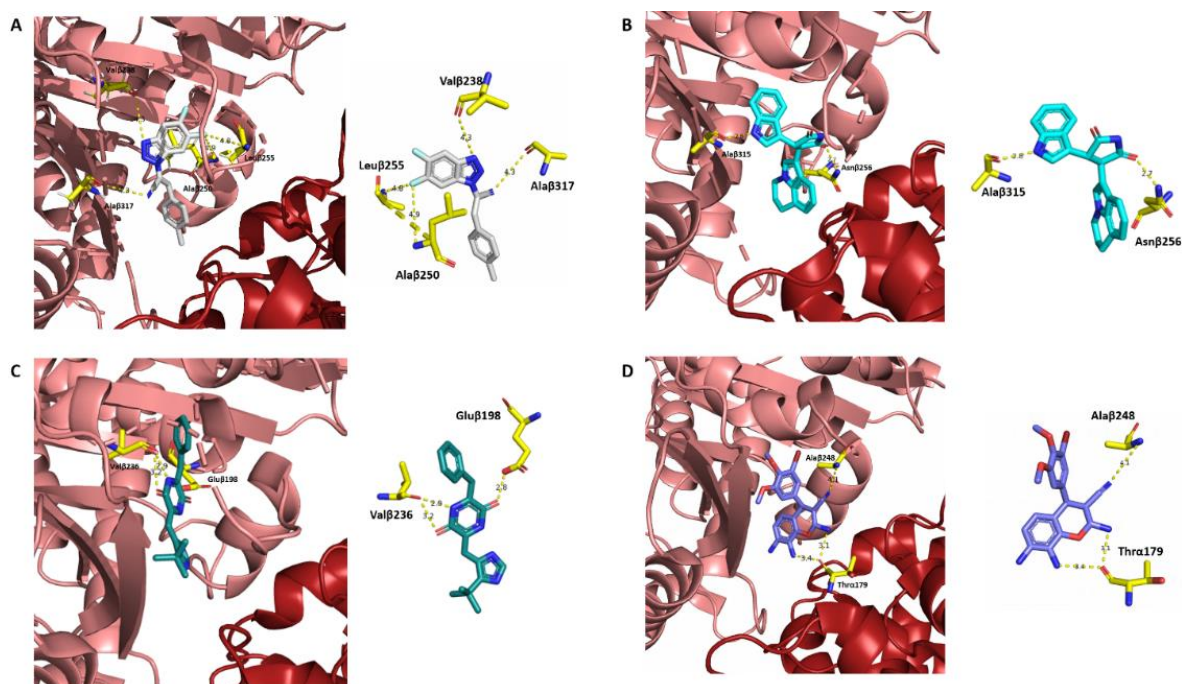**Figure 19.** Comparison of binding interactions of the best−predicted pose of compound **9a** (light grey, A, with 4O2B apo−form) and the crystal structures of tivantinib (marine blue, B, 5CB4),

plinabulin (dark green, C, 5C8Y) and crolibulin (violet, D, 6JCJ), with the colchicine−binding site on tubulin. The α−tubulin subunit is colored in brick red, while β−tubulin is salmon−colored. [126]

5.1.6. Physicochemical, pharmacokinetic and drug−likeness predictions

Due to a large number of clinical trial failures, physicochemical, pharmacokinetic and drug−likeness predictions are rising a growing interest in the Drug Development process. Preliminary evaluation of these properties could be of help in designing better Drug Candidates. SwissADME (http://www.swissadme.ch) algorithms were applied to our MTAs to predict physicochemical, pharmacokinetic and drug−likeness properties as reported in Table 2 (the whole SwissADME reports are reported in SM of our published paper). [126] The molecules possess a molecular weight in the range of 262 and 372 g/mol. Rotatable bonds are from 2 and 5. In general, H−bond donors are absent, while H−bond acceptors range from 2 to 5. TPSA (topological polar surface area) is from 54.50 to 100.32 $Å^2$. The lipophilicity/hydrophilicity balance is quite equilibrated, with cLog$P_{o/w}$ 2.18−3.83 and Log$S$ going from −3.63 to −4.98. Most of the molecules are expected to be moderately water−soluble, with few exceptions.

Regarding the pharmacokinetic profile, all compounds are expected to be adsorbed through the gastrointestinal (GI) membrane and to cross the blood−brain barrier (BBB). They are predicted to be bad substrates of P−gp, even if we experimentally recognized compound **9a** to be client of EPs. All compounds showed to possess drug−likeness potential, respecting the Lipinski rule−of−five (0 violations) and showing a bioavailability score of 0.55. [126]

Table 2. SwissADME prediction of the physicochemical and pharmacokinetic properties, solubility and drug−likeness of compounds **9a−j**, **10e**, **11a,b** and **13d,j**. [126]

COMPOUND	Phisicochemical properties				Lipophilicity	Water Solubility		Pharmacokinetics			Druglikeness	
	Rotatable bonds	H-bond A	H-bond D	TPSA	CLog $P_{o/w}$	Log S	Solubility class	GI absorption	BBB permeant	P-gp substrate	Lipinski	BS
9a	2	5	0	54.50	3.53	-4.37	soluble (m)	High	Yes	No	Yes (0)	0.55
9b	3	6	0	63.73	3.19	-4.14	soluble (m)	High	No	No	Yes (0)	0.55
9c	5	8	0	82.19	3.18	-4.27	soluble (m)	High	No	No	Yes (0)	0.55
9d	2	6	1	74.73	2.79	-3.93	soluble (m)	High	Yes	No	Yes (0)	0.55
9e-10e	3	7	0	100.32	2.63	-4.12	soluble (m)	High	Yes	No	Yes (0)	0.55
9f	2	6	0	54.50	3.50	-4.23	soluble (m)	High	Yes	No	Yes (0)	0.55
9g	2	5	0	54.50	3.73	-4.67	soluble (m)	High	Yes	No	Yes (0)	0.55
9h	2	5	0	54.50	3.83	-4.98	soluble (m)	High	Yes	No	Yes (0)	0.55
9i	2	7	0	72.96	3.04	-4.17	soluble (m)	High	Yes	No	Yes (0)	0.55
9j	2	6	0	67.39	3.39	-4.55	soluble (p)	High	Yes	No	Yes (0)	0.55
11a	2	5	0	54.50	3.51	-4.73	soluble (m)	High	Yes	No	Yes (0)	0.55
11b	3	6	0	63.73	3.16	-4.49	soluble (m)	High	Yes	No	Yes (0)	0.55
13d	2	4	1	74.73	2.18	-3.63	soluble	High	Yes	No	Yes (0)	0.55
13j	2	4	0	67.39	2.79	-4.25	soluble (m)	High	Yes	No	Yes (0)	0.55

In "physicochemical properties", A is acceptors and D donors. TPSA stands for Topological Polar Surface Area, calculated in A^2. CLog $P_{o/w}$ is the consensus Log P. Log S is a common unit for measuring the solubility, and it is calculated with the ESOL method. For the solubility, (m) stands for "moderately" and (p) for "poorly".

GI means gastrointestinal, BBB blood−brain barrier. Drug−likeness of the molecules are evaluated through the Lipinski 'rule of five' and (0) refers to the number of violations related to this rule. BS is the bioavailability score.

5.2. Conclusions and future outlook

The entire work is focused on a computational and experimental approach aimed at the development of a new series of microtubule−destabilizing agents (MDAs). An initial molecular docking study was accomplished on the previous lead **34** [118] and its analog **9b**, which bears two fluorine atoms in C−5' and C−6' on the benzotriazole scaffold. The docking prediction for the new compound displayed an interesting pattern of interactions with the colchicine−binding site at the interface of α− and β−tubulin, justifying further experimental investigation. The new series of 5',6'−difluoro−benzotriazolacrylonitrile derivatives was synthesized and *E/Z* final products **9a−j**, **10e**, **11a−b** and **13d,j** were characterized by NMR spectroscopy. Their antiproliferative activity was confirmed through the NCI *in vitro* screening against 60 tumor cell lines of 9 types of cancers. This preliminary assessment allowed to select the *p*−CH_3 derivative **9a**, as the most potent compound to be further investigated. At 1 μM, compound **9a** showed growth inhibition percentages between 40 and 60% against eight cancer cell lines and 70−100% against further seven tumor cell lines. Compound **9a** was then proposed as a microtubule−destabilizing agent (MDA); to confirm this mechanism of action, a cell cycle analysis was performed on HeLa cells, after treatment with **9a**. Our new lead was demonstrated to block most of the cells in the G2/M−phase, causing an increased number of cell division defects and an IC_{50} value of 3.2 μM. An analysis at fluorescence microscopy showed slowed cytokinesis in HeLa cells after treatment, while high−content confocal microscopy showed tubulin disassembly. The binding to the colchicine−binding site was then confirmed through a competition assay with colchicine. Interestingly, the co−administration of compound **9a** with an extrusion pump inhibitor (EPI), **SS26**, at a standard concentration of 1 μM, showed an increased antiproliferative potency on four drug−resistant cell lines (resistance through overexpression of P−gp). All synthesized compounds showed a good profile of pharmacokinetic and drug−likeness properties. In summary, compound **9a** demonstrated to be endowed with a satisfying although preliminary anticancer profile. In Chapter 6 the design, synthesis and biological assessment of a parental series of compounds will be discussed, as a follow−up of the series presented in Chapter 5.

6. A new class of microtubule destabilizing agents (MDAs): design, synthesis and biological screening of 4'−fluoro−benzotriazole−acrylonitrile derivatives

6.1. Rationale and Molecular Modeling Design

The starting point for the Rational Design of this project is the above–discussed previous lead **34**, computationally and experimentally recognized as CBSI, [119] and the 5',6'–difluoro–substituted lead **9a**. [126] The present project aimed to follow the path of the fluorine substitution on the benzotriazole scaffold, functionalized in different positions on the triazole ring with an acrylonitrile moiety. We decided to reinsert hydrogen atoms in C–5' and C–6' positions, as reported for compound **34**, exploring at the same C–4' position, not considered for substitution in the previous series. The *p*–tolyl–, *p*–methoxyphenyl– and *p*–bromophenyl moieties were selected to be linked at the acrylonitrile middle chain. [126] A similar synthetic approach was followed to obtain this new class of (*E*)-2-(4'-fluoro-1*H*-benzo[*d*][1,2,3]triazol-1(2)-yl)-3-(*R*)acrylonitrile (**5–10**) and (*E*)-2-(7'-fluoro-1*H*-benzo[*d*][1,2,3]triazol-1-yl)-3-(*R*)acrylonitrile (**11–13**). Compound **5**, which differs from **34** just for the fluorine on C–4', was initially subjected to a preliminary docking prediction. The best–predicted pose of compound **5**, docked in the colchicine–binding site at the interface of α,β–tubulin, was more in–depth studied, analyzing its mode of binding, protein–ligand electrostatic and van der Waals interactions. The polar term of the binding seems to be more relevant comparing its preliminary docking study and those of compounds **34** and **9a**, reported in Chapter 5. Each of the three pharmacophoric regions (benzotriazole, middle linker and *p*–substituted phenyl moieties) of the molecule generates two H–bonds with some amino acids of the CBS (colchicine–binding site), but interestingly the amino acids all belongs to the α–chain on tubulin. The 4'–fluoro benzotriazole scaffold interacts with a fluorine bond between fluorine in C–4' and the donor side–chain amine group of Asnα206, which in turn also donates an H–bond to triazole N–3'. Nitrile nitrogen in the middle linker contacts two side–chain hydroxyl groups of Tyrα224 and Serα178. Methoxyl group is oriented to bind with the intrinsic NH and the side–chain hydroxyl group of Thrα145. The preferred binding to α–chain on tubulin suggests a new binding mode of these molecules with respect to previous lead compounds of the series. [126] Given the potential binding of this molecule, compounds **5–13** were considered for synthesis. To further support the

rational design of this series of derivatives, they were subjected to a prediction of pharmacokinetic and drug–likeness properties through the SwissADME website (http://www.swissadme.ch). In general, M_ws of the derivatives are in the range of 278–343 Da and they present a certain degree of rigidity, with 2–3 rotatable bonds. They possess H–bond acceptor atoms but not donors, as already seen in docking studies. These derivatives have a good lipophilic profile, with a Log P range of 2.86–3.54. All designed compounds are predicted to be moderately soluble in water, while compound **5** is supposed to completely dissolve in the same solvent. Considering the pharmacokinetic properties, they are predicted to be highly absorbable from GI (gastrointestinal) barrier and BBB (blood–brain barrier), but they are predicted to be bad P–gp substrates. They are considered to possess drug–likeness properties, as suitable compounds with 0 violations of Lipinski's rule of five and a bioavailability score of 0.55. Only compound **5** is predicted to have lead–likeness properties. Docking and ADME predictions suggested continuing to work on this class of molecules.
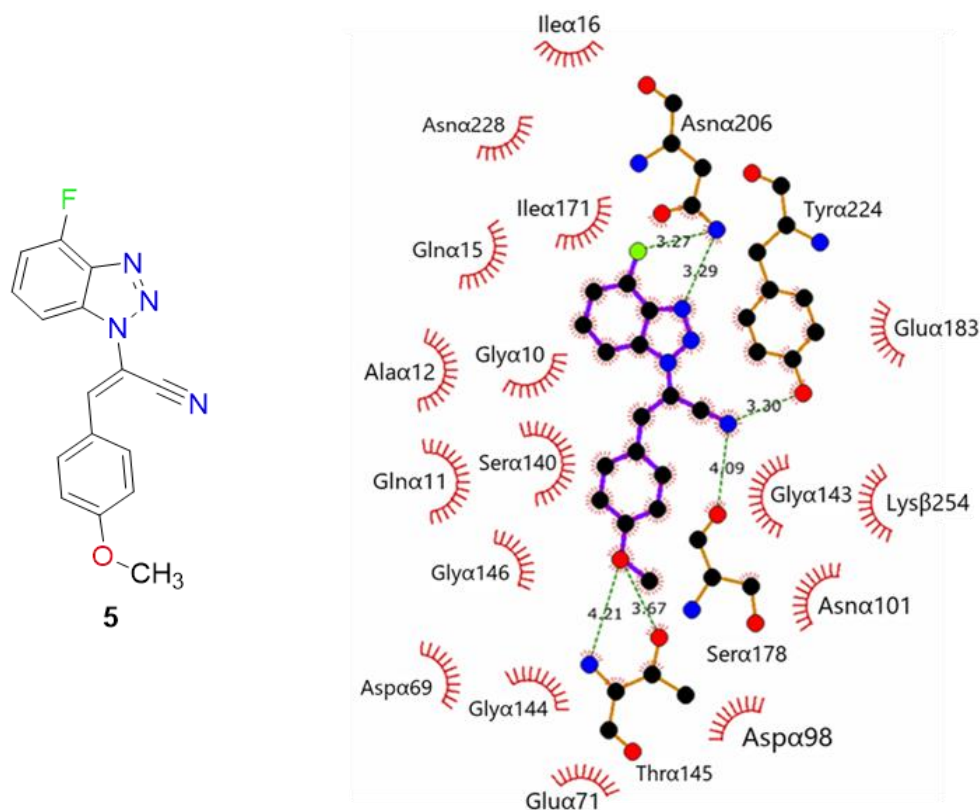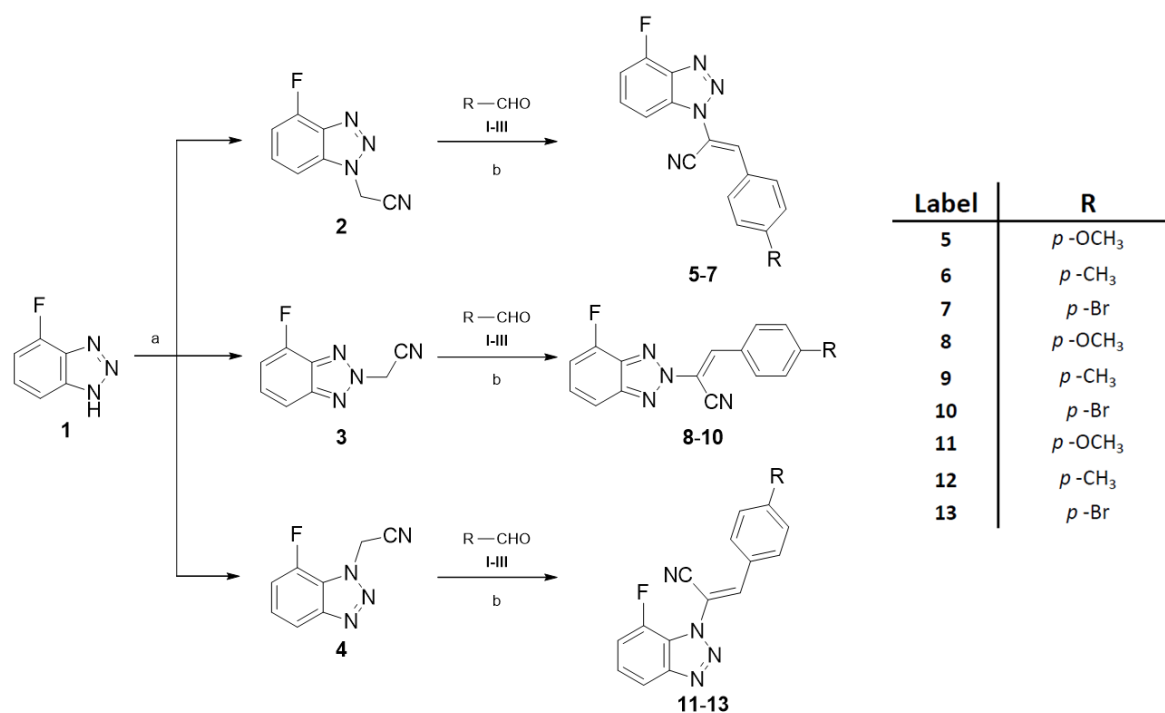

Figure 20. Docking representation of the best–predicted binding pose of compound **5** and its polar/nonpolar interactions with the exposed amino acids of active site at the interface of α,β–tubulin. 2D picture obtained through LigPlot⁺ software. [152]

6.2. Results and Discussion

6.2.1. Chemistry

The synthesis of final compounds **5−7**, **8−10** and **11−13** is described in Scheme 3. Benzotriazole intermediate **1** was achieved as previously described. [126,153] The side acetonitrile chain was attached to compound **1**, in basic conditions, with chloroacetonitrile. The alkylation reaction occurs on all the nitrogen atoms on the triazole ring, generating a mixture of three different derivatives carrying on the side chain in three different positions: isomers **2**, **3** and **4** in N−1, N−2 and N−3, respectively. The three isomers were separated by flash chromatography and characterized by 2D−NOESY NMR experiments. The last Knoevenagel condensation, in basic conditions, carried out on each isomer (**2**, **3** or **4**) with different aromatic aldehydes **I−III**, led to desired acrylonitrile derivatives **5−7**, **8−10** and **11−13**. *R*−groups on aromatic aldehydes were selected from the same library used for the previously synthesized MTAs. [44,45,48−51] Depending on the reactivity of the chosen isomer, or the selected aldehyde, different reaction conditions were necessary, in terms of solvent and base/catalyst: dimethylamine (DMA) for compounds **9**, **10**, **12**; cesium carbonate (Cs₂CO₃) for compounds **8**, **11**, **13**; dimethylammonium dimethylcarbammate (DIMCARB) [133] as base and catalyst for derivatives **5−7**.

Label	R
5	*p* -OCH₃
6	*p* -CH₃
7	*p* -Br
8	*p* -OCH₃
9	*p* -CH₃
10	*p* -Br
11	*p* -OCH₃
12	*p* -CH₃
13	*p* -Br

Scheme 3. Synthetic route followed for (*E*)-2-(4'-fluoro-1*H*-benzo[*d*][1,2,3]triazol-1-yl)-3-(*R*)acrylonitrile (**5–8**), (*E*)-2-(4'-fluoro-2*H*-benzo[*d*][1,2,3]triazol-2-yl)-3-(*R*)acrylonitrile (**9–12**),

(*E*)-2-(7'-fluoro-1*H*-benzo[*d*][1,2,3]triazol-1-yl)-3-(*R*)acrylonitrile derivatives (**13−16**). Reaction conditions: [a] chloroacetonitrile/KOH (1:1.2), CH$_3$CN, reflux, o/n. [b] (A) DMA (ratio 1:1.2), CH$_3$CN; (B) DIMCARB (ratio 1:1.2), CH$_3$CN; (C) Cs$_2$CO$_3$ (ratio 1:1.2), toluene.

6.2.2. Biology

6.2.2.1. NCI60 in vitro screening: antiproliferative activity assay

As previously assessed for 5',6'−difluoro−derived compounds (Chapter 5), newly−synthesized derivatives **5−7**, **8−10** and **11−13** were screened through the NCI60 *in vitro* assay offered by the Developmental Therapeutics Program (DTP) of the National Cancer Institute (NCI) of Bethesda (USA). The followed protocol was already explained in Chapter 5; a first single dose of a compound at 10 µM is performed, then, if the antiproliferative activity satisfies NCI parameters, the entire panel of tumor cell lines (60 lines of 9 solid and hematological types of cancers) is treated with 5 different doses of the compounds, with a range of 100 µM – 10 nM. As previously shown in different parental series of molecules, [119,121,122,126,153] derivatives bearing the acrylonitrile chain in N–2' of the triazole ring (**8–10** for this project), showed an antiproliferative activity on the outermost part of the cancer cell lines, insufficient to be selected for further 5−dose *in vitro* screening. As regards the N–3'– and N–1'–substituted derivatives, they all demonstrated high potency in the inhibition of tumor cell growth at 10 µM. Hence, derivatives **5–7** and **8–10** were further tested through the 5−doses NCI60 *in vitro* assay.

As for the N–3'−substituted derivatives, compound **11** triggers a good antiproliferative activity (70−100%) on the entire panel of tumor cell lines. The same effect was evidenced in 9 tumor cell lines at 1 µM. A cytotoxic effect was displayed against 21 or three cell lines, at 10 and 1 µM respectively. Compound **13** showed the most potent cytotoxic effect of this series on the NCI60 panel. At 10 µM, it almost completely inhibited the cellular growth of all cell lines, with a cytotoxic rate of 57 affected lines out of the 60 total cancer lines. At 1 µM, a cytostatic effect (growth inhibition range of 70−100%) was detected on twelve lines; cytotoxicity was expressed on two cancer lines. As well as derivative **11**, compound **12** exerts an overall inhibition of cellular growth ranging from 70 to 100%; interestingly, at 1 µM, the overall inhibition is around 40−60%. All the leukemia NCI60 panel resulted to be sensible to the treatment with compound **12** at 1 µM, with cellular growth ranging from 0 to 15%. Lethality was displayed on nine cancer lines. Its cytostatic effect is also consistent at 0.1 µM (100 nM), with growth inhibition percentages of 40−50% against five cell lines of

leukemia (K−562 and SR), non−small cell lung cancer − NSCLC (NCI−H522), melanoma (MDA−MB−435) and renal cancer (CAKI−1). As for N–1'−substituted derivatives **5** and **7**, they showed the most potent overall antiproliferative activity, compared to N–2'− and N–3'−substituted ones. Compound **6** is currently under evaluation at NCI, hence data for compound **6** are not discussed. At 10 µM, compound **7** displayed an overall 80−100% cell growth inhibition. This derivative, together with compound **13**, is one of the most cytotoxic compounds of the entire series, with lethal activity on 48 cancer lines. At 1 µM, the most affected lines are those of leukemia, NSCL, colon, CNS, ovarian and breast cancers, with growth inhibition of 78−94% on 10 lines. At 100 nM, a 50% antiproliferative activity was expressed on HOP−92 NSCLC cell line.

Overall, the *p*−OCH$_3$ N–1'−substituted derivative **5**, is the most potent antiproliferative agent of the series, preserving a remarkable activity also at 100 nM. At 10 µM, compound **5** has a 75−100% cytostatic effect on the complete panel of cancer cells, whilst at 1 µM the overall growth inhibition reaches values of ∼ 50%, with higher values of 75−100% on entire leukemia, colon, CNS and prostate tumor lines. A cytotoxic effect was detected also in other cancer lines, but in general consistently lower than other compounds, such as **7** and **13**. Notably, compound **5** at 100 nM provides an antiproliferative effect ranging from 40 to 80% against 9 leukemia, NSCL, colon, ovarian, renal cancer and melanoma lines. Higher inhibition rates were reached against MDA−MB−435 (80%) and K−562 (73%) leukemia cell lines. No cytotoxic effect is shown at this concentration for compound **5**.

Derivative **5** was selected for further biochemical assessment, due to its overall noteworthy antiproliferative effect on a wide range of cancer cell lines at 100 nM. Also, N–3'−derivative **12** was included in some biological assays, due to its notably cytostatic effect at 100 nM.
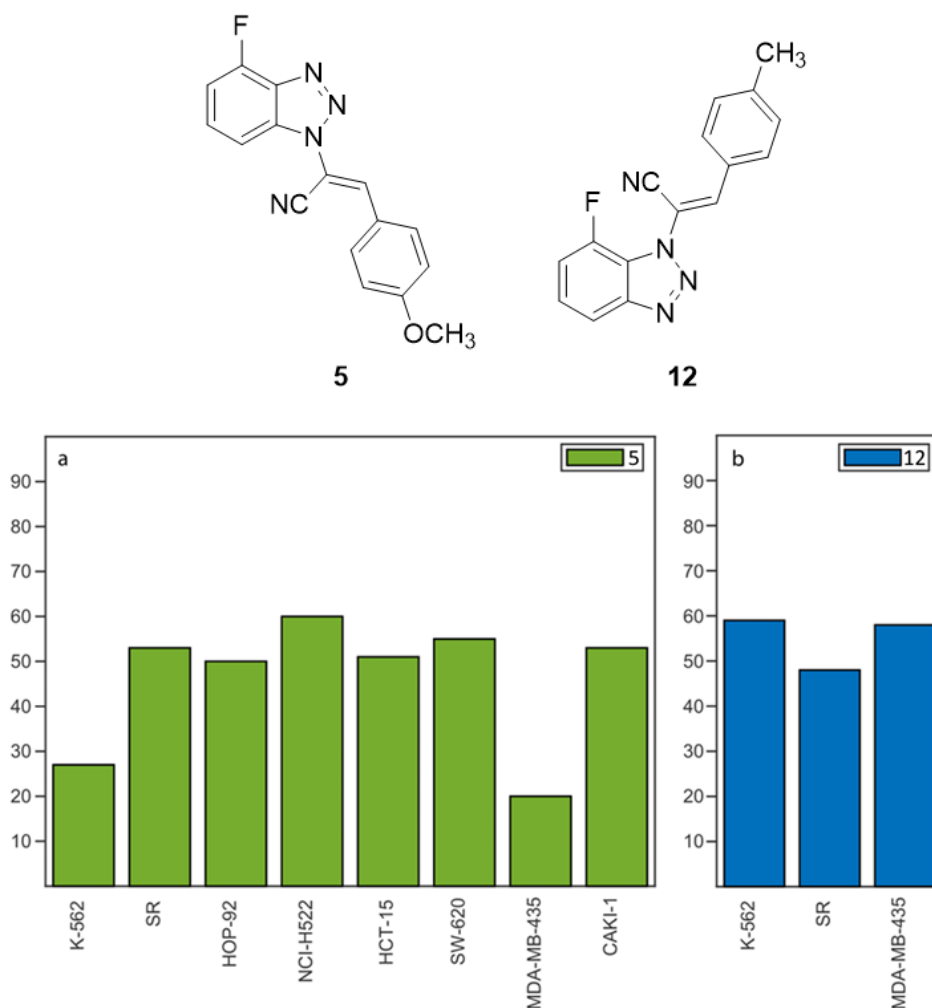
Figure 21. NCI60 cancer analysis on compounds **5** (a) and **12** (b). The histograms depict the growth percentage of NCI60 cancer cells after administration of compounds **5** and **12** at a concentration of 100 nM.

*The following investigation of the mechanism of action of compounds **5** and **12**, the Annexin V assay for their pro–apoptotic effect against HeLa and MCF–7 cells, and the Western Blotting assay were performed by Prof. Bagella group (Department of Biomedical Sciences, University of Sassari, Italy; Sbarro Institute for Cancer Research and Molecular Medicine, Center for Biotechnology, College of Science and Technology, Temple University, Philadelphia, USA).*

6.2.2.2. Antiproliferative effect and mechanism of action of compounds 5 and 12 against HeLa and MCF−7 cells

Initially, HeLa cell line (cervical cancer) was selected for further investigations. XTT colorimetric assay was performed on HeLa cells after 48 hours of treatment with compounds **5** and **12**, with different concentrations from 0.1 to 2 μM. DMSO was used as control and compound **34**, lead compound of the previous series, was used as positive control. After 48 h, compounds **5** and **12** displayed a 50% reduction of alive cells with IC_{50} of 0.6 μM and 0.45 μM, respectively.

After the first preliminary screening, biological investigations were carried out to assess if compounds **5** and **12** were implicated in cell cycle impairment, as described for previously reported compounds. [119,121,126] Compounds **5** and **12** were subjected to a flow cytometry analysis on HeLa and MCF−7 (breast cancer) cells, in order to observe potential changes in DNA content. An increase of cells in phase G2/M was displayed in HeLa cells at 24 h after treatment with 1 and 2 μM of compounds **5** and **12**, as depicted in Figure 22A. At 2 μM, 68% of cells in G2/M−phase were found for compound **5**, whilst the percentage increases to 83% for compound **12**, compared to **34** as positive control (63%).

Figure 22B reports the cell cycle analysis on MCF−7 cells after 24 h treatment with 1 and 2 μM concentrations of compounds **5** and **12**. At 2 μM, an increase of 54% for treatment with derivative **5** and ~ 70% with compound **12**. At 1 μM, cells in G2/M phase are 40% and 41% of the total amount for compounds **5** and **12**, respectively, compared to control (~ 16%). This assay proved the cell cycle impairment caused by treatment with compounds **5** and **12**.
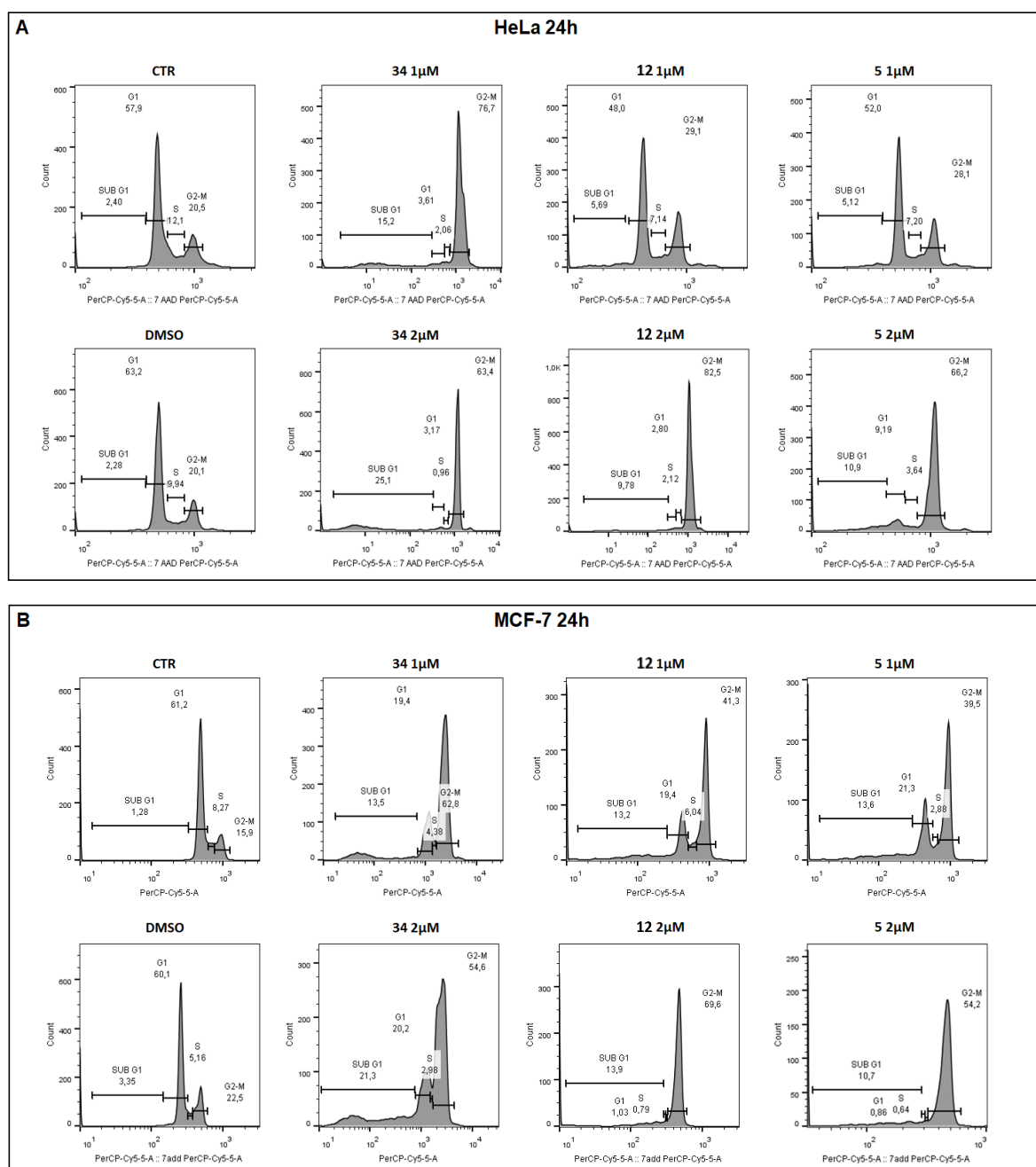
Figure 22. Cell cycle analysis on A) HeLa and B) MCF−7 cancer lines after administration of compounds **5** and **12** at a concentration of 2 and 1 μM for 24 h. A) At 2 μM, for 24 h, they cause cell blockade in G2/M−phase. At 1 μM, they do not show significant differences compared to control and DMSO. B) Compounds **5** and **12** cause cell blockade in G2/M−phase compared to compound **34** (positive control) and DMSO at both concentrations.

6.2.2.3. Annexin V assay uncovers apoptosis activation in HeLa and MCF−7 cell lines with compound 5 and 12 treatment

Subsequently, flow cytofluorimetric analysis was performed using Annexin V−FITC/PI double staining kit, to investigate a potential pro–apoptotic effect of compounds **5** and **12**. First, HeLa and MCF−7 cells were treated with compounds **5** and **12**. A considerable activity on the above–mentioned cell cycle analysis was observed at 2 μM, hence the same concentration of the compounds was chosen for the present assay. After 24 h of treatment, both cell lines were stained with FITC (fluorescein isothiocyanate) and PI (propidium iodide) and the analysis was done with BD FACSCanto™ II system. As shown in Figure 23A, both compounds **5** and **12** activated apoptosis on HeLa cells; an increased amount of late apoptotic cells, from 6.83% in CTR (control) cells and 5.83% in DMSO control, to ~ 14% in treated cells was detected. Regarding early apoptotic cells, cells treated with derivative **5** reached percentages of 13.1%, compared to CTR cells (1.22%) and DMSO (0.82%). As well as derivative **5**, treatment with compound **12** generates a 13.8% percentage of cells in late apoptosis, but also a higher early apoptosis rate of ~ 16%. The pro–apoptotic effect of compounds **5** and **12** approximate compound **34** rates of 19.4 and 13.8% in late and early apoptosis, respectively. As for the treatment of MCF−7 cells with compounds **5** and **12**, depicted in Figure 23B, percentages of 15.1% and 11.2% for early and late apoptosis, respectively, were displayed, compared to control cells (2.46%) and DMSO control (2.54%). The early apoptosis rate is higher than the effect of treatment with compound **34** (9.08%).
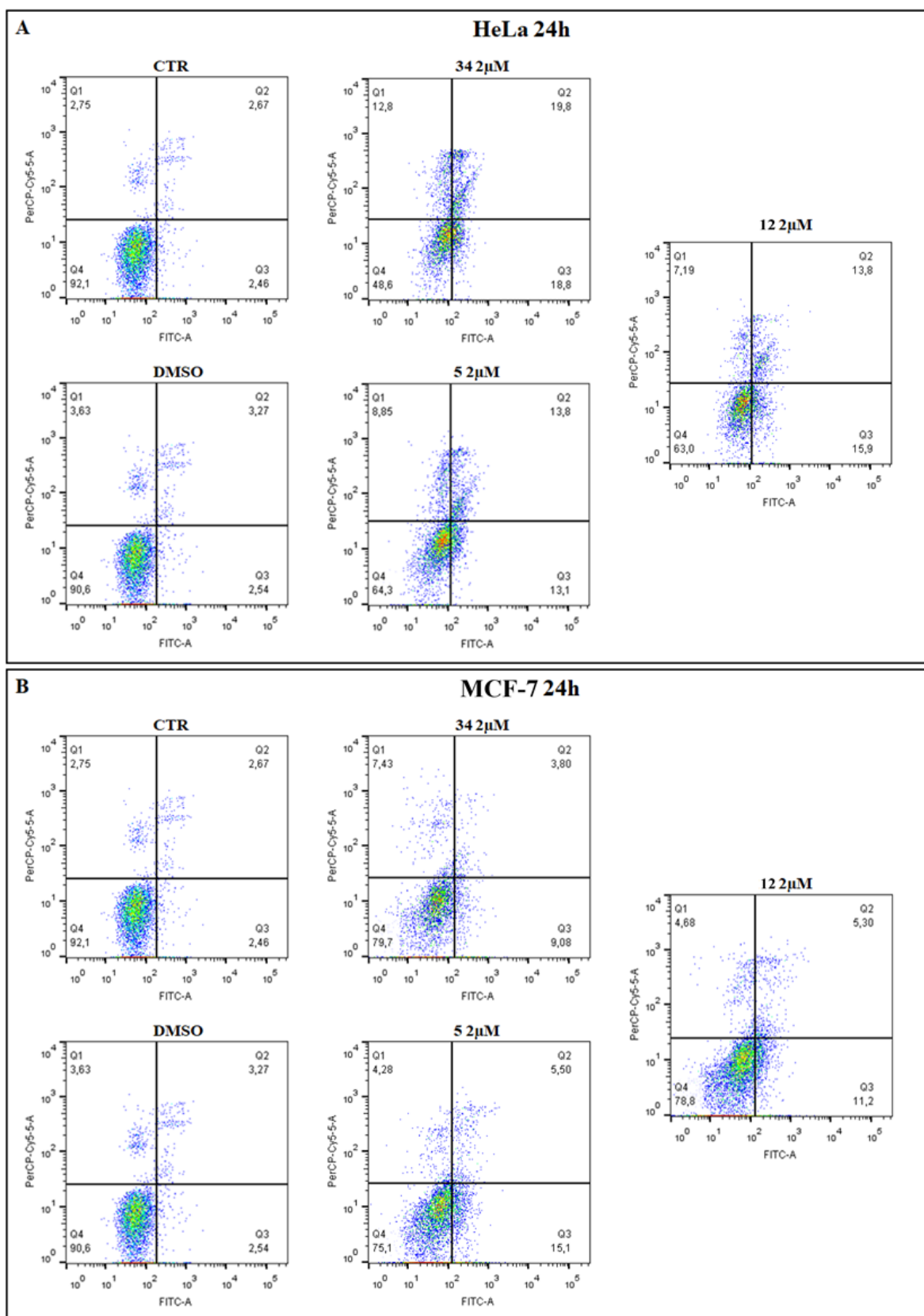
Figure 23. Annexin V analysis against A) HeLa and B) MCF−7 cell lines after treatment with compounds **5** and **12**. Cells were treated at the concentration of 2 μM of both compounds. DMSO is used as control (CTR) and compound **34** as positive control. Apoptotic, necrotic, and live cells were stained with Annexin V FITC/PI and plotted through BD FACS DIVA software.

6.2.2.4. Compounds 5 and 12 cause activation of PARP−1

Later, a deeper investigation of the pro–apoptotic effect of compounds **5** and **12** was accomplished through Western Blot analysis. Different concentrations of the compounds were administered to HeLa and MCF−7 cells in order to quantify the levels of protein expression of PARP−1 and cleaved PARP−1. Cleavage of PARP−1 indicates activation of cell death by apoptosis. After 24 h of treatment, western blotting was performed on the collected pellets. Figure 24 shows how compounds **5** and **12** are able to activate PARP−1, confirming the results obtained in the Annexin V analysis. In addition, the production of cleaved PARP−1 was observed in both HeLa and MCF–7 cell lines.
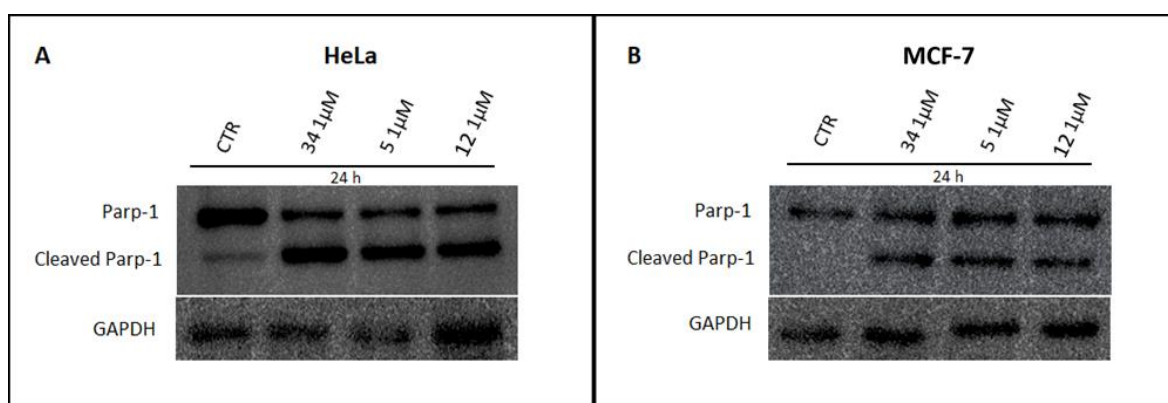
Figure 24. Western blotting analysis of the levels of protein expression of PARP−1 and cleaved PARP−1 in HeLa and MCF−7 cell lines after treatment with derivatives **5** and **12**. Results are normalized by GAPDH.

6.3. Conclusions and future outlook

Based on previous leads **34** [121] and **9a**, [126] this project aimed to functionalize position C–4' on benzotriazole to evaluate if this manipulation could be beneficial for the antiproliferative activity. The C–4' fluorinated analog of **34**, derivative **5** was selected for a preliminary docking simulation to verify if it could interact with the colchicine–binding site on tubulin. The best–predicted pose of compound **5** established different H–bonds and a fluorine bond with different amino acids of the pocket, mainly with the α–chain of tubulin. As reported in previous Chapter 5, compounds **34** and **9a** are predicted to bind preferably to β–chain, so it is interesting how compound **5** could define a new binding mode to tubulin. Pharmacokinetic and ADME predictions were performed on the whole series; they showed a good profile in terms of pharmacokinetics, lipophilicity, water solubility and drug/lead–

likeness. Hence, the series of new 4'–fluorobenzotriazole–acrylonitrile derivatives were synthesized and subjected to biological assessment. The first NCI *in vitro* screening showed variable antiproliferative profiles. Due to their remarkable activity, compound **5** and **12** were selected for further investigation. XXT colorimetric assay on Hela cells at 24 h showed IC$_{50}$ values of 0.6 and 0.45 μM for **5** and **12**, respectively. The mechanism of action as microtubule–targeting agents (MTAs) was confirmed through a flow cytometry assay in both HeLa and MCF–7 cells, assessing the change in DNA content. An increase of cells blocked in G2/M–phase for both compounds **5** and **12** at 2 and 1 μM was displayed. Then, flow cytometry assay on HeLa cells stained for Annexin V–FITC/PI showed an increased early apoptosis elicited by both compounds **5** and **12** at 2 μM concentration. Derivatives **5** and **12** promoted an increase of early apoptotic events also on MCF–7 cells, overcoming the effect produced by compound **34**. Lastly, the pro−apoptotic effect of compounds **5** and **12** was confirmed by western blotting, to measure the protein expression of PARP–1 and cleaved PARP–1 after 24 h of treatment. Both protein expressions were activated by 1 μM of both compounds, confirming results from the Annexin V assay, hence indicating activation of cell death by apoptosis.

In conclusion, both compounds **5** and **12** behave as CBSIs and trigger antiproliferative and pro−apoptotic effects on cancer cells.

The interest in these molecules opens to new modifications on the main scaffold, which could further improve the effectiveness of the antiproliferative activity of this type of compounds.

7. Project #3: A Lead−Based Fragment Library Screening of the Glycosyltransferase WaaG from *Escherichia coli*

7.1. Introduction

Bacteria can easily spread through goods, animals and humans. Acquired antibiotic resistance is an alarming problem worldwide, causing issues in major surgery and cancer treatment. This leads to public health expenses. [154] Some bacteria strains demonstrated drug resistance to last−resort antibiotics. [155,156] There are several mechanisms to develop antibiotic resistance, which will be better described in this Introduction, *e.g.* the production of enzymes that destroy the structure of drugs (β–lactamases or carbapenemases), [4] the biosynthesis of a more selective and resistant outer membrane, [158–161] or the over−expression of drug efflux pumps. [157] As for the antibacterial treatment, only three new classes of antibiotics were successful in clinical trials in the last 50 years, [158,159] and, unfortunately, the current antibiotic pipeline is unlikely to deliver new solutions. [160] Therefore, Drug Repurposing process for the already−existing antibiotics is a strategy intensely pursued to find new antibiotic agents. [161–165] Gram−negative bacteria can cause a wide range of diseases such as gastroenteritis, urinary, blood and CNS (central nervous system) infections. [166] As regards multi−drug resistant (MDR) bacteria, there is a lack of effective treatment, for example, for gram−negative bacteria such as *Klebsiella pneumoniae* and *Escherichia coli*, as reported in the list of priority pathogens of World Health Organization (WHO) in 2017. [167] Focusing on *E. coli*, some strains have raised interest for their spreading around the world. In 2011, many countries of WHO European Region faced a significant *E. coli* outbreak. In Germany and 15 other European and North American countries, there was a high number of cases of bloody diarrhea and hemolytic syndrome (HUS), traceable to infections of verocytotoxin−producing *E. coli* O104:H4. [168] As above mentioned, there are many ways of developing resistance to bacteria. Some strains

of *E. coli*, but also different other bacteria of the *Enterobacteriaceae* class, are called "nightmare bacteria", [4] because they produce enzymes called β−lactamases and carbapenemases, which inhibit potent antibiotics such as penicillins or carbapenems (used to treat extended−spectrum β−lactamases *Enterobacteriaceae* – ESBL). [4] Another issue regarding *E. coli* is its resistance to fluoroquinolone antibiotics in the treatment of urinary tract infections. [169] Intrinsic resistance can also be produced through the outer membrane in gram−negative bacteria. [170–173] Outer membrane acts as a selective permeability barrier to let in nutrients and ions, but stop the cellular entry of different classes of antibiotics. [174,175]

One way to overcome intrinsic resistance in *E. coli* could be the inhibition of proteins involved in antibiotic modification, drug efflux or outer membrane biogenesis. For instance, the enzyme glycosyltransferase I (WaaG, or RfaG) catalyzes the transfer of an α–D–glucosyl group from UDP−Glc onto L–glycero–D–manno–heptose–II, contributing to the core region synthesis of the lipopolysaccharide (LPS). [176] The structure of LPS can vary in different gram−negative bacteria, and in their different strains. The general structure of LPS includes different parts: Lipid A, outer/inner core, O−antigen. Lipid A is a lipophilic portion composed of glucosamine dimers (D−GlcN), bound to acyl chains. Lipid A is directly bound to the core region, consisting of hexosamines and hexoses, in addition to Kdo (3–deoxy–D–manno–2–octulosonic acid) and L,D−Hep (L–glycero–D–manno–heptose) residues. The O−antigen is made of polysaccharides linked to the core region [177–180] and it is involved in different pathways aimed to bypass the immune system of the host. [176,181]

Figure 25. SFNG [182] representation of outer and inner core (R1), and lipid A of LPS. [183] Acyl groups linked to glucosamine residues of Lipid A are reported as R^1 and R^2.

As regards the mechanism of action of LPS, it firstly targets phagocytic cells, such as macrophages, monocytes, neutrophils and dendritic cells. Their binding triggers a series of intracellular chain reactions, supported also by caspase−4, −5 and −11, [184] which initiates the production of cytokines with a pro−inflammatory effect (IL−1β and IL−18 [185]). This cascade of enzymatic reactions leads to a type of programmed cell death by pyroptosis. [186] As a result of the bacterial infection, fever occurs as the macroscopic result of the activation of this pathway. On this basis, this project focuses on the inhibition of WaaG.

A focus on the target structure: the glycosyltransferase WaaG. WaaG is a glycosyltransferase constituted by 371 amino acids. The protein can be structurally divided into two portions, N− and C−domains. In the RCSB PDB database, two crystal structures are deposited, one co−crystallized with UDP (uridine diphosphate), with PDB ID 2iv7 and one with UDP-2-fluoro-2-deoxy-D-glucose or U2F (2iw1). [187] Due to its higher resolution (1.5 Å), the crystal structure with PDB ID 2iw1 was selected. Firstly, the structure of the domains and their composition was analyzed. N−domain can be recognized between amino acids Met1 – Gln163. A hinge region (H) links N− and C− domain and it is composed of amino acids between Ile164 and Pro171; C−domain consists of amino acids between Asp172 and Gly371. The oligopeptide portion between Gln355 and Tyr358 is the last part of the C−domain, but it is spatially assimilated in the hinge region (in yellow). C−terminus helix is considered part of the C−domain, even if it is spatially located in N−domain. Figure 26 depicts WaaG distinguishing its portions by different colors and including UDP−Glc^{2-} in its specific binding site on WaaG.
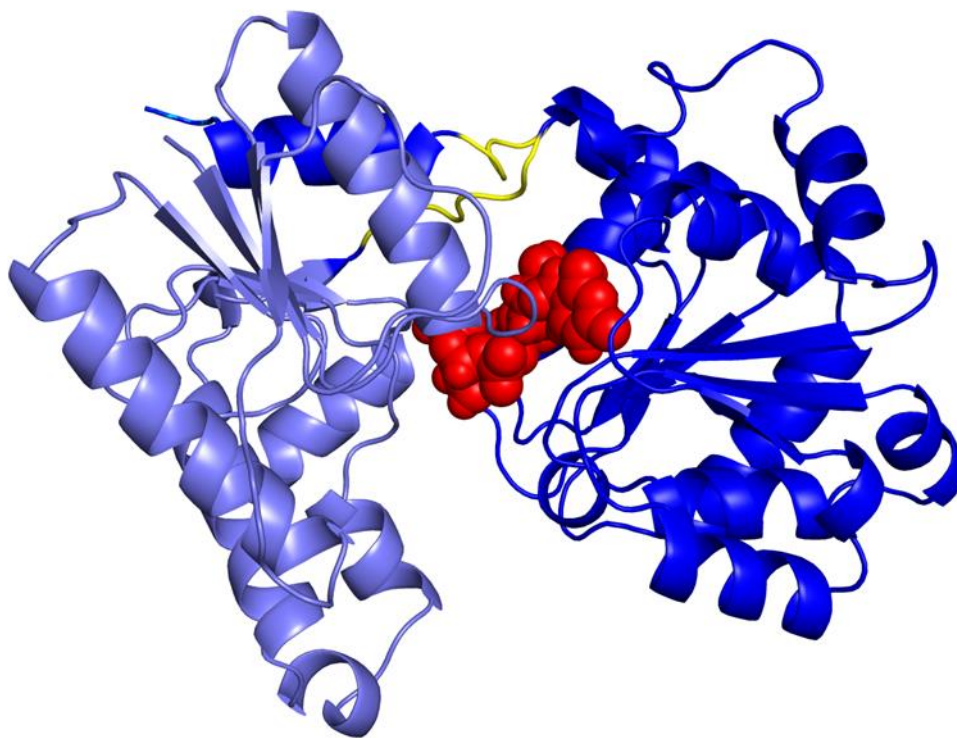
Figure 26. Conformation of UDP−Glc^{2-} in WaaG active site, derived from co−crystallized U2F in deposited crystal structure with WaaG (PDB ID: 2iw1). Colors: slate (N-domain), blue (C-domain), yellow (hinge region) and red (UDP−Glc^{2-}).

WaaG is a strategic target since the deletion of the gene encoding for it interferes with the phosphorylation of the LPS core, creating truncated LPS after the inner core heptose residues. All these actions destabilize the outer membrane of *E. coli*. [188] As a consequence, *E. coli* results more susceptible to several types of antibiotics: nitrofurans, nitroimidazoles, rifamycins, aminoglycosides, polymyxins, phenols and chlorophenols. [189] Due to the different pathways leading to antibiotic resistance, the availability of molecular agents to be co–administered with well−known and potent antibiotics, such as rifampicin and chloramphenicol, could represent an efficacious strategy. Therefore, the following project discusses a fragment−based drug design process to design new WaaG inhibiting agents.

7.2. Construction of libraries and Rational workflow

The present project takes glycosyltransferase WaaG [190] as target for further fragment−based investigations. The fragment−based drug discovery (FBDD) process on WaaG started from previous studies, where 500 structures of the Ro3 Maybridge 2006

Library were screened through STD−NMR spectroscopy, molecular docking and molecular mechanics in sequence to test their affinity to WaaG protein. [191] Three bicyclic compounds (reported here as **A1** – **A3** in Figure 28) demonstrated to compete with UDP−Glc for the binding with WaaG. [192] Docking studies on these molecules showed how uridine, UDP, **A1** and **A3** bind in the same portion of the pocket, the uridine portion, while **A2** docks in the glucosyl portion. [191] Figure 27 shows a scaffold−based representation of the ligands of the three libraries.
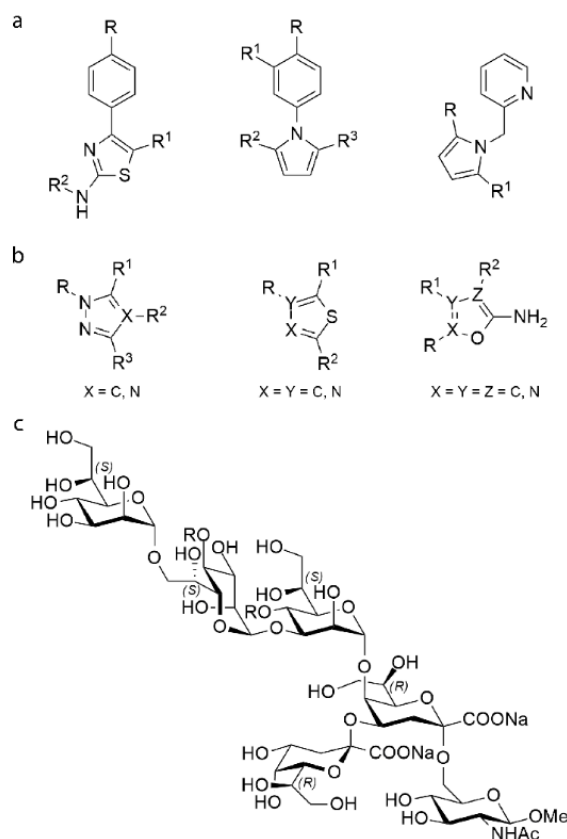
Figure 27. General representation of chemical scaffolds of libraries A (a) and B (b); in the oligosaccharide−based library C (c) R = HPO$_3$Na.

Therefore, in the initial part of this project, **A1** – **A3** were used as starting point for building library A, made of 20 bicyclic fragment compounds **A1** – **A20**, with molecular weights (M$_w$s) ranging from 158 to 257 Da. The main scaffolds phenylthiazole, phenylpyrrole and methylpyridine−pyrrole of **A1** – **A3**, respectively, were variously functionalized with several polar (*e.g.*, hydroxyl, carboxyl, amide, aldehyde) and nonpolar (*e.g.*, methyl, ethyl, phenyl, halogen atoms) functional groups, in order to construct the first library A. Further scaffold modifications involved an indole thiazole on ligand **A14**, while compound **A13** is an acetate

salt of a phenylthiazole derivative. Library B was created to find drug−like inhibitors. It is composed of 37 ligands, structurally expanded from those of library A, and the range of M_ws is 176 – 391 Da. Small molecules with higher M_ws were devised through a fragment growing process. [193] Figure 28 depicts all the ligands of libraries A and B.
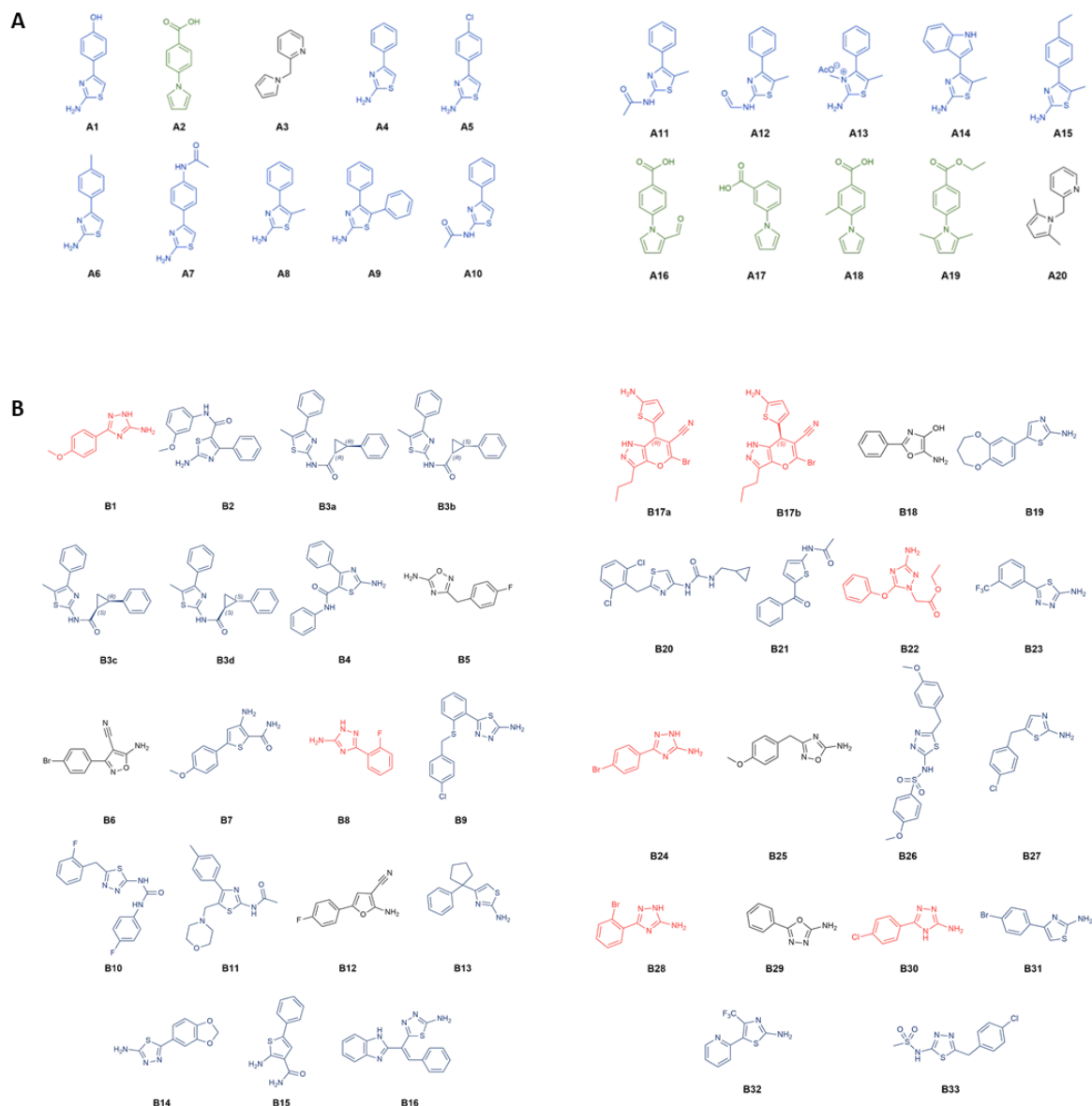

Figure 28. A) Ligands of library A (**A1** − **A20**) and B) library B (**B1** − **B16**, **B17a** −**B33**). For library A, **A1**−derived compounds **A4** − **A15** are colored in blue, **A2**−derived compounds **A16** − **A19** are colored in green and **A3**−derived compound **A20** is in black. For library B (**B1** − **B16)**, triazole−derived compounds **B1** and **B8** are colored in red. Thiazole−derived compounds **B2** – **B4**, **B7**, **B9** − **B11**, **B13** − **B16** are colored in blue. The other compounds (**B5**, **B6**, **B12**) are colored in black. For the other ligands of library B (**B17a** − **B33**), pyrazole− or triazole−derived compounds **B17a** – **B17b**, **B22**, **B24**, **B28** and **B30** are colored in red. Thiophene−, thiadiazole− or thiazole−derived compounds **B19** – **B21**, **B23**, **B26** – **B27**, **B31** – **B33** are colored in blue. The other compounds (**B18**, **B25**, **B29**) are colored in black.

Library C was constructed aiming to study the interaction between WaaG and its target portion on LPS, Hep−II. The inner core and lipid A portions of LPS were fragmented to investigate the interaction at the disaccharide (**C1** – **C5**), tetra− and hexasaccharide (**C6** – **C12**) levels. The different structures are reported in Figure 29. Disaccharide **C1** is a mannose−based disaccharide, α-D-Man*p*-(1→3)-α-D-Man*p*-OMe. Four disaccharides mimic the building block of the inner core of LPS: L-α-D-Hep*p*-(1→3)-L-α-D-Hep*p*-OMe (**C2**), L-α-D-Hep*p*-(1→3)-L-α-D-Hep*p*4*P*-OMe (**C3**), L-α-D-Hep*p*4*P*-(1→3)-L-α-D-Hep*p*4*P*-OMe (**C4**) and L-α-D-Hep*p*-(1→7)-L-α-D-Hep*p*4*P*-OMe (**C5**). Focusing on the interface between inner core and lipid A, the disaccharide structure were expanded to have: L-α-D-Hep*p*-(1→7)-L-α-D-Hep*p*4*P*-(1→3)-L-α-D-Hep*p*4*P*-(1→4)-α-Kdo*p* (**C6**), L-α-D-Hep*p*-(1→7)-L-α-D-Hep*p*-(1→3)-L-α-D-Hep*p*4*P*-(1→4)-α-Kdo*p* (**C7**), L-α-D-Hep*p*-(1→7)-L-α-D-Hep*p*4*P*-(1→3)-L-α-D-Hep*p*-(1→4)-α-Kdo*p* (**C8**), L-α-D-Hep*p*-(1→7)-L-α-D-Hep*p*-(1→3)-L-α-D-Hep*p*-(1→4)-α-Kdo*p* (**C9**). A further extension at the reducing end of the tetrasaccharide structure led to hexasaccharide ligands: L-α-D-Hep*p*-(1→7)-L-α-D-Hep*p*4*P*-(1→3)-L-α-D-Hep*p*4*P*-(1→5)-[α-Kdo*p*(2→4)]-α-Kdo*p* (**C10**), L-α-D-Hep*p*-(1→7)-L-α-D-Hep*p*4*P*-(1→3)-L-α-D-Hep*p*4*P*-(1→5)-[α-Kdo*p*(2→4)]-α-Kdo*p*-OMe (**C11**), L-α-D-Hep*p*-(1→7)-L-α-D-Hep*p*4*P*-(1→3)-L-α-D-Hep*p*4*P*-(1→5)-[α-Kdo*p*(2→4)]-α-Kdo*p*-(2→6)-β-D-Glc*p*NAc-OMe (**C12**). Oligosaccharides of library C are reported in Figure 29.
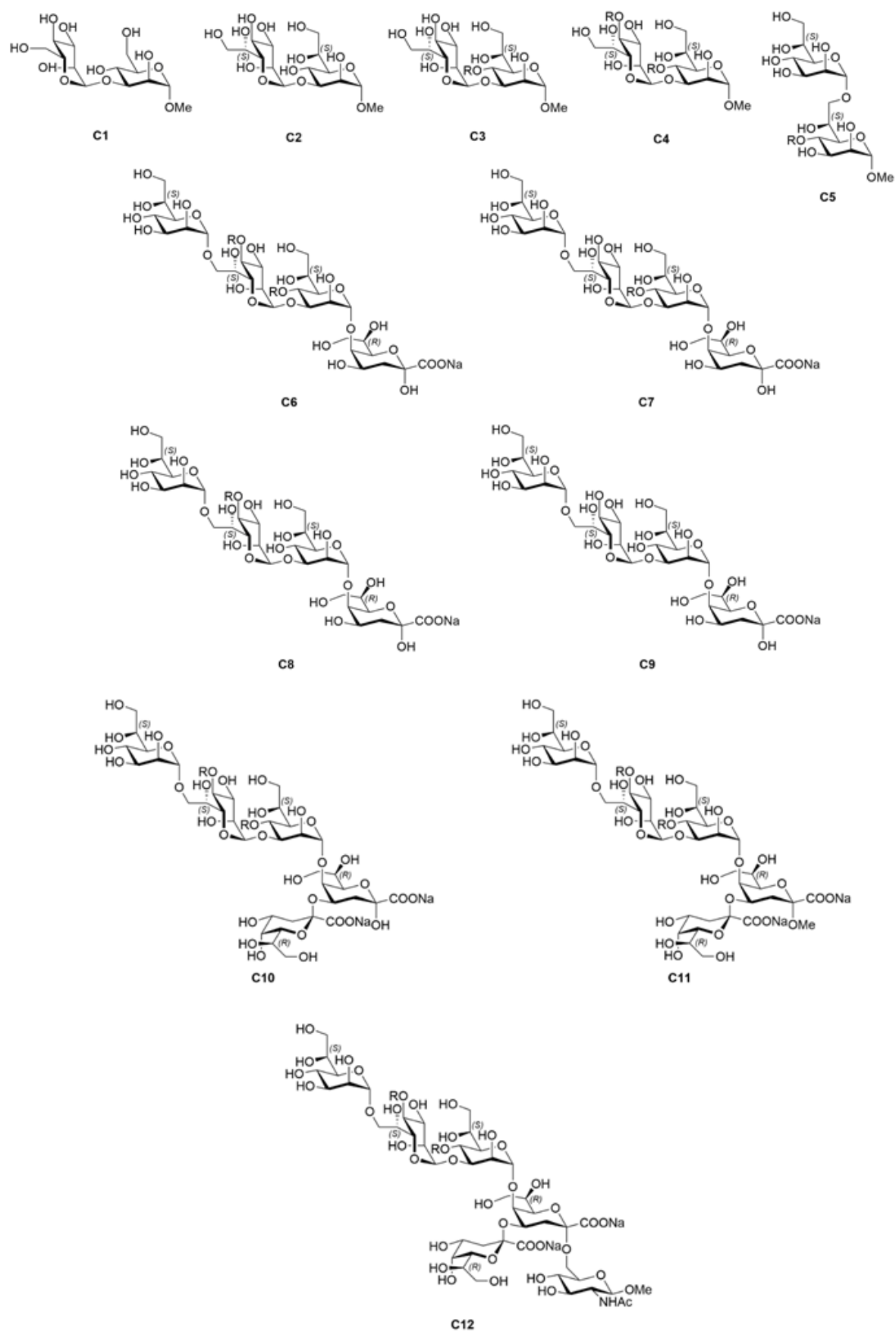
Figure 29. Ligands of library C (**C1** – **C12**). R = HPO₃Na.

After the three libraries were constructed, molecular docking studies were employed to identify which could be the most interesting scaffolds and functional groups that can potentially lead to a better affinity to WaaG binding site. The best−predicted poses of the ligands that showed a higher docking affinity energy were utilized for molecular dynamics (MD) calculations. Saturation Transfer Difference (STD) experiments were conducted to assess the strength of the interactions between ligands and WaaG protein. This technique is good for its versatility and low susceptibility to false positives. [194] It is also suitable for the small quantity of unlabeled protein required, and it is often combined with docking predictions to investigate the conformational state of a ligand in a protein binding site. [195] Lastly, *in vitro* biochemical assessment on libraries A and B experimentally explored the inhibition activity of the ligands for WaaG protein. The general workflow of this project is outlined in Scheme 4.
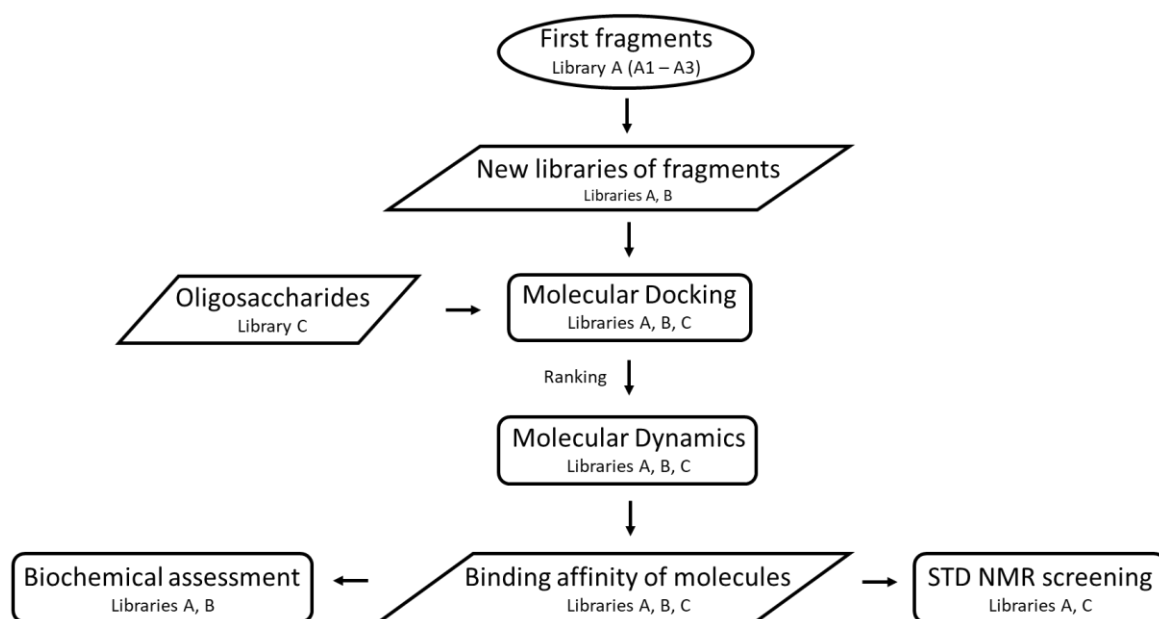
Scheme 4. Flowchart diagram of the different analyses made on libraries A, B and C.

7.3. Results

7.3.1. Molecular Docking

Once built the different libraries, a docking study was employed, and the docking programs were chosen for their sampling and scoring functions. [196] Four docking programs, AutoDock Vina, [197] LeDock, [198] rDock, [199] and GOLD [200] were selected. They are based on different algorithms; hence, even if they often produce similar best−predicted

poses, their affinity energy could be different. Each docking program created ten binding poses, but the affinity energy of the best−predicted one was mainly considered. The docking ranking report of the different ligands is outlined in Table 1. Docking simulations were conducted in two different conditions: in the presence of the *apo*−form of WaaG (protein without ligands in the active site) and in the presence of WaaG−UDP−Glc^{2-} complex. In the first case, with *apo*−form of WaaG, it was possible to consider if the ligands could bind preferably in UDP−Glc^{2-} uridine−sub−pocket, or in the UDP−Glc^{2-} diphosphate region, or in another portion of the binding pocket. In the presence of WaaG−UDP−Glc^{2-}, it was possible to see the binding mode of ligands in the outer part of the binding pocket and their conformational disposition in front of the natural ligand UDP−Glc^{2-}. Interactions between ligands and binding pocket were also highlighted.

Docking with WaaG apo−form: library A. Best−predicted ligands for library A were compounds **A1**, **A7**, **A9**, **A14** and **A16**, which ranged AutoDock Vina affinity energies from −6.6 to −8.7 kcal·mol^{-1}. Compound **A1** binds in the uridine sub−pocket on WaaG. As well as O3' atom of UDP−Glc^{2-} have an H−bond with the carboxylate group of Glu289, [187] the amino group and the nitrogen atom of the thiazole ring of compound **A1** interacts with the same carboxylate group of Glu289. Compound **A7** docks in the UDP−Glc^{2-} diphosphate region of the binding pocket, and its thiazole nitrogen is the acceptor of the H−bond with the NH$_3^+$ group of Lys209; on the other hand, its amino group is a donor for the H−bond with the carboxylate of Glu281. This is proof that the phenyl−aminothiazole portion is an adequate pharmacophoric scaffold for the binding to WaaG. Superimposing compound **A9** with the crystal structure of UDP−Glc^{2-}, it is clear how the phenylthiazole scaffold of **A9** almost overlaps with the uridine of UDP−Glc^{2-}. Regarding the interactions undertaken by **A9**, its thiazole nitrogen contacts the ureidic amine group of Arg173, while the donor amine group binds to the carboxylate of Glu289. The best−predicted pose of ligand **A14** binds in the uridine sub−pocket; its indole moiety is oriented in the same way as the uracil, superimposing it with UDP−Glc^{2-}, while the ribose sub−pocket is occupied by the thiazole ring of the ligand. Derivative **A16** binds in UDP−Glc^{2-} pocket, particularly the carboxyl group overlaps with the α−phosphate (the one linked to the ribosyl portion). A noteworthy role is covered by the carboxyl group of **A16** because it binds to Ile285 and Val286. These amino acids are known to bind to the α−phosphate group of UDP−Glc^{2-}.

Docking with WaaG apo−form: library B. The same docking process was applied on ligands of library B. Top−predicted ligands ranked affinity energies values on AutoDock Vina

program ranging from -7.0 to -8.8 kcal·mol^{-1}. Between compounds **B3a−d**, the SS−diastereomer **B3d** is the top−ranked one, hence it was selected for further MD simulations. The other high−scoring ligands, which bind in the same UDP−Glc^{2-} region of the binding pocket are derivatives **B16**, **B22**, **B26** and **B33**. As for compound **B16**, the benzimidazole ring overlaps with UDP−Glc^{2-} ribose sub−pocket, while the thiadiazole is in the diphosphate linker region. In addition, nitrogens of the thiadiazole ring are important as they accept H−bonds from NH$_3^+$ group of Lys209 and from the ureidic amine of Arg208. The O−phenyl moiety of ligand **B22** binds in the uracil sub−pocket, whilst the ester chain docks in the UDP−Glc^{2-} phosphate region. Derivative **B26** is in UDP−Glc^{2-} portion and points towards the pocket entrance with a methoxyphenyl group. Ligand **B26** has a conformation state similar to **B16** since the thiadiazole nitrogens interact with the NH$_3^+$ group of Lys209. Its sulfonamide carbonyl group is the acceptor of two H−bonds with Gly15 and Leu16. Compound **B33** has different electrostatic interactions with WaaG binding pocket. Its lateral sulfonamide NH donates an H−bond with the carbonyl group of Glu281. The oxygens of the sulfonamide group accept H−bonds from NH groups of Ala283 and Ile285.

Docking with WaaG apo−form: library C. For library C, the top−ranked oligosaccharides presented affinity energies ranging from -8.8 to -8.2 kcal·mol^{-1}. Ligands of this library generally bind to the outer portion of the binding pocket, compared to the fragments of the other libraries. Ligands that are more interesting for docking studies were **C6** and **C10**. Tetrasaccharide **C6** docks in the deep portion of the binding pocket with the non−reducing end (Hep−III), overlapping with the UDP−Glc^{2-} sub−pocket, and the Kdo residue points towards the entrance. Pentasaccharide **C10** has two Kdo residues pointing out of the active site, whilst Hep−III almost binds in UDP−Glc^{2-} ribose sub−pocket, and Hep−II (heptose residue which binds to Hep−III) phosphate group docks in UDP−Glc^{2-} β−phosphate sub−pocket.

Protein−ligand interactions will be more in−depth discussed and visually considered for the selected ligands during the analysis of the subsequent molecular dynamics trajectories.

Ranking of ligands in docking to WaaG																	
		apo-WaaG[a]								WaaG+UDPGlc[a]							
	#	AD	Affinity E	LD	Score	rD	Score	G	Score	AD	Affinity E	LD	Score	rD	Score	G	Score
A	1	9	-8.7	7	-7.2	1	-34.6	16	62.6	9	-7.8	7	-6.6	1	-42.8	14	53.9
	2	11	-8.0	11	-6.4	7	-33.8	19	60.0	15	-7.3	9	-6.3	13	-37.8	1	52.2
	3	7	-8.0	14	-6.3	9	-30.2	18	59.7	14	-7.2	11	-6.1	17	-37.5	7	51.0
	4	14	-7.9	9	-6.3	14	-30.0	17	58.1	12	-7.1	10	-6.0	14	-37.3	15	51.0
	5	16	-7.3	10	-6.2	15	-29.4	11	56.0	16	-7.0	12	-6.0	8	-36.9	5	50.4
B	1	3d	-9.8	26	-9.5	22	-39.1	3d	77.8	16	-8.8	16	-8.3	33	-42.1	16	64.7
	2	10	-9.7	10	-8.9	16	-38.0	3a	77.7	3d	-9.1	3d	-6.6	18	-38.3	3d	64.5
	3	3a	-9.7	33	-8.8	7	-36.9	10	76.8	3a	-8.5	3a	-6.9	13	-38.2	10	63.2
	4	2	-9.3	16	-8.4	17a	-35.5	26	71.2	10	-8.8	10	-8.7	28	-37.8	9	62.1
	5	26	-8.8	9	-8.2	6	-33.3	20	70.7	3b	-8.5	3b	-6.1	29	-37.1	26	61.7
C	1	6	-8.8	6	-11.5	6	-180.0	10	79.9	8	-8.4	10	-15.1	6	-94.2	10	73.7
	2	9	-8.8	8	-11.2	3	-51.9	9	79.3	10	-7.6	6	-14.0	5	-22.3	11	67.2
	3	8	-8.7	9	-11.1	4	-51.6	7	76.1	5	-7.5	8	-13.8	3	-19.7	12	63.1
	4	10	-8.5	4	-10.0	5	-47.0	6	70.6	7	-7.5	7	-12.8	2	-19.4	6	55.9
	5	5	-8.2	3	-9.5	1	-34.7	5	66.3	6	-7.4	9	-12.0	1	-17.6	7	55.4

[a] Crystal structure used (PDB ID: 2iw1).
AD = AutoDock Vina; Affinity E = Affinity Energy; LD = LeDock; rD = rDock; G = GOLD.
Italics for phosphate-substituted oligosaccharides.

Table 1. Affinity energy ranking of ligands in docking to WaaG for compounds of libraries A, B, and C.

7.3.2. STD−NMR experiments

STD−NMR experiments were carried out by Alessandro Ruda in Prof. Göran Widmalm group (Department of Organic Chemistry, Stockholm University, Stockholm, Sweden).

STD (Saturation Transfer Difference) [195] analysis was conducted on different ligands of library A and disaccharides **C1**, **C2**, **C3**, **C5**. For library A, compounds **A4** and **A15** showed a good affinity for WaaG, giving a remarkable STD signal. Both showed a >70% STD signal. The experiments were also conducted in the presence of ligands and UDP as a competitor for the WaaG binding site. Compound **A15** demonstrated to compete with UDP for the binding to WaaG, showing a 70% STD signal; the same effect was observed for **A4**, with a >40% STD signal. For both ligands, all the signals are altered by the STD effect; hence, all protons in the ligands are involved in the binding with WaaG. All other ligands, including the disaccharides, gave a less than 1% STD signal, therefore, we did not proceed in further investigation. This is not surprising for oligosaccharides, since binding constants for them

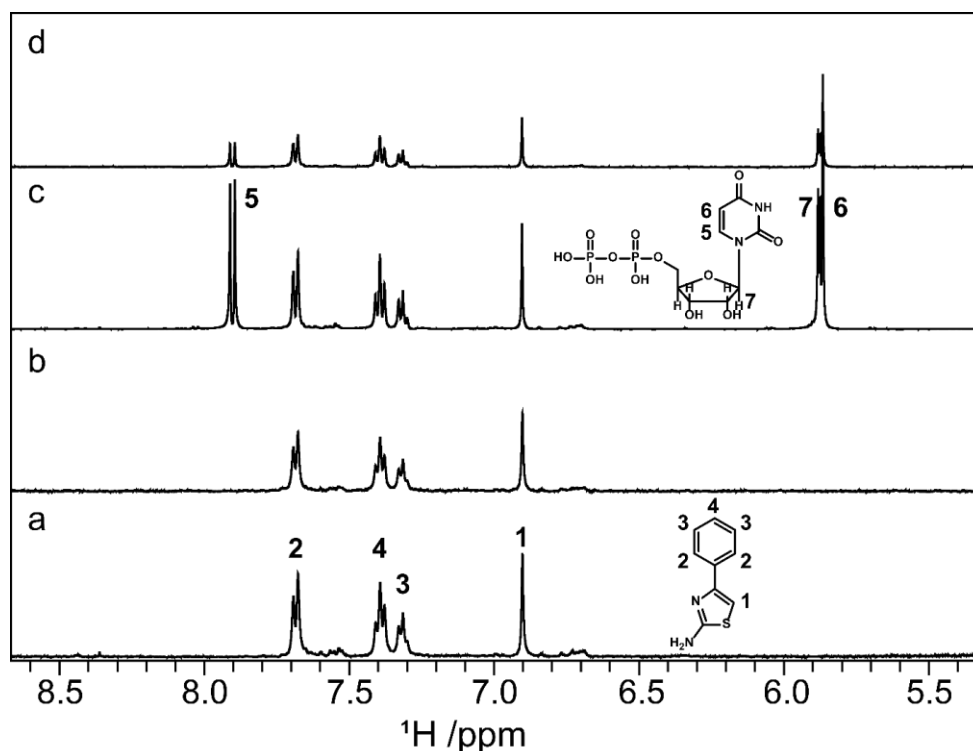are generally in the mM scale [201] and the general working span of STD NMR experiments is µM−low mM range.

Figure 30. STD−NMR spectra of compound **A4** and WaaG were performed in the presence or absence of UDP as competitor. From the bottom to the top, 1D ^{1}H STD off−resonance (a) and on−resonance (b) irradiation of WaaG in the presence of **A4** and off−resonance (c) and on−resonance (d) irradiation with UDP added to the protein−ligand mixture. Compound **A4** interacts with WaaG also in the presence of the competitor UDP.

7.3.3. Molecular Dynamics

Molecular Dynamics (MD) simulations were employed to investigate the interactions between ligands of libraries A, B and C and WaaG. The simulations produced 10 ns−trajectories for ligands and WaaG−ligand complexes, to be further studied in a post−MD analysis. Ligands **A4**, **A8** and **A15** were selected from STD−NMR experiments. Affinity energy ranking from docking studies was applied as a filter to select the best−predicted ligands. For ligands of libraries A and B, the first of the ten best−predicted poses was considered as a starting point. Top−ranked poses of disaccharides **C1**, **C2**, **C3**, **C4** of library C were considered for MD calculations. In this regard, the protonation state of the phosphate group on position C−4 of the different disaccharides was regulated to mimic the physiological environment; thus, phosphate−substituted disaccharides **C3** and **C4** were considered in a protonated (**C3** and **C4**) and a monocharged form (**C3^{-1}** and **C4^{-2}**). For each

ligand and protein−ligand complex, 10 ns−molecular dynamics simulations (explicit solvent) were used with a 100 Å water square box, neutralized with NaCl salts. Timesteps were considered by default 2 fs; in few cases, time−step was extended to 1 and 0.1 fs for unstable trajectories.

7.3.4. Binding free energy (BFE) calculations

Once obtained the trajectory outputs for each ligand and protein−ligand complex, binding free energy (BFE) calculations were carried out to evaluate the affinity for each complex. Linear Interaction Energy (LIE) was applied as method. [202,203] The outputs considered were the ΔG_{bind} (variation in Gibbs Free Energy of Binding, expressed as kcal·mol^{-1}) and K_D (dissociation constant) values, obtained applying the equation and expressed in mM. The top−down values of ΔG_{bind} and K_D are reported in Table 1, divided by libraries. Starting from the fragments of library A, ligands **A4** and **A7** have a good profile as fragments, with K_Ds values lower than mM. Compound **A9** is in the range of mM (~ 5 mM). Values > mM are reported for derivatives **A15**, **A14** and **A1**, demonstrating a weak binding. Even weaker are ligands **A8** and **A16**, with predicted values in M (molar) range; they do not show to bind to WaaG protein. Within the small molecules library B, **B33** possesses the best−predicted BFE value of its library. As regards library B, K_D value of compound **B33** is 40 μM. On the other hand, compounds **B16** and **B22** have K_Ds in mM range, whilst derivatives **B3d** and **B26** show a weak binding to WaaG protein. Library C was used to verify which disaccharides are better binders for WaaG active site, and, to some extent, to evaluate which is the portion of LPS that interacts better with WaaG. Double−phosphorylated heptose−3−heptose **C4**, in both protonation states, demonstrated to have the best BFE value of the library. The double phosphorylation showed to be beneficial for the binding: in fact, both protonated and monocharged forms (**C4**$^{-2}$ and **C4**) have K_Ds of 0.4 and 0.8 μM, respectively. On the other hand, the total absence of phosphate groups on heptose residues in ligand **C2** gives a good binding, with K_D value of 70 μM. Interestingly, the mono phosphorylation on heptose anomeric position on disaccharide **C3** seems not to be beneficial for the binding, even weaker is its monocharged form **C3**$^{-1}$. Lastly, as well as **C3**, ligand **C1** has a K_D in mM range.

Table 1. Computed ΔG_{bind} and related K_D values for compounds of libraries A, B and C.

LIGAND	ΔG_{bind}	Calc K_D (mM)	LIGAND	ΔG_{bind}	Calc K_D (mM)	LIGAND	ΔG_{bind}	Calc K_D (mM)
A7	-5.65	0.11	B33	-6.29	0.04	$C4^{2-}$	-9.14	0.0004
A4	-4.58	0.62	B16	-3.89	1.89	C4	-8.70	0.0008
A9	-3.34	4.55	B22	-3.18	5.97	C2	-5.97	0.07
A15	-1.73	61.10	B3d	-2.19	29.09	C3	-4.21	1.13
A14	-0.81	269.26	B26	-1.03	190.48	C1	-4.20	1.15
A1	-0.64	354.70				$C3^{-1}$	-0.72	0.31
A8	> 0	$> 10^3$						
A16	> 0	$> 10^3$						

7.3.5. Root−mean−square deviation (RMSD) analysis

In order to more in−depth analyze the MD results, the root−mean−square distribution (RMSD) was calculated for the entire 10−ns trajectory of every WaaG−ligand complex, focusing on the WaaG backbone fluctuation. Figure 31a−c depicts the RMSD distribution referring to the WaaG protein backbone during the 10 ns−MD simulation of each complex. Figure 31a−c reports the same RMSD values depicted as a function of the duration of the MD calculation. Table 2 reports numerical values of avRMSD (average RMSD) as an average for the backbone fluctuation for the entire 10 ns−MD simulations, combined with the SD (standard deviation) values. In Figure 31, the reference curve in black reports the fluctuation of the backbone in *apo*−form, and avRMSD is 1.31 Å ± 0.16. For Library A, the presence of compound **A4** in WaaG binding pocket generates a narrow ΔRMSD distribution, compared to most of the other ligands of the library, with an avRMSD 1.43 Å ± 0.21. Another good RMSD distribution of backbone trajectory is given by WaaG−**A7** complex (even if there is a low−populated state at the beginning of the production phase). Compounds **A7** and **A14** give a narrow distribution of RMSD for WaaG backbone. Fragments **A1** and **A9** have similar behavior, with a broad RMSD profile. For library B, there is a general increase in backbone flexibility. Between them, the best stability is given by ligand with avRMSD 1.29 Å ± 0.25. This stability expressed through RMSD analysis confirms the remarkable BFE value of **B33**. For library C, disaccharide **C1** gives two main conformations of WaaG backbone (broad RMSD variation, ∼ 2.5 Å variation for each conformational state). Compound **C2** generates two states of the protein backbone, well−distinguishable and similar population profile. Disaccharide $\textbf{C4}^{-2}$ gives great stability to WaaG skeleton, with a ΔRMSD ∼ 0.5 Å, justifying the good BFE and K_D values. Its RMSD distribution is similar to that of ligand **C3**. **C3** gives more stability than $\textbf{C3}^{-1}$, also in terms of K_D, as seen before.
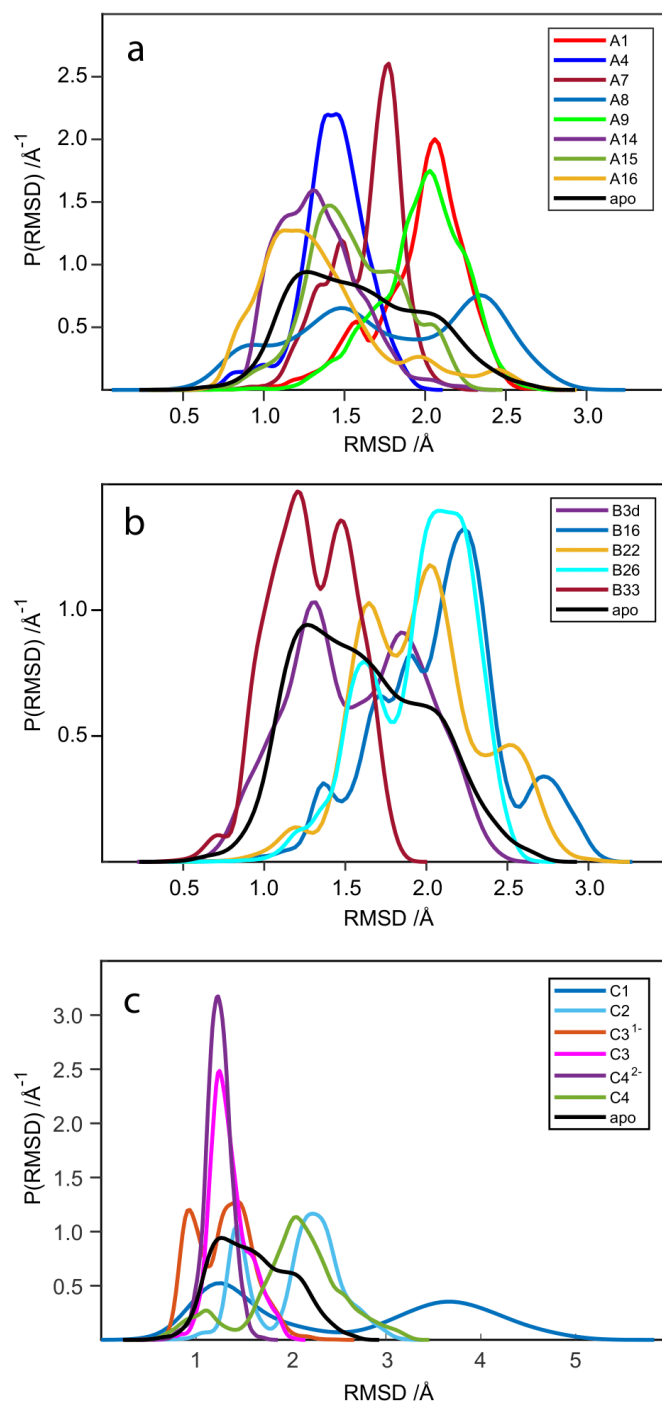
Figure 31. Kernel density estimation to calculate the RMSD probability distributions, using a normal distribution function. The focus is on the backbone of the *apo*−protein of WaaG and the various WaaG−ligand complexes.
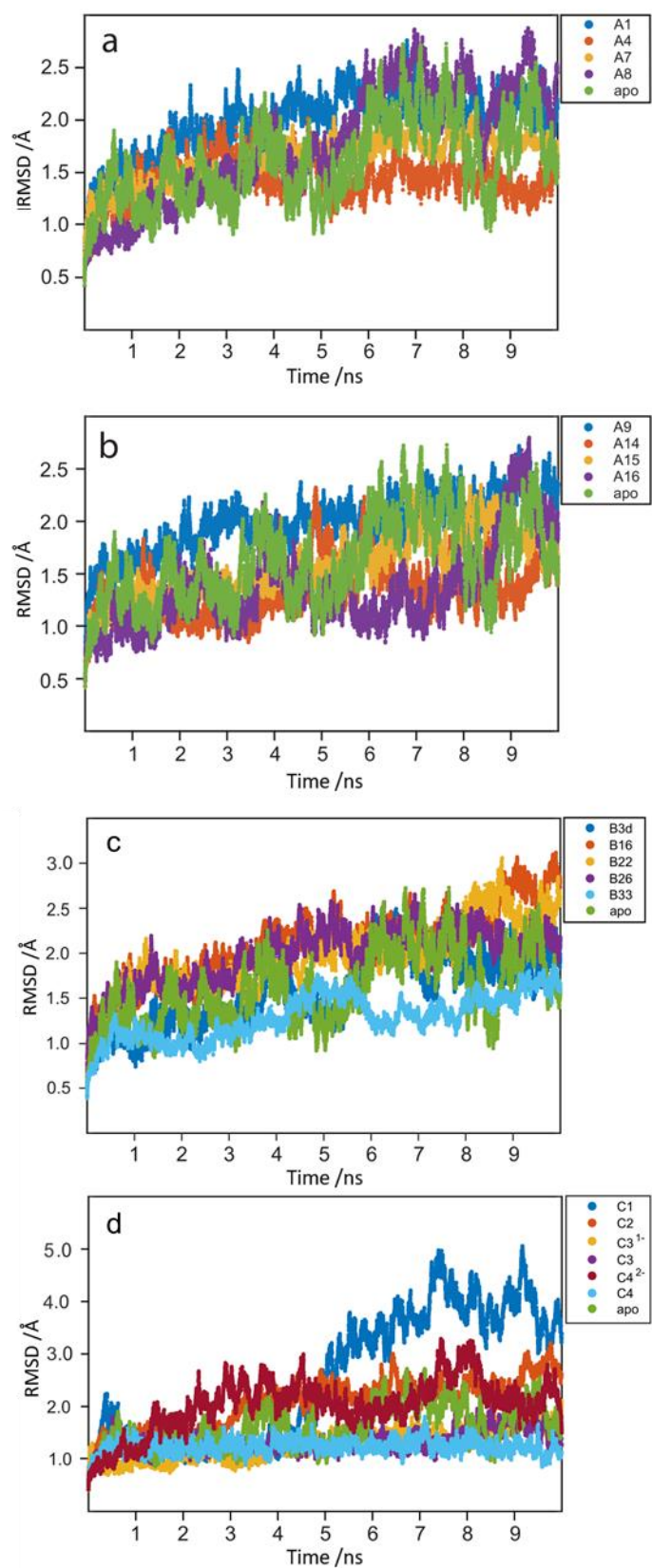
Figure 32. RMSD distribution of the backbone of the *apo*−protein and each WaaG−ligand complex for library A (a), B (b, c) and C (d) during the 10−ns productions.

Table 2. Average RMSD (avRMSD) and standard deviation (SD) values for the backbone of WaaG *apo*−protein and each WaaG/ligand complex.

	avRMSD	SD
apo	1.31	0.16
A1	1.97	0.28
A4	1.43	0.21
A7	1.63	0.22
A8	1.78	0.56
A9	1.98	0.27
A14	1.33	0.25
A15	1.56	0.29
A16	1.37	0.40
B3d	1.43	0.21
B16	1.63	0.22
B22	1.96	0.38
B33	1.29	0.25
C1	2.54	1.24
C2	2.04	0.46
C3^{1-}	1.29	0.30
C3	1.35	0.21
C4^{2-}	1.24	0.14
C4	2.03	0.50

7.3.6. Electrostatic and van der Waals contributions to WaaG−ligand binding

Later, we wanted to investigate the contribution of the electrostatic term or the vdW (van der Waals) term to the WaaG−ligand binding for each complex. For library A, the van der Waals contribution is more relevant than the electrostatic one. Some of them provide a good balance between the two terms, like ligand **A4**. Only compounds **A9** and **A14** showed an inverse tendency, with a higher electrostatic term. A predominant vdW term can be also observed in ligands of library B, more evident in compounds **B22** and **B33**. On the other hand, disaccharides of library C have a predominant electrostatic term, due to the high amount of hydroxyl groups. This effect is more relevant for protonated phosphate−derived ligands **C3^{-1}** and **C4^{-2}**. Figure 33a−c presents histograms of electrostatic (in blue) and vdW (in red) contributions in kcal·mol^{-1}, for each ligand when bound to WaaG active site.
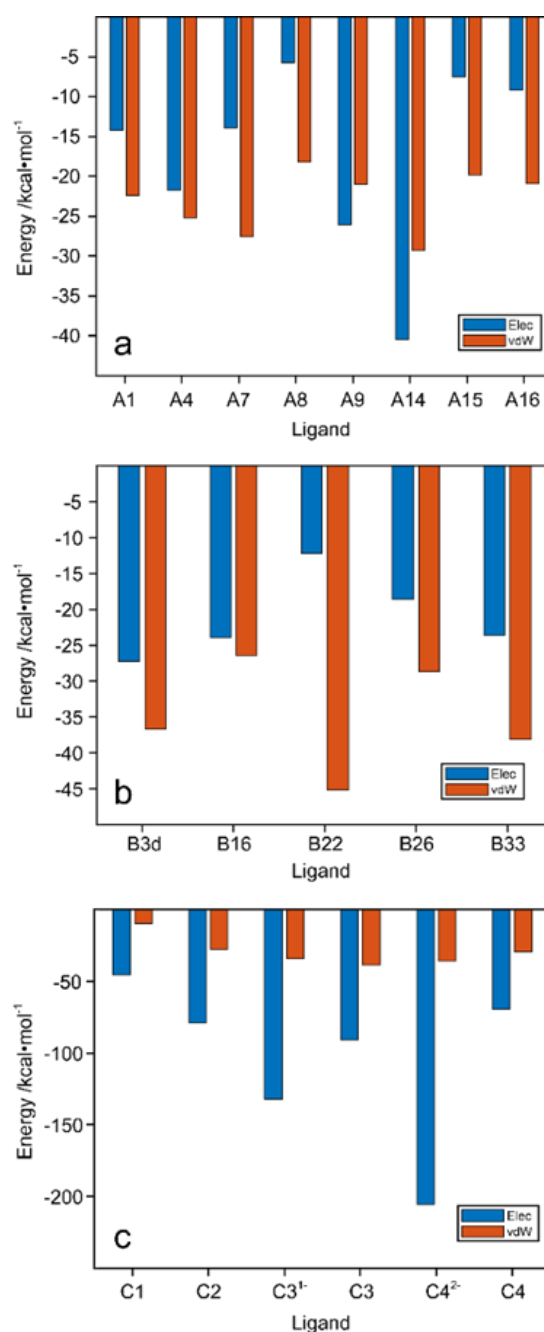
Figure 33. Electrostatic (Elec) and van der Waals (vdW) contributions to the interactions between WaaG and each ligand.

7.3.7. Hydrogen bonds

Once considered the electrostatic contribution for each protein−ligand interaction, a deeper investigation on the established hydrogen bonds was undertaken. The considered H−bonds have at least 30% of occupancy (term of y−axis, presence during the 10 ns−MD simulations), and only the amino acids (x−axis term) involved in these polar interactions are reported in Figure 34a−c, for ligands of libraries A−C, respectively. Compounds **A8** and **A16** are

confirmed as weak binders, as they do not show H−bonds with any amino acid with at least 30% occupancy. Some ligands show a good selectivity, engaging H−bonds with some amino acids which do not bind with anyone else. For example, Phe13 has a selective H−bond for compound **A15**, while Arg18 for **A4**, which, in turn, binds with Glu289. Also compound **A7** binds to Glu289, confirming to be a good binder for WaaG active site, and also presenting two selective H−bonds with Asp19 and Ala99. Ligand **A1** interacts with glutamine and an arginine residue, while **A14** confirms its high electrostatic term thanks to the binding with two highly representative H−bonds with Ser204 and Gln236.

Regarding library B, derivative **B33** showed a ~ 50% occupancy for hydrogen bonds with Ala283 and Gly284. Ligand **B26** has a selective H−bond with Ala283 which is present almost for the entire 10 ns trajectory (>90% occupancy). Ser204 binds with a 40−55% occupancy to compounds **B16** and **B22**. Disaccharides of library C have a high number of H−bonds due to the high amount of hydroxyl groups, confirming the result reported in Paragraph 7.3.6. **C1** forms selective H−bonds (60−65% occupancy) with two asparagine residues (Asp172 and Asp173). **C2** provides a larger amount of H−bonds compared to **C1**; hydrogen bonds with Asp205, Lys209, Gln280, Glu281 and Ile285 are the most representative (occupancies ranging from 70 to 90%). Derivatives **C3** and **C3^{-1}** bind with different WaaG amino acids; in support of that, **C3^{-1}** engages two important H−bonds with Gly15 and Ala99 (65%), while **C3** has several H−bond, with Lys209 and Glu281 being the most present. Regarding **C4**, it has 75% occupancy for a polar contact with Arg208 and ~ 100% with Glu281. On the other hand, monocharged phosphate−substituted disaccharide **C4^{-2}** has ~ ten H−bonds with 30−40% occupancy, but the most representative H−bonds are with Asp100 and Arg173.
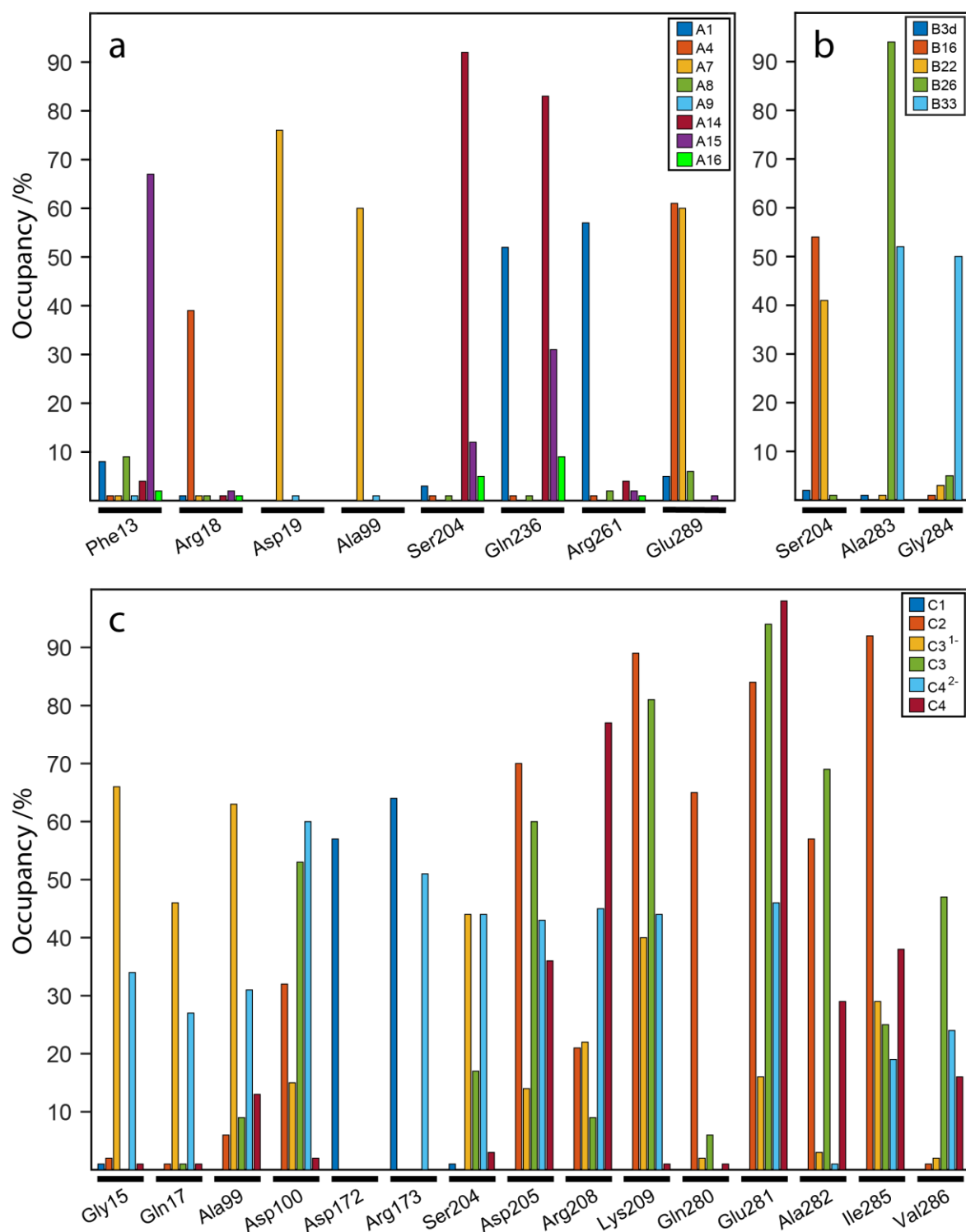
Figure 34. Occupancy percentage of the hydrogen bonds between each ligand and the amino acids of WaaG binding pocket. Reported amino acids have at least 30% occupancy for one protein−ligand H−bonds.

7.3.8. N− and C− domains of WaaG protein have a twisting−like fashion

Focusing on the *apo*−form of WaaG protein, its behavior during the 10 ns−MD simulation was further investigated. The behavior was evaluated making the first alignment on the entire protein backbone (Figure 35a), then aligning on the N− domain (8b) or on the C−domain (8c). The analysis consists of the RMSD evaluation on the entire MD simulation. Figure 35a shows that there is no considerable difference between the RMSD distribution of the *apo*− (in red) and the singular N− and C−domains. In Figure 35b,c, where the alignment is built on the N− or C−domains respectively, is evident how, aligning on a specific domain, the opposite domain backbone displays a very broad RMSD distribution. This indicates a relative dynamic behavior of N− and C−domain, moving one against each other in a twisting−like fashion.

To prove this relative internal dynamic behavior over the entire MD simulation, a further investigation was carried out aimed to select strategic amino acids on the different portions of WaaG protein and recognize the changes in Å regarding distances, angles *et cetera*. Results of this analysis are depicted in Figure 36a−c. Figure 36a reports the variation of the angle between the Cα atoms of His62 (N−domain), Lys248 (C−domain) and Gly168 (hinge region), while Figure 36b shows the variation in distance between the Cα atoms of His62 (N−domain) and Lys248 (C−domain). The two graphs show a similar trend, suggesting a twisting−like movement. The correlation between these two variables was plotted in Figure 36c. For this purpose, the Spearman correlation coefficient r_s or *rho* (generally ranging from −1 to +1, showing perfect negative or positive correlation) was calculated reporting a value of 0.9028, which indicates a good correlation between these two variables. The correlation is quite linear, therefore this post−MD prediction confirmed the twisting−like movement.
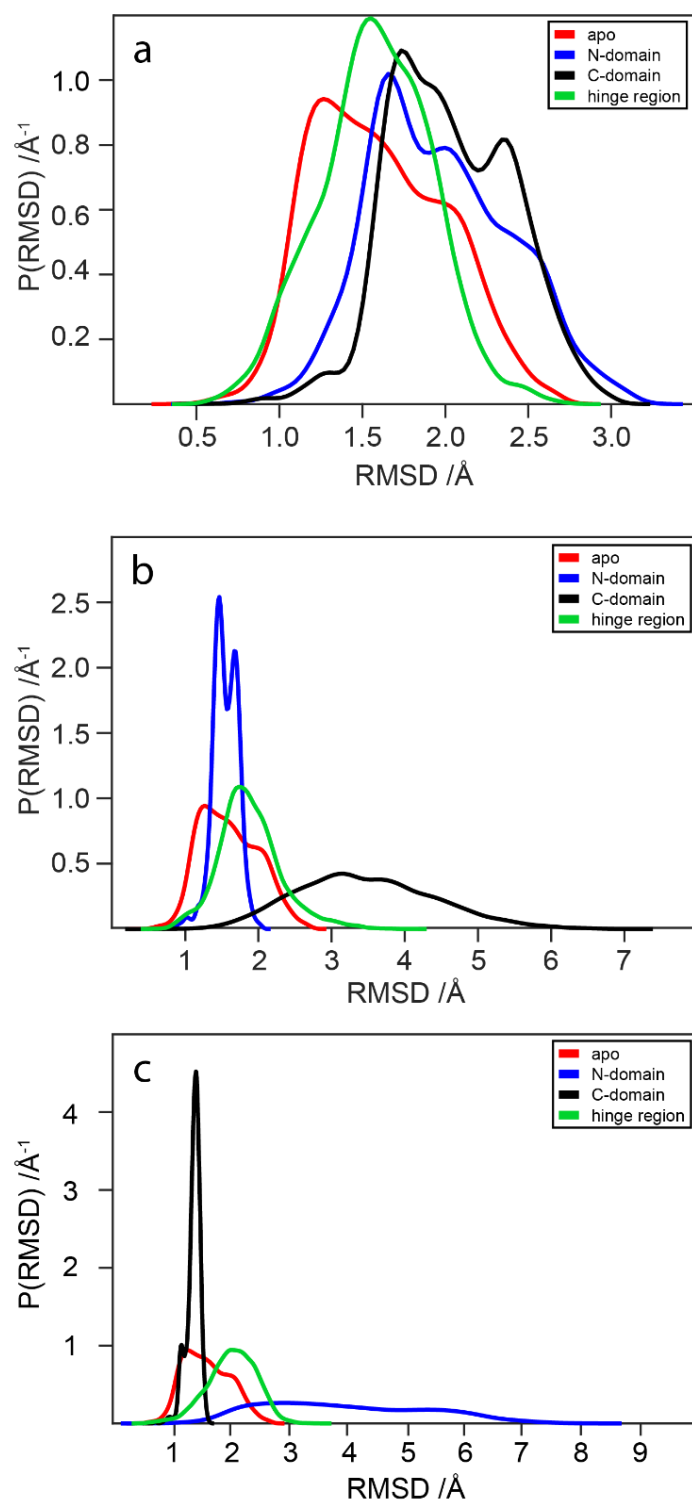
Figure 35. Kernel density estimation of the RMSD probability distributions through normal distribution function. The calculation focuses on the protein backbone of the *apo*−form of WaaG (from 2iw1, red) as a reference of RMSD values. Alignment of (a) the entire protein backbone, (b) N−domain, and (c) C−domain of *apo*, then RMSD calculation of N− and C−domain and hinge region.
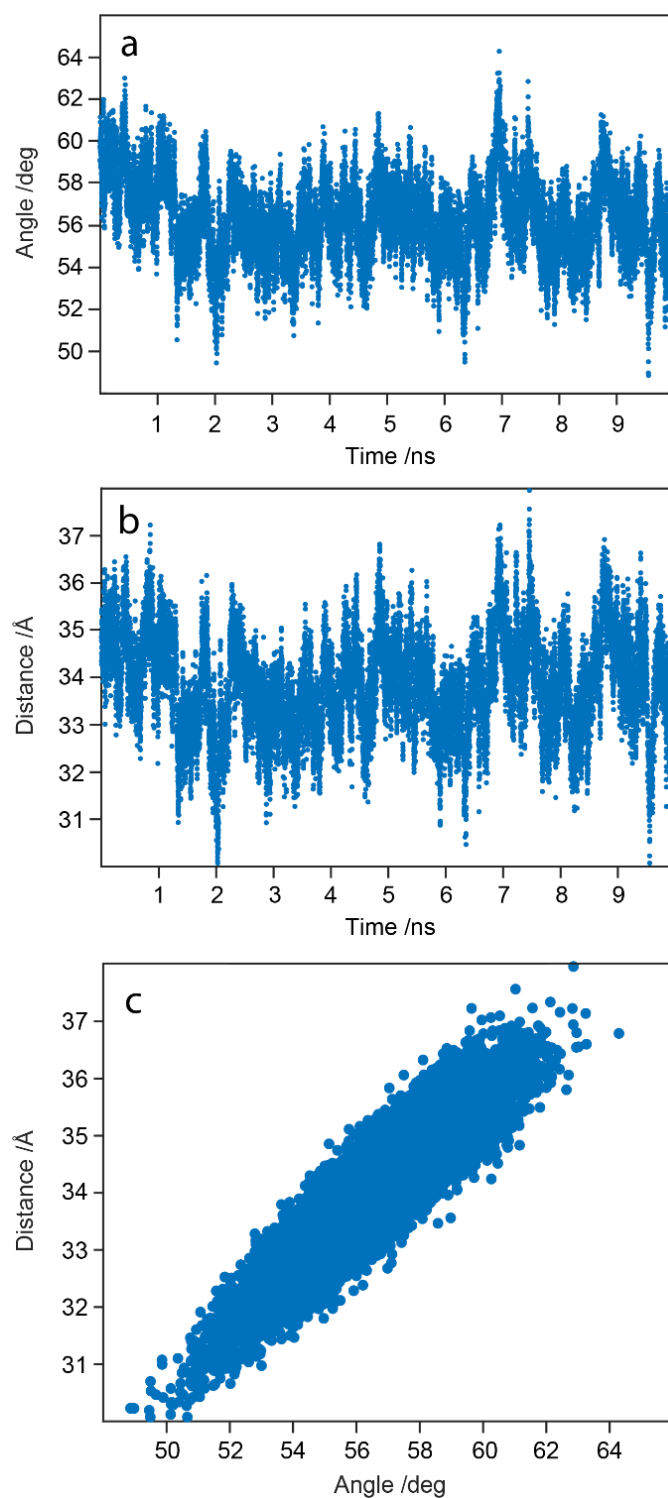
Figure 36. Plots depicting (a) the variation of the angle over time between the Cα atoms of His62 (N−domain), Lys248 (C−domain) and Gly168 (hinge region) and (b) distance fluctuation over time between the Cα atoms of His62 and Lys248, during the 10−ns MD calculation. (c) Scatter plot of the two variables against each other.

7.3.9. *In vitro* biochemical assessment

In vitro biochemical assessment was carried out by Dr. Claudio Muheim in Prof. Daniel O. Daley group (Department of Biochemistry and Biophysics, Arrhenius Laboratory, Stockholm University, Stockholm, Sweden).

The activity of the ligand belonging to library A against WaaG was assessed through different biological assays, as previously described. [40] The same biological assays are still ongoing for ligands of library B.

The first assay was assessed to evaluate the potential inhibition of WaaG protein after treatment with the ligands, in the presence of ^{14}C−labeled UDP−Glc. Results from SDS–PAGE for compound **A1** are shown in Figure 37. The inhibition effect of compound **A1**, at 1 mM concentration, was quantified and normalized using DMSO as control (100%). The percentage for **A1** spot was 58.2%, indicating that compound **A1** has a good activity at 1 mM.
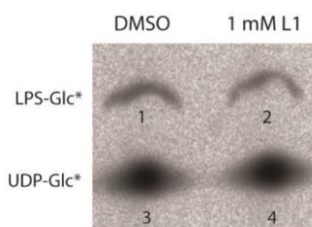
Figure 37. Activity of WaaG in the presence of DMSO or 1 mM **A1** (here reported as L1).

Regarding library A, some ligands showed an interesting WaaG inhibitory activity. Figure 38 shows SDS−PAGE analysis on ligands **A2**−**A20**, with UDP−Glc* used as reference, at 25 mM. In particular, compounds **A16** and **A18**, showed ~ 80% of inhibition, while compounds **A8** and **A17** reached inhibition percentages around 50−60%. At this concentration, a good result was displayed for ligands **A16** and **A18**.
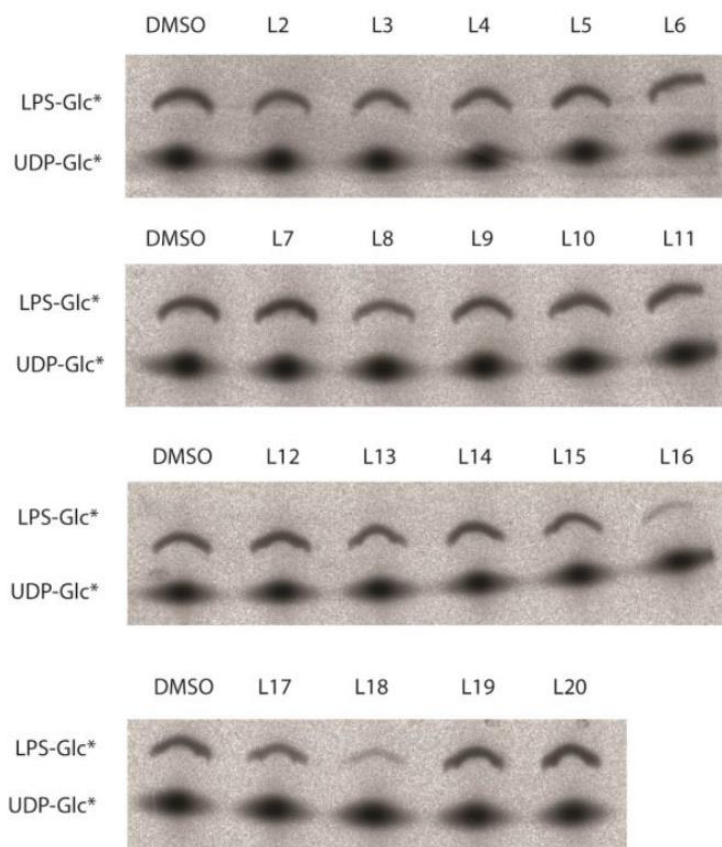
Figure 38. SDS−PAGE analysis in the presence of DMSO or compounds **A2** – **A20** (here reported as L2−L20) at 25 mM concentration.

The pH of the administration solution was checked for each analysis. After treatment with compounds **A16**, **A17** and **A18**, the pH of the solution became more acidic, ~ 5, while control pH in DMSO is around 7−8. Treatment with **A8** does not significantly affect pH, as well as the treatment with ligand **A2** which slightly decreases the pH to 6 (Figure 39). This could be considered as proof of the relationship between the activities of these ligands and a pH shift. The activity of compounds **A16** and **A18** could be increased by pH shift in the administration solution, and results are reported in Figure 39.
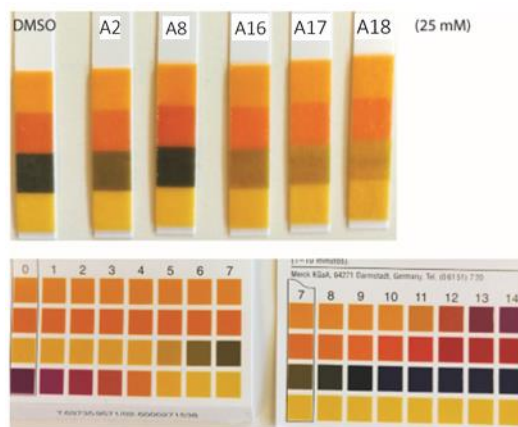
Figure 39. Images of solution pH shift at 25 mM after treatment with compounds **A2**, **A8**, **A16**, **A17** and **A18**.

Unfortunately, none of the ligands showed a significant effect on the cellular inhibition except for **A1**, which possesses an IC_{50} (half−maximal inhibitory concentration) of 1 mM. Further fragment growing or linking processes, as observed for library B, could lead to better biochemical results.

Further SDS PAGE analysis was accomplished to evaluate WaaG activity at different pHs. WaaG activity is detectable at pH 7, but also at a pH range of 6.2−7.7. Analysis at pH 5.2 or 9.2 demonstrated a low activity of WaaG, as shown in Figure 40.
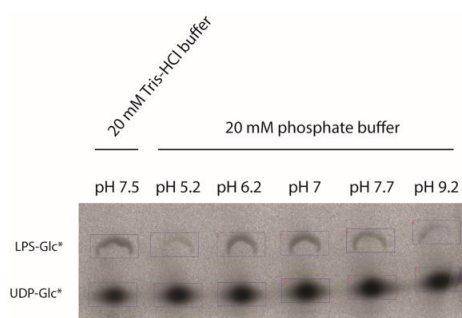
Figure 40. Activity of WaaG under different pH and buffer conditions.

7.4. Discussion and Conclusions

The present project is a combination of computational and experimental studies with a common aim: finding interesting fragments to sow the seeds for future WaaG inhibitors, study the mechanism of action of WaaG during its behavior as glycosyltransferase, when it

catalyzes the reaction of leaving glucose from UDP−Glc^{2-} to Hep−II on LPS, and study the conformational movement of the different portions of WaaG over time, in a simulated physiological environment. The background base is an ensemble of NMR, docking, MD and biochemical experiments, leading to the identification of compound **A1** of library A as a starting point for the libraries construction, as a bland binder to WaaG. Compounds of the newly−built libraries A and B were docked in *apo*−form of WaaG or in the presence of WaaG−UDP−Glc^{2-} complex, investigating their conformation in the active site environment, the interactions with the exposed amino acids, and the relative conformation through their superimposition with the structure of UDP−Glc^{2-}, natural binder of WaaG. Compounds **A1**, **A7**, **A9**, **A14** and **A16**, **B3d**, **B16**, **B22**, **B26** and **B33** from libraries A and B were selected by energy affinity from docking filtering, while ligands **A4** and **A15** from STD−NMR experiments. More in−depth, **A4** and **A15**, among the tested ligands, were the best in NMR studies with a higher STD signal, >70% with *apo*−form of WaaG, and >40% and >70%, respectively, in the presence of UDP as competitor for the binding. Once selected the ligands, the best−docked pose was taken for each of them and used as starting point for further MD simulations. A first binding free energy (BFE) calculation was conducted on the 10 ns−MD trajectories produced, and the energy values were also converted in K_{D}s. Compounds **A4**, **A7** and **B33**, among the selected ligands, showed the best affinity profile, with > mM values (0.11, 0.62 and 0.04 mM, respectively). Among libraries A and B, several ligands demonstrated are worth being further investigated and manipulated with fragment growing or fragment linking/merging techniques. In this Discussion, we will focus on the ligands **A4** and **B33,** as the most interesting compounds from both libraries. Analyzing each 10−ns MD simulation, an investigation on the backbone stability during the calculation was performed through an RMSD distribution analysis on the *apo*−form of WaaG or with WaaG−ligand complexes. Compound **A4** is undoubtedly the one of library A which gives better stability to the protein when bound to it, compared to *apo*−form, with avRMSD of 1.43 Å ± 0.21. For library B, ligand **B33** generates considerable stability of the WaaG backbone, with an avRMSD value of 1.29 Å ± 0.25. A further investigation on the polar or nonpolar contributions to the interactions between WaaG and the ligands was performed. Compound **A4** reported a remarkable equilibrium between the two terms, with an average energy of 25 kcal·mol^{-1} for both. Compound **B33** has, on the contrary, a higher polar term contributing to the binding, compared to the hydrophobic one. Considering the electrostatic term, the H−bonds established by the ligands were analyzed. Derivative **A4** electrostatically binds to Arg18 and Glu289, while **B33** to Ala283 and Gly284. MD trajectories for both

ligands **A4** and **B33** were analyzed through cluster analysis. This analysis groups all the conformational states of the ligand during the simulation in clusters, and the most representative pose of the most populated cluster was taken as the best predicted by the MD simulation. The discrimination between all the poses is RMSD, with a cutoff of 1 Å. Results of their interactions with the exposed amino acids of WaaG are reported in Figure 41a−d.
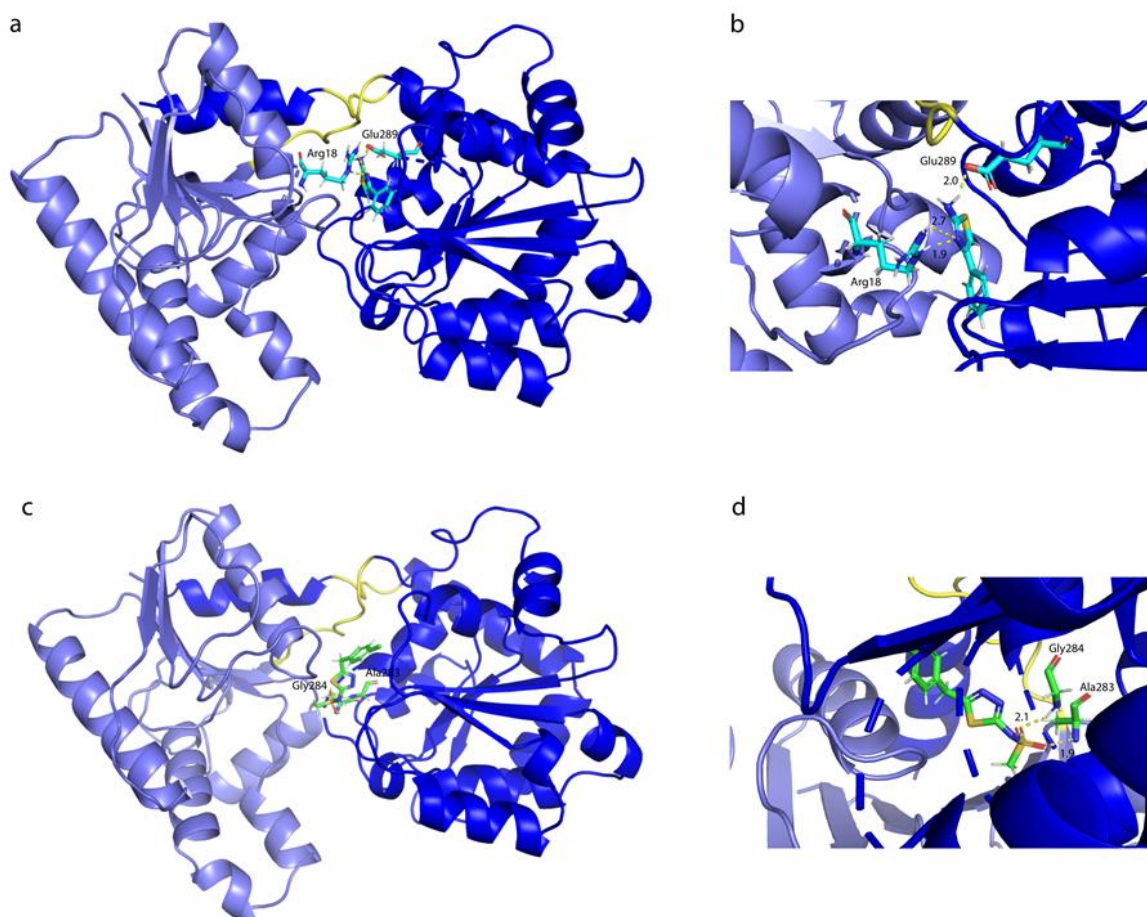

Figure 41. Molecular dynamics representation and interactions of ligands a,b) **A4** and c,d) **B33** with WaaG binding pocket. The structures are the most representative of the different clusters identified for each ligand.

As already discussed, WaaG is a glycosyltransferase that catalyzes the transfer of an α−D−glucose residue from UDP−Glc (generating UDP) on a Hep−II residue on LPS at the interface between the outer and inner core. In this context, it is interesting to investigate the mode of approaching of WaaG to the specific portion of its binding on LPS, parts of the inner core, ending with O−antigen. The oligo− unit was fragmented in different oligosaccharides and a library ranging ligands from disaccharides (**C1 – C5**) to tetra− and hexasaccharides (**C6 – C12**) was built. Ligands **C1 – C12** were docked in WaaG *apo*−protein

binding site to see their docking ranking, both with *apo*−form and WaaG−UDP−Glc^{2-} complex. Then, only the disaccharides **C1** – **C4** were further investigated through molecular dynamics investigations. The idea was to investigate the β−1,3 linkage involving Hep−II, acceptor of the glucose residue from UDP−Glc inside the WaaG binding pocket. Disaccharides **C3** and **C4**, phosphate−substituted derivatives, were included in the MD library both in protonated (**C3** and **C4**) and monocharged forms at the phosphate groups (**C3^{-1}** and **C4^{-2}**). Compound **C4^{-2}** was the most interesting in terms of BFE and K_D (0.4 µM) values, confirming a good binding affinity with WaaG, but also in terms of RMSD distribution, hence stability, of the protein backbone when **C4^{-2}** is bound to its active site. After a clustering analysis, the most representative conformational state of **C4^{-2}** was isolated from the entire MD simulation. Its interactions with WaaG binding pocket were studied and visualized, then depicted in Figure 42, both in complex with WaaG *apo*−form (a) and WaaG−UDP−Glc^{2-} (b,c). In the presence of UDP−Glc^{2-}, **C4^{-2}** approaches the glucose−binding site on WaaG protein.
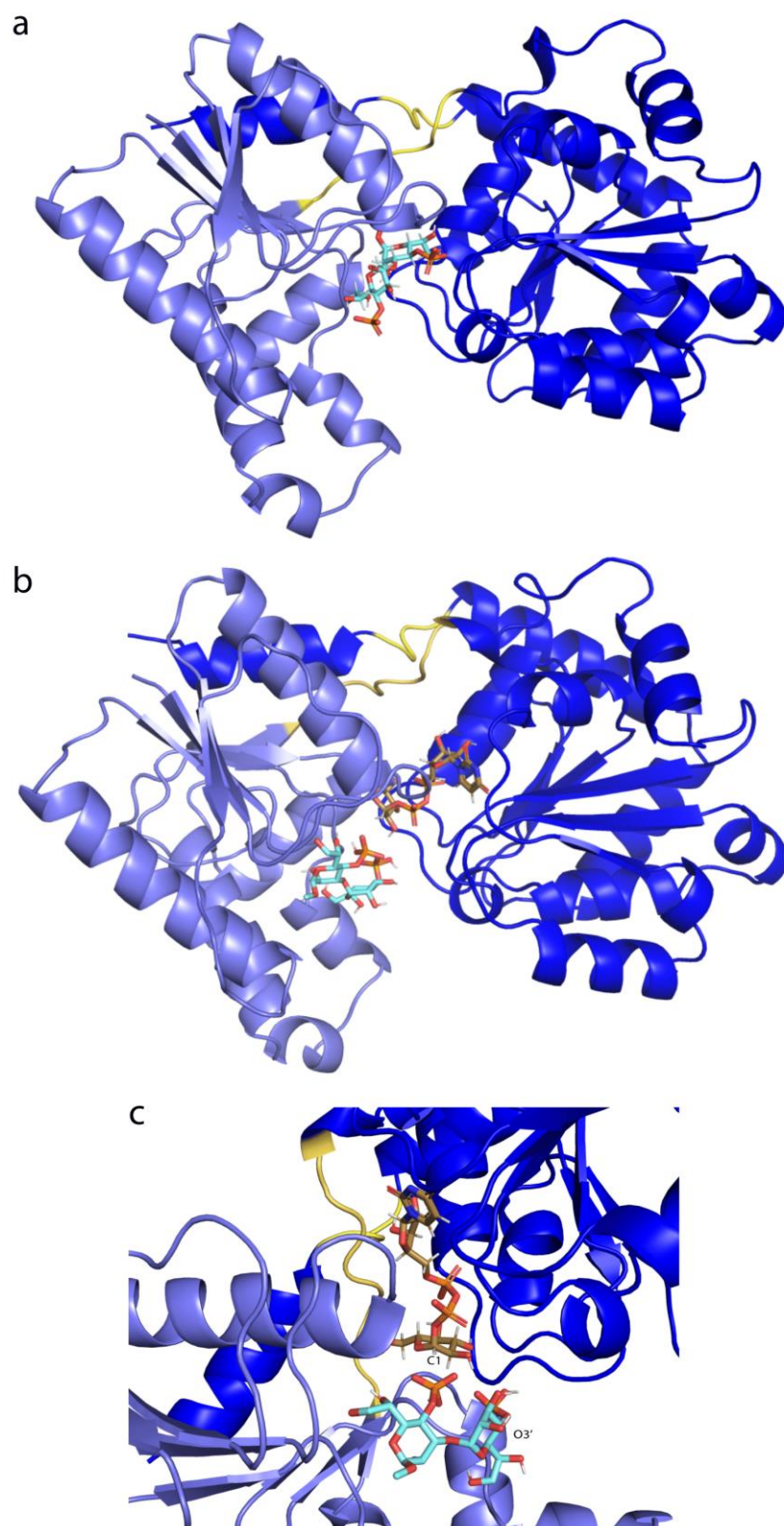
Figure 42. a) Molecular dynamics representation of **C4⁻²** and b,c) molecular docking conformation of **C4⁻²** with WaaG−UDP−Glc²⁻ complex.

As for the investigation involving WaaG behavior during the entire MD simulation, the movement of the entire protein backbone, or the single portions, N−, C−domain and hinge region was undertaken. Monitoring RMSD distribution, variation in distance and angle between domains, it was shown a relative dynamic behavior, predicting a twisting−like fashion.

Regarding the *in vitro* biochemical assessment, the inhibition activity assay for compounds of library A was performed. Compound **A1** demonstrated activity at 1 mM concentration, whilst in general, the other ligands of library A demonstrated a certain activity at 25 mM which decreased lowering the concentration to 1 mM. Remarkably, compounds **A16** and **A18** showed ~ 80% when administered at 25 mM. Further fragment growing or linking processes, as made for library B, could lead to more powerful compounds endowed with improved biochemical results. As proof of UDP−Glc activity on WaaG, an SDS−PAGE inhibition assay was performed using 1 and 5 mM concentrations of UDP−Glc, with a general ~ 80% of inhibition percentage. WaaG activity can also change at different pHs; in particular, the protein resulted to be active with a pH range from 6.2 to 7.7. At pHs 5.2 and 9.2, WaaG activity drastically decreases.

7.5. Future outlook

This project aimed to better explore, through computational and experimental studies, the binding of two sets of compounds, libraries A and B, to WaaG enzyme. Starting from the results obtained, future works will focus on carrying out fragment growing or fragment linking processes on selected compounds. In the fragment growing, some small functional groups could be removed/added on the main scaffold. In a fragment linking process, the most interesting ligands could be merged directly, or by rationally chosen linkers. A deeper biochemical assessment will be applied to ligands and their derivatives through the investigation of their inhibition mechanism on WaaG enzymatic activity. WaaG behavior and movement will be more in−depth investigated, both in its interactions with natural ligand UDP−Glc^{2-} also in other protonation states UDP−Glc$^{[\alpha-]}$ and UDP−Glc$^{[\beta-]}$, endowed with a formal charge on α− or β−phosphate, respectively.

8. Project #4: Synthesis of 1,2–*cis*–glycosylated oligosaccharides: application in the treatment of *Aeromonas salmonicida*

8.1. Introduction

"*Sakcharon*" was the Greek word to name the carbohydrates or sugars, from which the name "saccharide" originated. [204] The term "carbohydrate", though, originates from the French "hydrate de carbon", to indicate all the molecules with empirical formula $C_n(H_2O)_n$. Carbohydrates are the most abundant macromolecules on earth. From a chemical point of view, carbohydrates are polyhydroxylated aldehydes involving a certain number of carbon atoms, from 3 to 9. [205] Carbohydrates are divided into three major groups based on their structures: (1) simple sugars (monosaccharides and disaccharides), such as glucose or sucrose (made by glucose and fructose); (2) complex carbohydrates, such as glycogen, starch, and cellulose, which are glucose–based polymers; and (3) glycoconjugates, which are modified forms of glucose covalently attached to either lipids (glycolipids) or proteins (glycoproteins). [204]

Cellulose has a structural role for the cell wall in plants; it cannot be digested by animals because of the lack of enzymes able to hydrolyze it into monosaccharides (glucose, represented in its 6–ring cyclic form in Figure 43). However, they can break down starch into smaller glucose molecules. Another glucose–based molecule is glycogen, used by animals to store glucose in their body. There, it can be either catabolized for energy (ATP) or used for anabolic functions, such as the production of fatty acids. [204]

Glycoconjugates are involved in important functions, such as immunity, and as components of cell membranes. Sugar portions in glycoproteins and glycolipids differ from the process in which they are involved, such as development, tissue differentiation, cell activation and senescence. [206]
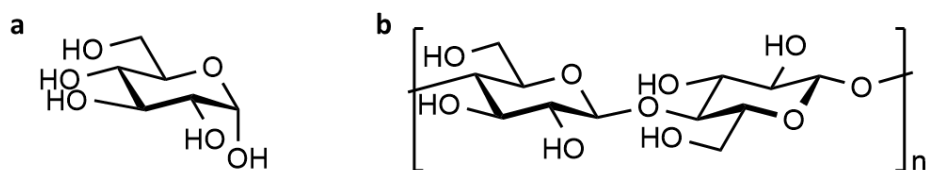

Figure 43. Chemical representation of the a) monosaccharide glucose (β–glucopyranose) in its 6–ring cyclic form and b) its polysaccharide cellulose.

Monosaccharides are divided into aldoses and ketoses. A common aldose is constituted by a carbon chain of secondary alcohols CHOH. Visually, the chain is reported in a vertical way, where the upper end (C–1 position, known as anomeric position) is represented by an aldehyde CHO, and the lower end is a primary alcohol CH_2OH. Ketoses are less common than aldoses in nature and are made of primary alcohols at both ends and a ketone along the carbon chain.

Both in aldoses and ketoses, each carbon of the chain is stereogenic in a three–dimensional point of view. To represent the stereochemistry of a monosaccharide in a 2D mean, the Fisher projection is frequently applied, allowing to distinguish between D– and L–enantiomers of the same structure. If a sugar has more than one stereogenic center, the different stereoisomers are intended as diastereomers. Diastereomers could be D– or L– sugars; it is determined by the absolute configuration of the secondary alcohol at the highest numbered chiral center (R– for D–sugars and S– for L–sugars). In nature, the majority of sugars are D–enantiomers, while the L–counterpart is less common. Diastereomers are also commonly distinguished in α– and β–sugars, and it depends whether the C–1 substituent is located in *cis* (α) or *trans* (β) to the oxygen atom at the highest numbered stereogenic center (C–5 in the Fischer projection – Figure 44b). More easily, α– is intended as axial (lower part in D–sugars) and β– as equatorial (upper part in D–sugars). [205]
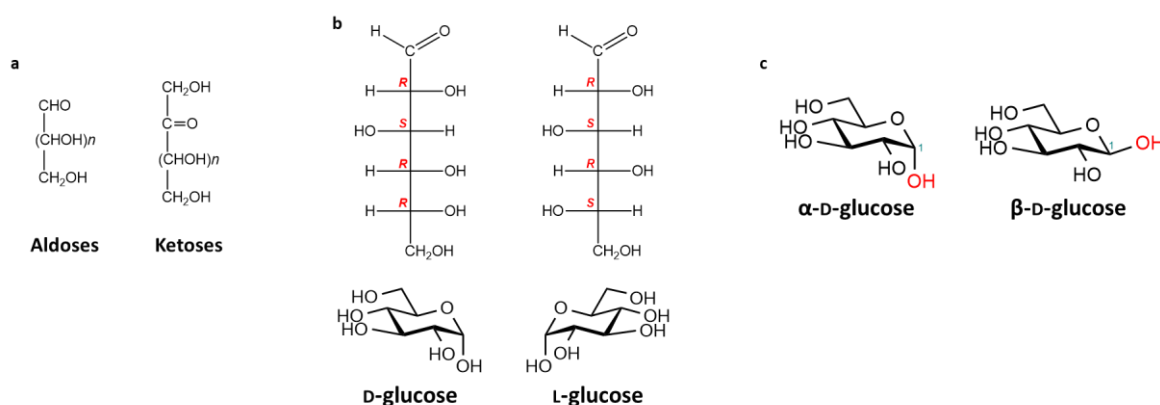

Figure 44. Representation of the difference between a) aldoses and ketoses; b) D– and L–sugars c) α– and β–saccharides.

In this last project, we will focus mainly on hexoses, which possess three and four stereogenic centers, respectively. In particular, we will concentrate our attention mainly on glucose and mannose (epimeric with glucose at C–2). [205]
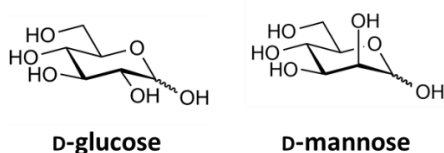
Figure 45. D–glucose and D–mannose (hexoses).

For the further discussion, it is useful to mention also other monosaccharides, such as L–fucose (6–deoxy–L–galactose) and L–rhamnose (6–deoxy–L–mannose). These deoxy sugars are biologically relevant, since they are involved in some crucial processes of recognition between cells (L–fucose), or predominant in plant cell walls (L–rhamnose). [205]
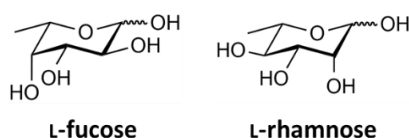

Figure 46. Examples of biologically relevant deoxy sugars: L–fucose and L–rhamnose.

Disaccharides, but in general oligo– and polysaccharides, are formed by single glycosidic linkages. Biologically relevant sugars are large oligosaccharides, where the formation of each glycosidic bond can be synthetically performed on an iterative basis. [205]

8.2. Results and Discussion

8.2.1. Rationale

In natural products there are different types of glycosidic bonds; the most abundant, but also the most synthetically challenging, are the *O*–glycosidic bonds. They are, for nomenclature, divided in α–, or 1,2–*cis* and β–, or 1,2–*trans* glycosides. However, in particular the 1,2–*cis* glycosylic residues (α–glycosides for D–glucose, D–galactose or β–glycosides for D–mannose, L–rhamnose) are the most challenging for chemists, hence the modern challenge is the stereoselective 1,2–*cis*–glycosylation, the most present as linkage of naturally occurring oligosaccharides of biological interest and therapeutic potential. [207–209]

Each reaction for a glycosidic linkage has two stereo–outcomes, α– or β–configurations. In general, the α– or *cis*–glycoside is more synthetically challenging. [210,211] Key role in this regard is represented by strategical protecting groups, [212] deeply affecting the reactivity of the sugars. [213] The disadvantage of *cis*–glycosylations, in comparison to *trans*– ones, is the difficulty in using a neighboring participant group. Synthetic glycochemistry is concentrated on finding new ways to improve the stereoselectivity of *cis*–glycosylations, as discussed in the following Paragraphs. [18]

Other challenges regard the directed β–mannosylation reactions. Also in this case, the protecting groups are fundamental to achieve the correct stereoselectivity. For example, the 4,6–*O*–benzylidene on mannose donors was found to have a key role in β–mannosylations. [214–216]

The following synthesis aims to build a trisaccharide structure that is inspired by a trisaccharide repeating unit found in the structure of the lipopolysaccharide (LPS) layer of a gram–negative bacterium, *A. salmonicida*.

Aeromonas salmonicida is a rod–shaped, oxidase–positive, facultative, anaerobic, non–spore–forming and non–motile, gram–negative bacterium. it can grow as single or paired rods of varying lengths from 0.5–6 µm and widths from 0.5–1 µm, or occasionally as coccoid cells, varying in diameter from 0.5–1 µm. [217] It causes furunculosis [218] in cold–blooded vertebrates at low temperatures, as salmonid fish. This disease causes furuncles (boil–like lesions), overall darker color, hemorrhaging in the fin bases, mouth, abdominal walls, reproductive organs, viscera, liver, pyloric caeca, and heart. Other symptoms are soft kidneys, erratic swimming, lack of feeding, muscle lesions, inflammation and congestion of the lower intestine, but also spleen enlargement, sepsis and septicemia, and acute mortality. It affects also fresh–water and marine fishes. [217,219]
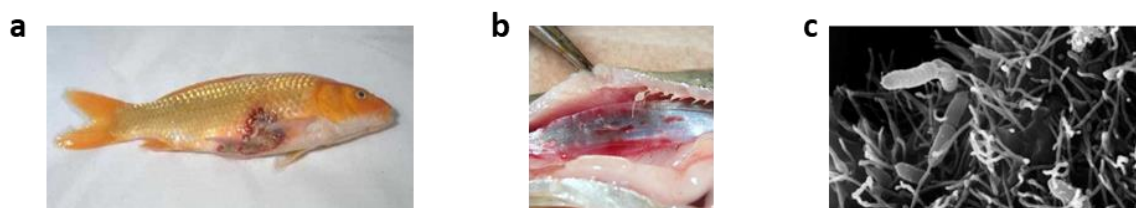

Figure 47. Images reporting the effects of *A. salmonicida* on salmonid fishes, a) externally and b) internally. c) Scanning electron micrograph of *Aeromonas sp.* bacteria adhering to human epithelial cells. [217]

The economic impact interests millions of dollars of investments. Like most of the gram–negative bacteria, *A. salmonicida* is an opportunistic pathogen that possesses an outer membrane composed of lipopolysaccharide (LPS), important for the host–cell invasion mediation, and, especially for the virulent strains; LPS is particularly involved in the assembly–maintenance of the protein array exposed to the surface of the virus. [220]

Among the five sub–species of *A. salmonicida*, [221] the *pectinolytica* is a mesophilic strain that can easily grow at 37 °C. The other ones, *salmonicida*, *smithia* and *masoucida*, are psychrophile strains, hence they can only grow at temperatures below 25 °C. Therefore, *pectinolytica* strains can also affect mammalians, hence also humans. [222] Until few years ago, there was no clinical background for the medical importance of *A. salmonicida* for humans. Then, in 2008, a 68–year–old diabetic woman with a clinical story of ambulatory peritoneal dialysis was infected by *A. salmonicida*, showing symptoms such as abdominal pain and cloudy peritoneal fluid. [223] Recently, some cases were reported in India, [224] even if the pathogenicity and the mechanism of action are unclear. More recently, some cases were reported in Spain, with symptoms as acute gastroenteritis and foot cellulitis. [221]
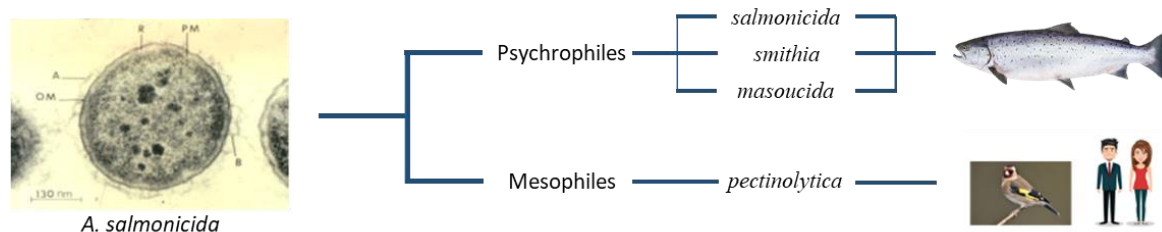

Figure 48. Schematic representation of the different strains of *A. salmonicida* and their preferred hosts: psychrophiles (which grow at 0–20 °C, as *salmonicida*, *smithia*, *masoucida* subspecies) and mesophiles (which grow at 20–45 °C, as *pectinolytica* subspecies). [225,226]

The LPS is divided into three portions, the *O*–antigen, core and lipid A. [227] The *O*–chain polysaccharide (*O*–PS) of *A. salmonicida* was previously investigated through an analysis involving compositional and methylation techniques, CE–ESMS (capillary electrophoresis–electrospray mass spectrometry) and 1D–2D NMR experiments. The result was the discovery of a branched polymer composed of trisaccharide–repeating units of L–rhamnose (Rha), D–glucose (Glc), 2–acetamido–2–deoxy–D–mannose (ManNAc) and *O*–acetyl group (OAc). The structure of the repeating unit, elucidated in 1983, is reported in Figure 49. The main building block can be recognized as a tri– or a tetrasaccharide repeating unit, where a partial *O*–acetylation (C–2 position on the rhamnose residue, 75%) and partial glucosylation

(α–D–Glc–(1→4), 35%) were identified. A study made on A449, 80204 and 80204–1 strains of *A. salmonicida*, grown under different conditions, confirmed that the *O*–PS structure was conserved in all the observed strains. Another ELISA–based serological study with native LPS–specific antisera, on the native *O*–PS and some derivatives, confirmed the importance of the *O*–PS backbone structure as an immunodominant determinant. [228]
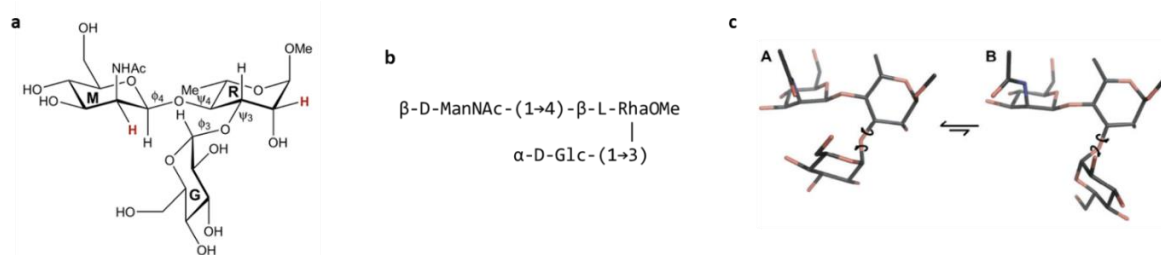

Figure 49. Torsional conformations of the trisaccharide β–D–Man*p*NAc–(1→4)[α–D–Glc*p*– (1→3)]–α–L–Rha*p*–OMe studied through MD simulations. a,b) 2D and explicit representation of the trisaccharide; c) 3D picture of the two conformational states (A and B) from the MD simulation. [229]

A biological function of a molecule is influenced by its conformational state, hence its flexibility. From this point of view, carbohydrates are molecules of interest to determine their structure and dynamics. In the case of the trisaccharide repeating unit contained in *O*–PS of *A. salmonicida*, the combination of hexopyranoses, as mannose and glucose, creates a good starting point for a deeper study on the dynamics of this structure. A microsecond MD simulation was previously done on this trisaccharide, which represents a model for the repeating unit of the *O*–antigen portion of *A. salmonicida*. [230] The trisaccharide contains three sugar residues in the polymer where D–glucose (G) residues make branches to the backbone of the polymer made from the L–rhamnose (R) and *N*–acetylmannosamine (M) residues. [228]

Focusing on Figure 49c, as an MD output, conformational state A of the trisaccharide was present in 95% of the simulation, while state B during 5%. From a comparison between the conformational states A and B, it is visible that the α–(1→3)–linkage is different, while the β–(1→4)–linkage only showed the presence of a single conformational state. [229] Subsequently, the above–mentioned computational studies explained the NMR results with an exchange process between two conformations concerning residue G. [229] The present project aims to synthesize a trisaccharide compound that replicates the repeating unit of the *O*–antigen of *A. salmonicida*. The trisaccharide can potentially be developed into a vaccine to prevent the economic damage caused by *A. salmonicida* in the future.

8.2.2. Chemistry

Main goal. Based on these promises, this project aims at three different goals: 1) improve the stereoselectivity of the α– and β–glycosylations; 2) investigate the 3D structure of the trisaccharide, already studied through MD simulations, [230] 3) investigate the biological interest of the trisaccharide repeating unit of the LPS *O*–Antigen in *A. salmonicida*. The experimental investigation of the trisaccharide conformation will involve NMR experiments such as NOE–Build up curves. The NOE (Nuclear Overhauser Effect) effect will be investigated both in the 2–OAc–functionalized trisaccharide and the non–functionalized one on the Rha residue. This will highlight the role of the partial 2–OAc functionalization. The correct stereochemistry of intermediates is analyzed by NMR– and ESI–TOF MS–experiments.

Synthetic approach. The entire synthetic route is reported in Scheme 5. An anti–clockwise synthetic route for the trisaccharide was planned. To improve the stereoselectivity of the two challenging selective 1,2–*cis*–glycosylations, it was crucial to strategically build the starting donor and acceptor residues. For the glucose donor, the anomeric position is functionalized with a thiophenyl group in α–configuration. [231] In C–6 position, a bulky directing group is needed to improve the α–stereoselectivity for the *cis*–glycosylation between the glucose donor and the rhamnose acceptor (1,3–linkage). Because of the challenging glycosylation in the latter steps, a bulky protecting group or an ester group at O–6 of the glucose residue was needed. [232] A TBDPS (tert-butyldiphenylsilyl) group was chosen between different bulky groups. The C–2, C–3, C–4 positions on the glucose are protected by stable and less bulky benzyl groups.

The rhamnose acceptor was meant to possess certain stability and have a C–3 position reactive for the glycosylation. The anomeric α–configuration is capped by an *O*–methyl group. In C–2 the *O*–acetyl group assures an α–configuration. As above–mentioned, an *O*–acetyl group in C–2 position as a second variant of the bacterial polysaccharide was identified, hence it was inserted in the rhamnose residue. [233] The functional groups at O–3 and O–4 should be able to be handled orthogonally depending on the order of glycosylation toward the target trisaccharide.

As for the TBDPS group on glucose, the C–4 position needed a directing group for the *cis*–glycosylation between rhamnose and glucose. A NAP (2-naphthylmethyl) group is inserted

in *β*–4 position on rhamnose, to direct the glycosylation, but also as a protecting group that can be feasibly hydrolyzed with DDQ (2,3-dichloro-5,6-dicyano-1,4-benzoquinone). [234]

As for the mannose substrate, it was planned to be a thiodonor, through the insertion of a thioethyl group in *β*–configuration of the anomeric position. Moreover, the *N*–acetylation in α–configuration in mannose C–2 position was assessed by conversion of a stable azide into an amide group after the *cis*–glycosylation reactions. Other substitutions, such as the 4,6–*O*–benzylidene and the picoloyl group in C–4 position in α–configuration, are relevant to ensure a high stereoselectivity in the subsequent 1,2–*cis*–glycosylation reaction. [235]
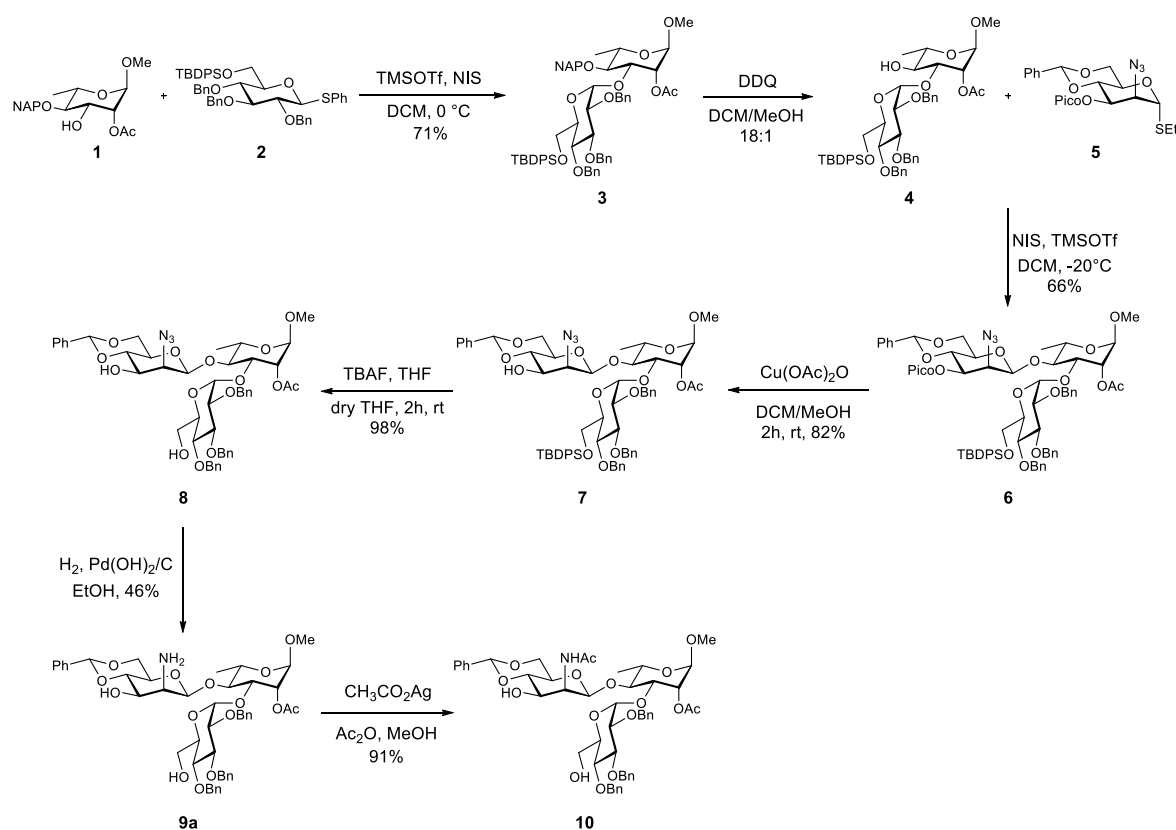
Scheme 5. Synthetic route for the trisaccharide **10**.

Building blocks **1**, **2** and **5** were obtained as reported in the following Schemes.
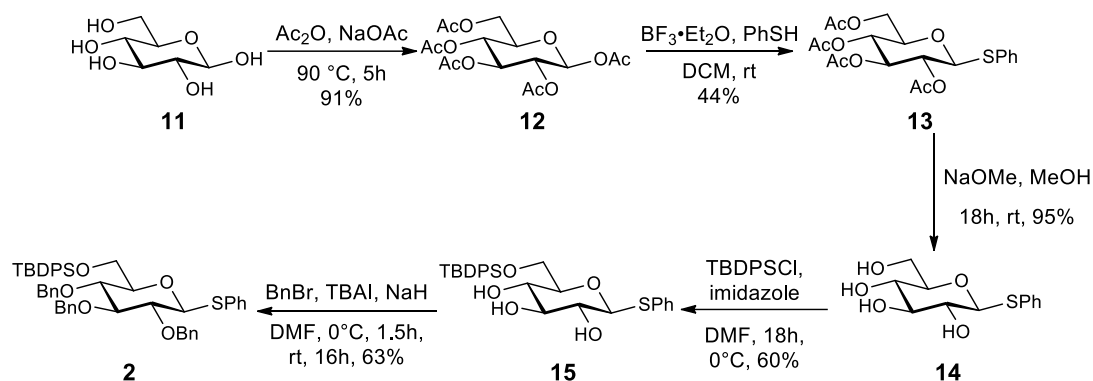

Scheme 6. Synthesis of the thiodonor **2**.

The thiodonor **2** was already published by Sasaki *et al.* [236] The following discussion aims to give more information on the synthetic route and characterization which were carried out for the building blocks.

As for the glucose residue, the first step corresponds to a peracetylation, a protection of all the hydroxyl groups on glucose with non–nucleophilic and stable acetyl groups. Compound **12** was thioglycosilated at the anomeric center, with thiophenol in the presence of boron trifluoride etherate (BF$_3$·Et$_2$O). It follows global deacetylation to give compound **14**. This fully deprotected thio–glucoside is regioselectively silylated in C–6 with the bulky TBDPS group because of the less–hindered primary hydroxyl group in C–6, in the presence of imidazole as nucleophilic catalyst. Compound **15** is converted in the desired thio–glucoside donor **2** with full protection of the remaining hydroxyls with benzyls groups.

The first idea was to go on with the synthesis of the thiodonor by synthesizing the imidate donor. The aim was to have a more reactive donor than the thio–one, for the subsequent glycosylation with the rhamnose acceptor. This synthetic route was not pursued since the thiodonor **2** was reactive enough for glycosylation with the rhamnose acceptor **1**.
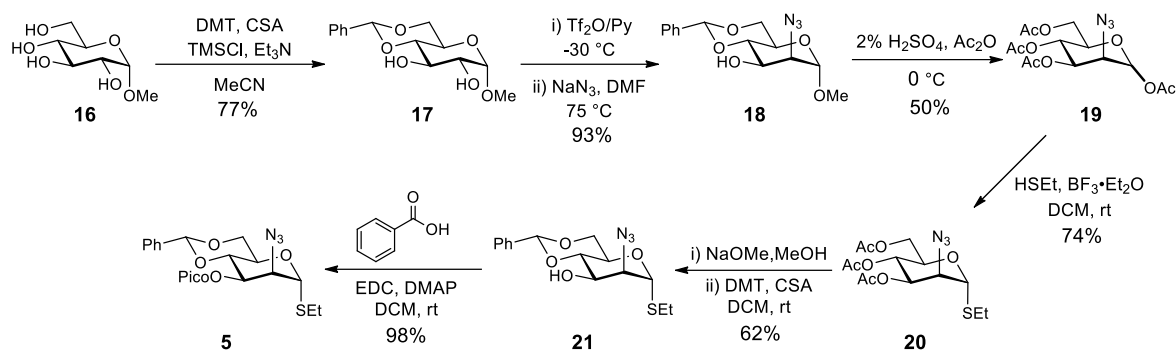
Scheme 7. Synthesis of key mannose donor **5**.

As for the mannose donor, derivatives **16**, **17** and **18** were recently reported by Demchenko *et al.* [237] Also intermediates **19**, **20** and **21** were already published by Demchenko *et al.* [238] The followed procedure was reported in Scheme 7, while the characterization was in accordance to what was published in the above–mentioned papers.
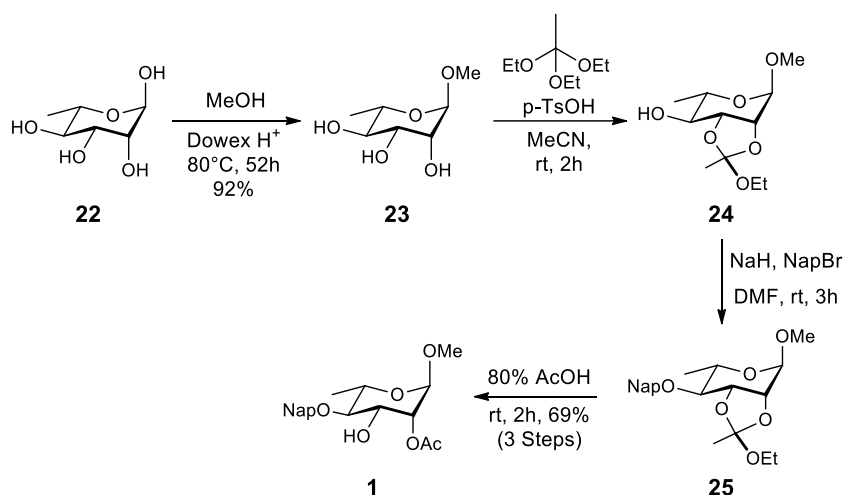
Scheme 8. Synthesis of the key rhamnose acceptor **1**.

Synthesis of rhamnose acceptor **1** was performed by Göran Widmalm group (Department of Organic Chemistry, Stockholm University, Sweden). Intermediates **22**, **23** and **24** were synthesized following procedures already reported in the literature. [239,240] Intermediate **25** is a 4–NAP–protected orthoester derivative: a rearrangement of the 2,3–orthoester protection in the presence of acetic acid brings to the rhamnose starting material **1** with the C–3 position selectively exposed for the glycosylation. In C–1 position, the OMe group, previously inserted in the first step of the synthetic route (Fischer glycosylation), stabilizes the α–configuration at the anomeric position, while the O–acetyl and NAP groups, in C–2

and C–4 positions respectively, assure the α–selectivity for the glycosylation with the glucose donor **2**.

Donor **2** and acceptor **1** were strategically substituted to give a good profile of yield/selectivity during the subsequent reaction of glycosylation, in the presence of activators (TMSOTf and NIS), in anhydrous CH_2Cl_2, giving disaccharide **3**. [232] In order to allow the following *cis*–glycosylation, the protection in C–4 position on rhamnose was removed [234], yielding compound **4**. The reaction of β–mannosylation between mannose donor **5** and disaccharide **4** [238] led to trisaccharide **6** with good yield and stereoselectivity.

The trisaccharide was then deprotected from the picoloyl group, [238] then desilylated [241–243] giving compound **8**. A reaction of hydrogenation/hydrogenolysis, in the presence of H_2 and Pd(OH)$_2$/C as catalyst, led to intermediate **9**. The reaction of *N*–acetylation on mannose residue was performed with $(CH_3CO)_2Ag$ and acetic anhydride in MeOH, to yield compound **10**.

8.3. Conclusions and future outlook

As a future plan, the study of the effect of the single protections on the spatial conformation of the trisaccharide could be carried out operating a full deprotection of the trisaccharide residue, followed by NMR and MD experiments. Then, a last synthetic step of 2–*O*–deacetylation could be pursued on the fully deprotected trisaccharide, in order to study the conformational effect of the acetyl group in position 2 of the rhamnose residue.

Last but not least, deuterium–substituted analog thereof, at the anomeric position of residue **G** could be synthesized following the same synthetic route, to facilitate further experimental NMR studies and to develop further efficient synthetic protocols for challenging glycosylation reactions.

9. Materials and Methods

9.1. Project #1

9.1.1. Molecular Docking

Molecular docking parameters were the same for both Projects #1 and #2.

For docking predictions, the academic program AutoDock Vina 1.1.2. [244] version 1.5.6 was selected for its known sampling and scoring functions. [245] The crystal structure of the tubulin–colchicine complex (PDB code: 4O2B; resolution: 2.30 Å) was retrieved by the Protein Data Bank (rcsb.org). [127] The starting point was the preparation of the protein structure, by removal of H_2O molecules, MES (buffer, 2–(N–morpholino)–ethanesulfonic acid), GOL (glycerol), ions (Ca^{2+}, Mg^{2+}), GTP (guanosine–5'–triphosphate), GDP (guanosine–5'–diphosphate), but also chains C, D, E, F, to analyze the docking poses of ligands in a free binding pocket. Programs for the docking analysis were PyMOL 2.3.4. AutoDockTools (ADT), [132] employed to obtain the PDBQT files of both protein structures and all ligands, but also to determine the docking Grid Box (30–30–30 Å for x,y,z coordinates). Docking was performed using the protein in its rigid form, or by making some amino acids flexible: Serα178, Thrα179, Alaα180, Alaα181. These amino acids are known to establish important H–bonds with the colchicine–binding pocket of tubulin. [128] The exhaustiveness value was set to 64 and the number of poses to 10 for each Vina docking calculation. The binding energy range was imposed to be ≤ 2 kcal/mol, above that of the best binding pose for each ligand. Binding poses and protein–ligand interactions were depicted in 2D–pictures elaborated through two molecular-graphics programs: LigPlot+ v.2.2. and Maestro (Schrödinger package). LigPlot+ processed in 2D–dimension the protein–ligand interaction with a cutoff of 5 Å from the center of the ligand. Maestro's Ligand Interaction Diagram is a 2D binding site representation known for its accuracy in the placement of residues. Structural superimposition of the docked pose of compound **9a** and the crystal structure of tubulin co–crystallized with colchicine, as well as other CBSIs, were represented with PyMOL. The crystallized structures of tubulin/ligand complexes were obtained from the Protein Data Bank: colchicine (PDB ID: 4O2B), tivantinib (TIV, PDB ID: 5CB4), plinabulin (PLI, PDB ID: 5C8Y), crolibulin (CRO, PDB ID: 6JCJ). The docking calculations

were conducted on a PC with an Intel® Core™ i7–9705H CPU @ 2.60 GHz with 8 GB RAM (operating system: Ubuntu 16.04, 6 CPUs for each simulation).

Same parameters for compound **5** of Project #2, which was docked in colchicine–binding site and the binding pose and protein–ligand interactions of its best–docked pose were represented in a 2D–image made with LigPlot⁺ and compared with docking outputs of previous leads **34** and **9a** (Project #1).

9.1.2. Chemistry

9.1.2.1. Materials and synthetic methods

3,4–difluoroaniline (**1**) and the aldehydes (**8a–j**) were commercially available. The synthetic route starts with the commercially available 3,4–difluoroaniline (**1**). Starting material 1 was acetylated with acetic anhydride, yielding compound **2**. The following nitration of the amidic compound **2** with a solution of KNO_3 in H_2SO_{4conc}, resulted in the formation of nitro–derivative **3**. Then, 4,5–difluoro–2–nitroaniline **4** was obtained by hydrolytic deprotection with H_2SO_{4conc}. The reduction of nitro group led to 4,5–difluorobenzene–1,2–diamine (**5**). The dianiline derivative **5** is cyclized with $NaNO_2$ in HCl, obtaining 5',6'–difluorobenzotriazole (**6**). The reaction of intermediate **6** with $ClCH_2CN$ was performed in the presence of KOH, in acetonitrile, to gain two geometric isomers bearing an acetonitrile chain on the triazole ring **7a,b**. The final step corresponds to a Knoevenagel reaction between each acetonitrile isomer (**7a,b**), separately, and different commercially purchased aromatic aldehydes (**8a–j**), bringing to final (*E*)(*Z*)-2-(5,6-difluoro-(1*H*)2*H*-benzo[*d*][1,2,3]triazol-1(2)-yl)-3-(*R*)acrylonitrile derivatives **9a–j**, **10e**, and **11a,b**. The final step generally brings to the sole formation of the *E*–isomer; only in one case a *Z*–isomer derivative was identified and purified from the reaction mixture (**10e**). A Knoevenagel condensation between 2-(1*H*-benzo[*d*][1,2,3]triazol-1-yl)acetonitrile **12a** and aldehydes **8d,j** gave final compounds **13d,j**. Compounds were purified by flash chromatography or by crystallization from EtOH. Mixtures of compounds were often purified through flash chromatography, employing the Merck silica gel 60, with a particle size of 0.040–0.063 mm (230–400 mesh ASTM); utilized eluents were petroleum spirit (PS), diethyl ether (DE), ethyl acetate (EA), chloroform ($CHCl_3$) and methanol (CH_3OH). Sodium sulfate was always used as the drying agent, while Celite® 545 was used as a filtering agent. Commercially available chemicals were purchased from Sigma Aldrich and Carlo Erba Reagents.

9.1.2.2. Chemical characterization

General chemical characterization is reported for both Projects #1 and #2. As for the characterization of intermediates and final compounds, retention factor (R_f) values were obtained utilizing a mixture of petroleum spirit (PS) and ethyl acetate (EA) as eluents, in 8:2 ratio; Thin Layer Chromatographies (TLCs) were developed on Merck F–254 plates. Melting points (m.p.) of the compounds were measured in a Köfler hot stage in open capillaries or Digital Electrothermal melting point apparatus and are uncorrected. Nuclear Magnetic Resonance (NMR) experiments were registered in solutions in DMSO–d_6 (deuterated DMSO) and recorded with a Bruker Avance III 400 NanoBay (400 MHz). ^{1}H– NMR chemical shifts are reported in parts per million (ppm), downfield from tetramethylsilane (TMS, internal standard). The chemical shift scale is in ppm (δ) and coupling constants (J) are calculated in Hertz (Hz). The assignment of exchangeable protons (OH and NH) was often confirmed by D_2O addition. The splitting of the signals is reported as s (singlet), d (doublet), dd (doublet of doublets), ddd (doublet of doublets of doublets), t (triplet), m (multiplet) and wm (wide multiplet). ^{13}C–NMR chemical shifts are reported downfield from tetramethylsilane (TMS, internal standard), and the jmod method was employed (J–modulated spin–echo for X–nuclei coupled to H–1 to determine the number of attached protons). For Project #2, 2D–NOESY spectra were acquired, to characterize the three geometric isomers **2**–**4**. For the E/Z–isomers characterization for Project #1, ^{1}H–NMR spectra were acquired on an Agilent INOVA–500 spectrometer with an operative Larmor frequency of 500.3 MHz, by using a 6.1 µs pulse (90°), 1 s delay time, 1.5 s acquisition time, 8 transients and a spectral width of 9 kHz. [1]H–[1]H correlation TOCSY experiments were recorded over the same spectral window using 2048 complex points and sampling each of the 256 increments with 8 scans and by applying 80 ms spin–lock with the MLEV–17 mixing scheme. The same acquisition parameters were applied for the acquisition of the NOESY experiments with a 200 ms mixing time. In addition, a series of selective DPFGSE (Double Pulse Field Gradient Spin–Echo) one–dimensional NOESY [246] was performed with the same parameters as for standard ^{1}H acquisition with 128 transients and either 250, 500 and 750 ms mixing time. Resonance assignments were obtained based on relative intensity, chemical shift and fine structure, together with results from TOCSY and NOESY 2D spectra as well as the database at www.nmrdb.org. [247]

As for the ESI–MS characterization, the compounds were dissolved in CH_3CN for HPLC (concentration of 1.0–2.0 ppm). Mass spectra (full mass) were obtained on a Q Exactive Plus

Hybrid Quadrupole–Orbitrap mass spectrometer (Thermo Fisher Scientific), in both positive– and negative–ion modes. The solutions were infused into the ESI chamber at a 5.00 µL/min flow rate. The spectra were recorded in the *m/z* range 150–800 at a resolution of 140 000 and accumulated for at least 2 min to increase the signal–to–noise ratio. Positive–ion spectra were acquired as follows: spray voltage of 2300 V, capillary temperature of 250 °C, sheath gas 10 (arbitrary units), auxiliary gas 3 (arbitrary units), sweep gas 0 (arbitrary units) and probe heater temperature of 50 °C. On the other hand, for negative−ion acquisitions, different parameters were imposed: spray voltage of −1900 V, capillary temperature of 250 °C, sheath gas 20 (arbitrary units), auxiliary gas 5 (arbitrary units), sweep gas 0 (arbitrary units), probe heater temperature of 50 °C. Post–processing of ESI–MS spectra was performed through the Thermo Xcalibur 3.0.63 software (Thermo Fisher Scientific), and the Xtract tool (integrated into the software) was used to extract the average deconvoluted monoisotopic masses.

9.1.3. Physicochemical, pharmacokinetic and drug–likeness predictions

SwissADME (http://www.swissadme.ch) predictions were performed for each final compound. [248] The prediction does not discriminate between *E*– and *Z*–isomer. Starting from the physicochemical properties, they include molecular characteristics, such as the Topological Polar Surface Area (TPSA). Lipophilicity is reported as Log $P_{o/w}$, calculated through different logarithms (iLOGP, XLOGP3, WLOGP, MLOGP, SILICOS–IT), contributing to the average value of consensus Log $P_{o/w}$. [249] The solubility and the Log S of each derivative are also determined through several methods. Pharmacokinetic predictions of the GI (gastrointestinal), BBB (blood–brain barrier) and skin absorption, but also the affinity (substrate or inhibitor) for some important proteins (*e.g.* P–gp) and metabolic enzymes are predicted. Drug–likeness is was forecast *e.g.* through Lipinski 'rule of five', [250] or the bioavailability score. Other algorithms predicted drug–likeness characteristics through Ghose, Veber, Egan and Muegge filters. Final considerations are the synthetic accessibility and the lead–likeness. SwissADME prediction characteristics are explained for both Projects #1 and #2.

9.1.4. Characterization of compounds

N-(3,4-difluorophenyl)acetamide (2)

Acetic anhydride (1 ml) was added dropwise to 3,4–difluoroaniline (**1**) (1 g, 0.8 ml, 7.8 mmol,) at 0 °C (10 min). The white precipitate was filtered off, washed to neutral pH, then dried over Na_2SO_4. $C_8H_7F_2NO$, MW: 171.14; 80% yield (1.1 g, 6.4 mmol), m.p. 107.3–109.4 °C; R_f 0.10.

^1H–NMR (DMSO–d_6): δ 10.16 (1H, s, NH), 7.77 (1H, ddd, $^1J_{H-F}$= 13.2 Hz, $^2J_{meta}$= 7.6 Hz, $^3J_{meta}$= 2.4 Hz, H–2), 7.36 (1H, dd, $^1J_{H-F}$= 19.3 Hz, $^2J_{meta}$= 9.2 Hz, H–5), 7.25 (1H, wm, H–6), 2.04 (3H, s, CH_3). ^{13}C–NMR (DMSO–d_6): δ 168.51 (C=O), 148.84 (C, dd, $^1J_{C-F}$= 242 Hz, $^2J_{C-F}$= 13 Hz, C–F), 144.99 (C, dd, $^1J_{C-F}$= 240 Hz, $^2J_{C-F}$= 13 Hz, C–F), 136.31 (C–N), 117.32 (CH), 115.11 (C, d, J_{C-F}= 8 Hz, CH–CF), 107.85 (C, d, J_{C-F}= 22 Hz, CH–CF), 23.86 (CH_3).

ESI–MS: *m/z* [M + H]$^+$ calcd for $C_8H_7F_2NO$ 172.05685, found 172.05676.

N-(4,5-difluoro-2-nitrophenyl)acetamide (3)

Intermediate **2** (1 g, 6.0 mmol) was dissolved in concentrated H_2SO_4 ($H_2SO_{4\ conc}$) at 0 °C. A solution of KNO_3 (1.22 g, 12.0 mmol) in $H_2SO_{4\ conc}$ (3.26 ml) was added dropwise. The solution was heated up to r.t. and stirred for 2 h. Next, the reaction was quenched with ice. The resulting precipitate was filtered off and washed with water to neutral pH. Pale–yellow solid; $C_8H_6F_2N_2O_3$, MW: 216.14; 79% yield (1 g, 4.6 mmol); m.p. 101.4–102.5 °C; R_f 0.60.

^1H–NMR (DMSO–d_6): δ 10.33 (1H, s, NH), 8.22 (1H, t, $^1J_{H-F}$= 8.8 Hz, H–5), 7.83 (1H, dd, $^1J_{H-F}$= 11.2 Hz, $^2J_{H-F}$= 7.6 Hz, H–2), 2.09 (3H, s, CH_3).

^{13}C–NMR (DMSO–d_6): δ 168.82 (C=O), 151.90 (C, dd, $^1J_{C-F}$= 253 Hz, $^2J_{C-F}$= 13 Hz, C–F), 145.04 (C, dd, $^1J_{C-F}$= 246 Hz, $^2J_{C-F}$= 14 Hz, C–F), 137.45 (C–N), 129.55 (CH), 114.89 (C, d, J_{C-F}= 10 Hz, CH–CF), 113.43 (C, d, J_{C-F}= 22 Hz, CH–CF), 23.39 (CH_3).

ESI–MS: *m/z* [M + H]$^+$ calcd for $C_8H_6F_2N_2O_3$ 217.10478, found 217.04193.

4,5-difluoro-2-nitroaniline (4)

Intermediate **3** (1 g, 4.6 mmol) was dissolved in 10 ml $H_2SO_{4\ conc}$ under reflux for 2 h. Next, the reaction was quenched with ice. The resulting precipitate was then filtered off and washed with water to neutral pH. Yellow solid; $C_6H_4F_2N_2O_2$, MW: 174.11; 61% yield (1.0 g, 5.7 mmol); m.p. 95.6–105.5 °C; R_f 0.53.

^{1}H–NMR (DMSO–d_6): δ 7.99 (1H, dd, $^1J_{H-F}$= 11.0 Hz, $^2J_{H-F}$= 8.4 Hz, H–5), 7.56 (2H, s, NH$_2$), 6.96 (1H, dd, $^1J_{H-F}$= 12.8 Hz, $^2J_{H-F}$= 7.2 Hz, H–2).

^{13}C–NMR (DMSO–d_6): δ 154.67 (C, dd, $^1J_{C-F}$= 126 Hz, $^2J_{C-F}$= 15 Hz, C–F), 144.63 (C, d, J_{C-F}= 12 Hz, C), 139.89 (C–F), 125.06 (C–NH$_2$), 110.93 (CH–CF), 105.41 (C, d, J_{C-F}= 21 Hz, CH–CF).

ESI–MS: m/z [M + H]$^+$ calcd for $C_6H_4F_2N_2O_2$ 175.03136, found 174.95352.

*4,5-difluorobenzene-1,2-diamine (**5**)*

Compound **4** (2 g, 11.5 mol) was dissolved in ethanol (200 ml). Pd/C (0.20 g, 10 % *w/w*) was added. The hydrogenation was performed with the shaking hydrogenation reactor (open tank, 1.5 h). The Pd/C was filtered off and the solution was concentrated *in vacuo* to yield a brown oil, which was purified *via* flash chromatography with DE. Brown solid; $C_6H_6F_2N_2$, MW: 144.12; 98% yield (1.62 g, 11.2 mmol); m.p. 111.6–117.2 °C; R$_f$ 0.10.

^{1}H–NMR (DMSO–d_6): δ 7.04 (2H, t, $^1J_{H-F}$= 10.4 Hz, H–2,5), 5.33 (4H, s, 2NH$_2$).

^{13}C–NMR (DMSO–d_6): δ 141.14 (2C, dd, $^1J_{C-F}$= 231 Hz, $^2J_{C-F}$= 15Hz, C–F), 131.46 (2C–NH$_2$), 102.34–101.71 (2C, m, CH–F).

ESI–MS: m/z [M + H]$^+$ calcd for $C_6H_6F_2N_2$ 145.05718, found 145.05730.

*5,6-difluoro-1H-benzo[d][1,2,3]triazole (**6**)*

Compound **5** (1.65 g, 11.0 mmol) was dissolved in HCl 2N (114 ml) at 0 °C. A solution of NaNO$_2$ (1.63 g, 0.3 mol) was added dropwise. The solution was heated up to r.t., then extracted with DE. Yellow solid; $C_6H_3F_2N_3$, MW: 155.11; 43% yield (0.8 g, 5.0 mmol); m.p. 179–181 °C; R$_f$ 0.16. Spectra correspondent to lit. [251]

ESI–MS: m/z [M – H]$^-$ calcd for $C_6H_4F_2N_4$ 154.02113, found 154.02127.

*Synthesis and characterization of the intermediates 2-(5,6-difluoro-2H-benzo[d][1,2,3]triazol-2-yl)acetonitrile (**7a**) and 2-(5,6-difluoro-1H-benzo[d][1,2,3]triazol-1-yl)acetonitrile (**7b**)*

Compound (**6**) (2.4 g, 15.3 mmol), KOH (0.95 g, 16.9 mmol) and chloroacetonitrile (0.9 ml, 1.0 g, 13.8 mmol) were dissolved in CH$_3$CN (20 ml), at 80 °C overnight. The solution was concentrated *in vacuo* and purified *via* flash chromatography (PS/EA 8/2). These reaction conditions led to selective formation of the N–1'–isomer compared to the N–2'–isomer (ratio 3:1).
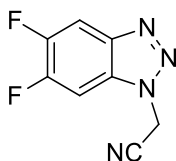
Intermediate **7a**:
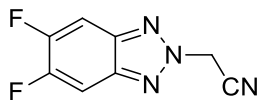
Orange solid; $C_8H_4F_2N_4$, MW: 194.14; 9% yield (0.26 g, 1.3 mmol); m.p. 97.3–99.1 °C; R_f 0.20.

^{1}H–NMR (DMSO–d_6): δ 8.17 (2H, t, $^1J_{H–F}$= 8.8 Hz, H–4,7), 6.28 (2H, s, CH_2).

^{13}C–NMR (DMSO–d_6): δ 150.85 (2C, d, $^1J_{C–F}$= 249.2 Hz, $^2J_{C–F}$= 19.3 Hz, C–F), 140.13 (2C, t, $^1J_{C–F}$= 6.0 Hz, C=N), 114.12 (C≡N), 104.30 (2C, m, CH–CF), 44.0 (CH_2).

ESI–MS: m/z [M – H]$^-$ calcd for $C_8H_4F_2N_4$ 193.03203, found 193.03246.

Intermediate **7b**:

Yellow solid; $C_8H_4F_2N_4$, MW: 194.14; 33% yield (0.98 g, 5.0 mmol); m.p. 129.2–131.3 °C; R_f 0.18 (PS/EA 7/3).

^{1}H–NMR (DMSO–d_6): δ 8.29 (1H, dd, $^1J_{H–F}$= 10.0 Hz, $^2J_{H–F}$= 7.2 Hz, H–4), 8.21 (1H, dd, $^1J_{H–F}$= 9.6 Hz, $^2J_{H–F}$= 6.8 Hz, H–7), 6.14 (2H, s, CH_2).

^{13}C–NMR (DMSO–d_6): δ 150.87 (1C, dd, $^1J_{C–F}$= 240.6 Hz, $^2J_{C–F}$= 16.8 Hz, C–F), 148.41 (1C, dd, $^1J_{C–F}$= 233.5 Hz, $^2J_{C–F}$= 22.0 Hz, C–F), 140.32 (1C, d, $^1J_{C–F}$= 11.0 Hz, C=N), 128.79 (1C, d, $^1J_{C–F}$= 12.0 Hz, C=N), 114.76 (C≡N), 106.65 (1C, dd, $^1J_{C–F}$= 20.4 Hz, CH), 98.53 (1C, d, $^1J_{C–F}$= 25.0 Hz, CH), 36.01 (CH_2).

ESI–MS m/z [M – H]$^-$ calcd for $C_6H_4F_2N_4$ 193.03203, found 193.03242.

General procedure for final derivatives 9a–j, 10e, 11a,b and 13d,j.

Compounds **9a–j** and **10e** were obtained from **7b** and **8a–j** (ratio 1:1), derivatives **11a,b** from **7a** and **8a,b** (ratio 1:1) and **13d,j** from **12a** and **8d,j** (ratio 1:1). Triethylamine (TEA, ratio 1:1.2) was used as a base for products **9a–c,e–j**, **10e** and **11a,b**, in toluene as a solvent at 110 °C. DIMCARB (ratio 1:1.2) was used as a catalyst for products **9d** and **13d**, in acetonitrile at 60 °C. Piperidine was used as a base for product **13j**, in acetonitrile at 60 °C. Some of the

final compounds were (1) filtered off and crystallized from EtOH, (2) some were worked–up through flash chromatography.

*(E)-2-(5,6-difluoro-1H-benzo[d][1,2,3]triazol-1-yl)-3-(p-tolyl)acrylonitrile (**9a**)*
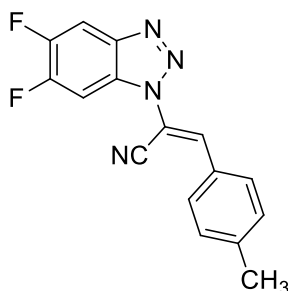
Work–up procedure (2): PS/EA 9.5/0.5. White solid; $C_{16}H_{10}F_2N_4$, MW: 296,28; 45% yield (0.24 g, 0.8 mmol); m.p. 121.4–122.5 °C; R_f 0.72.

^{1}H–NMR (DMSO–d_6): δ 8.50 (1H, dd, $^1J_{H–F}$= 10.0 Hz, $^2J_{H–F}$= 7.2 Hz, H–4'), 8.38 (1H, dd, $^1J_{H–F}$= 9.8 Hz, $^2J_{H–F}$= 7.2 Hz, H–7'), 8.28 (1H, s, =CH), 7.98 (2H, d, $^1J_{H–H}$= 8.0 Hz, H–2",6"), 7.51 (2H, d, $^1J_{H–H}$= 8.4 Hz, H–3",5"), 2.48 (3H, s, CH$_3$).

^{13}C–NMR (DMSO–d_6): δ 151.34 (1C, dd, $^1J_{H–F}$= 241.2 Hz, $^2J_{H–F}$= 16.6 Hz, C–F), 148.63 (1C, dd, $^1J_{H–F}$= 244.5 Hz, $^2J_{H–F}$= 16.2 Hz, C–F), 142.61 (C–CH$_3$), 142.43 (=CH), 140.6 (1C, d, $J_{H–F}$= 10.4 Hz, C=N), 129.80 (4C, m, CH), 128.08 (1C, d, $J_{H–F}$= 12.0 Hz, C=N), 127.68 (C), 114.15 (C≡N), 107.04 (1C, d, $^1J_{C–F}$= 20.8 Hz, CH–CF), 104.71 (C=CH), 99.65 (1C, d, $^1J_{C–F}$= 24.6 Hz, CH–CF), 21.15 (CH$_3$).

ESI–MS: *m/z* [M + H]$^+$ calcd for $C_{16}H_{10}F_2N_4$ 297.09463, 298.09798, found 297.09467, 298.09808.

*(E)-2-(5,6-difluoro-1H-benzo[d][1,2,3]triazol-1-yl)-3-(4-methoxyphenyl)acrylonitrile (**9b**)*
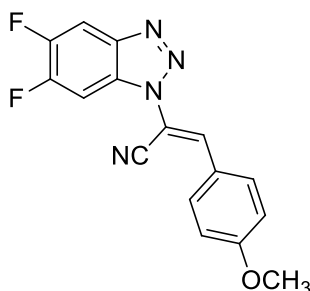
Work–up procedure (1). Brown solid; $C_{16}H_{10}F_2N_4O$, MW: 312,28; 37% yield (0.18 g; 0.6 mmol); m.p. 102.8–103.4 °C; R_f 0.48.

^{1}H–NMR (DMSO–d_6): δ 8.43 (1H, dd, $^1J_{H-F}$= 9.8 Hz, $^2J_{H-F}$= 7.2 Hz, H–4'), 8.29 (1H, dd, $^1J_{H-F}$= 9.4 Hz, $^2J_{H-F}$= 7.2 Hz, H–7'), 8.18 (1H, s, =CH), 8.02 (2H, d, J_{H-H}= 8.8 Hz, H–2",6"), 7.21 (2H, d, J_{H-H}= 8.8 Hz, H–3",5"), 3.89 (3H, s, OCH$_3$).

^{13}C–NMR (DMSO–d_6): δ 162.42 (C–OCH$_3$), 151.30 (1C, dd, $^1J_{H-F}$= 250.0 Hz, $^2J_{H-F}$= 16.7 Hz, C–F), 148.62 (1C, dd, $^1J_{H-F}$= 244.0 Hz, $^2J_{H-F}$= 16.3 Hz, C–F), 142.79 (=CH), 140.52 (1C, d, J_{H-F}= 10.4 Hz, C=N), 131.97 (2CH), 128.20 (1C, d, J_{H-F}= 12.3 Hz, C=N), 122.71 (C), 114.85 (2CH), 114.57 (C≡N), 106.99 (1C, d, $^1J_{C-F}$= 20.9 Hz, CH–CF), 102.57 (C=CH), 99.52 (1C, d, $^1J_{C-F}$= 24.6 Hz, CH–CF), 55.58 (CH$_3$).

ESI–MS: m/z [M + H]$^+$ calcd for $C_{16}H_{10}F_2N_4O$ 313.08954, 314.09290, found 313.08945, 314.09280.

(E)-2-(5,6-difluoro-1H-benzo[d][1,2,3]triazol-1-yl)-3-(2,3,4-trimethoxyphenyl)acrylonitrile (9c)
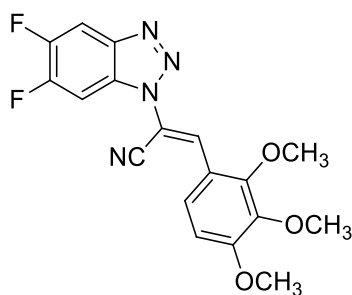
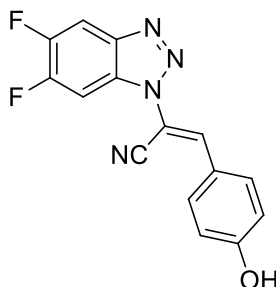Work–up procedure (2): PS/EA 9/1. Yellow solid; $C_{18}H_{14}F_2N_4O_3$, MW: 344,32; 21% yield (0.1 g, 0.3 mmol); m.p. 119.3–120.6 °C; R_f 0.43.

^{1}H–NMR (DMSO–d_6): δ 8.44 (1H, dd, $^1J_{H-F}$= 9.6 Hz, $^2J_{H-F}$= 7.2 Hz, H–4'), 8.21 (1H, dd, $^1J_{H-F}$= 9.6 Hz, $^2J_{H-F}$= 6.8 Hz, H–7'), 8.11 (1H, s, C=CH), 7.94 (1H, d, J_{H-H}= 8.8 Hz, H–6"), 7.13 (1H, d, J_{H-H}= 8.8 Hz, H–5"), 3.94 (3H, s, OCH$_3$), 3.90 (3H, s, OCH$_3$), 3.81 (3H, s, OCH$_3$).

^{13}C–NMR (DMSO–d_6): δ 156.99 (C–OCH$_3$), 153.14 (2C–OCH$_3$), 141.52 (C), 140.32 (CF), 138.04 (CH), 128.44 (CF), 123.56 (CH), 116.76 (2C), 114.30 (C≡N), 108.47 (CH), 107.06 (1C, d, $^1J_{C-F}$= 21.6 Hz, CH–CF), 104.09 (C=CH), 99.20 (1C, d, $^1J_{C-F}$= 24.7 Hz, CH–CF), 61.82 (OCH$_3$), 60.43 (OCH$_3$), 56.19 (OCH$_3$).

ESI–MS: m/z [M + H]$^+$ calcd for $C_{18}H_{14}F_2N_4O_3$ 373.11067, 374.11403, found 373.11124, 374.11432; m/z [M + Na]$^+$ calcd 395.092962, 396.09597, found 395.09296, 396.09625; m/z [M + K]$^+$ calcd 411.06656, found 411.06683.

(E)-2-(5,6-difluoro-1H-benzo[d][1,2,3]triazol-1-yl)-3-(4-hydroxyphenyl)acrylonitrile (9d)

Work–up procedure (1). Yellow solid; $C_{15}H_8F_2N_5O$, MW: 298.25; 29% yield (0.12 g, 0.40 mmol); m.p. 178.4–180,6 °C; R_f 0.18.

^{1}H–NMR (DMSO–d_6): δ 10.59 (1H, s, OH), 8.41 (1H, dd, $^1J_{H–F}$= 9.6 Hz, $^2J_{H–F}$= 7.2 Hz, H–4'), 8.25 (1H, dd, $^1J_{H–F}$= 9.0 Hz, $^2J_{H–F}$= 6.8 Hz, H–7'), 8.09 (1H, s, =CH), 7.92 (2H, d, $J_{H–H}$= 8.0 Hz, H–2'',6''), 7.0 (2H, d, $J_{H–H}$= 8.0 Hz, H–3'',5'').

^{13}C–NMR (DMSO–d_6): δ 161.54 (C–OH), 151.28 (1C, dd, $^1J_{H–F}$= 249.0 Hz, $^2J_{H–F}$= 17.0 Hz, C–F), 148.59 (1C, dd, $^1J_{H–F}$= 244.5 Hz, $^2J_{H–F}$= 17.0 Hz, C–F), 143.62 (CH=C), 140.46 (1C, d, $J_{H–F}$= 10.0 Hz, C=N), 132.31 (2CH), 128.30 (1C, d, $J_{H–F}$= 12.0 Hz, C=N), 121.11 (C), 116.23 (2CH), 114.81 (C≡N), 106.94 (1C, d, $^1J_{C–F}$= 21.0 Hz, CH–CF), 101.17 (C=C), 99.39 (1C, d, $^1J_{C–F}$= 25.0 Hz, CH–CF).

ESI–MS: m/z [M − H]$^-$ calcd for $C_{15}H_8F_2N_5O$ 297.05824, 298.06160, 299.06495, found 297.05939, 298.06268, 299.06622.

*(E)-2-(5,6-difluoro-1H-benzo[d][1,2,3]triazol-1-yl)-3-(4-nitrophenyl)acrylonitrile (9e)*
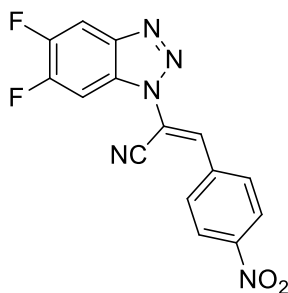
Work–up procedure (2): PS/EA 8/2. Yellow powder; $C_{15}H_7F_2N_5O_2$, MW: 327.25; 24% yield (0.11 g, 0.3 mmol); m.p. 151.1–152.6 °C; R_f 0.46.

^{1}H–NMR (DMSO–d_6): δ 8.51–8.42 (2H, m, H–4',7'), 8.48 (2H, d, $J_{H–H}$= 8.8 Hz, H–3",5"), 8.43 (1H, s, =CH), 8.23 (2H, d, $J_{H–H}$= 8.4 Hz, H–2",6").

^{13}C–NMR (DMSO–d_6): δ 151.47 (1C, dd, $^1J_{H–F}$= 249.5 Hz, $^2J_{H–F}$= 17.0 Hz, C–F), 148.70 (1C, dd, $^1J_{H–F}$= 245.0 Hz, $^2J_{H–F}$= 16.0 Hz, C–F), 148.48 (C–NO$_2$), 140.84 (1C, d, $J_{H–F}$= 10.0 Hz, C=N), 137.61 (=CH), 137.03 (C), 130.79 (2CH), 127.71 (1C, d, $J_{H–F}$= 12.0 Hz, C=N), 124.13 (2CH), 113.15 (C≡N), 109.56 (<u>C</u>=CH), 107.23 (1C, d, $^1J_{C–F}$= 20.0 Hz, <u>C</u>H–CF), 100.17 (1C, d, $^1J_{C–F}$= 24.0 Hz, <u>C</u>H–CF).

ESI–MS m/z [M + H]$^+$ calcd for $C_{15}H_7F_2N_5O_2$ 328.06406, found 328.06406.

*(E)-2-(5,6-difluoro-1H-benzo[d][1,2,3]triazol-1-yl)-3-(4-fluorophenyl)acrylonitrile (**9f**)*
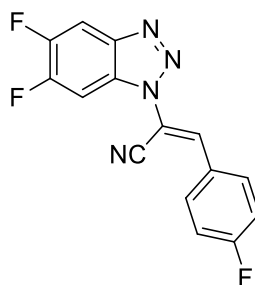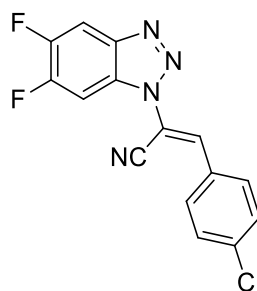

Work–up procedure (1). Light brown solid; $C_{15}H_7F_3N_4$, MW: 300,24; 19% yield (0.06 g, 0.2 mmol); m.p. 135.3–136.4 °C; R_f 0.67.

^{1}H–NMR (DMSO–d_6): δ 8.46 (1H, dd, $^1J_{H–F}$= 9.8 Hz, $^2J_{H–F}$= 7.2 Hz, H–4'), 8.35 (1H, dd, $^1J_{H–F}$= 10.0 Hz, $^2J_{H–F}$= 6.8 Hz, H–7'), 8.28 (1H, s, =CH), 8.10 (2H, dd, $J_{H–H}$= 8.4 Hz e $J_{H–H}$= 5.2 Hz, H–2",6"), 7.51 (2H, t, H–3",5").

^{13}C–NMR (DMSO–d_6): δ 165.11 (C), 162,40 (C), 151.39 (1C, dd, $^1J_{H–F}$= 251.3 Hz, $^2J_{H–F}$= 20.0 Hz, C–F), 148.65 (1C, dd, $^1J_{H–F}$= 245.1 Hz, $^2J_{H–F}$= 16.1 Hz, C–F), 140.80 (=CH), 140.64 (1C, d, $J_{H–F}$= 10.3 Hz, C=N), 132.38 (2C, d, $^1J_{C–F}$= 9.1 Hz, CH–CF), 128.01 (1C, d, $J_{H–F}$= 12.4 Hz, C=N), 127.16 (C), 116.47 (2C, d, $^1J_{C–F}$= 22.1 Hz, CH–CF), 113.88 (C≡N), 107.09 (1C, d, $^1J_{C–F}$= 20.7 Hz, <u>C</u>H–CF), 99.77 (1C, d, $^1J_{C–F}$= 24.9 Hz, <u>C</u>H–CF).

ESI–MS: m/z [M + H]$^+$ calcd for $C_{15}H_7F_3N_4$ 301.06956, 302.07291, found 301.06961, 302.07288.

*(E)-3-(4-chlorophenyl)-2-(5,6-difluoro-1H-benzo[d][1,2,3]triazol-1-yl)acrylonitrile (**9g**)*

Work–up procedure (2): PS/EA 9/1. Light brown solid; $C_{15}H_7ClF_2N_4$, MW: 316.70; 34% yield (0.27 g, 0.9 mmol); m.p. 147.3–149.7 °C; R_f 0.50.

^{1}H–NMR (DMSO–d_6): δ 8.46 (1H, dd, $^1J_{H-F}$= 9.6 Hz, $^2J_{H-F}$= 7.2 Hz, H–4'), 8.36 (1H, dd, $^1J_{H-F}$= 9.6 Hz, $^2J_{H-F}$= 6.8 Hz, H–7'), 8.28 (1H, s, =CH), 8.02 (2H, d, J_{H-H}= 8.8 Hz, H–2",6"), 7.73 (2H, d, J_{H-H}= 8.8 Hz, H–3",5").

^{13}C–NMR (DMSO–d_6): δ 151.39 (1C, dd, $^1J_{H-F}$= 249.0 Hz, $^2J_{H-F}$= 16.0 Hz, C–F), 148.69 (1C, dd, $^1J_{H-F}$= 245.0 Hz, $^2J_{H-F}$= 16.0 Hz, C–F), 140.69 (1C, d, J_{H-F}= 11.0 Hz, C=N), 140.13 (=CH), 136.49 (C), 131.38 (2CH), 129.46 (C–Cl), 129.33 (2CH), 127.91 (1C, d, J_{H-F}= 12.0 Hz, C=N), 113.69 (C≡N), 107.11 (1C, d, $^1J_{C-F}$= 20.0 Hz, <u>C</u>H–CF), 106.63 (<u>C</u>=CH), 99.85 (1C, d, $^1J_{C-F}$= 24.0 Hz, <u>C</u>H–CF).

ESI–MS: *m/z* [M + H]$^+$ calcd for $C_{15}H_7ClF_2N_4$ 317.04001, found 317.04178.

*(E)-3-(4-bromophenyl)-2-(5,6-difluoro-1H-benzo[d][1,2,3]triazol-1-yl)acrylonitrile (**9h**)*
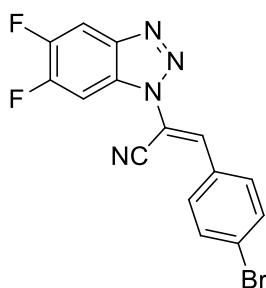
Work–up procedure (2): PS/DE 8/2. White powder; $C_{15}H_7BrF_2N_4$, MW: 361.15; 47% yield (0.35 g, 1.0 mmol); m.p. 150.0–151.6 °C; R_f 0.3.

^{1}H–NMR (DMSO–d_6): δ 8.46 (1H, dd, $^1J_{H-F}$= 9.8 Hz, $^2J_{H-F}$= 7.6 Hz, H–4'), 8.37 (1H, dd, $^1J_{H-F}$= 9.6 Hz, $^2J_{H-F}$= 6.8 Hz, H–7'), 8.26 (1H, s, =CH), 7.95 (2H, d, J_{H-H}= 8.8 Hz, H–2",6"), 7.87 (2H, d, J_{H-H}= 8.4 Hz, H–3",5").

^{13}C–NMR (DMSO–d_6): δ 151.41 (1C, dd, $^1J_{H–F}$= 250.0 Hz, $^2J_{H–F}$= 16.4 Hz, C–F), 148.67 (1C, dd, $^1J_{H–F}$= 245.0 Hz, $^2J_{H–F}$= 16.2 Hz, C–F), 140.69 (1C, d, $J_{H–F}$= 10.2 Hz, C=N), 140.13 (=CH), 132.20 (2CH), 131.43 (2CH), 129.75 (C), 127.85 (1C, d, $J_{H–F}$= 12.4 Hz, C=N), 125.43 (C–Br), 113.59 (C≡N), 107.01 (1C, d, $^1J_{C–F}$= 19.4 Hz, CH–CF), 106.67 (C=C), 99.72 (1C, d, $^1J_{C–F}$= 24.8 Hz, CH–CF).

ESI–MS: m/z [M + H]$^+$ calcd for C$_{15}$H$_7$BrF$_2$N$_4$ 359.98222, 361.98017, found 359.98376, 361.97989.

*(E)-3-(benzo[d][1,3]dioxol-4-yl)-2-(5,6-difluoro-1H-benzo[d][1,2,3]triazol-1-yl)acrylonitrile (9i)*
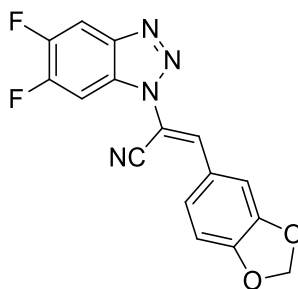
Work–up procedure (1). Yellow solid; C$_6$H$_8$F$_2$N$_4$O$_2$, MW: 326,26; 28% yield (0.13 g, 0.4 mmol); m.p. 164.6–165.2 °C; R$_f$ 0,41.

^{1}H–NMR (DMSO–d_6): δ 8.44 (1H, dd, $^1J_{H–F}$= 9.6 Hz, $^2J_{H–F}$= 7.2 Hz, H–4'), 8.28 (1H, dd, $^1J_{H–F}$= 9.6 Hz, $^2J_{H–F}$= 6.8 Hz, H–7'), 8.15 (1H, s, =CH), 7.62 (1H, d, $J_{H–H}$= 1.6 Hz, H–2"), 7.56 (1H, dd, $J_{H–H}$= 8.4 Hz e J= 1.6 Hz, H–6"), 7.20 (1H, d, $J_{H–H}$= 8.4 Hz, H–5"), 6.21 (2H, s, CH$_2$).

^{13}C–NMR (DMSO–d_6): δ 151.76 (1C, dd, $^1J_{H–F}$= 249.6 Hz, $^2J_{H–F}$= 16.6 Hz, C–F), 151.29 (C–O), 149.10 (1C, dd, $^1J_{H–F}$= 245.0 Hz, $^2J_{H–F}$= 16.2 Hz, C–F), 148.42 (C–O), 146.92 (=CH), 142.92 (CH), 141.06 (1C, d, $J_{H–F}$= 10.4 Hz, C=N), 128.59 (1C, d, $J_{H–F}$= 12.4 Hz, C=N), 127.52 (CH), 124.70 (C), 114.86 (C≡N), 109.49 (CH), 108.44 (CH), 107.46 (2CH, d, $^1J_{C–F}$= 28.0 Hz, CH–CF), 103.68 (C=CH), 102.76 (O–CH$_2$–O), 99.96 (2CH, d, $^1J_{C–F}$= 24.8 Hz, CH–CF).

ESI–MS: m/z [M + H]$^+$ calcd for C$_{16}$H$_8$F$_2$N$_4$O$_2$ 327.06881, 328.07216, found 327.06906, 328.07233.

*(E)-2-(5,6-difluoro-1H-benzo[d][1,2,3]triazol-1-yl)-3-(isoquinolin-5-yl)acrylonitrile (**9j**)*
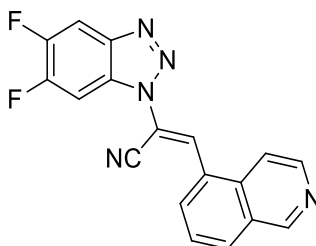
Work–up procedure (1). Light brown solid; $C_{18}H_9F_2N_5$, MW: 333.30; 33% yield (0.2 g, 0.6 mmol); m.p. 109.4–111.5 °C; R_f 0.10.

^{1}H–NMR (DMSO–d_6): δ 9.47 (1H, s, H–1"), 8.91 (1H, s, =CH), 8.64 (1H, d, $J_{H–H}$= 6 Hz, H–3"), 8.49 (1H, d, $J_{H–H}$= 7.2 Hz, H–8"), 8.44 (2H, m, H–4',7'), 8.39 (1H, d, $J_{H–H}$= 8.4 Hz, H–6"), 8.12 (1H, d, $J_{H–H}$= 6.0 Hz, H–4"), 7.93 (1H, t, $J_{H–H}$= 7.8 Hz, H–7").

^{13}C–NMR (DMSO–d_6): δ 153.05 (CH), 151.43 (1C, dd, $^1J_{H–F}$= 249.0 Hz, $^2J_{H–F}$= 16.0 Hz, C–F), 148.68 (1C, dd, $^1J_{H–F}$= 245.0 Hz, $^2J_{H–F}$= 16.0 Hz, C–F), 144.03 (CH), 140.73 (1C, d, $J_{C–F}$= 11.0 Hz, C=N), 138.08 (CH), 133.64 (C=CH), 131.45 (CH), 131.23 (CH), 128.18 (1C, d, $J_{C–F}$= 13.0 Hz, C=N), 128.06 (C), 127.50 (C), 127.17 (=CH), 117.25 (CH), 113.42 (C≡N), 109.82 (C), 107.07 (2CH, d, $^1J_{C–F}$= 21.0 Hz, CH–CF), 100.16 (2CH, d, $^1J_{C–F}$= 25.0 Hz, CH–CF).

ESI–MS: *m/z* [M + H]$^+$ calcd for $C_{18}H_9F_2N_5$ 334.08988, 335.09323, 336.09659, found 334.09045, 335.09366, 336.09689.

*(Z)-2-(5,6-difluoro-1H-benzo[d][1,2,3]triazol-1-yl)-3-(4-nitrophenyl)acrylonitrile (**10e**)*
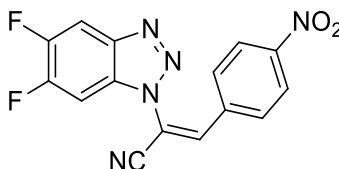
Work–up procedure (1). Red solid; $C_{15}H_7F_2N_5O_2$, MW: 327.25; 26% yield (0.12 g, 0.4 mmol); m.p. 179.3–181.2 °C; R_f 0,68.

^{1}H–NMR (DMSO–d_6): δ 8.53 (1H, dd, $^1J_{H–F}$= 10.0 Hz, $^2J_{H–F}$= 7.2 Hz, H–4'), 8.32 (2H, d, $J_{H–H}$= 8.8 Hz, H–3",5"), 7.74 (1H, dd, $^1J_{H–F}$= 9.6 Hz, $^2J_{H–F}$= 6.8 Hz, H–7'), 7.69 (2H, d, $J_{H–H}$= 8.8 Hz, H–2",6"), 7.27 (1H, s, =CH).

^{13}C–NMR (DMSO–d_6): δ 151.34 (1C, dd, $^1J_{C–F}$= 250.5 Hz, $^2J_{C–F}$= 16.0 Hz, C–F), 149.45 (C–NO$_2$), 148.70 (1C, dd, $^1J_{C–F}$= 227.5 Hz, $^2J_{C–F}$= 16.0 Hz, C–F), 147.63 (C), 140.59 (1C, d, $J_{H–F}$= 10.0 Hz, C=N), 137.20 (C=CH), 129.19 (2CH), 124.18 (1C, d, $J_{H–F}$= 17.0 Hz, C=N), 124.26 (2CH), 114.83 (C≡N), 107.43 (2CH, d, $^1J_{C–F}$= 20.0 Hz, CH–CF), 99.77 (1C, d, $^1J_{C–F}$= 25.0 Hz, CH–CF), 99.64 (=CH).

ESI–MS: m/z [M + H]$^+$ calcd for C$_{18}$H$_9$F$_2$N$_5$ 311.06467, found 311.25558.

*(E)-2-(5,6-difluoro-2H-benzo[d][1,2,3]triazol-2-yl)-3-(p-tolyl)acrylonitrile (11a)*
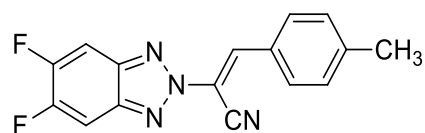
Work–up procedure (1). Yellow solid; C$_{16}$H$_{10}$F$_2$N$_4$, MW: 296,28; 42% yield (0.16 g, 0.5 mmol); m.p. 158.1–160.5 °C; R$_f$ 0,83.

^{1}H–NMR (DMSO–d_6): δ 8.66 (1H, s, =CH), 8.23 (2H, t, $^1J_{H–H}$= 8.8 Hz, H–4',7'), 7.96 (2H, d, $J_{H–H}$= 8.0 Hz, H–2",6"), 7.44 (2H, d, $J_{H–H}$= 8.0 Hz, H–3",5"), 2.42 (3H, s, CH$_3$).

^{13}C–NMR (DMSO–d_6): δ 151.39 (2C, dd, $^1J_{C–F}$= 250.5 Hz, $^2J_{C–F}$= 19.0 Hz, C–F), 142.87 (2C, t, $^1J_{C–F}$= 7.0 Hz, C=N), 138.24 (C=CH), 130.00 (2CH), 129.96 (2CH), 127.27 (C), 113.08 (C≡N), 110.45 (C=CH), 104.33 (2CH, m, CH–CF), 21.23 (CH$_3$).

ESI–MS: m/z [M + H]$^+$ calcd for C$_{16}$H$_{10}$F$_2$N$_4$ 297.09463, found 297.09482.

(E)-2-(5,6-difluoro-2H-benzo[d][1,2,3]triazol-2-yl)-3-(4-methoxyphenyl)acrylonitrile (11b)
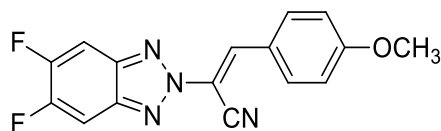
Work–up procedure (1). Brown solid; C$_{16}$H$_{10}$F$_2$N$_4$O, MW: 312,28; 39% yield (0.17 g, mmol); m.p. 148.6–149.3 °C; R$_f$ 0,43.

^{1}H–NMR (DMSO–d_6): δ 8.62 (1H, s, =CH), 8.21 (2H, t, $^1J_{H–H}$= 8.8 Hz, H–4',7'), 8.06 (2H, d, $J_{H–H}$= 8.8 Hz, H–2",6"), 7.18 (2H, d, $J_{H–H}$= 8.8 Hz, H–3",5"), 3.88 (3H, s, OCH$_3$).

^{13}C–NMR (DMSO–d_6): δ 162.52 (C–OCH$_3$), 151.27 (2C, dd, $^1J_{C-F}$= 250.5 Hz, $^2J_{C-F}$= 20.0 Hz, C–F), 140.37 (2C, t, $^1J_{C-F}$= 6.0 Hz, C=N), 138.07 (C=$\underline{C}$H), 132.23 (2CH), 122.32 (C), 114.97 (2CH), 113.43 (C≡N), 108.68 ($\underline{C}$=CH), 104.24 (2CH, m, CH–CF), 55.64 (CH$_3$).

ESI–MS: m/z [M + H]$^+$ calcd for C$_{16}$H$_{10}$F$_2$N$_4$O 313.08954, found 313.08975.

*(E)-2-(1H-benzo[d][1,2,3]triazol-1-yl)-3-(4-hydroxyphenyl)acrylonitrile (**13d**)*
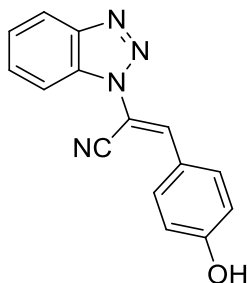
Work–up procedure (2): CHCl$_3$/CH$_3$OH 9.9/0.1. Yellow solid; C$_{15}$H$_{10}$N$_4$O, MW: 262.27; 28% yield (0.2 g, 0.8 mmol); m.p. 115.4–116.5 °C; R$_f$ 0.38.

^{1}H–NMR (DMSO–d_6): δ 8.22 (2H, d, $^1J_{H-H}$= 8.4 Hz, H–4'), 8.12 (1H, s, =CH), 7.98 (1H, d, J_{H-H}= 8.4 Hz, H–7'), 7.93 (2H, d, J_{H-H}= 8.4 Hz, H–2",6"), 7.73 (1H, d, J_{H-H}= 7.8 Hz, H–6'), 7.00 (2H, d, J_{H-H}= 8.4 Hz, H–3",5").

^{13}C–NMR (DMSO–d_6): δ 161.86 (C–OH), 145.71 (C=N), 143.31 (CH), 132.61 (2CH), 132.29 (C=N), 129.63 (CH), 125.68 (CH), 121.75 ($\underline{C}$–CH), 120.35 (CH), 116.73 (2CH), 115.39 (C≡N), 111.30 (CH), 102.06 (C).

ESI–MS: m/z [M – H]$^-$ calcd for C$_{15}$H$_{10}$N$_4$O 263.09274, found 263.53491.

*(E)-2-(1H-benzo[d][1,2,3]triazol-1-yl)-3-(isoquinolin-5-yl)acrylonitrile (**13j**)*
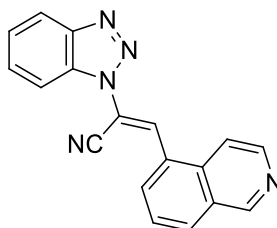
Work–up procedure (1). Brick red–brown powder. C$_{18}$H$_{11}$N$_5$, MW: 297.32; 35% yield (0.23 g, 0.8 mmol); m.p. 131.4 – 133.3 °C; R$_f$ 0.04.

^{1}H–NMR (DMSO–d_6): δ 9.47 (1H, s, H–1"), 8.92 (1H, s, =CH), 8.63 (1H, d, $J_{H–H}$= 5.6 Hz, H–3"), 8.50 (1H, d, $J_{H–H}$= 7.2 Hz, H–4'), 8.39 (1H, d, $J_{H–H}$= 8.0 Hz, H–4"), 8.28 (1H, d, $J_{H–H}$= 8.4 Hz, H–8"), 8.18 (1H, d, $J_{H–H}$= 8.4 Hz, H–7'), 8.14 (1H, d, $J_{H–H}$= 6 Hz, H–6"), 7.93 (1H, t, $J_{H–H}$= 8.0 Hz, H–6'), 7.79 (1H, t, $J_{H–H}$= 8.0 Hz, H–7"), 7.62 (1H, t, $J_{H–H}$= 8.0 Hz, H–5').

^{13}C–NMR (DMSO–d_6): δ 153.05 (CH=N isoq), 145.49 (C=N), 144.06 (CH=N isoq), 137.02 (CH), 133.65 (C=CH), 131.62 (C=N), 131.41 (CH), 131.09 (CH), 129.44 (CH), 128.09 (C), 127.60 (C), 127.20 (CH), 125.53 (CH), 119.99 (=CH), 117.20 (CH), 113.53 (CN), 111.51 (CH), 110.34 (C).

ESI–MS: m/z [M + H]$^+$ calcd for $C_{15}H_{10}N_4O$ 297.10145, 298.10480, found 297.06778, 298.07114.

9.2. Project #2

9.2.1. Chemistry

#### 9.2.1.1. Materials and synthetic methods

All starting materials and the different aldehydes (**I–III**) were commercially purchased. Compound **1** was synthesized as previously reported. [153] The synthetic route for benzotriazole intermediate **1** was reported by us. [153] The three geometric isomers (**2–4**) bearing an acetonitrile chain were fully characterized through NOESY experiments. This reaction was carried out with two different conditions: (A) TEA in DMF, as previously reported, [117] and (B) KOH in CH$_3$CN. Final derivatives **5–7**, **8–10** and **11–13** were obtained through Knoevenagel condensation between different aromatic aldehydes (**I–III**) and the acetonitrile intermediates **2–4**. Knoevenagel reaction conditions: (A) DMA (ratio 1:1.2), CH$_3$CN for compounds **9–10** and **12**; (B) DIMCARB (ratio 1:1.2), CH$_3$CN for **5** and **7**; (C) Cs$_2$CO$_3$ (ratio 1:1.2), toluene for **8**, **11**, **13**. Following work–up was performed in different ways: (A) filtration; (B) crystallization from EtOH; (C) flash chromatography (PS/EA 9/1). General characterization characteristics are reported in Chapter 8.1.

9.2.1.2. Characterization of compounds

General procedure for the synthesis of intermediates 2-(4-fluoro-1H-benzo[d][1,2,3]triazol-1-yl)acetonitrile (2), 2-(4-fluoro-2H-benzo[d][1,2,3]triazol-2-yl)acetonitrile (3) and 2-(7-fluoro-1H-benzo[d][1,2,3]triazol-1-yl)acetonitrile (4):

Method: Compound **1** / ClCH$_2$CN / KOH (1:1:1+10%), CH$_3$CN, reflux, overnight. General work–up: flash chromatography (PS/EA 9/1). C$_8$H$_5$FN$_4$; MW: 176.15.

Intermediate **2**:
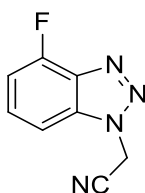
Yellow solid; 7% yield (0.18 g, 1.0 mmol); m.p. 73.4–75.6 °C. R$_f$ 0.19.

^{1}H NMR (DMSO–d_6): δ 7.82 (1H, d, $^1J_{H–H}$= 8.4 Hz, H–7), 7.69 (1H, dt, H–6), 7.34 (1H, dd, $^1J_{H–H}$= 10.8 Hz, $^2J_{H–H}$= 8.0 Hz, H–5), 6.22 (2H, s, CH$_2$).

^{13}C NMR (DMSO–d_6): δ 152.15 (C, d, $^1J_{C–F}$= 254.0 Hz, C–F), 135.26 (C, d, $^1J_{C–F}$= 7.0 Hz, C), 135.03 (C, d, $^1J_{C–F}$= 19.0 Hz, C), 129.74 (C, d, $^1J_{C–F}$= 7.0 Hz, CH), 114.67 (C≡N), 109.41 (C, d, $^1J_{C–F}$= 16.0 Hz, CH), 106.87 (C, d, $^1J_{C–F}$= 5.0 Hz, CH), 35.95 (CH$_2$).

ESI–MS: *m/z* [M + H]$^+$ calcd for C$_8$H$_5$FN$_4$ 177.05710, found 176.82510.

Intermediate **3**:
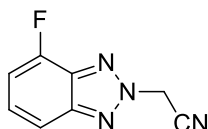
Yellow solid; 18% yield (0.45 g, 2.6 mmol); m.p. 85.2–87.1 °C; R$_f$ 0.58.

^{1}H NMR (DMSO–d_6): δ 7.92 (1H, d, $^1J_{H–H}$= 8.4 Hz, H–7), 7.58 (1H, dt, H–6), 7.42 (1H, dd, $^1J_{H–H}$= 3.0 Hz, $^2J_{H–H}$= 2.0 Hz, H–5), 6.40 (2H, s, CH$_2$).

^{13}C NMR (DMSO–d_6): δ 151.24 (C, d, ^1J= 255.0 Hz, C–F), 146.69 (C, d, $^1J_{C-F}$= 3.0 Hz, C), 135.17 (C, d, $^1J_{C-F}$= 16.0 Hz, C), 127.91 (C, d, $^1J_{C-F}$= 7.0 Hz, CH), 114.56 (C, d, $^1J_{C-F}$= 5.0 Hz, CH), 114.09 (C≡N) 110.83 (C, d, $^1J_{C-F}$= 16.0 Hz, CH), 44.18 (CH$_2$).

ESI–MS: *m/z* [M + H]$^+$ calcd for C$_8$H$_5$FN$_4$ 177.05710, found 177.09134.

Intermediate **4**:
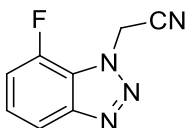
White solid; 11% yield (0.27 g, 1.5 mmol); m.p. 89.1–91.2 °C; R$_f$ 0.38.

^{1}H NMR (DMSO–d_6): δ 7.89 (1H, d, ^1J= 8.4 Hz, H–7), 7.56 (1H, dt, H–6), 7.39 (1H, dd, $^1J_{H-H}$= 3.0 Hz, $^2J_{H-H}$= 2.0 Hz, H–5), 6.38 (2H, s, CH$_2$).

^{13}C NMR (DMSO–d_6): δ 148.54 (C), 146.99 (C, d, C–F), 127.91 (C, d, $^1J_{C-F}$= 6.0 Hz, CH), 122.26 (C, d, $^1J_{C-F}$= 14.0 Hz, C), 115.98 (C, d, $^1J_{C-F}$= 5.0 Hz, CH), 110.83 (CH–CF), 114.83 (C≡N), 113.26 (C, d, $^1J_{C-F}$= 16.0 Hz, CH), 37.44 (CH$_2$).

ESI–MS: *m/z* [M + H]$^+$ calcd for C$_8$H$_5$FN$_4$ 177.05710, 178.06046, found 176.82530, 178.26268.

General synthesis for (E)-2-(4-fluoro-1H-benzo[d][1,2,3]triazol-1-yl)-3-(R)acrylonitrile (5–7), (E)-2-(4-fluoro-2H-benzo[d][1,2,3]triazol-2-yl)-3-(R)acrylonitrile (8–10), (E)-2-(7-fluoro-1H-benzo[d][1,2,3]triazol-1-yl)-3-(R)acrylonitrile derivatives (11–13).

Final derivatives **5–8** were synthesized *via* Knoevenagel condensation of intermediate **2** and the aromatic aldehydes **I–III**. N–2'–derived compounds **9–12** were yielded by reaction of intermediate **3** and **I–III**, while intermediate **4** and the aldehydes **I–III** led to derivatives **13–16**. Reaction conditions: (A) DMA (ratio 1:1.2), CH$_3$CN for **10–11** and **14**; (B) DIMCARB (ratio 1:1.2), CH$_3$CN for **5**, **6**, **7**, **8**, **12** and **16**; (C) Cs$_2$CO$_3$ (ratio 1:1.2), toluene for **9**, **13**, **15**. Work up: (A) filtration; (B) crystallization from EtOH; (C) flash chromatography (PS/EA 9/1).

*(E)-2-(4-fluoro-1H-benzo[d][1,2,3]triazol-1-yl)-3-(4-methoxyphenyl)acrylonitrile (**5**):*
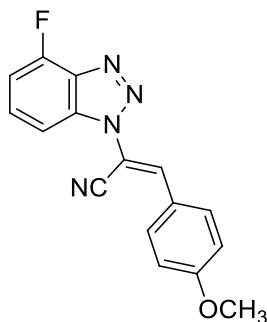
Work–up procedure (B). Yellow solid; $C_{16}H_{11}FN_4O$, MW: 294.28; 52% yield (0.23 g); m.p. 141.2 – 143.4 °C; R_f 0.35.

^{1}H NMR (400 MHz, DMSO–d_6): δ 8.23 (1H, s, =CH), 8.03 (2H, d, $^1J_{H-H}$= 8.8 Hz, H–3",5"), 7.86 (1H, d, $^1J_{H-H}$= 8.4 Hz, H–7'), 7.75 (1H, dt, H–6'), 7.43 (1H, dd, ^1J = 10.4 Hz, ^2J = 8.0 Hz, H–5'), 7.21 (2H, d, $^1J_{H-H}$= 8.4 Hz, H–2",6"), 3.89 (3H, s, OCH$_3$).

^{13}C NMR (DMSO–d_6): δ 162.48 (C), 152.27 (C, d, $^1J_{C-F}$= 255.0 Hz, C–F), 143.01 (=CH), 135.17 (C, d, $^1J_{C-F}$= 19.0 Hz, C), 134.57 (C, d, $^1J_{C-F}$= 6.0 Hz, C), 131.96 (2CH), 132.43 (2CH), 130.95 (C, d, $^1J_{C-F}$= 8.0 Hz, CH), 123.17 (C), 115.31 (2CH), 115.00 (C≡N), 105.42 (C, d, $^1J_{C-F}$= 16.0 Hz, CH), 108.08 (C, d, $^1J_{C-F}$= 5.0 Hz, CH), 102.99 (C), 56.12 (OCH$_3$).

ESI–MS: *m/z* [M + H]$^+$ calcd for $C_{16}H_{11}FN_4O$ 295.09897, 296.10232, found 295.09897, 296.10232.

*(E)-2-(4-fluoro-1H-benzo[d][1,2,3]triazol-1-yl)-3-(p-tolyl)acrylonitrile (**6**):*
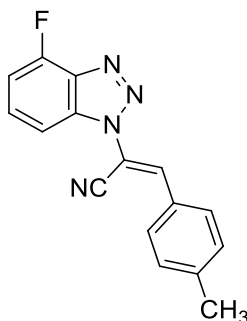
Work–up procedure (C, PS/EA 7/3). Yellow solid; $C_{16}H_{11}FN_4$, MW: 278.10; 50% yield (0.36 g); m.p. 128.1–130.3 °C; R_f 0.27.

^{1}H NMR (DMSO–d_6): δ 8.27 (1H, s, =CH), 7.93 (2H, d, $^1J_{H-H}$= 8.0 Hz, H–3",5"), 7.89 (1H, d, $^1J_{H-H}$= 8.0 Hz, H–7'), 7.75 (1H, dt, H–6'), 7.45 (2H, d, $^1J_{H-H}$= 8.0 Hz, H–2",6"), 7.44 (1H, m, H–5'), 2.43 (3H, s, CH$_3$).

^{13}C NMR (DMSO–d_6): δ 157.22 (C), 152.26 (C, d, $^1J_{C-F}$= 255.0 Hz, C–F), 142.73 (=CH), 135.23 (C, d, $^1J_{C-F}$= 19.0 Hz, C), 134.44 (C, d, $^1J_{C-F}$= 6.0 Hz, C), 130.58 (C, d, $^1J_{C-F}$= 7.0 Hz, CH), 129.90 (2CH), 129.74 (2CH), 127.65 (C), 114.11 (C≡N), 110.04 (C, d, $^1J_{C-F}$= 16.0 Hz, CH), 107.71 (C, d, $^1J_{C-F}$= 5.0 Hz, CH), 104.67 (C), 21.22 (OCH$_3$).

ESI–MS: *m/z* [M + H]$^+$ calcd for C$_{16}$H$_{11}$FN$_4$ 279.10405, 280.10741, found 279.11023, 280.10819.

*(E)-3-(4-bromophenyl)-2-(4-fluoro-1H-benzo[d][1,2,3]triazol-1-yl)acrylonitrile (**7**):*
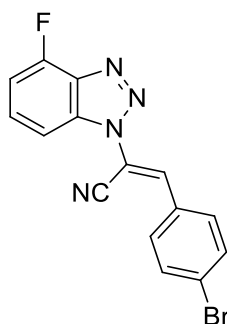

Work–up procedure (B). Yellow solid; C$_{15}$H$_8$BrFN$_4$, MW: 343.15; 35% yield (0.20 g); m.p. 158.6–160.3 °C; R$_f$ 0.55.

^{1}H NMR (DMSO–d_6): δ 8.31 (1H, s, =CH), 7.94 (3H, m, H–3",5",7'), 7.86 (2H, d, $^1J_{H-H}$= 8.8 Hz, H–2",6"), 7.77 (1H, dt, H–6'), 7.45 (1H, dd, ^1J = 10.6 Hz, ^2J = 2.0 Hz, H–5').

^{13}C NMR (DMSO–d_6): δ 152.25 (C, d, $^1J_{C-F}$= 255.0 Hz, C–F), 140.53 (CH), 135.29 (C, d, $^1J_{C-F}$=19.0 Hz, C), 134.24 (C, d, $^1J_{C-F}$= 6.0 Hz, C), 132.33 (2CH), 131.47 (2CH), 130.70 (C, d, $^1J_{C-F}$= 7.0 Hz, CH), 129.76 (C), 125.56 (C), 113.66 (C≡N), 110.18 (C, d, $^1J_{C-F}$= 16.0 Hz, CH), 107.89 (C, d, $^1J_{C-F}$= 4.0 Hz, CH), 106.67 (C).

ESI–MS *m/z* [M + H]$^+$ calcd for C$_{15}$H$_8$BrFN$_4$ 341.99164, 343.98959, found 341.99066, 343.98862.

(E)-2-(4-fluoro-2H-benzo[d][1,2,3]triazol-2-yl)-3-(4-methoxyphenyl)acrylonitrile (8):
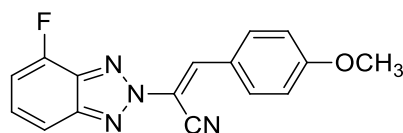
Work–up procedure (C). Yellow powder; $C_{16}H_{11}FN_4O$, MW: 294.28; 42% yield (0.23 g); m.p. 127.2–129.2 °C; R_f 0.69.

^{1}H NMR (DMSO–d_6): δ 8.72 (1H, s, =CH), 8.10 (2H, d, $^1J_{H-H}$= 8.8 Hz, H–2'',6''), 7.89 (1H, d, $^1J_{H-H}$= 8.4 Hz, H–7'), 7.55 (1H, dt, H–6'), 7.40 (1H, dd, ^1J = 11.0 Hz, ^1J = 8.0 Hz, H–5'), 7.20 (2H, d, $^1J_{H-H}$= 8.8 Hz, H–3'',5''), 3.89 (3H, s, OCH$_3$).

^{13}C NMR (DMSO–d_6): δ 162.63 (C), 151.10 (C, d, $^1J_{C-F}$= 256.0 Hz, C–F), 146.62 (C, d, $^1J_{C-F}$= 3.0 Hz, C), 138.84 (CH), 135.29 (C, d, $^1J_{C-F}$= 16.0 Hz, C), 132.37 (2CH), 128.53 (C, d, $^1J_{C-F}$= 6.0 Hz, CH), 122.32 (C), 115.00 (2CH), 114.50 (C, d, $^1J_{C-F}$= 5.0 Hz, CH), 113.48 (C≡N), 111.47 (C, d, $^1J_{C-F}$= 15.0 Hz, CH), 108.70 (C), 55.66 (OCH$_3$).

ESI–MS: *m/z* [M + H]$^+$ calcd for $C_{16}H_{11}FN_4O$ 295.09897, found 295.18033.

(E)-2-(4-fluoro-2H-benzo[d][1,2,3]triazol-2-yl)-3-(p-tolyl)acrylonitrile (9):
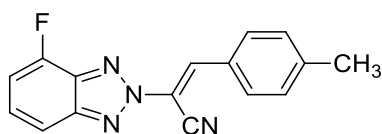
Work–up procedure (A). Yellow solid; $C_{15}H_8F_2N_4$. MW: 282.07; 58% yield (0.28 g); m.p. 135.6–137.2 °C; R_f 0.70. ^{1}H NMR (DMSO–d_6): δ 8.75 (1H, s, =CH), 7.99 (2H, d, $^1J_{H-H}$= 8.4 Hz, H–3'',5''), 7.90 (1H, d, $^1J_{H-H}$= 8.8 Hz, H–7'), 7.57 (1H, dt, H–6'), 7.44 (2H, d, $^1J_{H-H}$= 7.6 Hz, H–2'',6''), 7.41 (1H, m, H–5'), 2.42 (3H, s, CH$_3$).

^{13}C NMR (DMSO–d_6): δ 151.12 (C, d, $^1J_{C-F}$= 256.0 Hz, C–F), 146.66 (C, d, $^1J_{C-F}$= 4.0 Hz, C), 143.01 (C), 139.02 (CH), 135.40 (C, d, $^1J_{C-F}$= 16.0 Hz, C), 130.10 (2CH), 129.97 (2CH), 128.71 (C, d, $^1J_{C-F}$= 6.0 Hz, CH), 127.24 (C), 114.62 (C, d, $^1J_{C-F}$= 5.0 Hz, CH), 113.09 (C≡N), 111.61 (C, d, $^1J_{C-F}$= 16.0 Hz, CH), 110.46 (C), 21.24 (CH$_3$).

ESI–MS: *m/z* [M + H]$^+$ calcd for $C_{15}H_8F_2N_4$ 283.07898, 284.08233, found 283.98938, 284.15451.

*(E)-3-(4-bromophenyl)-2-(4-fluoro-2H-benzo[d][1,2,3]triazol-2-yl)acrylonitrile (**10**):*
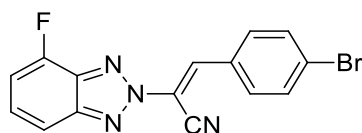
Work–up procedure (A). Light brown solid; $C_{15}H_8BrFN_4$, MW: 343.15; 31% yield (0.18 g); m.p. 137.2–138.1 °C; R_f 0.71.

^{1}H NMR (DMSO–d_6): δ 8.79 (1H, s, =CH), 8.01 (2H, d, $^1J_{H–H}$= 8.4 Hz, H–3",5"), 7.91 (1H, d, $^1J_{H–H}$= 8.8 Hz, H–7'), 7.85 (2H, d, $^1J_{H–H}$= 8.4 Hz, H–2",6"), 7.57 (1H, dt, H–6'), 7.42 (1H, dd, ^1J = 10.8 Hz, ^2J = 7.6 Hz, H–5').

^{13}C NMR (DMSO–d_6): δ 151.12 (C, d, $^1J_{C–F}$= 256.0 Hz, C–F), 146.72 (C, d, $^1J_{C–F}$= 3.0 Hz, C), 137.63 (CH), 135.53 (C, d, $^1J_{C–F}$= 16.0 Hz, C), 132.39 (2CH), 131.77 (2CH), 129.33 (C), 128.93 (C, d, $^1J_{C–F}$= 6.0 Hz, CH), 125.89 (C), 114.68 (C, d, $^1J_{C–F}$= 6.0 Hz, CH), 112.71 (C≡N), 112.0 (C), 111.79 (C, d, $^1J_{C–F}$= 16.0 Hz, CH).

ESI–MS: *m/z* [M + H]$^+$ calcd for $C_{15}H_8BrFN_4$ 344.99687, found 344.99655.

*(E)-2-(7-fluoro-1H-benzo[d][1,2,3]triazol-1-yl)-3-(4-methoxyphenyl)acrylonitrile (**11**):*
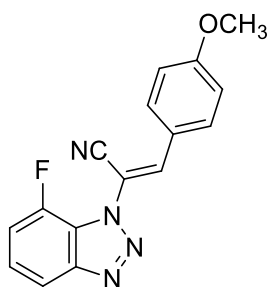
Work–up procedure (C). Yellow powder; $C_{16}H_{11}FN_4O$, MW: 294.28; 60% yield (0.25 g); m.p. 117.4–119.3 °C; R_f 0.35.

^{1}H NMR (DMSO–d_6): δ 8.28 (1H, s, =CH), 8.04 (2H, d, $^1J_{H–H}$= 9.2 Hz, H–3",5"), 7.64 (2H, m, H–5',6'), 7.27 (2H, d, $^1J_{H–H}$= 8.8 Hz, H–2",6"), 3.95 (OCH$_3$).

^{13}C NMR (DMSO–d_6): δ 162.67 (C), 148.16 (C, d, $^1J_{C–F}$= 16.0 Hz, C–F), 145.58 (CH), 131.90 (2CH), 126.11 (C, d, $^1J_{C–F}$= 6.0 Hz, C), 122.39 (C), 122.09 (C, d, $^1J_{C–F}$= 13.0 Hz, C), 116.26 (C, d, $^1J_{C–F}$= 4.0 Hz, CH), 115.10 (2CH), 114.88 (C≡N), 114.33 (C, d, $^1J_{C–F}$= 17.0 Hz, CH), 102.21 (C), 55.67 (OCH$_3$).

ESI–MS: *m/z* [M + H]$^+$ calcd for C$_{16}$H$_{11}$FN$_4$O 295.09897, found 295.09879.

*(E)-2-(7-fluoro-1H-benzo[d][1,2,3]triazol-1-yl)-3-(p-tolyl)acrylonitrile (**12**):*
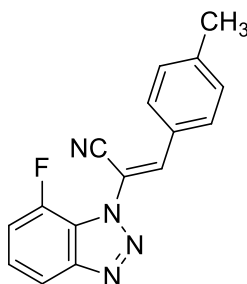
Work–up procedure (A). White powder; C$_{16}$H$_{11}$FN$_4$, MW: 278.10; 38% yield (0.18 g); m.p. 145.3–147.9 °C; R$_f$ 0.50.

^{1}H NMR (DMSO–d_6): δ 8.26 (1H, s, =CH), 8.09 (1H, d, $^1J_{H–H}$= 8.0 Hz, H–7'), 7.89 (2H, d, $^1J_{H–H}$= 8.4 Hz, H–2",6"), 7.60 (2H, m, H–5',6'), 7.46 (2H, d, $^1J_{H–H}$= 8.0 Hz, H–3",5"), 2.43 (3H, s, CH$_3$).

^{13}C NMR (DMSO–d_6): δ 148.13 (C, d, $^1J_{C–F}$= 19.0 Hz, C–F), 145.58 (=CH), 143.18 (C), 130.09 (2CH), 129.86 (C, d, $^1J_{C–F}$= 12.0 Hz, CH), 129.64 (2CH), 27.28 (C), 126.24 (C, d, $^1J_{C–F}$= 6.0 Hz, CH), 122.09 (C, d, $^1J_{C–F}$= 13.0 Hz, C), 116.25 (C, d, $^1J_{C–F}$= 9.0 Hz, CH), 114.43 (C, d, $^1J_{C–F}$= 22.0 Hz, CH), 114.49 (C≡N), 104.25 (C), 21.22 (OCH$_3$).

ESI–MS: *m/z* [M + H]$^+$ calcd for C$_{16}$H$_{11}$FN$_4$ 279.10405, found 279.10379.

*(E)-3-(4-bromophenyl)-2-(7-fluoro-1H-benzo[d][1,2,3]triazol-1-yl)acrylonitrile (**13**):*
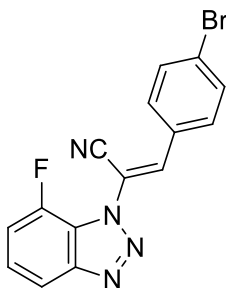
Work–up procedure (C). Beige powder; C$_{15}$H$_8$BrFN$_4$; MW: 343.15; 33% yield: (0.19 g); m.p. 109.1–111.2 °C; R$_f$ 0.45.

^{1}H NMR (DMSO–d_6): δ 8.30 (1H, s, =CH), 8.10 (1H, d, $^1J_{H–H}$= 4.0 Hz, H–7'), 7.91 (2H, d, $^1J_{H–H}$= 8.8 Hz, H–3",5"), 7.87 (2H, d, $^1J_{H–H}$= 7.6 Hz, H–2",6"), 7.56 (2H, m, H–5',6').

^{13}C NMR (DMSO–d_6): δ 148.15 (C, d, $^1J_{C-F}$= 25.0 Hz, C–F), 145.53 (C), 143.77 (=CH), 132.57 (2CH), 131.34 (2CH), 129.36 (C), 126.31 (C, d, $^1J_{C-F}$= 6.0 Hz, CH), 125.98 (C), 121.84 (C, d, $^1J_{C-F}$= 13.0 Hz, C), 116.34 (C, d, $^1J_{C-F}$= 5.0 Hz, CH), 114.60 (C, d, $^1J_{C-F}$= 17.0 Hz, CH), 114.02 (C≡N), 106.08 (C).

ESI–MS: *m/z* [M – H]⁻ calcd for $C_{15}H_8BrFN_4$ 340.98326, 342.98122, found 341.19571, 342.19904.

9.3. Project #3

9.3.1. Molecular Docking

Docking predictions were performed through four docking programs: AutoDock Vina, [197] LeDock (http://lephar.com), [198] rDock [199] and GOLD, [200] selected for their well-known sampling and scoring functions. [196] In Protein Data Bank (rcsb.org), two crystal structures of WaaG protein are reported, [127] *viz.*, one in complex with uridine-5'-diphosphate-2-deoxy-2-fluoro-α-D-glucose (U2F) and one co–crystallized with UDP (PDB IDs 2iw1 and 2iv7, [187] respectively). Docking predictions were conducted on ligands of libraries A, B and C. Crystal structure 2iw1 was selected; U2F structure was removed from the binding pocket, in order to analyze the docking pose of ligands in a free WaaG active site. Additional docking predictions were conducted in the presence of WaaG *apo*–protein in complex with UDP–Glc. UDP–Glc was gained by manipulation of U2F, with Avogadro [252] version 1.1.1, taken from 2iw1 crystal structure. Docking outputs were analyzed with PyMOL 2.3.4 or VMD [253] version 1.9.3. Calculations were performed running Ubuntu 16.04 as operating system on a PC with an Intel® Core™ i7–9705H CPU @ 2.60 GHz with 8 GB RAM, unless otherwise stated.

AutoDock Vina 1.1.2. was the first selected docking program. AutoDockTools (ADT) [132] version 1.5.6 was employed to generate the PDBQT files of the protein structure and all ligands. Different Grid Boxes were utilized for docking (Table 1 of this Paragraph). Docking was performed employing the rigid form of the protein, or by making flexible some amino acids, *viz.*, Arg173, Arg261 and Glu289. These amino acids are known to establish important H–bonds with UDP uridine portion in the active site of WaaG protein. As docking parameters, exhaustiveness value was set to 64 and the number of generated poses to 10 for

each simulation. The binding energy range was imposed as ≤ 2 kcal·mol^{-1}, above that of the best–predicted pose for each simulation.

LeDock was used as the second docking program. Open Babel 2.3.2 [254] was employed to generate the mol2 (Tripos MOL2) files of the ligands, from the original pdb files. Docking pre–processing was performed through LePro, which adds hydrogen atoms to the original protein pdb file in automatic mode, and assigns the coordinates of the protein active site (Table 1 of this Paragraph), generating the input file for LeDock. Ten binding poses were generated from each simulation.

Mol2 format of the protein and sdf (MDL SD) files of the ligands were utilized to carry out rDock simulations. The docking site was prepared with *rbcavity*, employing the "two sphere method"; sphere radius was set to 10 Å. The number of docking poses was set to 10 and the output was obtained in MDL SD format reporting the affinity scores for each generated pose of the ligands.

The academic program GOLD requires pdb files of both protein and ligand structures. WaaG structure was automatically protonated; the co–crystallized structures and water molecules were removed. XYZ coordinates were edited and the active site radius was set to 10 Å. Ligands were docked into the rigid form of the *apo*–protein. To facilitate flexibility at the surface of the binding pocket, ten amino acids were made flexible (Phe13, Asp100, Arg173, Arg208, Lys209, Arg261, Glu281, Ile285, Val286 and Glu289), selected by checking how UDP and UDP–Glc interact with the protein. The chosen fitness function was ChemPLP (Piecewise Linear Potential). The number of generated poses was set to 10. GOLD was instructed to terminate docking of a ligand if it reached a state in which the best ten solutions found so far were all within a 2 Å heavy atom RMSD. Search efficiency (predictive reliability) was set to 100% (around 30.000 GA operations for each simulation). The docking studies were conducted with a Windows 10 Pro operating system on a PC with an Intel® Core™ i7–9700H CPU @ 3.00 GHz with 16 GB RAM.

apo -WaaG			
Docking program	**Active site center** (x,y,z)	**Active site dimension** (x,y,z)	**Flexible aminoacids**
AutoDock Vina	-5.694/10.389/-17.222	22-22-22 points	
	-5.639/10.528/-19.833	24-26-26 points	
	-5.694/10.389/-17.222	22-22-22 points	Arg173-Arg261-Glu289
LeDock	-5.694/10.389/-17.222	22-22-22 points	
rDock	-5.694/10.389/-17.222	10.0 radius	
GOLD	-5.694/10.389/-17.222	16 Å	
	-5.694/10.389/-17.222	16 Å	Phe13-Asp100-Arg173-Arg208-Lys209-Arg261-Glu281-Ile285-Val286-Glu289

WaaG+UDPGlc			
Docking program	**Active site center** (x,y,z)	**Active site dimension** (x,y,z)	**Flexible aminoacids**
AutoDock Vina	-3.000/22.306/-17.222	18-22-22 points	
LeDock	-2.083/24.750/-16.583	18-22-22 points	
rDock	-3.000/22.306/-17.222	10 Å radius	
GOLD	-3.000/22.306/-17.222	18 Å radius	

Table 1. Parameters for dockings of ligands to WaaG (Libraries A/B/C).

9.3.2. Molecular Dynamics

The best–docked poses of the ligands (*vide infra*) were selected for molecular dynamics (MD) simulations. MD simulations were performed with NAMD [255] version 2.12. VMD *psfgen* tool generated the files for both protein and ligands. The CHARMM36 force field [57–59] was employed and several sections of CHARMM–GUI website were used: *PDB R&M* (Reader and Modeler) [256,257] for WaaG structure, *Ligand R&M* [258] for ligands of libraries A and B, *Glycan R&M* [259–261] for oligosaccharides of library C. Ligands and ligand–protein complexes were solvated in a 50 Å water box, employing a TIP3P water model [262] and adding NaCl ions (0.2 M).

An initial potential energy minimization (1000 steps) was performed on solvent molecules and ions of the systems utilizing conjugate gradient, imposing a harmonic restraining potential to ligands and complexes of 500 kcal·mol^{-1}·Å^{-2}. Then, a minimization of 100 ps was conducted on solvated ligands and complexes without any restraint. A 6 ps heating step from 1 to 310 K was applied gradually to each system, then equilibrated during 600 ps. 10 ns production simulations were performed with a time–step of 2, 1, or 0.1 fs in NPT (isothermal–isobaric) ensemble with a Langevin damping coefficient, set to 1 ps^{-1}. The

temperature was kept constant at 310 K with a stochastic Langevin thermostat (1 ps^{-1} as damping coefficient), whilst the pressure was kept stable at 1 atm (oscillating time = 100 fs; damping time constant = 50 fs). Coordinates were recorded every 1 fs. The rigidity of the water hydrogens was assured by the ShakeH algorithm and the PME (Particle Mesh Ewald) method was used for the calculation of non–bonded interactions, with grid spacing = 1 Å. Electrostatic and van der Waals interactions were forced to 0 at the cutoff distance of 12 Å (switching function from 10 Å). As for ligand **B33**, a 1.64 Å constraint was set between the chlorine atom and the lone pair (LP, as generated by CHARMM *Ligand Reader & Modeler*). MD simulations were carried out at the National Supercomputer Centre – NSC (part of Linköping University and the Swedish National Infrastructure for Computing – SNIC). Computations were performed on the Tetralith cluster using Slurm to submit jobs and ThinLinc (Cendio AB, Linköping, Sweden) as a remote desktop.

9.3.3. Binding free energy (BFE) calculations

CaFE (Calculation of Free Energy) 1.0 [263] was used for the BFE simulations, post–processing the PSF (coordinate) and DCD (trajectory) files generated by NAMD. CaFE is implemented as a plugin consisting of several Tcl scripts. These scripts are submitted to the Tk scripting console of the VMD package, which, in turn, utilizes NAMD as a back–end program for molecular mechanical calculations. CaFE predicts binding affinity with an end–point method, *viz.*, LIE (Linear Interaction Energy), [202,203] which is described as an approximation of the linear response. [202] PSF and DCD (of the entire 10–ns MD trajectory) files of both solvated ligands and protein–ligand complexes are required. CaFE generates for both settings a difference in electrostatic (polar term) and van der Waals (vdW) interactions (nonpolar term) between the ligand and the enclosing background; then, the sum of these individual energy components leads to the total BFE, [263] reported as ΔG_{calc} in kcal·mol^{-1}. The dissociation constant K_D can be calculated from the following relationship:

$$\Delta G = RT\ln(K_D/c^*)$$

R is the ideal gas constant with a numerical value of $1.987 \cdot 10^{-3}$ kcal·K^{-1}·mol^{-1}, T is the absolute temperature with a value of 310 K and c^* is a standard reference concentration defined as 1 M. [264] MD trajectories were analyzed every 5 frames, with a stride value of 5. LIE predefined coefficients α, β and γ are default values, 0.18, 0.33 and 0, respectively.

9.3.4. Root–mean–square deviation (RMSD) analysis

The root–mean–square–deviations (RMSDs) throughout the MD simulation were calculated during the 10–ns production with the *RMSD Trajectory Tool* of VMD. For each simulation, the reference structure is the first frame of the MD simulation. The RMSD analysis starts with an alignment concerning the rigid–body structure. Protein flexibility during MD simulation was calculated on VMD. The stride value was set to 1 therefore each frame of the calculation was taken for the RMSD analysis. A .dat file is generated with a list of RMSD values recorded at different frames. Averaged RMSDs (avRMSDs) were calculated, as well as the RMSD standard deviation (SD) values for each RMSD distribution. RMSD analysis was performed with MATLAB® version 7.11.0.584 (R2020b), utilizing in–house–built scripts.

9.3.5. MD post–processing: protein–ligand interactions and protein behavior

After an alignment of WaaG backbone, the electrostatic and vdW contributions to the protein–ligand binding were calculated through an in–house Tcl script submitted in the VMD Tk Console, employing NAMD Energy 1.4 as a processing program. As concerns the H–bonds identification, the DCD and PSF files of each WaaG/ligand complex were analyzed in VMD. The unique hydrogen bonds were considered, with a tolerance of the distance between donor and acceptor of 3.4 Å and an angle cutoff of 45 degrees. Lastly, the angle and the distance variations between the strategic amino acids were calculated through VMD, and the .dat output files were combined to calculate their Spearman correlation through an in–house script in MATLAB.

9.4. Project #4

9.4.1. Chemistry

9.4.1.1. Materials and synthetic methods

THF, CH_2Cl_2, MeCN, toluene and DMF were obtained as dry solvents from a VAC solvent purifier system (Hawthorne, CA, USA). Pyridine was distilled over CaH_2 and dried over molecular sieves (MS). MeOH was dried over molecular sieves. The inert atmosphere was used for some reactions through a nitrogen (or argon) atmosphere. Powdered molecular sieves (3 Å) were activated by heating under high vacuum. Purification by flash column chromatography was carried out using silica gel 60 for manual columns, or a Biotage Isolera flash chromatography system (Uppsala, Sweden) using KP–Sil and HP–Sil snap cartridges. Reactions were monitored by TLC using silica gel 60 F254 plates (20x20 cm, 0.2 mm thickness), analyzed with UV light (254–360 nm) or by a staining solution prepared from ammonium cerium(IV) sulfate (2 g) in EtOH (40 mL) and 2 M H_2SO_4 (40 mL) or by ESI–MS High–resolution mass spectra analysis; these analyses are recorded using a Bruker Daltonics micrOTOF or micrOTOFQ spectrometer (Massachusetts, USA), using electron–spray ionization (ESI) in positive mode. Samples were diluted to 1 mg·L^{-1} for analysis. High–resolution mass spectra (HRMS) using the same conditions. NMR spectra for characterization of all isolated compounds were recorded at 25 °C, on a Bruker Avance II spectrometer operating at 400.13 MHz (^{1}H) and 100.61 MHz (^{13}C). The chemical shifts (δ), reported in ppm were referenced to the residual solvent peaks for $CDCl_3$ $\delta = 7.26$ ppm and MeOH–d_4 $\delta = 3.31$ ppm, and TMS or TSP (sodium 3–trimethylsilyl–(2,2,3,3–2H4)–propanoate) as internal standards, $\delta H = 0.0$. ^{13}C shifts were referenced to the residual solvent peaks as well, for $CDCl_3$ $\delta = 77.16$ ppm and MeOH–d_4 $\delta = 49.00$. Some of the synthesized compounds are already fully characterized using 1D ^{1}H, 1D ^{1}H–decoupled ^{13}C, 2D ^{1}H,^{1}H–DQF–COSY, 2D ^{1}H and ^{13}C–multiplicity–edited–HSQC and HMBC NMR experiments. Splitting of NMR signals are reported as s (singlet), d (doublet), br d or wd (broad doublet or wide doublet), t (triplet), dd (doublet of doublet), dq (doublet of quadruplet), ddd (doublet of doublet of doublet), m (multiplet).

9.4.1.2. Characterization of compounds

For the synthesis of building blocks **1**, **2** and **5**, only the full characterization of the final step of their synthesis is reported below.
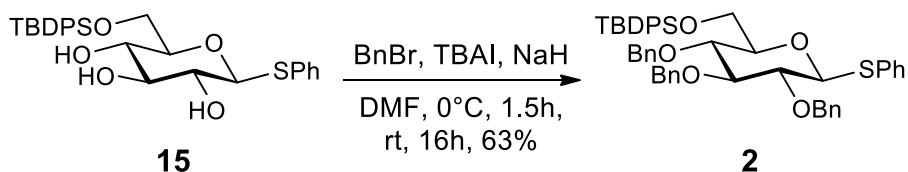
Compound **1**:
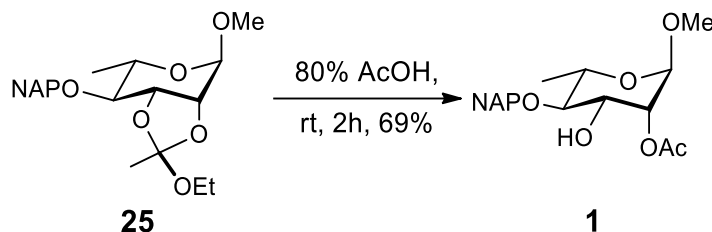
Compound **25** (0.97 g, 3.3 mmol) was dissolved in AcOH, 80% (4 mL) and stirred for 90 min at rt. The mixture was diluted with CH_2Cl_2 (25 mL) and washed with $NaHCO_3$ (3 x 50 mL) and brine (3 x 50 mL). The organic layer was dried over Na_2SO_4 and evaporated. The resulting mixture was purified by flash chromatography (pentane/EtOAc, 4:1) to afford compound **1** as a clear yellow oil in a 69% yield (0.58 g, 1.6 mmol). R_f 0.54 (toluene/EtOAc, 1:1).

^{1}H NMR (400 MHz, CDCl$_3$): δ 7.87–7.78 (m, 4H), 7.52–7.43 (m, 3H), 5.11 (dd, J = 3.66, 1.57, 1H), 4.94 (dd, J = 48.83, 11.49, 2H), 4.63 (d, J = 1.70, 1H), 4.17–4.1 (m, 1H), 3.81–3.71 (m, 1H), 3.41 (t, J = 9.53, 1H), 3.35 (s, 3H), 2.15 (s, 3H), 1.39 (d, J = 6.40, 3H) ppm.

^{13}C NMR (100 MHz, CDCl$_3$): δ 170.89, 135.77, 133.31, 133,06, 128.30, 127.96, 127.71, 126.62, 126.25, 126.03, 125.84, 98.41, 81.72, 75.22, 72.79, 70.30, 67.25, 54.95, 21.14, 18.05 ppm.

HR–MS: m/z [M + Na]$^+$ calcd for $C_{20}H_{24}O_6$ 383.1465, found 383.1470.

Compound **2**:

To a solution of compound **15** (357 mg, 0.70 mmol, 1eq) in dry DMF (8 mL) under nitrogen was added tetrabutylammonium iodide (34 mg, 0.13 eq) and sodium hydride (60% dispersion in oil, 86 mg, 3.61 mmol, 5.15 eq). After cooling down to 0 °C, benzyl bromide was added (0.48 mL, 4.01 mmol, 5.73 eq). The mixture was stirred for 1h 30, then heated up

to rt and stirred for 16h 30. The mixture was co–evaporated with toluene and extracted with CH_2Cl_2 (3 x 100 mL). The organic extract was dried over Na_2SO_4 and evaporated *in vacuo*. The mixture was purified by flash chromatography (PE/EtOAc 10/1) to give compound **2** in 63% yield (345 mg, 0.42 mmol) as an incolor syrup. R_f 0.48 (PE/EtOAc, 10/1).

^{1}H NMR (400 MHz, $CDCl_3$): δ 7.79–7.74 (m, 2H), 7.74–7.67 (m, 2H), 7.63–7.57 (m, 2H), 7.44–7.27 (m, 18H), 7.23–7.18 (m, 4H), 7.17–7.11 (m, 2H), 4.92–4.83 (m, 3H), 4.76–4.66 (m, 3H), 4.02–3.96 (dd, 1H, J = 11.23, 2.09), 3.96–3.90 (dd, 1H, J = 11.40, 3.80), 3.80 (t, 1H, J = 9.32), 3.72 (t, 1H, J = 8.98), 3.55 (t, 1H, J = 9.67), 3.43–3.37 (m, 1H), 1.09 (s, 7H) ppm.

^{13}C NMR (100 MHz, $CDCl_3$): δ 136.04, 135.80, 131.80, 129.83, 129.07, 128.65, 128.59, 128.32, 128.14, 128.01, 127.91, 127.83, 87.70, 87.05, 80.98, 76.12, 75.56, 75.31, 27.09, 19.46 ppm.

HR–MS: *m/z* [M + Na]$^+$ calcd for $C_{49}H_{52}O_5SSi$ 803.3146, found 803.3197.

Compound **5**:

To a solution of compound **21** (1.10 g, 3.26 mmol) in dry CH_2Cl_2 (15 mL), picolinic acid (0.60 g, mmol), ethylene dichloride (0.90 g, 4.71 mmol) and 4–dimethylaminopyridine (77 mg, 0.63 mmol) were added, and the resulting mixture was stirred under argon for 3 h at rt (the solution turns from yellow to red–purple). After that, the reaction mixture was diluted with CH_2Cl_2 (20 mL) and washed with H_2O (10 mL), satd aq. $NaHCO_3$ (10 mL), and H_2O (2 x 10 mL). The organic phase was separated, dried over Na_2SO_4, and concentrated under reduced pressure. The residue was purified by column chromatography (EtOAc/PE 1.5/3.5) to afford compound **5** as a yellow syrup in 98% yield (0.35 g, 0.79 mmol).

Characterization in accordance with the already–published paper of *Demchenko et al.* [238]
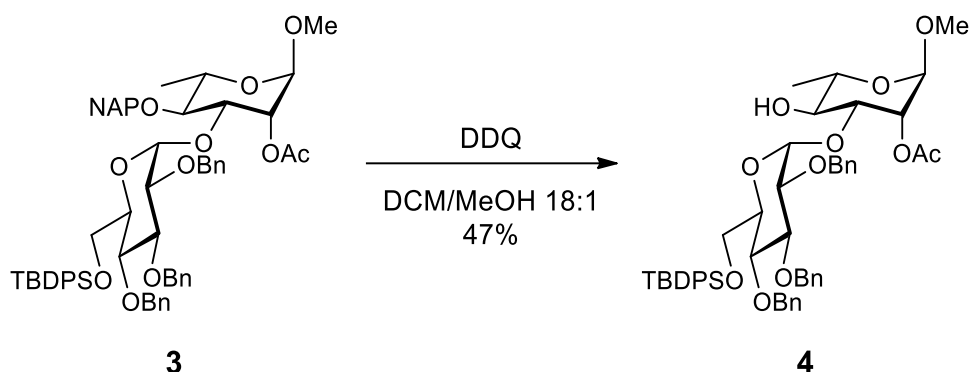
Compound **3**:

Glucosyl donor **2** (150 mg, 0.192 mmol) and rhamnosyl acceptor **1** (69 mg, 0.191 mmol) are azeotroped with toluene (3 x 3 mL) and dried *in vacuo* o.n. Then, the mixture was solubilized in CH_2Cl_2 (0.7 mL) and MS 4 Å (~40 mg) was added. The solution was stirred under inert atmosphere for 30 min at rt. The mixture was cooled to −30 °C, NIS (55 mg, 0.244 mmol) and TMSOTf (2 μL, 0.013 mmol) were added, the external cooling was brought to 0 °C. Then, the resulting mixture was stirred for 3 h going through 0 °C to rt. The reaction mixture was rinsed with CH_2Cl_2, washed with H_2O (3 mL), satd aq. $NaHCO_3$ (3 mL) and satd aq. $Na_2S_2O_3$ (3 mL) and H_2O (3 mL). The organic phase was separated, dried over Na_2SO_4, and concentrated under reduced pressure. The residue was purified by column chromatography on silica gel (EtOAc/PE 1/4 to 2/3) to obtain the title compound as a colorless syrup in 71% yield (49 mg, 0.052 mmol), with complete stereoselective conversion. R_f 0.16 (EtOAc/PE 1.5/3.5, *v/v*).

^{1}H NMR (400 MHz, $CDCl_3$): δ 7.75 – 7.67 (2H, m, H–3_{NAP}, H–7_{NAP}), 7.63 – 7.60 (2H, m, H–2_{NAP}, H–6_{NAP}), 7.48 – 6.99 (28H, m, H_{Ph}, H_{NAP}), 5.44 (1H, m, H–5_{Rha}), 5.23 (1H, d, *J* = 3.62 Hz, H–1_{Glc}), 5.14 (1H, d, *J* = 10.68 Hz, H–2_{Rha}), 5.02 (1H, d, *J* = 10.92 Hz, H–5_{Glc}), 4.87 (2H, m, H–4,3_{Glc}), 4.64 (1H, d, *J* = 1.65 Hz, H–1_{Rha}), 4.58 (1H, d, *J* = 11.15 Hz, H–4_{Rha}), 4.09 – 3.60 (8H, m, 3xCH_{2Bn}, CH_{2NAP}), 3.27 (2H, s, CH_{2TBDPS}), 2.30 (3H, s, OCH_3), 1.91 (3H, s, CH_{3Ac}), 1.37 (3H, d, *J* = 6.17 Hz, CH_{3Rha}), 1.06 (2H, s, CH_{2TBDPS}), 1.02 (9H, s, 3x$CH_{3t–but}$) ppm.

^{13}C NMR (100 MHz, $CDCl_3$): δ 170.86 (C=O_{Ac}), 138.73 (3xC–1_{Bn}), 135,91 (C–1,$2b_{NAP}$, 2xC–1_{TBDPS}), 133.16 (C–$6b_{NAP}$), 129.89 (3xCH–2,4,6_{TBDPS}), 129.72 (3xCH–3,5_{TBDPS}), 128.74 (3xCH–3,5_{Bn}), 128.03 (CH–6,7_{NAP}), 127.76 (3xCH–4_{Bn}), 126.85 (CH_{2NAP}), 126.55 (3xCH–2,6_{Bn}), 125.70 (CH–2_{NAP}, CH–3,4_{NAP}) ppm.

HR–MS: *m/z* [M + Na]$^+$ calcd for $C_{63}H_{70}O_{11}Si$ 1053.45851, found 1053.4960.

Compound **4**:

3 → **4**

DDQ
DCM/MeOH 18:1
47%

Compound **3** was firstly azeotroped with toluene (3 x 3 mL). Then, to a solution of **3** (150 mg, 0.145 mmol, 1 eq) in CH_2Cl_2, DDQ (0.083 g, 0.364 mmol) was added dropwise (recrystallized from $CHCl_3$), solubilized in MeOH (CH_2Cl_2/ MeOH, 4:1, 4:1 mL), at 0 °C under inert atmosphere. After 4 h at rt, the mixture is diluted with CH_2Cl_2 and washed with sat. aq. $NaHCO_3$ (10 mL) and H_2O (10 mL). Column chromatography (EtOAc/PE 1/4) to give compound **4** in 47% yield (61 mg, 0.069 mmol). R_f 0.23 (EtOAc/PE 1/4).

^1H NMR (400 MHz, $CDCl_3$): δ 7.62 – 7.57 (4H, m, $2xH–2,6_{TBDPS}$), 7.36 – 6.96 (17H, wm, $2xH–4_{TBDPS}$, $3xH–2,6_{Bn}$, $3xH–3,4,5_{Bn}$), 6.97–6.95 ($2xH–3,5_{TBDPS}$) 5.22 (1H, m, $H–5_{Rha}$), 4.92 (1H, d, $J = 3.53$ Hz, $H–1_{Glc}$), 4.87 (1H, d, $J = 10.81$ Hz, $H–2_{Rha}$), 4.71 (1H, d, $J = 1.35$ Hz, $H–1_{Rha}$), 4.70 (1H, s, $H–5_{Glc}$), 4.61 (1H, d, $J = 14.09$ Hz, $H–4_{Glc}$), 4.56 (1H, m, $H–3_{Glc}$), 4.41 (1H, d, $J = 10.76$ Hz, $H–4_{Rha}$), 3.92–3.85 (2H, m, CH_{2Bn}), 3.80–3.77 (2H, m, CH_{2Bn}), 3.69–3.65 (1H, m, $H–3_{Rha}$), 3.53–3.38 (4H, m, CH_{2Bn}, CH_{2TBDPS}) 3.26 (3H, s, OCH_3), 3.18 (1H, s, $H–2_{Glc}$), 1.91 (3H, s, CH_{3Ac}), 1.21 (3H, d, $J = 5.29$ Hz, CH_{3Rha}), 0.97 (9H, s, $3xCH_{3t–but}$) ppm.

^{13}C NMR (100 MHz, $CDCl_3$): δ 170.77 ($C=O_{Ac}$), 138.61 ($3xC–1_{Bn}$), 136.04 ($2xC–1_{TBDPSph}$), 133.48 ($2xCH–2,4,6_{TBDPSph}$), 129.98 ($2xCH–3,5_{TBDPSph}$), 128.74 ($3xCH–3_{Bn}$), 128.36 (CH–4_{Bn}), 128.06 (CH–$2,6_{Bn}$), 98.89 (CH–1_{Glc}), 96.16 (CH–1_{Rha}), 81.89 (CH–3_{Glc}), 80.28 (CH–2_{Glc}), 78.14 (CH–4_{Glc}), 75.98 (CH–5_{Glc}), 73.45 (CH–3_{Rha}), 72.81 (CH–5_{Rha}), 71.99 ($3xCH_{2Bn}$), 70.06 (C–4_{Rha}), 68.26 (CH–2_{Rha}), 63.63 ($CH_2–O_{TBDPS}$), 55.17 (OCH_3), 30.04 ($C_{t–but}$), 27.13 ($3xCH_{3t–but}$), 21.31 (CH_{3Ac}), 18.13 (CH_{3Rha}) ppm.

HR–MS: m/z calcd [M + Na]$^+$ for $C_{52}H_{62}O_{11}Si$ 913.39591, 914.39926, found 913.36877, 914.37134.

Compound **6**:
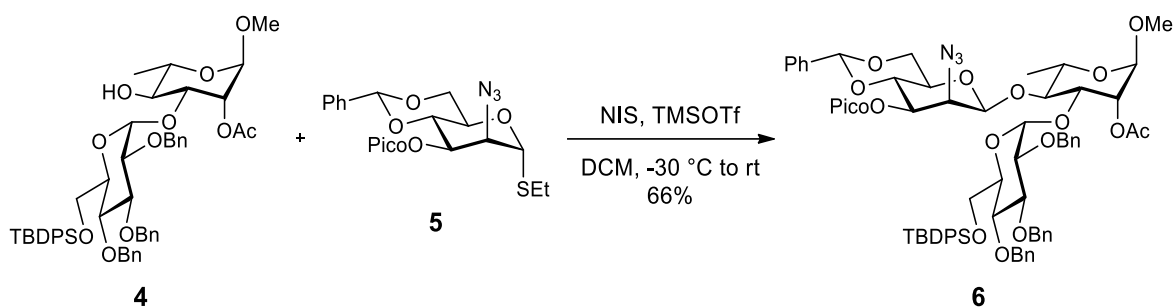
Mannosyl donor **5** (19 mg, 0.059 mmol) and disaccharide acceptor **4** (33 mg, 0.037 mmol) are azeotroped with toluene (3 x 3 mL) and dried *in vacuo* o.n. Then, the mixture was solubilized in 1,2–DCE (1.9 mL), and MS 4 Å (46 mg) was added. The solution was stirred under inert atmosphere for 30 min at rt. The mixture was cooled to −30 °C, NIS (23.5 mg, 0.105 mmol) and TfOH (1 μL, 0.01 mmol) were added, the external cooling was removed, and the resulting mixture was stirred for 3 h at rt. The reaction mixture was rinsed with CH_2Cl_2, washed with H_2O (3 mL), satd aq. $NaHCO_3$ (3 mL) and satd aq. $Na_2S_2O_3$ (3 mL) and H_2O (3 mL). The organic phase was separated, dried over Na_2SO_4, and concentrated under reduced pressure. The residue was purified by column chromatography on silica gel (pentane/EtOAc 0.5/4.5, then 1.5/3.5) to obtain compound **6** as a colorless syrup in 66% yield (28 mg, 0.024 mmol) with complete stereoselective conversion. R_f 0.50 (EtOAc/PE 2/3, *v/v*).

^{1}H NMR (400 MHz, $CDCl_3$): δ 7.72 – 7.55 (4H, m, H–1–4$_{Pico}$, H–1,5$_{Ph}$), 7.46 – 7.29 (23H, m, aromatic), 7.01 – 6.85 (5H, m, aromatic), 5.68 (1H, dd, ^1J = 10.06 Hz, ^2J = 3.64 Hz, H–3$_{Man}$), 5.59 (1H, s, C*H*Ph), 5.52 (1H, d, J = 1.75 Hz, H–1$_{Glc}$), 5.27 (2H, s, CH_2), 5.19 (2H, s, CH_2), 4.93 (1H, d, J = 12.16 Hz, H–2$_{Rha}$), 4.78 (1H, d, J = 4.23 Hz, H–1$_{Man}$), 4.75 (1H, J = 3.50 Hz, H–5$_{Rha}$), 4.68 (1H, wd, 1.25 Hz, H–1$_{Rha}$), 4.64 (1H, d, J = 12.42 Hz, H–2$_{Man}$), 4.41 (1H, dd, ^1J = 10.35 Hz, ^2J = 4.84 Hz, H–4$_{Man}$), 4.35 (1H, dd, ^1J = 9.64 Hz, ^2J = 2.74 Hz, H–4$_{Glc}$), 4.24 (1H, t, J = 9.91 Hz, H–5$_{Man}$), 4.01 – 3.73 (6H, m, H–5$_{Man}$, H–3,4$_{Rha}$, H–2,4$_{Glc}$), 3.64 (2H, d, J = 9.32 Hz, $CH_{2benzylidene}$), 3.28 (3H, s, OCH_3), 2.06 (4H, s, $2xCH_2$), 2.05 (3H, s, CH_{3Ac}), 1.45 (3H, d, J = 6.07 Hz, CH_{3Rha}), 1.07 (9H, s, $3xCH_{3t–but}$) ppm.

^{13}C NMR (100 MHz, $CDCl_3$): δ 170.75 (C=O$_{Ac}$), 163.66 (C=O$_{Pico}$), 150.09 (C–1$_{Pico}$), 147.35 (CH–3$_{Pico}$), 138.37 (CH–5$_{Pico}$), 136.91 (3xC–1$_{Bn}$), 135.80 (C–1$_{Ph}$), 133.98 (2xC–1$_{TBDPS}$), 129.67 (2xCH–2,4,6$_{TBDPS}$), 129.15 (2xCH–3,5$_{TBDPS}$), 128.66 (3xC–1$_{Ph}$), 128.40 (CH–3,5$_{Pico}$), 128.16 (3xCH–4$_{Bn}$), 127.75 (CH–4$_{Pico}$), 127.29 (3xCH–2,6$_{Bn}$), 127.10 (CH–4$_{Pico}$), 126.42 (CH–2,6$_{Pico}$), 125.32 (CH–6$_{Pico}$), 102.02 (CH–1$_{Glc}$), 101.23 (*C*HPh), 98.89 (CH–

1_{Man}), 91.46 (CH–1_{Rha}), 83.08 (CH–3_{Glc}), 79.82 (CH–4_{Rha}), 78.41 (CH–4_{Glc}), 77.83 (CH–2_{Glc}), 77.56 (CH–3_{Glc}), 76.05 (CH–3_{Rha}), 75.01 (CH–4_{Man}), 73.19 (3xCH_2), 71.96 (CH–5_{Rha}), 71.70 (CH–3_{Man}), 70.63 (CH–2_{Rha}), 68.66 (CH–5_{Man}), 67.46 ($CH_{2benzylidene}$), 63.14 (CH_{2TBDPS}), 62.74 (CH–2_{Man}), 55.14 (OCH_3), 29.95 (C_{t-but}), 26.99 (3xCH_3), 21.23 (CH_{3Ac}), 14.37 (CH_{3Rha}) ppm.

HR–MS: m/z [M + Na]$^+$ calcd for $C_{65}H_{74}N_3O_{14}Si$ 1293.50798, found 1293.5530.

Compound **7**:

6   **7**
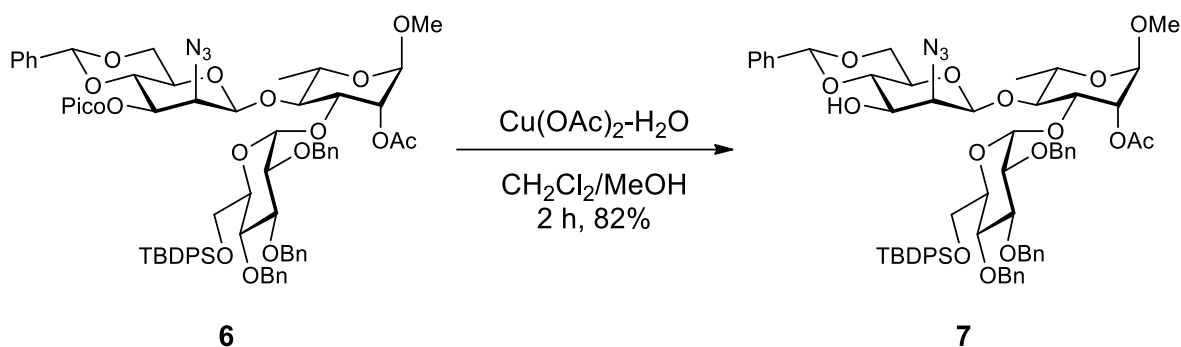
$Cu(OAc)_2$–H_2O (9 mg, mmol) was added to a solution of compound **6** (40 mg, 0.032 mmol) in CH_2Cl_2/MeOH (2.1 mL, 3/1, 1.58/0.53 mL, v/v) and the resulting mixture was stirred for 2 h at rt. After that, the reaction mixture was diluted with CH_2Cl_2 ($\sim$10 mL) and washed with H_2O (5 mL), sat. aq. $NaHCO_3$ (5 mL) and H_2O (5 mL). The organic phase was separated, dried over Na_2SO_4, and concentrated under reduced pressure. The residue was purified by column chromatography on silica gel (EtOAc/PE 2/3) to obtain compound **7** in 82% yield (30 mg, 0.026 mmol). R$_f$ 0.43 (EtOAc/PE, 2/3, v/v).

^{1}H NMR (600 MHz, $CDCl_3$): δ 7.87 (2H, dt, ^1J = 7.73 Hz, ^2J = 1.49 Hz, H–1,5_{Ph}), 7.71 (4H, m, 2xH–1,$5_{TBDPS,aromatic}$), 7.52 – 7.30 (24H, wm, $H_{Ph–TBDPS–Bn}$), 5.50 (1H, s, $H_{benzylidene}$), 5.19 (1H, d, J = 5.18 Hz, H–1_{Glc}), 5.01 (1H, d, J = 10.84 Hz, H–2_{Rha}), 4.94 (1H, d, J = 0.72 Hz, H–1_{Man}), 4.85 (1H, d, J = 2.05 Hz, H–4_{Rha}), 4.83 (1H, d, J = 2.54 Hz, H–4_{Man}), 4.71 (1H, s, H–5_{Rha}), 4.69 (1H, s, H–3_{Man}), 4.61 (1H, d, J = 1.60 Hz, H–1_{Rha}), 4.58 (1H, d, J = 10.56 Hz, H–5_{Man}), 4.32 (1H, dd, ^1J = 10.45 Hz, ^2J = 4.98 Hz, H–2_{Man}), 4.23 (1H, d, J = 3.19 Hz, H–2_{Glc}), 4.21 (1H, d, J = 3.12 Hz, H–4_{Glc}), 3.94 – 3.56 (12H, wm, H–3,5_{Glc}, CH_{2Bn}, CH_{2TBDPS}), 3.21 (3H, s, OCH_3), 1.97 (3H, s, CH_{3Ac}), 1.33 (3H, d, J = 6.07 Hz, CH_{3Rha}), 1.07 (9H, s, 3x$CH_{3t–but}$) ppm.

^{13}C NMR (100 MHz, $CDCl_3$): δ 170.75 (C=O_{Ac}), 138.55 (C–1_{Bn}), 138.34 (C–1_{Bn}), 138.19 (C–1_{Bn}), 137.37 (C–1_{Ph}), 135.90 (2xC–1_{TBDPS}), 133.74 (2xCH–2,4,6_{TBPDS}), 128.77 (2xCH–

3,5$_{TBDPS}$), 128.66 (3xCH–3,5$_{Bn}$), 128.53 (CH–3,5$_{Ph}$), 128.37 (3xCH–4$_{Bn}$), 128.21 (CH–4$_{Ph}$), 127.97 (3xCH–2,6$_{Bn}$), 126.55 (CH–2,6$_{Ph}$), 102.44 (CH–2$_{Glc}$), 100.86 (CHPh), 98.84 (CH–1$_{Man}$), 91.64 (CH–1$_{Rha}$), 82.43 (CH–3$_{Glc}$), 79.92 (CH–4$_{Rha}$), 78.52 (CH–2$_{Glc}$), 77.79 (CH–5$_{Glc}$), 75.93 (CH–4$_{Glc}$), 75.62 (CH–4$_{Man}$), 73.28 (CH–3$_{Rha}$), 71.81 (3xCH$_{2Bn}$), 71.09 (CH–5$_{Rha}$), 70.49 (CH–2$_{Rha}$), 68.62 (CH–5$_{Man}$), 67.42 (CH–3$_{Man}$), 67.30 (CH–2$_{benzylidene}$), 67.20 (CH–2$_{TBDPS}$), 64.41 (CH–2$_{Man}$), 55.17 (OCH$_3$), 29.95 (C$_{t–but}$), 27.04 (3xCH$_{3t–but}$), 21.0 (CH$_{3Ac}$), 18.14 (CH$_{3Rha}$) ppm.

HR–MS: m/z [M + Na]$^+$ calcd for C$_{65}$H$_{75}$N$_3$O$_{15}$Si 1188.48651, found 1188.5073.

Compound **8**:
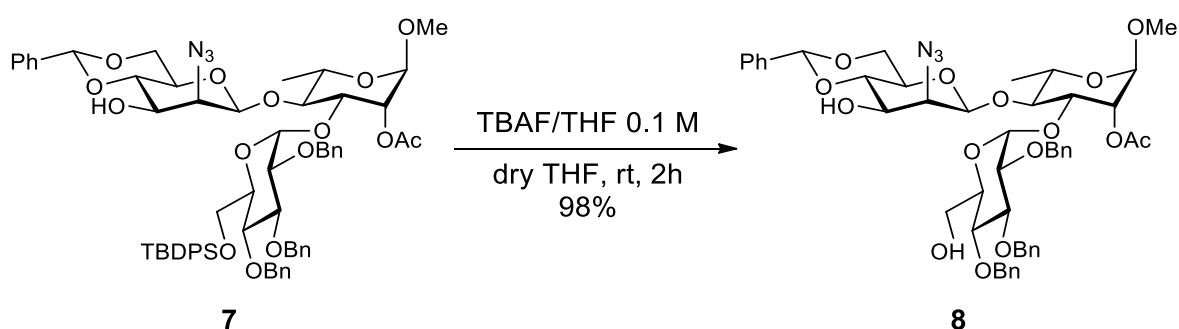
Tetra–n–butylammonium fluoride (0.076 mL, 1.0 M solution in THF) was added dropwise to a cooled (0 °C) solution of compound **7** (35.4 g, 0.03 mmol) in anhydrous THF (0.33 mL) under N$_2$. After stirring at rt for 2 h, the reaction mixture was quenched, H$_2$O (30 mL) was added and the mixture was extracted EtOAc (4 x 20 mL). The final organic layer was washed with H$_2$O (3 mL), brine (3 mL), evaporated and dried over Na$_2$SO$_4$. Finally, the residue was purified by liquid chromatography (EtOAc/pentane 2/3, then 1/1). Compound **8** was obtained in 98% yield (27.6 mg, 0.03 mmol). R$_f$ 0.35 (EtOAc/PE 2/3).

^{1}H NMR (600 MHz, CDCl$_3$): δ 7.41 (2H, m, H–1,5$_{Ph}$), 7.30 – 7.18 (18H, wm, H–2,3,4$_{Ph}$, H$_{Bn}$), 5.44 (1H, s, H$_{benzylidene}$), 5.05 (1H, d, J = 3.19 Hz, H–1$_{Glc}$), 4.93 (1H, d, J = 11.05 Hz, H–2$_{Rha}$), 4.86 (1H, wd, H–1$_{Man}$), 4.79 (1H, d, J = 10.85 Hz, H–5$_{Rha}$), 4.76 (1H, d, J = 10.96 Hz, H–4$_{Rha}$), 4.62 – 4.57 (3H, m, CH$_2$, H–3$_{Man}$), 4.53 (1H, d, J = 1.42 Hz, H–1$_{Rha}$), 4.27 – 4.22 (2H, m, CH$_2$), 4.04 (1H, dd, ^1J = 9.14 Hz, ^2J = 3.23 Hz, H–4$_{Rha}$), 3.78 – 3.56 (12H, wm, CH$_{benzylidene}$, H–2$_{Man}$, H–4$_{Man}$, CH$_2$, CH$_2$, H–3$_{Rha}$, H–5$_{Glc}$, H–4$_{Glc}$, H–3$_{Glc}$), 3.46 (1H, dd, ^1J = 9.70 Hz, ^2J = 3.08 Hz, H–2$_{Glc}$), 3.29 (3H, s, OCH$_3$), 1.90 (3H, s, CH$_{3Ac}$), 1.27 (3H, d, J = 5.16 Hz, CH$_{3Rha}$) ppm.

^{13}C NMR (100 MHz, CDCl$_3$): δ 170.77 (C=O$_{Ac}$), 138.69 (C–1$_{Bn}$), 138.26 (C–1$_{Bn}$), 138.21 (C–1$_{Bn}$), 137.44 (C–1$_{Ph}$), 129.57 (3xCH–3$_{Bn}$), 128.98 (CH–3,5$_{Ph}$), 128.83 (3xCH–4$_{Bn}$), 128.64 (CH–4$_{Ph}$), 128.20 (3xCH–2,6$_{Bn}$), 126.63 (CH–2,6$_{Ph}$), 102.54 (CH–1$_{Glc}$), 101.17 (CHPh), 98.92 (CH–1$_{Man}$), 92.61 (CH–1$_{Rha}$), 82.21 (CH–3$_{Glc}$), 79.74 (CH–3$_{Rha}$), 78.66 (CH–2$_{Glc}$), 72.84 (CH–4$_{Glc}$), 75.82 (CH–4$_{Man}$), 75.64 (CH–3$_{Rha}$), 73.51 (CH–5$_{Glc}$), 71.91 (3xCH$_{2Bn}$), 71.35 (CH–5$_{Rha}$), 70.42 (CH–2$_{Rha}$), 68.70 (CH–5$_{Man}$), 67.59 (CH–3$_{Man}$), 67.34 (CH$_{2benzylidene}$), 64.59 (CH$_2$–OH), 61.79 (CH–2$_{Man}$), 55.43 (OCH$_3$), 24.16 (CH$_{3Ac}$), 18.22 (CH–3$_{Rha}$) ppm.

HR–MS: m/z [M + Na]$^+$ calcd for C$_{49}$H$_{57}$N$_3$O$_{15}$ 950.36874, found 950.3818.

Compounds **9a** and **9b**:
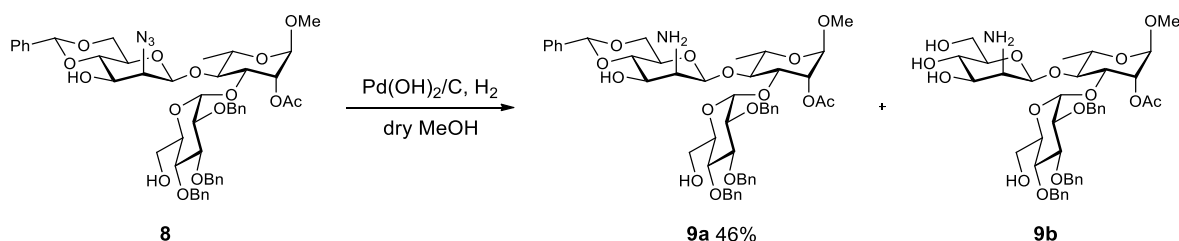
27.6 mg (0.03 mmol) of trisaccharide **8** were dissolved in 3 ml of dry MeOH (after degassing), and 5 mg of Pd(OH)$_2$/C were added. The mixture was allowed to stir at rt *o.n.*, with a balloon filled with H$_2$. After the night, two products were present: one minor product (**9b**), and one major product (**9a**), both visible at HR–MS. The solution was filtered through a pad of celite and the mixture was concentrated *in vacuo* and separated through flash chromatography (CH$_2$Cl$_2$/MeOH 9.8/0.2). It was not possible to isolate compound **9b** in a good amount to allow a proper characterization, while compound **9a** was isolated in 46% yield (12 mg, 0.013 mmol) and fully characterized. R$_f$ 0.53 (**9a**), 0.34 (**9b**).

^{1}H NMR (600 MHz, CDCl$_3$): δ 7.71 (2H, m, H–1,5$_{Ph}$), 7.30 – 7.08 (18H, wm, H–2,3,4$_{Ph}$, H$_{Bn}$), 5.51 (1H, s, H$_{benzylidene}$), 5.10 (1H, d, J = 3.21 Hz, H–1$_{Glc}$), 4.86 (1H, wd, J = 11.02 Hz, H–2$_{Rha}$), 4.82 (1H, wd, H–1$_{Man}$), 4.78 – 4.74 (2H, m, H–5$_{Rha}$ – H–4$_{Rha}$), 4.62 – 4.54 (3H, m, CH$_2$, H–3$_{Man}$), 4.50 (1H, wd, J = 1.21 Hz, H–1$_{Rha}$), 4.27 – 4.20 (2H, m , CH$_2$), 4.09 (1H, dd, ^1J = 9.59 Hz, ^2J = 3.22 Hz, H–4$_{Rha}$), 3.84 – 3.11 (12H, wm, CH$_{2benzylidene}$, H–2$_{Man}$, H–4$_{Man}$, CH$_2$, CH$_2$, H–3$_{Rha}$, H–5$_{Glc}$, H–4$_{Glc}$, H–3$_{Glc}$), 3.34 – 3.32 (1H, m, H–2$_{Glc}$), 3.25 (3H, s, OCH$_3$), 1.84 (3H, s, CH$_{3Ac}$), 1.21 (3H, d, J = 6.09 Hz, CH$_{3Rha}$) ppm.

^{13}C NMR (100 MHz, CDCl$_3$): δ 170.62 (C=O$_{Ac}$), 138.63 (3xC–1$_{Bn}$), 138.11 (C–1$_{Ph}$), 128.68 (3xCH–3,5$_{Bn}$, CH–3,5$_{Ph}$), 128.16 (3xCH–4$_{Bn}$, CH–4$_{Ph}$), 127.80 (CH–2,6$_{Bn}$), 126.27 (CH–2,6$_{Bn}$), 101.83 (CH–1$_{Man}$), 101.09 (CH–1$_{Glc}$), 98.48 (CH$_{benzylidene–Ph}$), 92.02 (CH–1$_{Man}$), 81.69 (CH–3$_{Glc}$), 79.68 (CH–4$_{Rha}$), 77.87 (CH–4$_{Glc}$, CH–2$_{Glc}$), 76.67 (CH–3$_{Rha}$), 75.21 (CH–5$_{Glc}$), 74.61 (CH–3$_{Man}$), 73.0 (3xCH$_2$), 71.70 (CH–5$_{Rha}$), 69.19 (CH–2$_{Rha}$), 68.21 (CH–5$_{Man}$), 68.37 (CH$_{2benzylidine}$), 67.29 (CH$_2$–OH), 60.85 (CH–2$_{Man}$), 54.14 (OCH$_3$), 34.17 (CH$_{3Ac}$), 29.58 (CH$_{3Rha}$) ppm.

HR–MS: **9a** *m/z* [M + H]$^+$ calcd for C$_{49}$H$_{59}$NO$_{15}$ 902.39391, found 902.39679; *m/z* [M + Na]$^+$ calcd 924.3784, found 924.38165.

9b *m/z* [M + H]$^+$ calcd for C$_{42}$H$_{55}$NO$_{15}$ 813.35717, found 813.35950.

Compound **10**:

9a   **10**
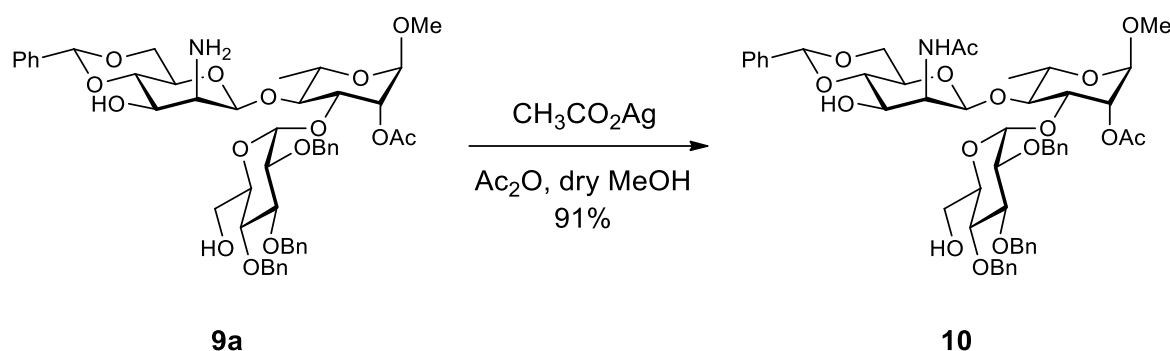
To a solution of 10 mg (0.001 mmol) of compound **9a** in 0.1 mL of dry MeOH, 7.5 mg (0.05 mmol) of silver acetate was added and 0.01 mL of Ac$_2$O, o.n., under inert atmosphere and controlled temperature of 0 °C. Then, the reaction mixture was heated up to rt, the precipitate was filtered and washed with MeOH (3 x 2 mL), CH$_2$Cl$_2$ (2 mL) and EtOAc (2 mL). The excess of acetic anhydride was removed by co–evaporation with toluene and *in vacuo* o.n., obtaining compound **10** in 91% yield (9.5 mg, 0.001 mmol). R$_f$ 0.52 (CH$_2$Cl$_2$ /MeOH 9.8 /0.2).

^{1}H NMR (600 MHz, CDCl$_3$): δ 7.42 – 7.39 (2H, m, H–1,5$_{Ph}$), 7.28 – 7.09 (18H, wm, H–2,3,4$_{Ph}$, CH$_{Bn}$), 5.51 (1H, s, H$_{benzylidene}$), 5.10 (1H, d, *J* = 3.28 Hz, H–1$_{Glc}$), 4.96 (1H, wd, *J* = 1.30 Hz, H–2$_{Rha}$), (1H, wd, H–1$_{Man}$), (2H, m, H–5$_{Rha}$ – H–4$_{Rha}$), (3H, m, CH$_2$, H–3$_{Man}$), (1H, wd, *J* = 1.51 Hz, H–1$_{Rha}$), (2H, m, CH$_2$), 4.04 (1H, dd, ^1J = 9.61 Hz, ^2J = 3.52 Hz, H–4$_{Rha}$), 3.84 – 3.31 (12H, wm, CH$_{2benzylidene}$, H–2$_{Man}$, H–4$_{Man}$, CH$_2$, CH$_2$, H–3$_{Rha}$, H–5$_{Glc}$, H–4$_{Glc}$, H–

3_{Glc}), 3.23 (3H, s, OCH$_3$), 1.96 (3H, s, CH$_{3Ac}$), 1.81 (3H, s, NHCOCH$_3$), 1.18 (3H, d, $J =$ 6.12 Hz, CH$_{3Rha}$) ppm.

^{13}C NMR (100 MHz, CDCl$_3$): δ 175.61 (NHCOCH$_3$), 172.77 (C=O$_{Ac}$), 140.86 (C$_{Bn}$), 140.28 (C$_{Bn}$), 140.01 (C$_{Bn}$), 129.69 (CH–3,5$_{Bn}$), 129.52 (CH–2,4$_{Bn}$), 129.41 (CH–2,4$_{Ph}$), 104.14 (CH–1$_{Man}$), 102.21 (CH–1$_{Glc}$), 100.69 (CHPh), 95.21 (CH–1$_{Rha}$), 83.70 (CH–3$_{Glc}$), 82.10 (CH–4$_{Man}$), 81.24 (CH–2$_{Glc}$), 79.70 (CH–4$_{Glc}$), 77.95 (CH–3$_{Rha}$), 77.23 (CH–5$_{Glc}$), 76.80 (CH$_{2Bn}$), 75.33 (CH$_{2Bn}$), 74.72 (CH$_{2Bn}$), 74.19 (CH–3$_{Man}$), 71.45 (CH–5$_{Rha}$), 70.33 (CH–5$_{Man}$), 69.46 (CH$_{2Ph}$), 66.96 (CH$_2$–OH), 63.00 (CH–2$_{Man}$), 56.18 (OCH$_3$), 24.97 (NHCOCH$_3$), 20.93 (CH$_{3Ac}$), 14.98 (CH$_{3Rha}$) ppm.

HR–MS: m/z [M + Na]$^+$ calcd for C$_{51}$H$_{61}$NO$_{16}$ 966.38880, found 966.38912.

10. Final conclusions and future perspectives

All the projects presented in this Thesis aimed to adopt computational and experimental approaches to a Drug Discovery process, in order to find new inhibitors for anticancer and antibacterial chemotherapy. Projects #1 and #2 aimed to obtain new series of microtubule–targeting agents (MTAs) acting as colchicine–binding site inhibitors (CBSIs). Two new series of 5',6'–difluoro– (Project #1) and 4'–fluoro–benzotriazole–acrylonitrile derivatives were rationally designed, synthesized and characterized. All the compounds were tested through *in vitro* biological assessment. A preliminary test through NCI60 *in vitro* screening was performed on each compound. Compounds **9a** (Project #1) and compounds **5** and **12** (Project #2) were selected as the most potent small molecules of the two series of derivatives. Compound 9a showed an important blockade of HeLa cell cycle in G2/M phase, with a negative effect on β–tubulin assembly starting from 50 nM. Derivative **9a** also competes with colchicine for the binding in the same binding pocket on tubulin, slowing tubulin polymerization. [126] Also compounds **5** and **12** in Project #2 showed interference in HeLa cell cycle, but, for these molecules, a pro–apoptotic effect was identified in HeLa and MCF–7 cell lines after treatment. The future goal for these projects will be to identify other strategic substitutions on the benzotriazole scaffold, but also on the acrylonitrile moiety, in order to improve polar and nonpolar interactions between tubulin and the ligands, hence enhancing the negative effect on the microtubule polymerization, even with a lower concentration of the administered compound.

Project #3 is a fragment–based drug discovery process to identify some potential fragments and inhibitors to interfere with WaaG catalytic activity. It aims to block the biosynthesis of LPS, the outer membrane of Gram–negative bacteria, such as *Escherichia coli*. From libraries A and B, compounds **A4** and **B33** from post–processing of molecular docking and molecular dynamics simulations. Further investigations will involve fragment growing, strategically substituting different positions on the main scaffolds of the fragments, or fragment linking processes, in order to obtain a synergic effect from different ligands, in terms of protein–ligand interactions, hence inhibitory activity on WaaG protein. Oligosaccharides of library C gave insights into the interactions between WaaG and the inner core of LPS. The behavior of the protein during MD trajectory will be more in–depth investigated, also in its contact with the oligosaccharide residues, to better comprehend WaaG catalytic interactions.

Project #4 produced a protected trisaccharide by synthetic approach, which could be further investigated in its conformational state, by NMR experiments. It could also be fully deprotected and, in the same conditions evaluated by NMR, to assess the effect of the protecting groups on the orientation of the trisaccharide. The outputs of these experiments will give more insights on the NMR behavior of this structure, which was also found in *A. salmonicida* LPS O–antigen as a repeating unit, gaining interest in Structure Elucidation and Biological studies.

11. Acknowledgements

Grazie alla mia famiglia italiana a Stoccolma. Ad Alessandro, Davide, Ester, Domenica, Stefano, Laura, Matteo, Luca, Davide Rigo, Francesco, Brando, Emanuele. Auguro a tutti di realizzare i propri sogni, ci vediamo in giro per il mondo. Thanks to Alba and Marie, and to the best Chinese guys, Jianping, Haibo and Yajuan. Un grazie a Oriana e Stefano, per le serate passate assieme a Stoccolma e per la vostra ospitalità.

Alla Dott.ssa Maria Orecchioni, grazie Mary per avermi sempre ascoltato, soprattutto sempre con il sorriso.

A Elena, Matteo e Alba, Ilenia e Diego, i tesisti migliori del mondo, mi avete regalato soddisfazioni quest'anno. Avete rallegrato e riempito le giornate lavorative di un povero Dottorando.

Last but not least, i miei amici. Manuele, Riccardo, Giovanni, Riccardo, Alberto, Giancarlo, Mirko, Marco, Giusi, Fabiola, Chiara, Cristina, Francesca, Antonella, Eleonora, Martina, Margherita, Sara, Chiara, Michela, Desi, Stefania e Chiara. Grazie a tutti per aver saputo, ognuno a proprio modo, rendere questi tre anni difficili un po' più leggeri.

È stato un percorso particolare, divertente, stressante, ma soddisfacente, posso solo dire che ne è valsa la pena!

Ad maiora.

12. References

[1]   N. Patra, Pharmaceutical/Medicinal Chemistry, in: Res. Dev. Pharm. Sci. (Volume I), 1st ed., Bhumi Publishing, 2021: pp. 97–98.

[2]   M.A. Murcko, What Makes a Great Medicinal Chemist? A Personal Perspective, J. Med. Chem. 61 (2018) 7419–7424. https://doi.org/10.1021/acs.jmedchem.7b01445.

[3]   V. Mnih, K. Kavukcuoglu, D. Silver, A.A. Rusu, J. Veness, M.G. Bellemare, A. Graves, M. Riedmiller, A.K. Fidjeland, G. Ostrovski, S. Petersen, C. Beattie, A. Sadik, I. Antonoglou, H. King, D. Kumaran, D. Wierstra, S. Legg, D. Hassabis, Human-level control through deep reinforcement learning, Nature. 518 (2015) 529–533. https://doi.org/10.1038/nature14236.

[4]   M.A. Sellwood, M. Ahmed, M.H.S. Segler, N. Brown, Artificial intelligence in drug discovery, Future Med. Chem. 10 (2018) 2025–2028. https://doi.org/10.4155/fmc-2018-0212.

[5]   C. Avendano, J.C. Menendez, Medicinal Chemistry of Anticancer Drugs, 2nd Edition, Elsevier Science, 2015.

[6]   D.C. Ress, M. Congreve, C.W. Murray, R. Carr, Fragment-based lead discovery, Nat. Rev. Drug Discov. 3 (2004) 660–672. https://doi.org/10.1038/nrd1467.

[7]   J.P. Renaud, T. Neumann, L. Van Hijfte, Fragment-Based Drug Discovery, Small Mol. Med. Chem. Strateg. Technol. 47 (2015) 221–249. https://doi.org/10.1002/9781118771723.ch8.

[8]   E.R. Zartler, M.J. Shapiro, Fragonomics: Fragment-based drug discovery, Curr. Opin. Chem. Biol. 9 (2005) 366–370. https://doi.org/10.1016/j.cbpa.2005.05.002.

[9]   B.J. Stockman, C. Dalvit, NMR screening techniques in drug discovery and drug design, Prog. Nucl. Magn. Reson. Spectrosc. 41 (2002) 187–231. https://doi.org/10.1016/S0079-6565(02)00049-3.

[10]   B. Meyer, T. Peters, NMR Spectroscopy Techniques for Screening and Identifying Ligand Binding to Protein Receptors., ChemInform. 34 (2003) 864–890. https://doi.org/10.1002/chin.200319274.

[11]   R. Carr, H. Jhoti, Structure-based screening of low-affinity compounds, Drug Discov. Today. 7 (2002) 522–527. https://doi.org/10.1016/S1359-6446(02)02245-6.

[12]   M.J. Hartshorn, C.W. Murray, A. Cleasby, M. Frederickson, I.J. Tickle, H. Jhoti, Fragment-based lead discovery using X-ray crystallography, J. Med. Chem. 48 (2005) 403–413. https://doi.org/10.1021/jm0495778.

[13]   A. Emwas, K. Szczepski, B.G. Poulson, K. Chandra, R.T. Mckay, M. Dhahri, F. Alahmari, L. Jaremko, J.I. Lachowicz, M. Jaremko, NMR as a "Gold Standard" Method in Drug Design and Discovery, 25 (2020) 4597. https://doi.org/https://doi.org/10.3390/molecules25204597.

[14]   A. Kumar, A. Voet, K.Y.J. Zhang, Fragment Based Drug Design: From Experimental to Computational Approaches, Curr. Med. Chem. 19 (2012) 5128–5147. https://doi.org/10.2174/092986712803530467.

[15]   J.L. Ludington, Virtual Fragment Preparation for Computational Fragment- Based

Drug Design, Fragm. Methods Drug Discov. 1289 (2015) 31–41. https://doi.org/10.1007/978-1-4939-2486-8_4.

[16] A. Miranker, M. Karplus, Functionality maps of binding sites: A multiple copy simultaneous search method, Proteins Struct. Funct. Bioinforma. 11 (1991) 29–34. https://doi.org/10.1002/prot.340110104.

[17] P.J. Hajduk, Fragment-based drug design: How big is too big?, J. Med. Chem. 49 (2006) 6972–6976. https://doi.org/10.1021/jm060511h.

[18] C.A. Lipinski, Drug-like properties and the causes of poor solubility and poor permeability, J. Pharmacol. Toxicol. Methods. 44 (2000) 235–249. https://doi.org/10.1016/S1056-8719(00)00107-6.

[19] C. Fernández, W. Jahnke, New approaches for NMR screening in drug discovery, Drug Discov. Today Technol. 1 (2004) 277–283. https://doi.org/10.1016/j.ddtec.2004.10.003.

[20] A. Vulpetti, U. Hommel, G. Landrum, R. Lewis, C. Dalvit, Design and NMR-based screening of LEF, a library of chemical fragments with different local environment of fluorine, J. Am. Chem. Soc. 131 (2009) 12949–12959. https://doi.org/10.1021/ja905207t.

[21] R. Campos-Olivas, NMR Screening and Hit Validation in Fragment Based Drug Discovery, Curr. Top. Med. Chem. 11 (2010) 43–67. https://doi.org/10.2174/156802611793611887.

[22] M. Mayer, B. Meyer, Characterization of ligand binding by saturation transfer difference NMR spectroscopy, Angew. Chemie - Int. Ed. 38 (1999) 1784–1788. https://doi.org/10.1002/(SICI)1521-3773(19990614)38:12<1784::AID-ANIE1784>3.0.CO;2-Q.

[23] C. Dalvit, P. Pevarello, M. Tato, M. Veronesi, A. Vulpetti, M. Sundström, Identification of compounds with binding affinity to proteins via magnetization transfer from bulk water, J. Biomol. NMR. 18 (2000) 65–68. https://doi.org/10.1023/A:1008354229396.

[24] C. Dalvit, G.P. Fogliatto, A. Stewart, M. Veronesi, B. Stockman, WaterLOGSY as a method for primary NMR screening: Practical aspects and range of applicability, J. Biomol. NMR. 21 (2001) 349–359. https://doi.org/10.1023/A:1013302231549.

[25] P.J. Hajduk, J. Greer, A decade of fragment-based drug design: Strategic advances and lessons learned, Nat. Rev. Drug Discov. 6 (2007) 211–219. https://doi.org/10.1038/nrd2220.

[26] V. Früh, Y. Zhou, D. Chen, C. Loch, A.B. Eiso, Y.N. Grinkova, H. Verheij, S.G. Sligar, J.H. Bushweller, G. Siegal, Application of Fragment Based Drug Discovery to Membrane Proteins: Biophysical Identification of Ligands of the Integral Membrane Enzyme DsbB, Chem Biol. 17 (2010) 881–891. https://doi.org/10.1016/j.chembiol.2010.06.011.

[27] A.M. Giannetti, From eperimental design to validated hits: A comprehensive walk-through of fragment lead identification using surface plasmon resonance, 1st ed., Elsevier Inc., 2011. https://doi.org/10.1016/B978-0-12-381274-2.00008-X.

[28] C.A. Wartchow, F. Podlaski, S. Li, K. Rowan, X. Zhang, D. Mark, K. Sen Huang,

Biosensor-based small molecule fragment screening with biolayer interferometry, J. Comput. Aided. Mol. Des. 25 (2011) 669–676. https://doi.org/10.1007/s10822-011-9439-8.

[29] P.C. Weber, F.R. Salemme, Applications of calorimetric methods to drug discovery and the study of protein interactions, Curr. Opin. Struct. Biol. 13 (2003) 115–121. https://doi.org/10.1016/S0959-440X(03)00003-4.

[30] M.D. Duong-Thi, E. Meiby, M. Bergström, T. Fex, R. Isaksson, S. Ohlson, Weak affinity chromatography as a new approach for fragment screening in drug discovery, Anal. Biochem. 414 (2011) 138–146. https://doi.org/10.1016/j.ab.2011.02.022.

[31] E.T. Larson, J.E. Kim, L.J. Castaneda, A.J. Napuli, Z. Zhang, E. Fan, F.H. Zucker, C.L.M.J. Verlinde, F.S. Buckner, W.C. Van Voorhis, W.G.J. Hol, E.A. Merritt, The double-length tyrosyl-tRNA synthetase from the eukaryote leishmania major forms an intrinsically asymmetric pseudo-dimer, J. Mol. Biol. 409 (2011) 159–176. https://doi.org/10.1016/j.jmb.2011.03.026.

[32] G.E. de Kloe, D. Bailey, R. Leurs, I.J.P. de Esch, Transforming fragments into candidates: small becomes big in medicinal chemistry, Drug Discov. Today. 14 (2009) 630–646. https://doi.org/10.1016/j.drudis.2009.03.009.

[33] M.J. Harner, A.O. Frank, S.W. Fesik, Fragment-based drug discovery using NMR spectroscopy, J. Biomol. NMR. 56 (2013) 65–75. https://doi.org/10.1007/s10858-013-9740-z.

[34] W.P. Jencks, On the attribution and additivity of binding energies, Proc. Natl. Acad. Sci. U. S. A. 78 (1981) 4046–4050. https://doi.org/10.1073/pnas.78.7.4046.

[35] R. Macarron, Critical review of the role of HTS in drug discovery, Drug Discov. Today. 11 (2006) 277–279. https://doi.org/10.1016/j.drudis.2006.02.001.

[36] L. Silverman, R. Campbell, J.R. Broach, New assay technologies for high-throughput screening, Curr. Opin. Chem. Biol. 2 (1998) 397–403. https://doi.org/10.1016/S1367-5931(98)80015-X.

[37] T.I. Oprea, H. Matter, Integrating virtual screening in lead discovery, Curr. Opin. Chem. Biol. 8 (2004) 349–358. https://doi.org/10.1016/j.cbpa.2004.06.008.

[38] B.K. Shoichet, Virtual screening of chemical libraries, Nature. 432 (2004) 862–865. https://doi.org/10.1038/nature03197.

[39] G. Scapin, Structural Biology and Drug Discovery, Curr. Pharm. Des. 12 (2006) 2087–2097. https://doi.org/10.2174/138161206777585201.

[40] C. Bissantz, B. Kuhn, M. Stahl, A medicinal chemist's guide to molecular interactions, J. Med. Chem. 53 (2010) 5061–5084. https://doi.org/10.1021/jm100112j.

[41] J. Lyu, S. Wang, T.E. Balius, I. Singh, A. Levit, Y.S. Moroz, M.J. O'Meara, T. Che, E. Algaa, K. Tolmachova, A.A. Tolmachev, B.K. Shoichet, B.L. Roth, J.J. Irwin, Ultra-large library docking for discovering new chemotypes, Nature. 566 (2019) 224–229. https://doi.org/10.1038/s41586-019-0917-9.

[42] B. Waszkowycz, Towards improving compound selection in structure-based virtual screening, Drug Discov. Today. 13 (2008) 219–226.

https://doi.org/10.1016/j.drudis.2007.12.002.

[43] D. Seeliger, B.L. De Groot, Ligand docking and binding site analysis with PyMOL and Autodock/Vina, J. Comput. Aided. Mol. Des. 24 (2010) 417–422. https://doi.org/10.1007/s10822-010-9352-6.

[44] D. Cappel, S. Jerome, G. Hessler, H. Matter, Impact of Different Automated Binding Pose Generation Approaches on Relative Binding Free Energy Simulations, J. Chem. Inf. Model. 60 (2020) 1432–1444. https://doi.org/10.1021/acs.jcim.9b01118.

[45] K.W. Lexa, H.A. Carlson, Protein flexibility in docking and surface mapping, Q. Rev. Biophys. 45 (2012) 301–343. https://doi.org/10.1017/S0033583512000066.

[46] Z. Gaieb, C.D. Parks, M. Chiu, H. Yang, C. Shao, W.P. Walters, M.H. Lambert, N. Nevins, S.D. Bembenek, M.K. Ameriks, T. Mirzadegan, S.K. Burley, R.E. Amaro, M.K. Gilson, D3R Grand Challenge 3: blind prediction of protein–ligand poses and affinity rankings, J. Comput. Aided. Mol. Des. 33 (2019) 1–18. https://doi.org/10.1007/s10822-018-0180-4.

[47] C.D. Parks, Z. Gaieb, M. Chiu, H. Yang, C. Shao, W.P. Walters, J.M. Jansen, G. McGaughey, R.A. Lewis, S.D. Bembenek, M.K. Ameriks, T. Mirzadegan, S.K. Burley, R.E. Amaro, M.K. Gilson, D3R grand challenge 4: blind prediction of protein–ligand poses, affinity rankings, and relative binding free energies, J. Comput. Aided. Mol. Des. 34 (2020) 99–119. https://doi.org/10.1007/s10822-020-00289-y.

[48] P. Ripphausen, D. Stumpfe, J. Bajorath, Analysis of structure-based virtual screening studies and characterization of identified active compounds, Future Med. Chem. 4 (2012) 603–613. https://doi.org/10.4155/fmc.12.18.

[49] C.D. Blundell, T. Nowak, M.J. Watson, Measurement, Interpretation and Use of Free Ligand Solution Conformations in Drug Discovery, 1st ed., Elsevier B.V., 2016. https://doi.org/10.1016/bs.pmch.2015.10.003.

[50] H. Kubinyi, Hydrogen Bonding: The Last Mystery in Drug Design?, in: Pharmacokinet. Optim. Drug Res., Verlag Helvetica Chimica Acta, Postfach, CH-8042 Zürich, Switzerland, 2007: pp. 513–524. https://doi.org/10.1002/9783906390437.ch28.

[51] P. Mukherjee, P. Desai, Y.D. Zhou, M. Avery, Targeting the BH3 domain mediated protein-protein interaction of Bcl-Xl through virtual screening, J. Chem. Inf. Model. 50 (2010) 906–923. https://doi.org/10.1021/ci1000373.

[52] P. Agnihotri, A.K. Mishra, S. Mishra, V.K. Sirohi, A.A. Sahasrabuddhe, J.V. Pratap, Identification of Novel Inhibitors of Leishmania donovani Glutamylcysteine Synthetase Using Structure-Based Virtual Screening, Docking, Molecular Dynamics Simulation, and in Vitro Studies, J. Chem. Inf. Model. 57 (2017) 815–825. https://doi.org/10.1021/acs.jcim.6b00642.

[53] D.L. Mobley, K.A. Dill, Binding of Small-Molecule Ligands to Proteins: "What You See" Is Not Always "What You Get," Structure. 17 (2009) 489–498. https://doi.org/10.1016/j.str.2009.02.010.

[54] G. Patrick, An Introduction to Medicinal Chemistry, 6th ed., Oxford University Press, 2017.

[55] A. Fischer, M. Smieško, M. Sellner, M.A. Lill, Decision Making in Structure-Based

Drug Discovery: Visual Inspection of Docking Results, J. Med. Chem. 64 (2021) 2489–2500. https://doi.org/10.1021/acs.jmedchem.0c02227.

[56] S.A. Adcock, J.A. McCammon, Molecular dynamics: Survey of methods for simulating the activity of proteins, Chem. Rev. 106 (2006) 1589–1615. https://doi.org/10.1021/cr040426m.

[57] B.L. de Jing Huang, Sarah Rauscher, Grzegorz Nawrocki, Ting Ran, Michael Feig, and A.D.M.J. Groot, Helmut Grubmüller, CHARMM36m: An Improved Force Field for Folded and Intrinsically Disordered Proteins, Nat Method. 14 (2017) 71–73. https://doi.org/10.1038/nmeth.4067.CHARMM36m.

[58] R.B. Best, X. Zhu, J. Shim, P.E.M. Lopes, J. Mittal, M. Feig, A.D. MacKerell, Optimization of the additive CHARMM all-atom protein force field targeting improved sampling of the backbone φ, ψ and side-chain χ1 and χ2 Dihedral Angles, J. Chem. Theory Comput. 8 (2012) 3257–3273. https://doi.org/10.1021/ct300400x.

[59] B.R. Brooks, C.L. Brooks III, A.D. Mackerell, L. Nilsson, R.J. Petrella, B. Roux, Y. Won, G. Archontis, C. Bartels, S. Boresch, A. Caflisch, L. Caves, Q. Cui, A.R. Dinner, M. Feig, S. Fischer, J. Gao, M. Hodoscek, W. Im, K. Kuczera, T. Lazaridis, J. Ma, V. Ovchinnikov, E. Paci, R.W. Pastor, C.B. Post, J.Z. Pu, M. Schaefer, B. Tidor, R.M. Venable, H.L. Woodcock, X. Wu, W. Yang, D.M. York, M. Karplus, CHARMM: The biomolecular simulation program, J. Comput. Chem. 30 (2009) 1545–1614. https://doi.org/10.1002/jcc.21287.

[60] M.A. González, Force fields and molecular dynamics simulations, Collect. SFN. 12 (2011) 169–200. https://doi.org/https://doi.org/10.1051/sfn/201112009.

[61] R. Galeazzi, Molecular Dynamics as a Tool in Rational Drug Design: Current Status and Some Major Applications, Curr. Comput. Aided-Drug Des. 5 (2009) 225–240. https://doi.org/10.2174/157340909789577847.

[62] M. Nikolaou, A. Pavlopoulou, A.G. Georgakilas, E. Kyrodimos, The challenge of drug resistance in cancer treatment: a current overview, Clin. Exp. Metastasis. 35 (2018) 309–318. https://doi.org/10.1007/s10585-018-9903-0.

[63] K. Machida, Existence of cancer stem cells in hepatocellular carcinoma: myth or reality?, Hepatol. Int. 11 (2017) 143–147. https://doi.org/10.1007/s12072-016-9777-7.

[64] M.F. Clarke, M. Fuller, Stem Cells and Cancer: Two Faces of Eve, Cell. 124 (2006) 1111–1115. https://doi.org/10.1016/j.cell.2006.03.011.

[65] V.S. Donnenberg, A.D. Donnenberg, Multiple drug resistance in cancer revisited: The cancer stem cell hypothesis, J. Clin. Pharmacol. 45 (2005) 872–877. https://doi.org/10.1177/0091270005276905.

[66] M. Körbling, Z. Estrov, Adult Stem Cells for Tissue Repair — A New Therapeutic Concept?, N. Engl. J. Med. 349 (2003) 570–582. https://doi.org/10.1056/nejmra022361.

[67] C.H.M. Jamieson, L.E. Ailles, S.J. Dylla, M. Muijtjens, C. Jones, J.L. Zehnder, J. Gotlib, K. Li, M.G. Manz, A. Keating, C.L. Sawyers, I.L. Weissman, Granulocyte–Macrophage Progenitors as Candidate Leukemic Stem Cells in Blast-Crisis CML, N. Engl. J. Med. 351 (2004) 657–667. https://doi.org/10.1056/nejmoa040258.

[68]   M. Dean, T. Fojo, S. Bates, Tumour stem cells and drug resistance, Nat. Rev. Cancer. 5 (2005) 275–284. https://doi.org/10.1038/nrc1590.

[69]   S. Marchini, M. D'Incalci, M. Broggini, New molecules and strategies in the field of anticancer agents, Curr Med Chem Anticancer Agents. 4 (2004) 247–262. https://doi.org/10.2174/1568011043352966.

[70]   N.C. Lloyd, H.W. Morgan, B.K. Nicholson, R.S. Ronimus, Salvarsan – The first Chemotherapeutic Compound, Chem. New Zeal. 69 (2005) 24–27.

[71]   F. Bosch, L. Rosich, The contributions of paul ehrlich to pharmacology: A tribute on the occasion of the centenary of his nobel prize, Pharmacology. 82 (2008) 171–179. https://doi.org/10.1159/000149583.

[72]   J.E. Lesch, The First Miracle Drugs: How the Sulfa Drugs Transformed Medicine, Perspect. Biol. Med. 50 (2007) 639–642. https://doi.org/10.1353/pbm.2007.0057.

[73]   E. Chain, H.W. Florey, M.B. Adelaide, A.D. Gardner, D.M. Oxfd, N.G. Heatley, M.A. Jennings, J. Orr-Ewing, A.G. Sanders, Penicillin As a Chemotherapeutic Agent, Lancet. 236 (1940) 226–228. https://doi.org/10.1016/S0140-6736(01)08728-1.

[74]   E.P. Abraham, E. Chain, C.M. Fletcher, H.W. Florey, A.D. Gardner, N.G. Heatley, M.A. Jennings, Further observations on penicillin, Lancet. 2 (1941) 177–189. https://doi.org/https://doi.org/10.1016/S0140-6736(00)72122-2.

[75]   D. Nathwani, M.J. Wood, Penicillins: A Current Review of their Clinical Pharmacology and Therapeutic Use, Drugs. 45 (1993) 866–894. https://doi.org/10.2165/00003495-199345060-00002.

[76]   F. Nasuhi Pur, K. Akbari Dilmaghani, Calixcephems: Clustered cephalosporins analogous to calixpenams as novel potential anti-MRSA agents, Turkish J. Chem. 38 (2014) 850–858. https://doi.org/10.3906/kim-1403-2.

[77]   A. Malabarba, T.I. Nicas, R.C. Thompson, Structural modifications of glycopeptide antibiotics, Med. Res. Rev. 17 (1997) 69–137. https://doi.org/10.1002/(SICI)1098-1128(199701)17:1<69::AID-MED3>3.0.CO;2-R.

[78]   M. Takahata, J. Mitsuyama, Y. Yamashiro, M. Yonezawa, H. Araki, Y. Todo, S. Minami, Y. Watanabe, H. Narita, In vitro and in vivo antimicrobial activities of T-3811ME, a novel des- F(6)-quinolone, Antimicrob. Agents Chemother. 43 (1999) 1077–1084. https://doi.org/10.1128/aac.43.5.1077.

[79]   A. Maxwell, DNA gyrase as a drug target, Trends Microbiol. 5 (1997) 102–109. https://doi.org/10.1016/S0966-842X(96)10085-8.

[80]   F.L. Alovero, X.S. Pan, J.E. Morris, R.H. Manzo, L.M. Fisher, Engineering the specificity of antibacterial fluoroquinolones: Benzenesulfonamide modifications at C-7 of ciprofloxacin change its primary target in Streptococcus pneumoniae from topoisomerase IV to gyrase, Antimicrob. Agents Chemother. 44 (2000) 320–325. https://doi.org/10.1128/AAC.44.2.320-325.2000.

[81]   E.J.C. Goldstein, Possible role for the new fluoroquinolones (levofloxacin, grepafloxacin, trovafloxacin, clinafloxacin, sparfloxacin, and DU-6859a) in the treatment of anaerobic infections: Review of current information on efficacy and safety, Clin. Infect. Dis. 23 (1996) 25–30. https://doi.org/10.1093/clinids/23.supplement_1.s25.

[82] B. Weisblum, Erythromycin resistance by ribosome modification, Antimicrob. Agents Chemother. 39 (1995) 577–585. https://doi.org/10.1128/AAC.39.3.577.

[83] J. Retsema, W. Fu, Macrolides: Structures and microbial targets, Int. J. Antimicrob. Agents. 18 (2001) 3. https://doi.org/10.1016/s0924-8579(01)00401-0.

[84] M.R. Barbachyn, The Oxazolidinones, Top. Med. Chem. 26 (2018) 97–121. https://doi.org/10.1007/7355_2017_15.

[85] D. Niccolai, L. Tarsi, R.J. Thomas, The renewed challenge of antibacterial chemotherapy, Chem. Commun. (1997) 2333–2342. https://doi.org/10.1039/a704497f.

[86] A. Damasceno, Noncommunicable Disease, in: Hear. Africa (Eds S. Stewart, K. Sliwa, A. Mocumbi, A. Damasceno M. Ntsekhe), 2016: pp. 155–157. https://doi.org/10.1002/9781119097136.part5.

[87] G. Bérubé, How to utilize academic research efforts in cancer drug discovery, Expert Opin. Drug Discov. 14 (2019) 331–334. https://doi.org/10.1080/17460441.2019.1582637.

[88] Y. Imoto, Y. Yoshida, F. Yagisawa, H. Kuroiwa, T. Kuroiwa, The cell cycle, including the mitotic cycle and organelle division cycles, as revealed by cytological observations, J. Electron Microsc. (Tokyo). 60 (2011) 117–136. https://doi.org/10.1093/jmicro/dfr034.

[89] S. Florian, T.J. Mitchison, Anti-microtubule drugs, Methods Mol. Biol. 1413 (2016) 403–421. https://doi.org/10.1007/978-1-4939-3542-0_25.

[90] G. Chandrasekaran, P. Tátrai, F. Gergely, Hitting the brakes: Targeting microtubule motors in cancer, Br. J. Cancer. 113 (2015) 693–698. https://doi.org/10.1038/bjc.2015.264.

[91] E. Mukhtar, V.M. Adhami, H. Mukhtar, Targeting microtubules by natural agents for cancer therapy, Mol. Cancer Ther. 13 (2014) 275–284. https://doi.org/10.1158/1535-7163.MCT-13-0791.

[92] A. Jordan, J.A. Hadfield, N.J. Lawrence, A.T. McGown, Tubulin as a target for anticancer drugs: Agents which interact with the mitotic spindle, Med. Res. Rev. 18 (1998) 259–296. https://doi.org/10.1002/(SICI)1098-1128(199807)18:4<259::AID-MED3>3.0.CO;2-U.

[93] R. Kaul, A.L. Risinger, S.L. Mooberry, Microtubule-Targeting Drugs: More than Antimitotics, J. Nat. Prod. 82 (2019) 680–685. https://doi.org/10.1021/acs.jnatprod.9b00105.

[94] Y.N. Cao, L.L. Zheng, D. Wang, X.X. Liang, F. Gao, X.L. Zhou, Recent advances in microtubule-stabilizing agents, Eur. J. Med. Chem. 143 (2018) 806–828. https://doi.org/10.1016/j.ejmech.2017.11.062.

[95] S.K. Coulup, G.I. Georg, Revisiting microtubule targeting agents: α-Tubulin and the pironetin binding site as unexplored targets for cancer therapeutics, Bioorganic Med. Chem. Lett. 29 (2019) 1865–1873. https://doi.org/10.1016/j.bmcl.2019.05.042.

[96] M.C. Wani, H.L. Taylor, M.E. Wall, P. Coggon, A.T. Mcphail, Plant Antitumor Agents.VI.The Isolation and Structure of Taxol, a Novel Antileukemic and Antitumor

Agent from Taxus brevifolia2, J. Am. Chem. Soc. 93 (1971) 2325–2327. https://doi.org/10.1021/ja00738a045.

[97] E. Rowinsky, Antimitotic Drugs. In: Chabner BA, Longo DL (eds) Cancer Chemotherapy and Biotherapy: Principles and Practice. Lippincott Williams & Wilkins, Philadelphia, 2011.

[98] E. Nogales, S. Grayer Wolf, I.A. Khan, R.F. Ludueña, K.H. Downing, Structure of tubulin at 6.5 Å and location of the taxol-binding site, Nature. 375 (1995) 424–427. https://doi.org/10.1038/375424a0.

[99] E. Nogales, S.G. Wolf, K.H. Downing, Structure of the αβ tubulin dimer by electron crystallography, Nature. 391 (1998) 199–203. https://doi.org/10.1038/34465.

[100] R.L. Noble, C.T. Beer, J.H. Cutts, Role of change observations in chemotheraphy: Vinca rosea, Ann. N.Y. Acad. Sci. 76 (1958) 882–894. https://doi.org/10.1111/j.1749-6632.1958.tb54906.x.

[101] B. Gigant, C. Wang, R.B.G. Ravelli, F. Roussi, M.O. Steinmetz, P.A. Curmi, A. Sobel, M. Knossow, Structural basis for the regulation of tubulin by vinblastine, Nature. 435 (2005) 519–522. https://doi.org/10.1038/nature03566.

[102] D.E. Pryor, A. O'Brate, G. Bilcer, J.F. Díaz, Y. Wang, Y. Wang, M. Kabaki, M.K. Jung, J.M. Andreu, A.K. Ghosh, P. Giannakakou, E. Hamel, The microtubule stabilizing agent laulimalide does not bind in the taxoid site, kills cells resistant to paclitaxel and epothilones, and may not require its epoxide moiety for activity, Biochemistry. 41 (2002) 9109–9115. https://doi.org/10.1021/bi020211b.

[103] T.N. Gaitanos, R.M. Buey, J. Fernando Díaz, P.T. Northcote, P. Teesdale-Spittle, J.M. Andreu, J.H. Miller, Peloruside A does not bind to the taxoid site on β-tubulin and retains its activity in multidrug-resistant cell lines, Cancer Res. 64 (2004) 5063–5067. https://doi.org/10.1158/0008-5472.CAN-04-0771.

[104] A. Wilmes, K. Bargh, C. Kelly, P.T. Northcote, J.H. Miller, Peloruside A synergizes with other microtubule stabilizing agents in cultured cancer cell lines, Mol. Pharm. 4 (2007) 269–280. https://doi.org/10.1021/mp060101p.

[105] S. Kobayashi, K. Tsuchiya, M. Nishide, T. Nishikiori, T. Nakagawa, N. Shimada, Pironetin, a Novel Plant Growth Regulator Produced by Streptomyces sp. NK10958 III. Biosynthesis, J. Antibiot. (Tokyo). 48 (1995) 893–895. https://doi.org/10.7164/antibiotics.48.893.

[106] M. Kondoh, T. Usui, S. Kobayashi, K. Tsuchiya, K. Nishikawa, T. Nishikiori, T. Mayumi, H. Osada, Cell cycle arrest and antitumor activity of pironetin and its derivatives, Cancer Lett. 126 (1998) 29–32. https://doi.org/10.1016/S0304-3835(97)00528-4.

[107] A.E. Prota, K. Bargsten, J.F. Diaz, M. Marsh, C. Cuevas, M. Liniger, C. Neuhaus, J.M. Andreu, K.H. Altmann, M.O. Steinmetz, A new tubulin-binding site and pharmacophore for microtubule-destabilizing anticancer drugs, Proc. Natl. Acad. Sci. U. S. A. 111 (2014) 13817–13821. https://doi.org/10.1073/pnas.1408124111.

[108] G. Markel, M. Imazio, A. Brucato, Y. Adler, Prevention of recurrent pericarditis with colchicine in 2012, Clin. Cardiol. 36 (2013) 125–128. https://doi.org/10.1002/clc.22098.

[109] N.M. Ter Haar, J. Frenkel, Treatment of hereditary autoinflammatory diseases, Curr. Opin. Rheumatol. 26 (2014) 252–258. https://doi.org/10.1097/BOR.0000000000000059.

[110] G. Cocco, D.C.C. Chu, S. Pandolfi, Colchicine in clinical medicine. A guide for internists, Eur. J. Intern. Med. 21 (2010) 503–508. https://doi.org/10.1016/j.ejim.2010.09.010.

[111] A. Massarotti, A. Coluccia, R. Silvestri, G. Sorba, A. Brancale, The tubulin colchicine domain: A molecular modeling perspective, ChemMedChem. 7 (2012) 33–42. https://doi.org/10.1002/cmdc.201100361.

[112] Y. Lu, J. Chen, M. Xiao, W. Li, D.D. Miller, An overview of tubulin inhibitors that interact with the colchicine binding site, Pharm. Res. 29 (2012) 2943–2971. https://doi.org/10.1007/s11095-012-0828-z.

[113] A.M. Tsimberidou, W. Akerley, M.C. Schabel, D.S. Hong, C. Uehara, A. Chhabra, T. Warren, G.G. Mather, B.A. Evans, D.P. Woodland, E.A. Swabb, R. Kurzrock, Phase I clinical trial of MPC-6827 (Azixa), a microtubule destabilizing agent, in patients with advanced cancer, Mol. Cancer Ther. 9 (2010) 3410–3419. https://doi.org/10.1158/1535-7163.MCT-10-0516.

[114] J.Y. Bruce, J. Eickhoff, R. Pili, T. Logan, M. Carducci, J. Arnott, A. Treston, G. Wilding, G. Liu, A phase II study of 2-methoxyestradiol nanocrystal colloidal dispersion alone and in combination with sunitinib malate in patients with metastatic renal cell carcinoma progressing on sunitinib malate, Invest. New Drugs. 30 (2012) 794–802. https://doi.org/10.1007/s10637-010-9618-9.

[115] P. Liu, Y. Qin, L. Wu, S. Yang, N. Li, H. Wang, H. Xu, K. Sun, S. Zhang, X. Han, Y. Sun, Y. Shi, A phase i clinical trial assessing the safety and tolerability of combretastatin A4 phosphate injections, Anticancer. Drugs. 25 (2014) 462–471. https://doi.org/10.1097/CAD.0000000000000070.

[116] D.M. Patterson, M. Zweifel, M.R. Middleton, P.M. Price, L.K. Folkes, M.R.L. Stratford, P. Ross, S. Halford, J. Peters, J. Balkissoon, D.J. Chaplin, A.R. Padhani, G.J.S. Rustin, Phase I clinical and pharmacokinetic evaluation of the vascular-disrupting agent OXi4503 in patients with advanced solid tumors, Clin. Cancer Res. 18 (2012) 1415–1425. https://doi.org/10.1158/1078-0432.CCR-11-2414.

[117] P. Sanna, A. Carta, M.E.R. Nikookar, Synthesis and antitubercular activity of 3-aryl substituted-2-(1H(2H) benzotriazol-1(2)-yl)acrylonitriles, Eur. J. Med. Chem. 35 (2000) 535–543. https://doi.org/10.1016/S0223-5234(00)00144-6.

[118] P. Sanna, A. Carta, L. Gherardini, Synthesis and antimycobacterial activity of 3-aryl-, 3-cyclohexyl- and 3-heteroaryl-, Farm. 57 (2002) 79–87. https://doi.org/https://doi.org/10.1016/S0014-827X(01)01174-0.

[119] A. Carta, P. Sanna, M. Palomba, L. Vargiu, M. La Colla, R. Loddo, Synthesis and antiproliferative activity of 3-aryl-2-(1H-benzotriazol-1-yl)acrylonitriles. Part III, Eur. J. Med. Chem. 37 (2003) 891–900. https://doi.org/10.1016/S0223-5234(02)01411-3.

[120] A. Carta, M. Palomba, G. Boatto, B. Busonera, M. Murreddu, R. Loddo, Synthesis and antiproliferative activity of 3-aryl-2-[1H(2H)-benzotriazol- 1(2)-yl]acrylonitriles variously substituted: Part 4, Farmaco. 59 (2004) 637–644.

https://doi.org/10.1016/j.farmac.2004.03.004.

[121] A. Carta, I. Briguglio, S. Piras, G. Boatto, P. La Colla, R. Loddo, M. Tolomeo, S. Grimaudo, A. Di Cristina, R.M. Pipitone, E. Laurini, M.S. Paneni, P. Posocco, M. Fermeglia, S. Pricl, 3-Aryl-2-[1H-benzotriazol-1-yl]acrylonitriles: A novel class of potent tubulin inhibitors, Eur. J. Med. Chem. 46 (2011) 4151–4167. https://doi.org/10.1016/j.ejmech.2011.06.018.

[122] I. Briguglio, E. Laurini, M.A. Pirisi, S. Piras, P. Corona, M. Fermeglia, S. Pricl, A. Carta, Triazolopyridinyl-acrylonitrile derivatives as antimicrotubule agents: Synthesis, in vitro and in silico characterization of antiproliferative activity, inhibition of tubulin polymerization and binding thermodynamics, Eur. J. Med. Chem. 141 (2017) 460–472. https://doi.org/10.1016/j.ejmech.2017.09.065.

[123] S. Purser, P.R. Moore, S. Swallow, V. Gouverneur, Fluorine in medicinal chemistry, Chem. Soc. Rev. 37 (2008) 320–330. https://doi.org/10.1039/b610213c.

[124] H. van de W. and D.K.W. D. A. Smith, Methods and Principles in Medicinal Chemistry, vol. 31: Pharmacokinetics and Metabolism in Drug Design, , Wiley-VCH, Weinheim, 2006.

[125] B.E. Smart, Fluorine substituent effects (on bioactivity), J. Fluor. Chem. 109 (2001) 3–11. https://doi.org/10.1016/S0022-1139(01)00375-X.

[126] F. Riu, L. Sanna, R. Ibba, S. Piras, V. Bordoni, M.A. Scorciapino, M. Lai, S. Sestito, L. Bagella, A. Carta, A comprehensive assessment of a new series of 5′,6′-difluorobenzotriazole-acrylonitrile derivatives as microtubule targeting agents (MTAs), Eur. J. Med. Chem. 222 (2021) 113590. https://doi.org/10.1016/j.ejmech.2021.113590.

[127] H.M. Berman, T. Battistuz, T.N. Bhat, W.F. Bluhm, P.E. Bourne, K. Burkhardt, Z. Feng, G.L. Gilliland, L. Iype, S. Jain, P. Fagan, J. Marvin, D. Padilla, V. Ravichandran, B. Schneider, N. Thanki, H. Weissig, J.D. Westbrook, C. Zardecki, The protein data bank, Acta Crystallogr. Sect. D Biol. Crystallogr. 58 (2002) 899–907. https://doi.org/10.1107/S0907444902003451.

[128] A.E. Prota, F. Danel, F. Bachmann, K. Bargsten, R.M. Buey, J. Pohlmann, S. Reinelt, H. Lane, M.O. Steinmetz, The novel microtubule-destabilizing drug BAL27862 binds to the colchicine site of tubulin with distinct effects on microtubule organization, J. Mol. Biol. 426 (2014) 1848–1860. https://doi.org/10.1016/j.jmb.2014.02.005.

[129] L. Schrödinger, W. DeLano, PyMOL, (2020). http://www.pymol.org/pymol.

[130] Maestro, Schrödinger Release 2021-4, (2021).

[131] K. Eskandari, M. Lesani, Does fluorine participate in halogen bonding?, Chem. - A Eur. J. 21 (2015) 4739–4746. https://doi.org/10.1002/chem.201405054.

[132] G.M. Morris, R. Huey, W. Lindstrom, M.F. Sanner, R.K. Belew, D.S. Goodsell, A.J. Olson, AutoDock4 and AutoDockTools4: Automated docking with selective receptor flexibility, J. Comput. Chem. 30 (2009) 2785–2791. https://doi.org/10.1002/jcc.21256.AutoDock4.

[133] N. Mase, T. Horibe, Organocatalytic knoevenagel condensations by means of carbamic acid ammonium salts, Org. Lett. 15 (2013) 1854–1857. https://doi.org/10.1021/ol400462d.

[134] C.S. See, M. Kitagawa, P.J. Liao, K.H. Lee, J. Wong, S.H. Lee, B.W. Dymock, Discovery of the cancer cell selective dual acting anti-cancer agent (Z)-2-(1H-indol-3-yl)-3-(isoquinolin-5-yl)acrylonitrile (A131), Eur. J. Med. Chem. 156 (2018) 344–367. https://doi.org/10.1016/j.ejmech.2018.07.011.

[135] L. Sanna, R. Piredda, I. Marchesi, V. Bordoni, S.V. Forcales, D.F. Calvisi, L. Bagella, "Verteporfin exhibits anti-proliferative activity in embryonal and alveolar rhabdomyosarcoma cell lines," Chem. Biol. Interact. 312 (2019) 108813. https://doi.org/10.1016/j.cbi.2019.108813.

[136] J. Barretina, G. Caponigro, N. Stransky, K. Venkatesan, A.A. Margolin, S. Kim, C.J. Wilson, J. Lehár, G. V. Kryukov, D. Sonkin, A. Reddy, M. Liu, L. Murray, M.F. Berger, J.E. Monahan, P. Morais, J. Meltzer, A. Korejwa, J. Jané-Valbuena, F.A. Mapa, J. Thibault, E. Bric-Furlong, P. Raman, A. Shipway, I.H. Engels, J. Cheng, G.K. Yu, J. Yu, P. Aspesi, M. De Silva, K. Jagtap, M.D. Jones, L. Wang, C. Hatton, E. Palescandolo, S. Gupta, S. Mahan, C. Sougnez, R.C. Onofrio, T. Liefeld, L. MacConaill, W. Winckler, M. Reich, N. Li, J.P. Mesirov, S.B. Gabriel, G. Getz, K. Ardlie, V. Chan, V.E. Myer, B.L. Weber, J. Porter, M. Warmuth, P. Finan, J.L. Harris, M. Meyerson, T.R. Golub, M.P. Morrissey, W.R. Sellers, R. Schlegel, L.A. Garraway, The Cancer Cell Line Encyclopedia enables predictive modelling of anticancer drug sensitivity, Nature. 483 (2012) 603–607. https://doi.org/10.1038/nature11003.

[137] Y. Wang, H. Zhang, B. Gigant, Y. Yu, Y. Wu, X. Chen, Q. Lai, Z. Yang, Q. Chen, J. Yang, Structures of a diverse set of colchicine binding site inhibitors in complex with tubulin provide a rationale for drug discovery, FEBS J. 283 (2016) 102–111. https://doi.org/10.1111/febs.13555.

[138] Z. Zhang, C. Wang, L. Ma, X. Jiang, C. Wu, Y. Wang, Y. Jiang, W. Zheng, Y. Yang, Y. Ma, J. Yang, Molecular mechanism of crolibulin in complex with tubulin provides a rationale for drug design, Biochem. Biophys. Res. Commun. 511 (2019) 381–386. https://doi.org/10.1016/j.bbrc.2019.02.064.

[139] E.R. Caremoli, R. Labianca, Tivantinib: Critical review with a focus on hepatocellular carcinoma, Expert Opin. Investig. Drugs. 23 (2014) 1563–1574. https://doi.org/10.1517/13543784.2014.949339.

[140] Y.K. Kang, K. Muro, M.H. Ryu, H. Yasui, T. Nishina, B.Y. Ryoo, Y. Kamiya, S. Akinaga, N. Boku, A phase II trial of a selective c-Met inhibitor tivantinib (ARQ 197) monotherapy as a second- or third-line therapy in the patients with metastatic gastric cancer, Invest. New Drugs. 32 (2014) 355–361. https://doi.org/10.1007/s10637-013-0057-2.

[141] J.W. Goldman, I. Laux, F. Chai, R.E. Savage, D. Ferrari, E.G. Garmey, R.G. Just, L.S. Rosen, Phase 1 dose-escalation trial evaluating the combination of the selective MET (mesenchymal-epithelial transition factor) inhibitor tivantinib (ARQ 197) plus erlotinib, Cancer. 118 (2012) 5903–5911. https://doi.org/10.1002/cncr.27575.

[142] A. Aoyama, R. Katayama, T. Oh-hara, S. Sato, Y. Okuno, N. Fujita, Tivantinib (ARQ 197) exhibits antitumor activity by directly interacting with tubulin and overcomes ABC transporter-mediated drug resistance, Mol. Cancer Ther. 13 (2014) 2978–2990. https://doi.org/10.1158/1535-7163.MCT-14-0462.

[143] M.M. Mita, M.A. Spear, L.K. Yee, A.C. Mita, E.I. Heath, K.P. Papadopoulos, K.C. Federico, S.D. Reich, O. Romero, L. Malburg, M.J. Pilat, G.K. Lloyd, S.T.C.

Neuteboom, G. Cropp, E. Ashton, P.M. LoRusso, Phase 1 first-in-human trial of the vascular disrupting agent plinabulin (NPI-2358) in patients with solid tumors or lymphomas, Clin. Cancer Res. 16 (2010) 5892–5899. https://doi.org/10.1158/1078-0432.CCR-10-1096.

[144] M. Millward, P. Mainwaring, A. Mita, K. Federico, G.K. Lloyd, N. Reddinger, S. Nawrocki, M. Mita, M.A. Spear, Phase 1 study of the novel vascular disrupting agent plinabulin (NPI-2358) and docetaxel, Invest. New Drugs. 30 (2012) 1065–1073. https://doi.org/10.1007/s10637-011-9642-4.

[145] R.O. Carlson, New tubulin targeting agents currently in clinical development, Expert Opin. Investig. Drugs. 17 (2008) 707–722. https://doi.org/10.1517/13543784.17.5.707.

[146] J.J. Field, A. Kanakkanthara, J.H. Miller, Microtubule-targeting agents are clinically successful due to both mitotic and interphase impairment of microtubule function, Bioorganic Med. Chem. 22 (2014) 5050–9. https://doi.org/10.1016/j.bmc.2014.02.035.

[147] T.F. Greene, S. Wang, L.M. Greene, S.M. Nathwani, J.K. Pollock, A.M. Malebari, T. McCabe, B. Twamley, N.M. OBoyle, D.M. Zisterer, M.J. Meegan, Synthesis and Biochemical Evaluation of 3-Phenoxy-1,4-diarylazetidin-2-ones as Tubulin-Targeting Antitumor Agents, J. Med. Chem. 59 (2016) 90–113. https://doi.org/10.1021/acs.jmedchem.5b01086.

[148] J. Kalmuk, M. Folaron, J. Buchinger, R. Pili, M. Seshadri, Multimodal imaging guided preclinical trials of vascular targeting in prostate cancer, Oncotarget. 6 (2015) 24376–24392. https://doi.org/10.18632/oncotarget.4463.

[149] M. Folaron, M. Seshadri, Bioluminescence and MR Imaging of the Safety and Efficacy of Vascular Disruption in Gliomas, Mol. Imaging Biol. 18 (2016) 860–869. https://doi.org/10.1007/s11307-016-0963-8.

[150] W.L. Read, P. Rosen, P. Lee, S. Anthony, R. Korn, N. Raghunand, B. Tseng, J. Whisnant, D. Von Hoff, R. Tibes, Pharmacokinetic and pharmacodynamic results of a 4-hr IV administration phase I study with EPC2407, a novel vascular disrupting agent, J. Clin. Oncol. 27 (2009) 3569. https://doi.org/10.1200/jco.2009.27.15_suppl.3569.

[151] I.M. Subbiah, D.J. Lenihan, A.M. Tsimberidou, Cardiovascular Toxicity Profiles of Vascular-Disrupting Agents, Oncologist. 16 (2011) 1120–1130. https://doi.org/10.1634/theoncologist.2010-0432.

[152] L. RA, S. MB, LigPlot+: multiple ligand-protein interaction diagrams for drug discovery, J. Chem. Inf. Model. 51 (2011) 2778–2786.

[153] A. Carta, A. Bua, P. Corona, S. Piras, I. Briguglio, P. Molicotti, S. Zanetti, E. Laurini, S. Aulic, M. Fermeglia, S. Pricl, Design, synthesis and antitubercular activity of 4-alkoxy-triazoloquinolones able to inhibit the M. tuberculosis DNA gyrase, Eur. J. Med. Chem. 161 (2019) 399–415. https://doi.org/10.1016/j.ejmech.2018.10.031.

[154] S. Levin, The crisis in antibiotic resistance, Infect. Dis. Clin. Pract. 2 (1993) 53. https://doi.org/10.1097/00019048-199301000-00013.

[155] P.G. Higgins, C. Dammhayn, M. Hackel, H. Seifert, Global spread of carbapenem-

resistant Acinetobacter baumannii, J. Antimicrob. Chemother. 65 (2009) 233–238. https://doi.org/10.1093/jac/dkp428.

[156] M. McKenna, Antibiotic resistance: The last resort, Nature. 499 (2013) 394–396. https://doi.org/10.1038/499394a.

[157] J. Vila, J.L. Martinez, Clinical Impact of the Over-Expression of Efflux Pump in Nonfermentative Gram-Negative Bacilli, Development of Efflux Pump Inhibitors, Curr. Drug Targets. 9 (2008) 797–807.

[158] R.E. Christoffersen, Antibiotics - An investment worth making?, Nat. Biotechnol. 24 (2006) 1512–1514. https://doi.org/10.1038/nbt1206-1512.

[159] K. Lewis, Platforms for antibiotic discovery, Nat. Rev. Drug Discov. 12 (2013) 371–387. https://doi.org/10.1038/nrd3975.

[160] L.R. Peterson, Bad Bugs, No Drugs: No ESCAPE Revisited, Clin. Infect. Dis. 49 (2009) 992–993. https://doi.org/10.1086/605540.

[161] P. Bernal, C. Molina-Santiago, A. Daddaoua, M.A. Llamas, Antibiotic adjuvants: Identification and clinical use, Microb. Biotechnol. 6 (2013) 445–449. https://doi.org/10.1111/1751-7915.12044.

[162] L. Ejim, M.A. Farha, S.B. Falconer, J. Wildenhain, B.K. Coombes, M. Tyers, E.D. Brown, G.D. Wright, Combinations of antibiotics and nonantibiotic drugs enhance antimicrobial efficacy, Nat. Chem. Biol. 7 (2011) 348–350. https://doi.org/10.1038/nchembio.559.

[163] P.L. Taylor, L. Rossi, G. De Pascale, G.D. Wright, A forward chemical screen identifies antibiotic adjuvants in Escherichia coli, ACS Chem. Biol. 7 (2012) 1547–1555. https://doi.org/10.1021/cb300269g.

[164] T.L. Harris, R.J. Worthington, L.E. Hittle, D. V. Zurawski, R.K. Ernst, C. Melander, Small molecule downregulation of PmrAB reverses lipid a modification and breaks colistin resistance, ACS Chem. Biol. 9 (2014) 122–127. https://doi.org/10.1021/cb400490k.

[165] R.J. Worthington, C. Melander, Combination approaches to combat multidrug-resistant bacteria, Trends Biotechnol. 31 (2013) 177–184. https://doi.org/10.1016/j.tibtech.2012.12.006.

[166] M.A. Croxen, B.B. Finlay, Molecular mechanisms of Escherichia coli pathogenicity, Nat. Rev. Microbiol. 8 (2010) 26–38. https://doi.org/10.1038/nrmicro2265.

[167] World Health Organization, Prioritization of pathogens to guide discovery, research and development of new antibiotics for drug resistant bacterial infections, including tuberculosis, (2017).

[168] World Health Organization, Outbreaks of E. coli O104:H4 infection, 2011.

[169] World Health Organization, Antimicrobial resistance, 2020.

[170] A.H. Delcour, Outer membrane permeability and antibiotic resistance, Biochim. Biophys. Acta - Proteins Proteomics. 1794 (2009) 808–816. https://doi.org/10.1016/j.bbapap.2008.11.005.

[171] J.M. Pagès, C.E. James, M. Winterhalter, The porin and the permeating antibiotic: A

selective diffusion barrier in Gram-negative bacteria, Nat. Rev. Microbiol. 6 (2008) 893–903. https://doi.org/10.1038/nrmicro1994.

[172] G. Cox, G.D. Wright, Intrinsic antibiotic resistance: Mechanisms, origins, challenges and solutions, Int. J. Med. Microbiol. 303 (2013) 287–292. https://doi.org/10.1016/j.ijmm.2013.02.009.

[173] J.M. Bolla, S. Alibert-Franco, J. Handzlik, J. Chevalier, A. Mahamoud, G. Boyer, K. Kieć-Kononowicz, J.M. Pags, Strategies for bypassing the membrane barrier in multidrug resistant Gram-negative bacteria, FEBS Lett. 585 (2011) 1682–1690. https://doi.org/10.1016/j.febslet.2011.04.054.

[174] H. Nikaido, Outer membrane. In: Neidhardt F C, Curtiss III R, Ingraham J L, Lin E C C, Low K B Jr, Magasanik B, Reznikoff W S, Riley M, Schaechter M, Umbarger H E, editors. Escherichia coli and Salmonella: cellular and molecular biology. 2nd ed. Washington, D.C: Amer, Microbiol. Mol. Biol. Rev. 67 (1996) 29–47. https://doi.org/10.1128/MMBR.67.4.593.

[175] N. Ruiz, T. Wu, D. Kahne, T.J. Silhavy, Probing the barrier function of the outer membrane with chemical conditionality., ACS Chem. Biol. 1 (2006) 385–395. https://doi.org/10.1021/cb600128v.

[176] C.R.H. Raetz, C. Whitfield, Lipopolysaccharide endotoxins, Annu. Rev. Biochem. 71 (2002) 635–700. https://doi.org/10.1146/annurev.biochem.71.110601.135414.

[177] J. Ståhle, G. Widmalm, Lipopolysaccharides of gram-negative bacteria: Biosynthesis and structural aspects, Trends Glycosci. Glycotechnol. 31 (2019) E159–E171. https://doi.org/10.4052/tigg.1749.7E.

[178] H. Heine, E.T. Rietschel, A.J. Ulmer, The biology of endotoxin, Appl. Biochem. Biotechnol. - Part B Mol. Biotechnol. 19 (2001) 279–296. https://doi.org/10.1385/MB:19:3:279.

[179] M. Caroff, D. Karibian, Structure of bacterial lipopolysaccharides, Carbohydr. Res. 338 (2003) 2431–2447. https://doi.org/10.1016/j.carres.2003.07.010.

[180] R. Jerala, Structural biology of the LPS recognition, Int. J. Med. Microbiol. 297 (2007) 353–363. https://doi.org/10.1016/j.ijmm.2007.04.001.

[181] F. Di Lorenzo, K.A. Duda, R. Lanzetta, A. Silipo, C. De Castro, A. Molinaro, A Journey from Structure to Function of Bacterial Lipopolysaccharides, Chem. Rev. (2021). https://doi.org/10.1021/acs.chemrev.0c01321.

[182] S. Neelamegham, K. Aoki-Kinoshita, E. Bolton, M. Frank, F. Lisacek, T. Lütteke, N. O'Boyle, N.H. Packer, P. Stanley, P. Toukach, A. Varki, R.J. Woods, Updates to the Symbol Nomenclature for Glycans guidelines, Glycobiology. 29 (2019) 620–624. https://doi.org/10.1093/glycob/cwz045.

[183] E. V. Vinogradov, K. Van Der Drift, J.E. Thomas-Oates, S. Meshkov, H. Brade, O. Holst, The structures of the carbohydrate backbones of the lipopolysaccharides from Escherichia coli rough mutants F470 (R1 core type) and F576 (R2 core type), Eur. J. Biochem. (1999). https://doi.org/10.1046/j.1432-1327.1999.00280.x.

[184] N.A. Thornberry, Caspases: A decade of death research, Cell Death Differ. 6 (1999) 1023–1027. https://doi.org/10.1038/sj.cdd.4400607.

[185] R.& Ruddiman, N.A. Thornberry, H.G. Bull, J.R. Calaycay, K.T. Chapman, A.D. Howard, M.J. Kostura, D.K. Miller, S.M. Molineaux, J.R. Weidner, J. Aunins, K.O. Elliston, J.M. Ayala, F.J. Casano, J. Chin, G.J.-F. Ding, L.A. Egger, E.P. Gaffney, G. Limjuco, O.C. Palyha, S.M. Raju, A.M. Rolando, J.P. Salley, T.-T. Yamin, T.D. Lee, J.E. Shively, M. MacCross, R.A. Mumford, J.A. Schmidt, M.J. Tocci, A novel heterodimeric cysteine protease is required for interleukin-1β processing in monocytes, Nature. 355 (1992) 242–244. https://doi.org/10.1038/355242a0.

[186] S.L. Fink, B.T. Cookson, Apoptosis, pyroptosis, and necrosis: Mechanistic description of dead and dying eukaryotic cells, Infect. Immun. 73 (2005) 1907–1916. https://doi.org/10.1128/IAI.73.4.1907-1916.2005.

[187] C. Martinez-Fleites, M. Proctor, S. Roberts, D.N. Bolam, H.J. Gilbert, G.J. Davies, Insights into the Synthesis of Lipopolysaccharide and Antibiotics through the Structures of Two Retaining Glycosyltransferases from Family GT4, Chem. Biol. 13 (2006) 1143–1152. https://doi.org/10.1016/j.chembiol.2006.09.005.

[188] J.A. Yethon, E. Vinogradov, M.B. Perry, C. Whitfield, Mutation of the lipopolysaccharide core glycosyltransferase encoded by waaG destabilizes the outer membrane of Escherichia coli by interfering with core phosphorylation, J. Bacteriol. 182 (2000) 5620–5623. https://doi.org/10.1128/JB.182.19.5620-5623.2000.

[189] A. Liu, L. Tran, E. Becket, K. Lee, L. Chinn, E. Park, K. Tran, J.H. Miller, Antibiotic sensitivity profiles determined with an Escherichia coli gene knockout collection: Generating an antibiotic bar code, Antimicrob. Agents Chemother. 54 (2010) 1393–1403. https://doi.org/10.1128/AAC.00906-09.

[190] A.J. Price, S. Howard, B.D. Cons, Fragment-based drug discovery and its application to challenging drug targets, Essays Biochem. 61 (2017) 475–484. https://doi.org/10.1042/EBC20170029.

[191] J. Landström, K. Persson, C. Rademacher, M. Lundborg, W. Wakarchuk, T. Peters, G. Widmalm, Small molecules containing hetero-bicyclic ring systems compete with UDP-Glc for binding to WaaG glycosyltransferase, Glycoconj. J. 29 (2012) 491–502. https://doi.org/10.1007/s10719-012-9411-4.

[192] C. Muheim, A. Bakali, O. Engström, Å. Wieslander, D.O. Daley, G. Widmalm, Identification of a fragment-based scaffold that inhibits the glycosyltransferase WaaG from Escherichia Coli, Antibiotics. 5 (2016) 10. https://doi.org/10.3390/antibiotics5010010.

[193] Y. Bian, X.Q. (Sean) Xie, Computational Fragment-Based Drug Design: Current Trends, Strategies, and Applications, AAPS J. 20 (2018) 59. https://doi.org/10.1208/s12248-018-0216-7.

[194] B. Meyer, T. Peters, NMR spectroscopy techniques for screening and identifying ligand binding to protein receptors, Angew. Chemie - Int. Ed. 42 (2003) 864–890. https://doi.org/10.1002/anie.200390233.

[195] S. Walpole, S. Monaco, R. Nepravishta, J. Angulo, STD NMR as a Technique for Ligand Screening and Structural Studies, 1st ed., Elsevier Inc., 2019. https://doi.org/10.1016/bs.mie.2018.08.018.

[196] Z. Wang, H. Sun, X. Yao, D. Li, L. Xu, Y. Li, S. Tian, T. Hou, Comprehensive evaluation of ten docking programs on a diverse set of protein-ligand complexes: The

prediction accuracy of sampling power and scoring power, Phys. Chem. Chem. Phys. 18 (2016) 12964–12975. https://doi.org/10.1039/c6cp01555g.

[197] A. Allouche, Software News and Updates Gabedit — A Graphical User Interface for Computational Chemistry Softwares, J. Comput. Chem. 32 (2012) 174–182. https://doi.org/10.1002/jcc.

[198] N. Liu, Z. Xu, Using LeDock as a docking tool for computational drug design, IOP Conf. Ser. Earth Environ. Sci. 218 (2019) 012143. https://doi.org/10.1088/1755-1315/218/1/012143.

[199] S. Ruiz-Carmona, D. Alvarez-Garcia, N. Foloppe, A.B. Garmendia-Doval, S. Juhos, P. Schmidtke, X. Barril, R.E. Hubbard, S.D. Morley, rDock: A Fast, Versatile and Open Source Program for Docking Ligands to Proteins and Nucleic Acids, PLoS Comput. Biol. 10 (2014) 1–7. https://doi.org/10.1371/journal.pcbi.1003571.

[200] J.W. Liebeschuetz, J.C. Cole, O. Korb, Pose prediction and virtual screening performance of GOLD scoring functions in a standardized test, J. Comput. Aided. Mol. Des. 26 (2012) 737–748. https://doi.org/10.1007/s10822-012-9551-4.

[201] J. Landström, M. Bergström, C. Hamark, S. Ohlson, G. Widmalm, Combining weak affinity chromatography, NMR spectroscopy and molecular simulations in carbohydrate-lysozyme interaction studies, Org. Biomol. Chem. 10 (2012) 3019–3032. https://doi.org/10.1039/c2ob07066a.

[202] J. Åqvist, C. Medina, J.E. Samuelsson, A new method for predicting binding affinity in computer-aided drug design, Protein Eng. Des. Sel. 7 (1994) 385–391. https://doi.org/10.1093/protein/7.3.385.

[203] E.A. Rifai, M. van Dijk, D.P. Geerke, Recent Developments in Linear Interaction Energy Based Binding Free Energy Calculations, Front. Mol. Biosci. 7 (2020) 1–7. https://doi.org/10.3389/fmolb.2020.00114.

[204] N.S. Chandel, Carbohydrate metabolism, Cold Spring Harb. Perspect. Biol. 13 (2021) 1–15. https://doi.org/10.1101/cshperspect.a040568.

[205] B.G. Davis, A.J. Fairbanks, Carbohydrate Chemistry, Oxford University Press, Oxford, 2002.

[206] K. Furukawa, K. Takamiya, M. Okada, M. Inoue, S. Fukumoto, K. Furukawa, Novel functions of complex carbohydrates elucidated by the mutant mice of glycosyltransferase genes, Biochim. Biophys. Acta - Gen. Subj. 1525 (2001) 1–12. https://doi.org/10.1016/S0304-4165(00)00185-9.

[207] C. Zhao, M. Li, Y. Luo, W. Wu, Isolation and structural characterization of an immunostimulating polysaccharide from fuzi, Aconitum carmichaeli, Carbohydr. Res. 341 (2006) 485–491. https://doi.org/10.1016/j.carres.2005.11.032.

[208] V.C.B. Bittencourt, R.T. Figueiredo, R.B. Da Silva, D.S. Mourão-Sá, P.L. Fernandez, G.L. Sassaki, B. Mulloy, M.T. Bozza, E. Barreto-Bergter, An α-glucan of Pseudallescheria boydii is involved in fungal phagocytosis and toll-like receptor activation, J. Biol. Chem. 281 (2006) 22614–22623. https://doi.org/10.1074/jbc.M511417200.

[209] S.S. Nigudkar, A. V. Demchenko, Stereocontrolled 1,2-cis glycosylation as the driving force of progress in synthetic carbohydrate chemistry, Chem. Sci. 6 (2015)

2687–2704. https://doi.org/10.1039/c5sc00280j.

[210] D. Crich, Mechanism of a chemical glycosylation reaction, Acc. Chem. Res. 43 (2010) 1144–1153. https://doi.org/10.1021/ar100035r.

[211] D. Crich, Methodology development and physical organic chemistry: A powerful combination for the advancement of glycochemistry, J. Org. Chem. 76 (2011) 9193–9209. https://doi.org/10.1021/jo2017026.

[212] M. Miljkovic, T. Satoh, M. Konopka, E.A. Davidson, D. Miljkovic, Neighboring-Group Participation in Carbohydrate Chemistry. IV.1 Neighboring-Group Reaction of the 6-Benzamido Group in a Nucleophilic Displacement of a 5-Mesylate, J. Org. Chem. 38 (1973) 716–719. https://doi.org/10.1021/jo00944a022.

[213] B. Fraser-Reid, J.C. Lopez, Armed–Disarmed Effects in Carbohydrate Chemistry: History, Synthetic and Mechanistic Studies, Top Curr Chem. 301 (2011) 1–29. https://doi.org/10.1007/128_2010_105.

[214] Y. Bai, T.L. Lowary, 2,3-Anhydrosugars in Glycoside Bond Synthesis. Application to α-d-Galactofuranosides, J. Org. Chem. 71 (2006) 9658–9671. https://doi.org/https://doi.org/10.1021/jo061713o.

[215] X. Zhu, S. Kawatkar, Y. Rao, G.J. Boons, Practical approach for the stereoselective introduction of β-arabinofuranosides, J. Am. Chem. Soc. 128 (2006) 11948–11957. https://doi.org/10.1021/ja0629817.

[216] D. Crich, C.M. Pedersen, A.A. Bowers, D.J. Wink, On the use of 3,5-O-benzylidene and 3,5-O-(Di-tert-butylsilylene)-2-O- benzylarabinothiofuranosides and their sulfoxides as glycosyl donors for the synthesis of β-arabinofuranosides: Importance of the activation method, J. Org. Chem. 72 (2007) 1553–1565. https://doi.org/10.1021/jo061440x.

[217] R.M. Kipp, A.K. Bogdanoff, A. Fusaro, R. Sturtevant, Aeromonas salmonicida Emmerich and Weible, 1890: U.S. Geological Survey, Nonindigenous Aquatic Species Database, Gainesville, FL, and NOAA Great Lakes Aquatic Nonindigenous Species Information System, Ann Arbor, MI, (2021).

[218] M. Hiney, G. Olivier, Furunculosis (Aeromonas salmonicida), in: Fish Dis. Disord. III Viral, Bact. Fungal Infect., 1st ed., CAB International Publishing, Wallingford, 1999: pp. 341–425.

[219] G.L. Bullock, B.R. Griffin, H.B. Stuckey, Detection of Corynebacterium salmoninus by direct fluorescent antibody test, Can. J. Fish. Aquat. Sci. 37 (1980) 719–721. https://doi.org/https://doi.org/10.1139/f80-092.

[220] H. Chart, D.H. Shaw, E.E. Ishiguro, T.J. Trust, Structural and immunochemical homogeneity of Aeromonas salmonicida lipopolysaccharide, J. Bacteriol. 158 (1984) 16–22. https://doi.org/10.1128/jb.158.1.16-22.1984.

[221] A.T. Vincent, A. Fernández-Bravo, M. Sanchis, E. Mayayo, M.J. Figueras, S.J. Charette, Investigation of the virulence and genomics of Aeromonas salmonicida strains isolated from human patients, Infect. Genet. Evol. 68 (2019) 1–9. https://doi.org/10.1016/j.meegid.2018.11.019.

[222] M.E. Pavan, S.L. Abbott, J. Zorzópulos, J.M. Janda, Aeromonas salmonicida subsp. pectinolytica subsp. nov., a new pectinase- positive subspecies isolated from a heavily

polluted river, Int. J. Syst. Evol. Microbiol. 50 (2000) 1119–1124. https://doi.org/10.1099/00207713-50-3-1119.

[223] X. Yang, Q.Q. Yang, Q.Y. Guo, C.Y. Yi, H.P. Mao, J.X. Lin, Z.P. Jiang, X.Q. Yu, Aeromonas salmonicida peritonitis after eating fish in a patient undergoing CAPD, Perit. Dial. Int. 28 (2008) 316–317. https://doi.org/10.1177/089686080802800323.

[224] R. Tewari, M. Dudeja, S. Nandy, A.K. Das, Isolation of Aeromonas salmonicida from human blood sample: A case report, J. Clin. Diagnostic Res. 8 (2014) 139–140. https://doi.org/10.7860/JCDR/2014/6883.4032.

[225] W.D. Paterson, R.J. Douglas, I. Grinyer, L.A. McDermott, Isolation and Preliminary Characterization of Some Aeromonas salmonicida Bacteriophages , J. Fish. Res. Board Canada. 26 (1969) 629–632. https://doi.org/10.1139/f69-056.

[226] A.T. Vincent, M. V. Trudel, L. Freschi, V. Nagar, C. Gagné-Thivierge, R.C. Levesque, S.J. Charette, Increasing genomic diversity and evidence of constrained lifestyle evolution due to insertion sequences in Aeromonas salmonicida, BMC Genomics. 17 (2016) 1–12. https://doi.org/10.1186/s12864-016-2381-3.

[227] R. Ruhal, K. Rashmi, Biofilm patterns in gram-positive and gram-negative bacteria, Microbiol. Res. 251 (2021) 126829. https://doi.org/https://doi.org/10.1016/j.micres.2021.126829.

[228] D.H.S.Y. Lee, M.J. Squires, O. Luderitz, Structural Studies on the O-Antigen of Aeromonas salmonicida, Eur J Biochem. 638 (1983) 633–638. https://doi.org/10.1111/j.1432-1033.1983.tb07310.x.

[229] J. Landström, G. Widmalm, Glycan flexibility: insights into nanosecond dynamics from a microsecond molecular dynamics simulation explaining an unusual nuclear Overhauser effect, Carbohydr. Res. 345 (2010) 330–333. https://doi.org/10.1016/j.carres.2009.11.003.

[230] J. Landström, G. Widmalm, Glycan flexibility: insights into nanosecond dynamics from a microsecond molecular dynamics simulation explaining an unusual nuclear Overhauser effect, Carbohydr. Res. 345 (2010) 330–333. https://doi.org/10.1016/j.carres.2009.11.003.

[231] F. Nicotra, C. Airoldi, F. Cardona, Synthesis of C- and S-Glycosides, Compr. Glycosci. From Chem. to Syst. Biol. 1–4 (2007) 647–683. https://doi.org/10.1016/B978-044451967-2/00017-9.

[232] B.S. Komarova, Y.E. Tsvetkov, N.E. Nifantiev, Design of α-Selective Glycopyranosyl Donors Relying on Remote Anchimeric Assistance, Chem. Rec. 16 (2016) 488–506. https://doi.org/10.1002/tcr.201500245.

[233] Z. Wang, E. Vinogradov, S. Larocque, B.A. Harrison, J. Li, E. Altman, Structural and serological characterization of the O-chain polysaccharide of Aeromonas salmonicida strains A449, 80204 and 80204-1, Carbohydr. Res. 340 (2005) 693–700. https://doi.org/10.1016/j.carres.2005.01.009.

[234] J. Xia, S.A. Abbas, R.D. Locke, C.F. Piskorz, J.L. Alderfer, K.L. Matta, Use of 1,2-dichloro 4,5-dicyanoquinone (DDQ) for cleavage of the 2- naphthylmethyl (NAP) group, Tetrahedron Lett. 41 (2000) 169–173. https://doi.org/10.1016/S0040-4039(99)02046-8.

[235] D. Crich, N.S. Chandrasekera, Mechanism of 4,6-O-benzylidene-directed β-mannosylation as determined by α-deuterium kinetic isotope effects, Angew. Chemie - Int. Ed. 43 (2004) 5386–5389. https://doi.org/10.1002/anie.200453688.

[236] M. Sasaki, K. Tachibana, H. Nakanishi, An efficient and stereocontrolled synthesis of the nephritogenoside core structure, Tetrahedron Lett. 32 (1991) 6873–6876. https://doi.org/10.1016/0040-4039(91)80430-E.

[237] C. Alex, S. Visansirikul, Y. Zhang, J.P. Yasomanee, J. Codee, A. V. Demchenko, Synthesis of 2-azido-2-deoxy- and 2-acetamido-2-deoxy-D-manno derivatives as versatile building blocks, Carbohydr. Res. 488 (2020) 107900. https://doi.org/10.1016/j.carres.2019.107900.

[238] C. Alex, S. Visansirikul, A. V. Demchenko, A versatile approach to the synthesis of mannosamine glycosides, Org. Biomol. Chem. 18 (2020) 6682–6695. https://doi.org/10.1039/d0ob01640c.

[239] B. Mukhopadhyay, R.A. Field, A simple one-pot method for the synthesis of partially protected mono- and disaccharide building blocks using an orthoesterification-benzylation-orthoester rearrangement approach, Carbohydr. Res. 338 (2003) 2149–2152. https://doi.org/10.1016/S0008-6215(03)00349-5.

[240] A.L. Chauvin, S.A. Nepogodiev, R.A. Field, Synthesis of a 2,3,4-triglycosylated rhamnoside fragment of rhamnogalacturonan-II side chain a using a late stage oxidation approach, J. Org. Chem. 70 (2005) 960–966. https://doi.org/10.1021/jo0482864.

[241] J. seong Yoon, D.B. Jarhad, G. Kim, A. Nayak, L.X. Zhao, J. Yu, H.R. Kim, J.Y. Lee, V.A. Mulamoottil, G. Chandra, W.S. Byun, S.K. Lee, Y.C. Kim, L.S. Jeong, Design, synthesis and anticancer activity of fluorocyclopentenyl-purines and – pyrimidines, Eur. J. Med. Chem. 155 (2018) 406–417. https://doi.org/10.1016/j.ejmech.2018.06.003.

[242] J.C. Lee, S. Francis, D. Dutta, V. Gupta, Y. Yang, J.Y. Zhu, J.S. Tash, E. Schönbrunn, G.I. Georg, Synthesis and evaluation of eight- and four-membered iminosugar analogues as inhibitors of testicular ceramide-specific glucosyltransferase, testicular β-glucosidase 2, and other glycosidases, J. Org. Chem. 77 (2012) 3082–3098. https://doi.org/10.1021/jo202054g.

[243] N.D. Vetter, R.C. Jagdhane, B.J. Richter, D.R.J. Palmer, Carbocyclic Substrate Analogues Reveal Kanosamine Biosynthesis Begins with the α-Anomer of Glucose 6-Phosphate, ACS Chem. Biol. 15 (2020) 2205–2211. https://doi.org/10.1021/acschembio.0c00409.

[244] O. Trott, A.J. Olson, AutoDock Vina: Improving the Speed and Accuracy of Docking with a New Scoring Function, Efficient Optimization, and Multithreading, J. Comput. Chem. 31 (2010) 455–461. https://doi.org/10.1002/jcc.21334.

[245] Z. Wang, H. Sun, X. Yao, D. Li, L. Xu, Y. Li, S. Tian, T. Hou, Comprehensive evaluation of ten docking programs on a diverse set of protein-ligand complexes: The prediction accuracy of sampling power and scoring power, Phys. Chem. Chem. Phys. 18 (2016) 12964–12975. https://doi.org/10.1039/c6cp01555g.

[246] K. Stott, J. Keeler, Q.N. Van, A.J. Shaka, One-Dimensional NOE Experiments Using Pulsed Field Gradients, J. Magn. Reson. 125 (1997) 302–324.

https://doi.org/10.1006/jmre.1997.1110.

[247] Y. Binev, M.M.B. Marques, J. Aires-de-Sousa, Prediction of1H NMR coupling constants with associative neural networks trained for chemical shifts, J. Chem. Inf. Model. 47 (2007) 2089–2097. https://doi.org/10.1021/ci700172n.

[248] A. Daina, O. Michielin, V. Zoete, SwissADME: A free web tool to evaluate pharmacokinetics, drug-likeness and medicinal chemistry friendliness of small molecules, Sci. Rep. 7 (2017) 42717. https://doi.org/10.1038/srep42717.

[249] A. Daina, O. Michielin, V. Zoete, iLOGP: A Simple, Robust, and Efficient Description of n -Octanol/Water Partition Coefficient for Drug Design Using the GB/SA Approach, J. Chem. Inf. Model. 54 (2014) 3284–3301. https://doi.org/10.1021/ci500467k.

[250] C.A. Lipinski, F. Lombardo, B.W. Dominy, P.J. Feeney, Experimental and computational approaches to estimate solubility and permeability in drug discovery and development settings, Adv. Drug Deliv. Rev. 46 (2012) 3–26. https://doi.org/10.1016/j.addr.2012.09.019.

[251] R.J. Faggyas, N.L. Sloan, N. Buijs, A. Sutherland, Synthesis of Structurally Diverse Benzotriazoles via Rapid Diazotization and Intramolecular Cyclization of 1,2-Aryldiamines, European J. Org. Chem. 2019 (2019) 5344–5353. https://doi.org/10.1002/ejoc.201900463.

[252] E.Z. and G.R.H. Marcus D Hanwell1,2*,DonaldECurtis3, David C Lonie4, Tim Vandermeersch5, Avogadro: an advanced semantic chemical editor, visualization, and analysis platform, Adv. Math. (N. Y). 262 (2014) 476–483. https://doi.org/10.1016/j.aim.2014.05.019.

[253] W. Humphrey, A. Dalke, K. Schulten, VMD: Visual Molecular Dynamics, J. Mol. Graph. 14 (1996) 33–38. https://doi.org/https://doi.org/10.1016/0263-7855(96)00018-5.

[254] N.M. O'Boyle, M. Banck, C.A. James, C. Morley, T. Vandermeersch, G.R. Hutchison, Open Babel, J. Cheminform. 3 (2011) 1–14. https://doi.org/10.1186/1758-2946-3-33.

[255] J.C. Phillips, R. Braun, W. Wang, J. Gumbart, E. Tajkhorshid, E. Villa, C. Chipot, R.D. Skeel, L. Kalé, K. Schulten, Scalable molecular dynamics with NAMD, J. Comput. Chem. 26 (2005) 1781–1802. https://doi.org/10.1002/jcc.20289.

[256] S. Jo, T. Kim, V.G. Iyer, W. Im, CHARMM-GUI: A Web-based Graphical User Interface for CHARMM, J. Chem. Theory Comput. 29 (2008) 1859–1865. https://doi.org/0.1002/jcc.20945.

[257] S. Jo, X. Cheng, S.M. Islam, L. Huang, H. Rui, A. Zhu, H.S. Lee, Y. Qi, W. Han, K. Vanommeslaeghe, J. A.D. MacKerell, B. Roux, W. Im, CHARMM-GUI PDB Manipulator for Advanced Modeling and Simulations of Proteins Containing Non-standard Residues, Adv. Protein Chem. Struct. Biol. 96 (2014) 235–265. https://doi.org/10.1016/bs.apcsb.2014.06.002.

[258] S. Kim, J. Lee, S. Jo, C.L. Brooks III, S. Lee, W. Im, CHARMM-GUI Ligand Reader and Modeler for CHARMM Force Field Generation of Small Molecules, J. Comput. Chem. 38 (2017) 1879–1886. https://doi.org/10.1002/jcc.24829.

[259] S. Jo, K.C. Song, H. Desaire, J. A.D. MacKerell, W. Im, Glycan Reader: Automated Sugar Identification and Simulation Preparation for Carbohydrates and Glycoproteins, J. Comput. Chem. (2011) 3135–3141. https://doi.org/10.1002/jcc.21886.

[260] S.-J. Park, J. Lee, D.S. Patel, H. Ma, H.S. Lee, S. Jo, W. Im, Glycan Reader is Improved to Recognize Most Sugar Types and Chemical Modifications in the Protein Data Bank, Bioinformatics. (2017) 3051–3057. https://doi.org/https://doi.org/10.1093/bioinformatics/btx358.

[261] S.-J. Park, J. Lee, Y. Qi, N.R. Kern, H.S. Lee, S. Jo, I. Joung, K. Joo, J. Lee, W. Im, CHARMM-GUI Glycan Modeler for Modeling and Simulation of Carbohydrates and Glycoconjugates, Glycobiology. (2019) 320–331. https://doi.org/10.1093/glycob/cwz003.

[262] S.R. Durell, B.R. Brooks, A. Ben-Naim, Solvent-induced forces between two hydrophilic groups, J. Phys. Chem. 98 (1994) 2198–2202. https://doi.org/10.1021/j100059a038.

[263] H. Liu, T. Hou, CaFE: A tool for binding affinity prediction using end-point free energy methods, Bioinformatics. 32 (2016) 2216–2218. https://doi.org/10.1093/bioinformatics/btw215.

[264] P. Lecca, I. Laurenzi, F. Jordan, Deterministic chemical kinetics, Determ. Versus Stoch. Model. Biochem. Syst. Biol. (2013) 1–34. https://doi.org/10.1533/9781908818218.1.